JSCSEN 89(10) 1255-1399 (2024)

ISSN 1820-7421(Online)

Journal of the Serbian Chemical Society

Electronic version

VOLUME 89

NO 10

BELGRADE 2024

Available on line at

www.shd.org.rs/JSCS/

The full search of JSCS is available through

DOAJ DIRECTORY OF OPEN ACCESS JOURNALS

www.doaj.org

The **Journal of the Serbian Chemical Society** (formerly Glasnik Hemijskog društva Beograd), one volume (12 issues) per year, publishes articles from the fields of chemistry. The **Journal** is financially supported by the **Ministry of Education, Science and Technological Development of the Republic of Serbia.**

Articles published in the **Journal** are indexed in **Clarivate Analytics products: Science Citation Index-Expanded™** – accessed *via* **Web of Science®** and **Journal Citation Reports®**.

Impact Factor announced on 28 June, 2023: **1.000; 5-year Impact Factor**: **1.100**.

Articles appearing in the **Journal** are also abstracted by: **Scopus, Chemical Abstracts Plus (CAplus℠), Directory of Open Access Journals, Referativnii Zhurnal (VINITI), RSC Analytical Abstracts, EuroPub, Pro Quest** and **Asian Digital Library.**

Publisher:	**Serbian Chemical Society**, Karnegijeva 4/III, P. O. Box 36, 1120 Belgrade 35, Serbia tel./fax: +381–11–3370–467, E-mails: **Society** – shd@shd.org.rs; **Journal** – jscs@shd.org.rs Home Pages: **Society** – http://www.shd.org.rs/, **Journal** – http://www.shd.org.rs/JSCS/
Internet Service:	Contents, Abstracts and full papers (from Vol 64, No. 1, 1999) are available in the electronic form at the Web Site of the **Journal** (http://www.shd.org.rs/JSCS/).
Former Editors:	**Nikola A. Pušin** (1930–1947), **Aleksandar M. Leko** (1948–1954), **Panta S. Tutundžić** (1955–1961), **Miloš K. Mladenović** (1962–1964), **Đorđe M. Dimitrijević** (1965–1969), **Aleksandar R. Despić** (1969–1975), **Slobodan V. Ribnikar** (1975–1985), **Dragutin M. Dražić** (1986–2006).
Editor-in-Chief:	BRANISLAV Ž. **NIKOLIĆ**, Serbian Chemical Society (E-mail: jscs-ed@shd.org.rs)
Deputy Editor:	DUŠAN **SLADIĆ**, Faculty of Chemistry, University of Belgrade
Sub editors:	
Organic Chemistry	DEJAN **OPSENICA**, Institute of Chemistry, Technology and Metallurgy, University of Belgrade JÁNOS **CSANÁDI**, Faculty of Science, University of Novi Sad
Biochemistry and Biotechnology	OLGICA **NEDIĆ**, INEP – Institute for the Application of Nuclear Energy, University of Belgrade
Inorganic Chemistry	BILJANA **GLIŠIĆ**, Faculty of Science, University of Kragujevac
Theoretical Chemistry	IVAN **JURANIĆ**, Serbian Chemical Society
Physical Chemistry	LJILJANA **DAMJANOVIĆ-VASILIĆ**, Faculty of Physical Chemistry, University of Belgrade
Electrochemistry	SNEŽANA **GOJKOVIĆ**, Faculty of Technology and Metallurgy, University of Belgrade
Analytical Chemistry	RADA **BAOŠIĆ**, Faculty of Chemistry, University of Belgrade
Polymers	BRANKO **DUNJIĆ**, Faculty of Technology and Metallurgy, University of Belgrade
Thermodynamics	MIRJANA **KIJEVČANIN**, Faculty of Technology and Metallurgy, University of Belgrade
Chemical Engineering	TATJANA **KALUĐEROVIĆ RADOIČIĆ**, Faculty of Technology and Metallurgy, University of Belgrade
Materials	RADA **PETROVIĆ**, Faculty of Technology and Metallurgy, University of Belgrade
Metallic Materials and Metallurgy	ANA **KOSTOV**, Mining and Metallurgy Institute Bor, University of Belgrade
Environmental and Geochemistry	VESNA **ANTIĆ**, Faculty of Agriculture, University of Belgrade
History of and Education in Chemistry	DRAGICA **TRIVIĆ**, Faculty of Chemistry, University of Belgrade
English Language Editors:	LYNNE **KATSIKAS**, Serbian Chemical Society VLATKA **VAJS**, Serbian Chemical Society JASMINA **NIKOLIĆ**, Faculty of Technology and Metallurgy, University of Belgrade
Technical Editors:	VLADIMIR **PANIĆ**, Institute of Chemistry, Technology and Metallurgy, University of Belgrade, MARIO **ZLATOVIĆ**, Faculty of Chemistry, University of Belgrade
Journal Manager & Web Master:	MARIO **ZLATOVIĆ**, Faculty of Chemistry, University of Belgrade
Office:	VERA **ĆUŠIĆ**, Serbian Chemical Society

Editorial Board

From abroad: **R. Adžić**, Brookhaven National Laboratory (USA); **A. Casini**, University of Groningen (The Netherlands); **G. Cobb**, Baylor University (USA); **D. Douglas**, University of British Columbia (Canada); **G. Inzelt**, Etvos Lorand University (Hungary); **J. Kenny**, University of Perugia (Italy); **Ya. I. Korenman**, Voronezh Academy of Technology (Russian Federation); **M. D. Lechner**, University of Osnabrueck (Germany); **S. Macura**, Mayo Clinic (USA); **M. Spiteller**, INFU, Technical University Dortmund (Germany); **M. Stratakis**, University of Crete (Grecce); **M. Swart**, University de Girona (Cataluna, Spain); **G. Vunjak-Novaković**, Columbia University (USA); **P. Worsfold**, University of Plymouth (UK); **J. Zagal**, Universidad de Santiago de Chile (Chile).

From Serbia: **B. Abramović**, **V. Antić**, **R. Baošić**, **V. Beškoski**, **J. Csanadi**, **Lj. Damjanović-Vasilić**, **A. Dekanski**, **V. Dondur**, **B. Dunjić**, **M. Đuran**, **B. Glišić**, **S. Gojković**, **I. Gutman**, **B. Jovančićević**, **I. Juranić**, **T. Kaluđerović Radoičić**, **L. Katsikas**, **M. Kijevčanin**, **A. Kostov**, **V. Leovac**, **S. Milonjić**, **V.B. Mišković-Stanković**, **O. Nedić**, **B. Nikolić**, **J. Nikolić**, **D. Opsenica**, **V. Panić**, **M. Petkovska**, **R. Petrović**, **I. Popović**, **B. Radak**, **S. Ražić**, **D. Sladić**, **S. Sovilj**, **S. Šerbanović**, **B. Šolaja**, **Ž. Tešić**, **D. Trivić**, **V. Vajs, M. Zlatović**.

Subscription: The annual subscription rate is **150.00 €** including postage (surface mail) and handling. For Society members from abroad rate is **50.00 €**. For the proforma invoice with the instruction for bank payment contact the Society Office (E-mail: shd@shd.org.rs) or see JSCS Web Site: http://www.shd.org.rs/JSCS/, option Subscription.

Godišnja pretplata: Za članove SHD: **2.500,00 RSD**, za penzionere i studente: **1000,00 RSD**, a za ostale: **3.500,00 RSD**:za organizacije i ustanove: **16.000,00 RSD**. Uplate se vrše na tekući račun Društva: **205-13815-62**, poziv na broj **320**, sa naznakom "pretplata za JSCS".

Nota: Radovi čiji su svi autori članovi SHD prioritetno se publikuju.

Odlukom Odbora za hemiju Republičkog fonda za nauku Srbije, br. 66788/1 od 22.11.1990. godine, koja je kasnije potvrđena odlukom Saveta Fonda, časopis je uvršten u kategoriju međunarodnih časopisa (**M-23**). Takođe, aktom Ministarstva za nauku i tehnologiju Republike Srbije, 413-00-247/2000-01 od 15.06.2000. godine, ovaj časopis je proglašen za publikaciju od posebnog interesa za nauku. **Impact Factor** časopisa objavljen 28. juna 2023. godine je **1,000**, a petogodišnji **Impact Factor 1,100**.

Journal of the Serbian Chemical Society
JSCS-info@shd.org.rs • www.shd.org.rs/JSCS

J. Serb. Chem. Soc. Vol. 89, No. 10 (2024)

CONTENTS*

Organic Chemistry

F. Đurković, M. Zlatović, D. Sladić, I. Novaković, F. Bihelović and *Z. Ferjančić*: *N*-2 Alkylated analogues of aza-galactofagomine as potential inhibitors of *β*-glucosidase .. 1255

Biochemistry and Bioengineering

N. Surudžić, M. Simić, M. Crnoglavac Popović, R. El Gahwash, M. Spasojević Savković, R. Prodanović and *O. Prodanović*: Immobilization of periodate-oxidized horseradish peroxidase by adsorption on sepiolite 1269

Theoretical Chemistry

S. Aytaç: Synthesis of and theoretical research on some azine derivatives and investigation of their antimicrobial activities 1285

R. R. Guminilovych, P. *Y. Shapoval, M. A. Sozanskyi, V. Y. Stadnik* and *L. R. Deva*: Mathematical approaches to a method of semiconductor materials films synthesis type $A^{II}B^{VI}$ for photosensitive structures used in alternative energy 1299

Physical Chemistry

S. Rabii, A. Lahmidi, S. Chtita, M. El Kouali, M. Talbi and *A. Errougui*: Molecular dynamics modelling of the structural, dynamic and dielectric properties of the LiF––ethylene carbonate energy storage system at various temperatures 1311

Electrochemistry

M. M. Kubota, R. V. Fernandes and *H. de Santana*: Electrical, optical and structural characterization of interfaces containing poly(3-alkylthiophenes) (P3ATs) and polydiphenylamine on ITO/TiO_2: Interaction between P3ATs polymeric segments and TiO_2 1323

Analyical Chemistry

A. Moghadasi, S. Yousefinejad, E. Soleimani, S. Taghvaei and *S. Jafai*: Dispersive liquid–liquid microextraction for determining urinary muconic acid as benzene biological indicator 1337

J. A. Teixeira, A. S. de Souza, L. D. S. M. K. de Melo and *T. A. D. Colman*: Characterization of enalapril maleate: An approach using thermoanalytical, thermokinetic and spectroscopic techniques 1353

Polymers

M. Dhiman, A. Upmanyu, D. Pal Singh and *K. C. Juglan*: Ultrasonic and spectroscopic investigations of molecular interactions in binary mixture of PEG-400 and DMSO at different temperatures 1363

Metallic Materials and Metallurgy

S. Sundaram and *M. Kumarasamy*: Joint characteristics and process parameters optimization on friction stir welding of AA 2024-T6 and AA 5083-H111 aluminum alloys 1387

Published by the Serbian Chemical Society
Karnegijeva 4/III, P.O. Box 36, 11120 Belgrade, Serbia
Printed by the Faculty of Technology and Metallurgy
Karnegijeva 4, P.O. Box 35-03, 11120 Belgrade, Serbia

* For colored figures in this issue please see electronic version at the Journal Home Page: http://www.shd.org.rs/JSCS/

Journal of the Serbian Chemical Society
JSCS@tmf.bg.ac.rs • www.shd.org.rs/JSCS
J. Serb. Chem. Soc. *89* (10) 1255–1267 (2024)
JSCS–5785
Original scientific paper
Published 28 August, 2024

N-2 Alkylated analogues of aza-galactofagomine as potential inhibitors of *β*-glucosidase

FILIP ĐURKOVIĆ[1], MARIO ZLATOVIĆ[1#], DUŠAN SLADIĆ[1#], IRENA NOVAKOVIĆ[2#], FILIP BIHELOVIĆ[1]* and ZORANA FERJANČIĆ[1#]**

[1]*University of Belgrade – Faculty of Chemistry, Studenstki trg 12–16, Belgrade, Serbia and* [2]*University of Belgrade – Institute of Chemistry, Technology and Metallurgy, Njegoševa 12, Belgrade, Serbia*

(Received 15 March, revised 23 April, accepted 16 June 2024)

Abstract: The synthesis of four *N*-2-alkylated aza-galactofagomine (AGF) analogues was achieved by intermolecular reductive hydrazination or alkylation of suitably protected AGF. The synthesized compounds were evaluated as potential *β*-glucosidase inhibitors. The preliminary screening of inhibitor activity, conducted with sweet almond *β*-glucosidase immobilized in agar, as well as the standard inhibition assay with the same enzyme, showed the inhibitory potency of the synthesized analogues. In addition, these results are in a good agreement with the docking analysis of the human acid *β*-glucosidase, the enzyme implicated in Gaucher's disease.

Keywords: iminosugars; glycosidase inhibitor; Gaucher's disease.

INTRODUCTION

Glycosidases represent a large group of hydrolytic enzymes that catalyse the breaking of glycosidic bonds in various sugars. As enzymatic hydrolysis of carbohydrates is a widespread biological process, therefore glycosidase inhibitors have a wide range of applications, from agriculture to medicine. Glycosidases are involved in the biosynthesis of oligosaccharide chains of glycoproteins in the endoplasmic reticulum and the Golgi apparatus. Inhibition of these glycosidases has an impact on post-translational modifications, transport and secretion of glycoproteins, which play a role in communication between cells and cell–virus recognition, among other things. Inhibition of glycosidases results in an impact on these processes, and glycosidase inhibitors can potentially be used to treat viral diseases, cancer and genetic disorders.[1]

* Corresponding authors. E-mail: (*)filip@chem.bg.ac.rs; (**)zferjan@chem.bg.ac.rs
# Serbian Chemical Society member.
https://doi.org/10.2298/JSC240315062D

Glucosidase inhibitors are currently of interest owing to their promising therapeutic potential in the treatment of disorders such as diabetes, human immunodeficiency virus (HIV) infection, metastatic cancer, and lysosomal storage diseases.[2]

Over the last two decades polyhydroxylated azaheterocycles, also known as iminosugars,[3,4] have attracted notable interest among scientific community because of their ability to act as pharmacological chaperones (PC) for a variety of glycosidases.[5] This concept is very attractive from the medical point of view and considered as a promising new tool for the treatment of a range of pathologies known as lysosomal storage disorders.[6] The mutations associated with these diseases cause various glycosidases from lysosome to fold improperly, resulting in partially or totally inactive enzymes, that cannot pass quality control in endoplasmic reticulum. In cases where the disease is caused by misfolding of glycosidases, pharmacological chaperone therapy (PCT) is often effective.[7]

β-Glucosidase catalyses the hydrolysis of various *β*-glucosidic bonds within di- and oligosaccharides, as well as glucoconjugates. It is significant from a medical aspect, as the deficiency of lysosomal acid *β*-glucosidase leads to the accumulation of glucocerebroside in some cells, which is characteristic for Gaucher's disease.[8–10] Furthermore, *β*-glucosidase has been confirmed to be overexpressed in breast, liver and gastric cancer cells.[11] In breast cancer, it has been shown that the inhibition of *β*-glucosidase might be an alternative therapeutic strategy to overcome chemoresistance.[12] On the other hand, malfunction or deficiency of lysosomal *β*-galactocerebrosidase causes progressive demyelination in the central nervous system and neurodegeneration.[13] This rare and severe genetic neurological disorder is known as the Krabbe disease.[14] Given that both of these glycosidases act in lysosomes, there is a possibility that some glucosidase inhibitors may act as multi-target molecules. The fact that aza-galactofagomine (**1**) (AGF, Fig. 1) acts as a competitive inhibitor of *β*-galactocerebrosidase,[15,16] prompted us to investigate whether AGF derivatives can also be inhibitors of *β*-glucosidases. Recently, we have developed an enantioselective method for the preparation of AGF (**1**), that relies on a tactical combination of organocatalyzed aldolization/reductive hydrazination and this short synthesis offers an easy access to *N*-2 analogues of AGF.[17] Therefore, our goal was to synthesize *N*-2 AGF analogues containing hydrophobic alkyl chains of different length, including those with aromatic ring, and to test them as the inhibitors of *β*-glucosidases. Our preliminary modelling studies suggested that interactions of

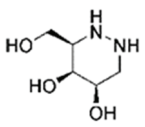

1

Fig. 1. Structure of aza-galactofagomine **1** (AGF).

these hydrophobic groups with enzyme should be relevant for the activity. A commercially available *β*-glucosidase from sweet almond (*Prunus dulcis*) was selected as a widely used model enzyme, as it shows a broad substrate specificity. The results of this study are presented herein.

EXPERIMENTAL

All chromatographic separations were performed on silica gel 60 (0.063–0.200 mm), Merck. Standard techniques were used for the purification of reagents and solvents. NMR spectra were recorded on Varian/Agilent 400 (^{1}H-NMR at 400 MHz; ^{13}C-NMR at 100 MHz) and on Bruker Avance III 500 (^{1}H-NMR at 500 MHz; ^{13}C-NMR at 125 MHz), in deuterated chloroform, if not otherwise stated. Chemical shifts are expressed in ppm (δ) using tetramethylsilane as internal standard, coupling constants (J) are in Hz. IR spectra were recorded on Thermo Scientific Nicolet Summit FT-IR instrument, and are expressed in cm^{-1}. Mass spectra were obtained on Orbitrap Exploris 240 spectrometer.

For all synthesized compounds detailed experimental procedures, spectral data and copies of NMR spectra are given in Supplementary material to this paper.

Chemistry

Four AGF analogues **12**–**14** and **22** were obtained from the key intermediate **6**. Compound **6** was obtained according to the slightly modified literature procedure.[17] Compounds **12**–**14** were obtained by reductive hydrazination of **6**, followed by deprotection. Compound **22** was obtained by silylation of **6**, followed by alkylation/deprotection sequence.

Biochemical and computational methods

Preliminary screening of β*-glucosidase inhibitory activity.*[18] Enzyme *β*-glucosidase from sweet almond was immobilized in agar by gelling. As a substrate, esculin was used, which is transformed into esculetin and glucose after an enzymatic reaction. The released esculetin forms complexes with the added $FeCl_3$, developing a dark gel colour. If light spots appear on the agar after inoculation of the compounds and enzyme–substrate reaction, the compounds show enzyme inhibition. In 7 mL sodium acetate buffer (0.1 M, pH 5) 0.07 g of agar powder was dissolved at 80–100 °C. After cooling at 60 °C, 1.2 mL of 0.5 % $FeCl_3$ and 40 μL of enzyme *β*-glucosidase (0.02 IU mL^{-1}) were added. The final volume was adjusted to 10 mL with acetate buffer and the solution was poured into a Petri dish. After solidification of the agar, 5 μL of each compound (concentration of 1 μg μL^{-1}) were inoculated on the agar surface. As a positive control, conduritol *β*-epoxide was used. The plate was incubated for 15 min at room temperature to allow reaction between the enzyme and inhibitors, after which 7 mL of 0.2 % esculin solution was added to cover the agar surface. Afterwards, the plate was incubated for 30 min at room temperature for enzyme–substrate reaction, and clear zones were observed.

β-*Glucosidase inhibition assay*.[19] The enzyme activity was determined by measuring (absorbance at 405 nm) the hydrolysis rate of *p*-nitrophenyl-*β*-D-glucopyranoside (pNGP). The amount of released *p*-nitrophenol (pNP) was determined from the previously constructed standard curve of absorbance *vs*. pNP concentration (the range of concentration was 1–7 mM). After incubation (15 min at 50 °C) of the enzyme (0.02 IU) with different concentrations of the tested compounds (the concentration range was 5–0.075 μg/1.5 mL reaction solution), the amount of released pNP was determined and the percentage of enzyme inhibition was calculated. From the curve of dependence of the percentage of inhibition *vs*. the compound con-

centrations, the IC_{50} value (concentration at which 50 % of the enzyme was inhibited) was calculated. 100 μL of *β*-glucosidase solution (0.03 IU mL^{-1}) was mixed with 5 μL of test compounds and incubated at 50 °C for 15 min. Then, 900 μL of pNPG solution (5 mM) in citrate buffer (50 mM, pH 7.0) was added to that solution and incubated for another 10 min at the same temperature, after which 495 μL of ice-cold sodium carbonate (0.5 M) was added and absorbance at 405 nm was measured. All experiments were performed in triplicate.

Molecular docking studies. Crystal structure of human acid *β*-glucosidase from lysosome (PDB ID 2NSX)[20] was downloaded from RSCB database.[21] Protein structure was prepared using Protein Preparation Wizard from Schrödinger Suite 2021-3 and chain B was used. Small molecules were prepared using Maestro and their pK_a values were determined using Schrödinger Suite 2021-3.[22] Figures were prepared using the academic version of Maestro viewer from Schrödinger Suite 2024-1.[23]

RESULTS AND DISCUSSION

Our synthetic pathway toward AGF analogues started with organocatalyzed asymmetric aldol reaction between 2,2-dimethyl-1,3-dioxan-5-one (**3**, dioxanone) and protected hydrazinoaldehyde **2** (Scheme 1). The reactions proceed smoothly when (*R*)-proline was used as a catalyst, giving optically pure aldol adduct **4** in 55 % yield. Removal of the Cbz protecting group in aldol **4** was effected by catalytic hydrogenation using a 10 % Pd/C catalyst in methanol to give compound **5**, which is sufficiently pure for the use in the next step without further purification. Treatment of crude **5** with excess $NaBH_3CN$, in a mixture of AcOH/ /methanol = 4:1 volume ratio, gave the cyclic product of reductive hydrazination **6** in good yield (65 %, over two steps). Compound **6**, with free *N*-2 and protected *N*-1 atoms on the piperazine ring, is a suitable precursor of *N*-2 analogues of AGF.

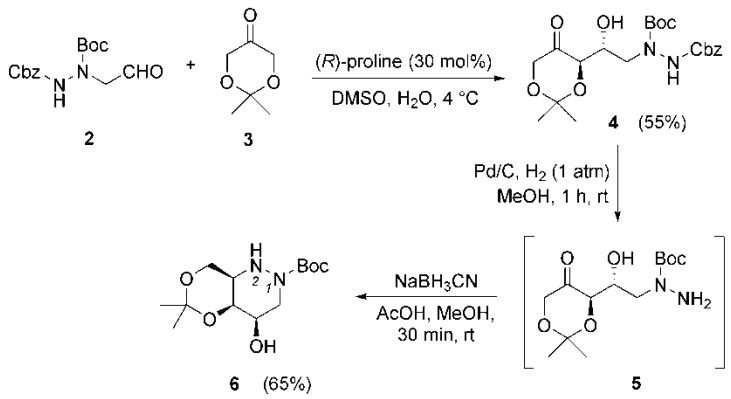

Scheme 1. Synthesis of compound **6** – a precursor of *N*-2 analogues of AGF.

We decided to derivatize *N*-2 nitrogen atom in **6** through reductive hydrazination or protection/alkylation sequence. First, we explored the possibility of reductive hydrazination by applying the protocol that Lopez developed for the alkylation of aza-fagomine (Scheme 2).[24] A mixture of the compound **6** and a proper

aldehyde was exposed to a hydrogen atmosphere, with palladium on charcoal as a catalyst. Under these conditions the intermediate **6** reacted smoothly with unhindered aldehydes and the products **7**–**9** were obtained in high yields. However, *β*-branched aldehydes, such as 2-phenylacetaldehyde and 2-cyclohexylacetaldehyde, failed to react, probably due to the presence of a bulky Boc protective group on the *N*-1 atom of hydrazine. Moreover, the reductive hydrazination of **6** with $NaBH_3CN$, as an alternative reagent, was also ineffective with branched aldehydes (similar results were obtained by Lopez on aza-fagomine).[24] Removal of both protecting groups was carried out under acidic conditions, giving analogs of AGF **12**–**14** in high yields, in the form of hydrazine hydrochloride salts.

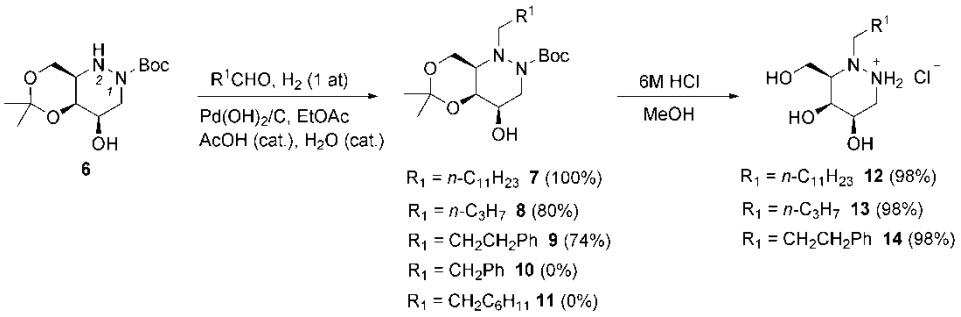

Scheme 2. Synthesis of *N*-2 alkylated analogues **12**–**14** of aza-galactofagomine by reductive hydrazination.

Alternatively, *N*-2 substitution in **6** can be accomplished by alkylation, albeit only with highly reactive alkylating agents (Scheme 3). The free OH group in compound **6** was protected as a silyl ether, and the resulting product **15** was treated with benzyl or alkyl halide in the presence of cesium carbonate at elevated temperature. Although an excess of both the base and the alkylating agent were used, the reaction does not go to completion even with prolonged reaction time. In addition to the reaction products **16**–**18**, obtained in moderate yields in all cases, smaller amounts of the starting substrate **15** were isolated. Removal of silyl and acetal protecting groups was effected with methanolic HCl, furnishing **19**–**21**. Boc deprotection of **19** with 6M HCl afforded AGF analogue **22**-HCl in quantitative yield. Unfortunately, under the same reaction conditions **20** and **21** gave a complex mixture of products.

In the end, derivatization of the *N*-2 position was also attempted through acylation (Scheme 4). Treatment of the intermediate **15** with benzoyl or butanoyl chloride gave *N*-2-acylated derivatives **23** and **24** in high yields. Acetal and TBS groups were cleanly removed with a diluted acid (3M HCl, MeOH), resulting in excellent yields of compounds **25** and **26**. However, the attempts to deprotect *N*-1

atom in **25** or **26** were unsuccessful: with either 6M HCl/MeOH or TFA/CH_2Cl_2 a complex mixture of products was obtained.

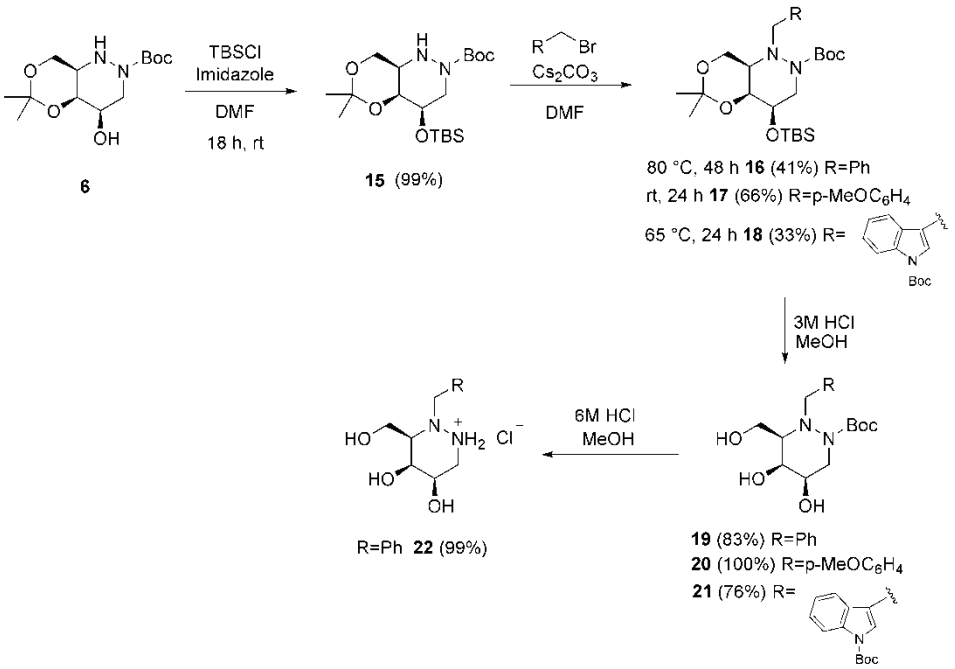

Scheme 3. Synthesis of *N*-2 alkylated analogue **22** of aza-galactofagomine by alkylation.

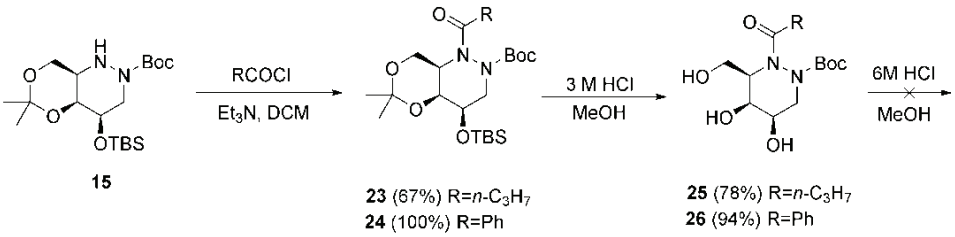

Scheme 4. *N*-2 Acylation of compound **15**.

Preliminary screening of potential β-glucosidase inhibitors

Despite the fact that the enzyme is immobilized in agar and the migration of compounds is aggravated, this test is good for rapid screening of potential enzyme inhibitors. The preliminary test results, presented in Fig. 2, confirmed that the synthesized compounds inhibit *β*-glucosidase, given that light spots appeared on the agar after the inoculation of the compound and the enzyme–substrate reaction.

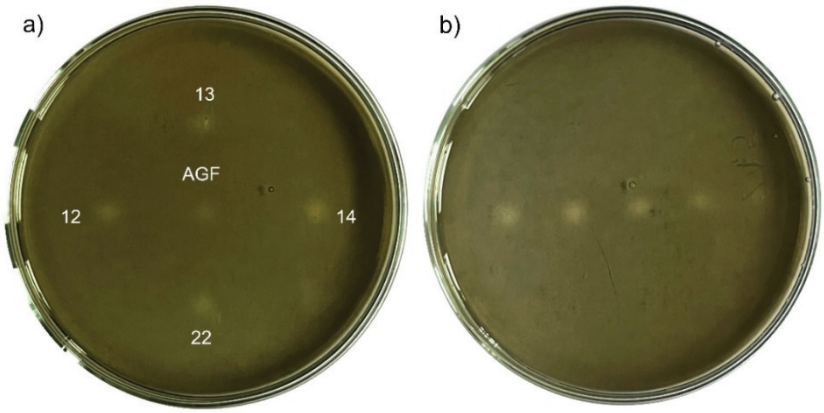

Fig. 2. *β*-Glucosidase inhibition using the agar plate method. a) Tested compounds were inoculated on agar surface in doses of 5 μg. b) Conduritol *β*-epoxide in different doses: 2.5, 1, 0.5, 0.1 and 0.05 μg, from left to right.

β-Glucosidase inhibition assay

Based on the results obtained by *β*-glucosidase inhibition assay (Table I) it can be concluded that the strongest inhibition effect was observed for compound **14**. This compound expressed only two times weaker inhibition than the control compound conduritol *β*-epoxide. A somewhat lower degree of inhibition was shown by compound **12**, while compounds **13** and **22** showed some inhibitory potential, but at slightly higher micromolar concentrations. If the structures of the compounds and their inhibitory capacity are compared, it can be observed that longer substituents on the iminosugar moiety increase the inhibition of the enzyme. By comparing the activity of compounds **14** and **22**, it can be seen that a longer linker between the bulky phenyl group and the iminosugar core, also increases the inhibitory potential of the compound. Previously, it was reported that compound **1** showed strong inhibitory effect on *β*-glucosidase from almond.[25] In the enzyme assay that we applied all synthesized compounds showed better enzyme inhibition than the parent compound AGF (**1**). Such encouraging preliminary results can provide guidelines for the rational design and the synthesis of new compounds that would show better grade of inhibition.

TABLE I. Inhibition of *β*-glucosidase results

Compound	**12**	**13**	**14**	**22**	AGF (**1**)	Conduritol *β*-epoxide
IC_{50} / μM	3.03±0.04	10.72±0.13	2.08±0.05	5.90±0.09	14.29±0.07	1.06±0.06

Molecular docking studies

In order to investigate the possibility of bioactivity of synthesized compounds in humans, we simulated binding of five derivatives to human acid-*β*-

-glucosidase using molecular docking. As a target protein we used previously prepared structure of human acid β-glucosidase from lysosome (PDB ID 2NSX).[20] Having in mind that lysosomes maintain rather acidic environment of pH 4.5–5.0,[26] pK_a values for nitrogen atoms in small molecules were determined using Epik module from Schrödinger Suite 2021-3 at pH 5.00±2.00. Results showed that compounds **12**–**14** would have a protonated substituted nitrogen atom at pH 5.00±2.00 in given environment. For the structure **22** a small energy difference between neutral and protonated form was predicted, in favour of the protonated molecule, and structure of compound AGF (**1**) is predominantly neutral (Table II). The protonation state does influence binding, as we also considered binding of less probable, neutral forms. Binding energies in protonated state are twice as large as those where docking simulations were done with the neutral form. As for cellular uptake, all compounds are neutral at pH 7.4, so the compounds retain membrane permeability. Only when the compounds pass the lysosome membrane, they enter acidic environment, and the protonation becomes likely.

TABLE II. pK_a values predicted by Epik

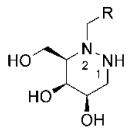

Compound	pK_a *N*-2	pK_a *N*-1
12	5.83±2.22	5.23±2.22
13	5.82±2.22	5.21±2.22
14	5.57±2.22	5.10±2.22
22	4.93±2.22	4.47±2.22
AGF (**1**)	4.98±0.94	4.41±0.94

Docking simulations were performed using Glide docking from Schrödinger Suite 2021-3,[22] using XP precision. The best docking poses for all tested molecules were selected and investigated. The results of docking simulations, the both values of Glide score and E_{model} values were in good agreement with the biological assay (Table III), with small discordance for molecules **12** and **14**, where docking scores showed better bonding for molecule **12**, although the results of biological assay showed that molecule **14** binds stronger. This kind of disagreement can emerge because of different structures of human lysosomal acid β-glucosidase and enzyme used in tests. Unfortunately, there is no crystal structure of sweet almond β-glucosidase, that was used in bioassay, and we could not compare bonding to those two proteins. Nevertheless, from the results of bioassay and docking structures, it is clear that molecules with similar structures can have significant potential as inhibitors of lysosomal acid β-glucosidase. Better binding

can be expected from molecules with bulkier, nonpolar substituent at *N*-2, preferably with a moiety capable of various π-interactions with amino acids nearby.

TABLE III. Docking scores and bioassay activities of investigated molecules

Compound	Activity	Glide score, kJ mol^{-1}	E_{model} / kJ mol^{-1}
12	3.03±0.04	–44.42	–266.45
14	2.08±0.05	–41.13	–243.25
22	5.90±0.09	–39.99	–228.12
13	10.72±0.13	–31.37	–194.34
AGF (**1**)	14.29±0.07	–23.89	–168.32

The results in Table III indicate that we can expect ligands with the same basic structure, with a longer *N*-substituent and a structure capable of aromatic interactions, to be more active at the binding site. From ligand interactions schemes (Fig. 3, other figures are in the Supplementary material) it can be seen that there are several key amino acids involved in bonding of the main scaffold. Compounds **12**, **14** and **22** bind almost identically, as seen in Fig. 4. The only possible difference was observed for the behaviour of hydroxymethyl group on C3. Hydroxyl moiety from that group can be involved in the intramolecular H-bonding with OH group from C4, or in the case of ligand **22**, in the intramole-

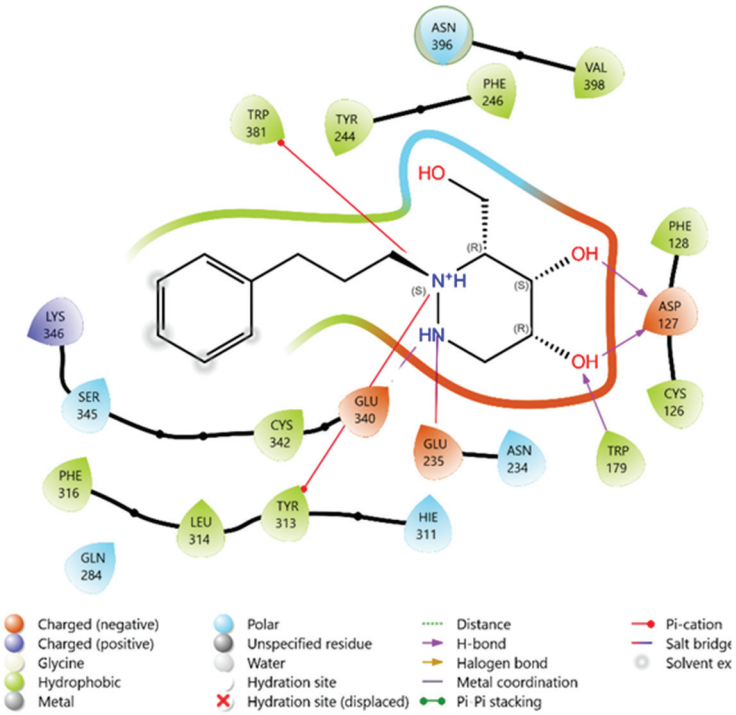

Fig. 3. Ligand interactions for molecule **14** bound to β-glucosidase.

cular π-interaction with the aromatic ring. Structures **13** and AGF (**1**) bind in the slightly different position, especially structure AGF (**1**), Fig. 5. Both have less interactions, mainly charged ones with lower binding scores, resulting in weaker binding and thus in lower activities.

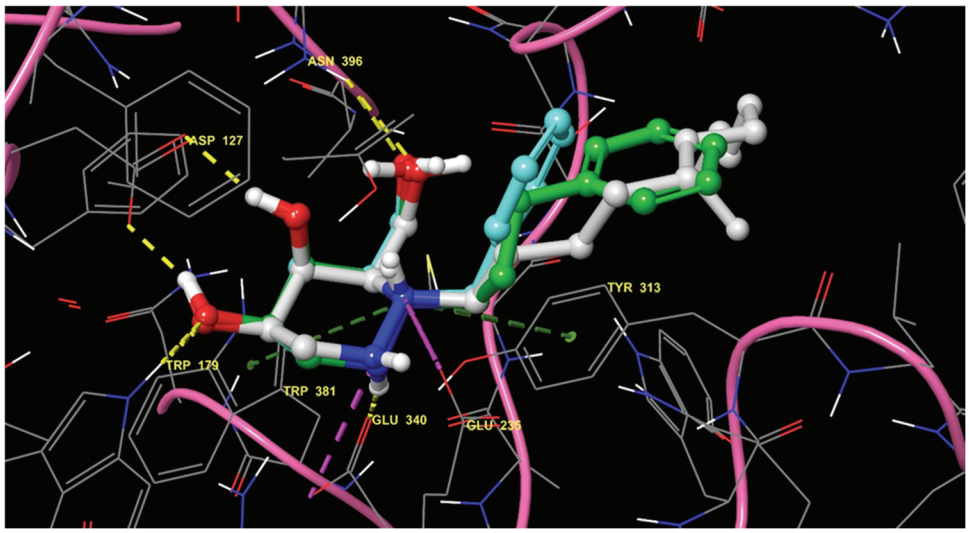

Fig. 4. Compounds **12** (grey), **14** (green) and **22** (cyan) in the binding site of human lysosomal acid *β*-glucosidase.

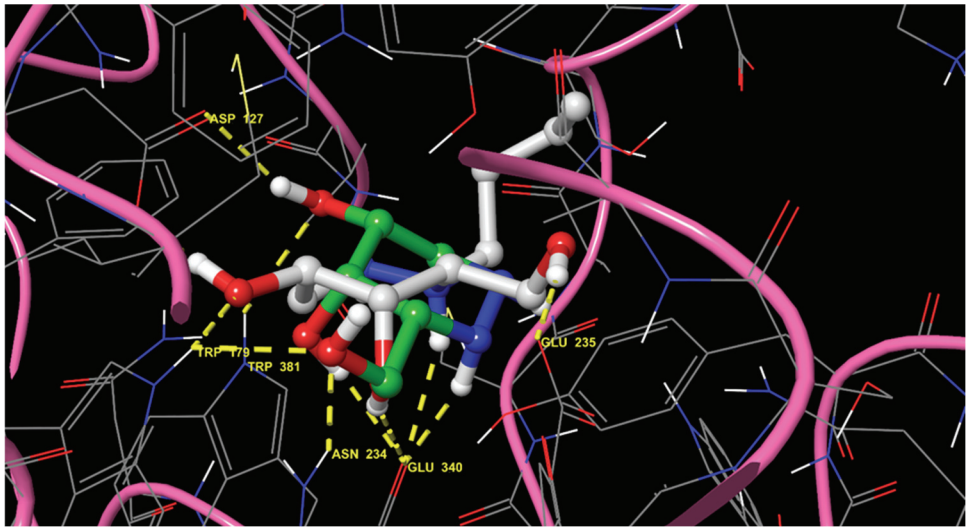

Fig. 5. Compounds **13** (grey) and **AGF** (green) in the binding site of human lysosomal acid *β*-glucosidase.

CONCLUSION

To summarize, we have reported a synthesis of four *N*-2 alkylated aza-galactofagomines, relying on the intermolecular reductive hydrazination of the suitably protected heterocyclic core, obtained in a tactical sequence comprising of enantioselective organocatalytic aldolization and intramolecular reductive hydrazination. It was shown that these analogues, containing nonpolar alkyl- or phenylalkyl-side chains are potent inhibitors of *β*-glucosidase. Compound **14**, possessing 3-phenylpropyl side-chain showed the highest inhibitory activity (2.08 μM), which is comparable to conduritol *β*-epoxide, which was a control compound. The enzyme assay results correspond well with the results of docking analysis of the human acid *β*-glucosidase. It is worth noting that *β*-glucosidase from sweet almond is a good and cheap model enzyme for preliminary testing of potential inhibitors of human acid *β*-glucosidase from lysosomes. The obtained results are encouraging for the rational design and synthesis of new iminosugar derivatives as the potential inhibitors of a human acid *β*-glucosidase, which is one of the key enzymes for Gaucher's disease.

SUPPLEMENTARY MATERIAL

Additional data and information are available electronically at the pages of journal website: https://www.shd-pub.org.rs/index.php/JSCS/article/view/12846, or from the corresponding author on request.

Acknowledgement. This research was supported by the Ministry of Science, Technological Development and Innovation of Republic of Serbia, contract numbers: 451-03-65/ /2024-03/200168 and 451-03-66/2024-03/200026.

И З В О Д

АЛКИЛОВАНИ АНАЛОЗИ АЗА-ГАЛАКТОФАГОМИНА КАО ПОТЕНЦИЈАЛНИ ИНХИБИТОРИ БЕТА-ГЛУКОЗИДАЗА

ФИЛИП ЂУРКОВИЋ[1], МАРИО ЗЛАТОВИЋ[1], ДУШАН СЛАДИЋ[1], ИРЕНА НОВАКОВИЋ[2], ФИЛИП БИХЕЛОВИЋ[1] и ЗОРАНА ФЕРЈАНЧИЋ[1]

[1]Универзитет у Београду – Хемијски факултет, Студентски трг 12–16, Београд и [2]Универзитет у Београду – Институт за хемију, технологију и металургију, Његошева 12, Београд

Четири N-2 алкилована аналога аза-галактофагомина су синтетисана применом интермолекулског редуктивног хидразиновања или алкиловања адекватно заштићеног облика аза-галактофагомина. Испитивано је инхибиторно дејство синтетисаних аналога према *β*-глукозидази. Прелиминарни тестови инхибиторне активности су урађени на *β*-глукозидази имобилисаној у агару. Овај тест, као и стандардни инхибиторни есеј са истим ензимом, указују на снажно инхибиторно дејство синтетисаних аналога. Добијени резултати се добро корелишу са резултатима докинг анализе хумане киселе *β*-глукозидазе, ензима битног за Гошеову болест.

(Примљено 15. марта, ревидирано 23. априла, прихваћено 16. јуна 2024)

REFERENCES

1. N. Asano, *Glycobiology* **13** (2003) 93R (https://doi.org/10.1093/glycob/cwg090)
2. E. Borges de Melo, A. da Silveira Gomes, I. Carvalho, *Tetrahedron* **62** (2006) 10277 (https://doi.org/10.1016/j.tet.2006.08.055)
3. *Iminosugars*: *From Synthesis to Therapeutic Applications*, P. Compain, O. R. Martin, Eds., Wiley, Chichester, 2007 (ISBN: 978-0-470-03391-3)
4. R. J. Nash, A. Kato, C.-Y. Yu, G. W. J. Fleet, *Future Med. Chem*. **3** (2011) 1513 (https://doi.org/10.4155/fmc.11.117)
5. N. J. Leidenheimer, *Targeting Trafficking in Drug Development*. Springer, Cham, 2017, p. 135 (https://doi.org/10.1007/978-3-319-74164-2)
6. R. E. Boyd, G. Lee, P. Rybczynski, E. R. Benjamin, R. Khanna, B. A. Wustman, K. J. Valenzano, *J. Med. Chem*. **56** (2013) 2705 (https://doi.org/10.1021/jm301557k)
7. E. M. Sanchez-Fernandez, J. M. Garcia Fernandez, C. O. Mellet, *Chem. Commun*. **52** (2016) 5497 (https://doi.org/10.1039/C6CC01564F)
8. L. Smith, S. Mullin, A. H.V. Schapira, *Exp. Neurol.* **298** (2017) 180 (https://doi.org/10.1016/j.expneurol.2017.09.010)
9. J. M. Benito, J. M. García Fernández, C. O. Mellet, *Expert Opin. Ther. Pat*. **21** (2011) 885 (https://doi.org/10.1517/13543776.2011.569162)
10. A. Trapero, A. Llebaria, *Future Med. Chem*. **5** (2013) 573 (https://doi.org/10.4155/fmc.13.14)
11. H. Martin, L. Ramírez Lázaro, T. Gunnlaugsson, E. M. Scanlan, *Chem. Soc. Rev.* **51** (2022) 9694 (https://doi.org/10.1039/D2CS00379A)
12. X. Zhou, Z. Huang, H. Yang, Y. Jiang, W. Wei, Q. Li, Q. Mo, J. Liu, *Biomed. Pharmacother.* **91** (2017) 504 (https://doi.org/10.1016/j.biopha.2017.04.113)
13. M. L. Feltri, N. I. Weinstock, J. Favret, N. Dhimal, L. Wrabetz, D. Shin, *Glia* **69** (2021) 2309 (https://doi.org/10.1002/glia.24008)
14. A. N. D'Agostino, G. P. Sayre, A. B. Hayles, *Arch. Neurol.* **8** (1963) 82 (https://doi.org/10.1001/archneur.1963.00460010098012)
15. C. H. Hill, A. H. Viuff, S. J. Spratley, S. Salamone, S. H. Christensen, R. J. Read, N. W. Moriarty, H. H. Jensen, J. E. Deane, *Chem. Sci*. **6** (2015) 3075 (https://doi.org/10.1039/C5SC00754B)
16. A. H. Viuff, H. H. Jensen, *Org. Biomol. Chem.* **14** (2016) 8545 (https://doi.org/10.1039/C6OB01309K)
17. J. Marjanovic Trajkovic, Z. Ferjancic, R. N. Saicic, *Tetrahedron* **73** (2017) 2629 (https://doi.org/10.1016/j.tet.2017.03.052)
18. S. Pandey, A. Sree, S.S. Dash, D.P. Sethi, *BMC Microbiol.* **13** (2003) 55 (https://doi.org/10.1186/1471-2180-13-55)
19. O. G. Korotkova, M. V. Semenova, V. V. Morozova, I. N. Zorov, L. M. Sokolova, T. M. Bubnova, O. N. Okunev, A. P. Sinitsyn, *Biochemistry (Moscow)* **74** (2009) 569 (https://doi.org/10.1134/S0006297909050137)
20. R. Lieberman, B. Wustman, P. Huertas, A. C. Powe Jr, C. W. Pine, R. Khanna, M. G. Schlossmacher, D. Ringe, G. A. Petsko, *Nat. Chem. Biol.* **3** (2007) 101 (https://doi.org/10.1038/nchembio850)
21. RCSB PDB: Protein Data Bank, https://www.rscb.org
22. *Schrödinger Release 2021-3: Protein Preparation Wizard; Maestro; Epik*; *Glide*, Schrödinger, LLC, New York, 2021
23. *Schrödinger Release 2024-1: Maestro,* Schrödinger, LLC, New York, 2024

24. O. L. Lopez, M. Bols, *ChemBioChem* **8** (2007) 657 (https://doi.org/10.1002/cbic.200700012)
25. H. H. Jensen, M. Bols, *J. Chem. Soc., Perkin Trans. 1* (2001) 905 (https://doi.org/10.1039/B007973L)
26. R. Chen, M. Jäättelä, B. Liu, *Cancers* **12** (2020) 2437 (https://doi.org/10.3390/cancers12092437).

Journal of the Serbian Chemical Society
JSCS-info@shd.org.rs • www.shd.org.rs/JSCS
J. Serb. Chem. Soc. *89* (10) S299–S337 (2024) *Supplementary material*

SUPPLEMENTARY MATERIAL TO

N-2 Alkylated analogues of aza-galactofagomine as potential inhibitors of *β*-glucosidase

FILIP ĐURKOVIĆ[1], MARIO ZLATOVIĆ[1], DUŠAN SLADIĆ[1], IRENA NOVAKOVIĆ[2], FILIP BIHELOVIĆ[1]* and ZORANA FERJANČIĆ[1]**

[1]*University of Belgrade – Faculty of Chemistry, Studenstki trg 12–16, Belgrade, Serbia and* [2]*University of Belgrade – Institute of Chemistry, Technology and Metallurgy, Njegoševa 12, Belgrade, Serbia*

J. Serb. Chem. Soc. *89* (10) (2024) 1255–1267

TABLE OF CONTENTS:

GENERAL EXPERIMENTAL S300

EXPERIMENTAL PROCEDURES S301

β-GLUCOSIDASE INHIBITION ASSAY FOR COMPOUNDS 12, 13, 14, 22, AGF AND CONDURITOL *β*-EPOXIDE S314

LIGAND INTERACTIONS SCHEMES FOR COMPOUNDS 12, 13, 22 AND AGF S317

COPIES OF NMR SPECTRA S321

* Corresponding authors. E-mail: (*)filip@chem.bg.ac.rs; (**)zferjan@chem.bg.ac.rs

GENERAL EXPERIMENTAL

All chromatographic separations* were performed on Silica gel 60 (0.063-0.2 mm), Merck. Standard techniques were used for the purification of reagents and solvents.† NMR spectra were recorded on Varian/Agilent 400 (^{1}H NMR at 400 MHz, ^{13}C NMR at 100 MHz) and on Bruker Avance III 500 (^{1}H NMR at 500 MHz, ^{13}C NMR at 125 MHz), in deuterated chloroform, if not otherwise stated. Chemical shifts are expressed in ppm (δ) using tetramethylsilane as internal standard, coupling constants (J) are in Hz. IR spectra were recorded on Thermo Scientific Nicolet Summit FT-IR instrument, and are expressed in cm^{-1}. Mass spectra were obtained on Orbitrap Exploris 240 spectrometer. Melting point was determined on LLG-uniMELT 2 melting point apparatus, and it is uncorrected. Optical rotation was measured on Rudolph Research Analytical AUTOPOL IV Automatic Polarimeter.

* For description of the technique of dry-flash chromatography, *see*: a) L. M. Harwood, *Aldrichimica Acta,* **1985**, *18*, 25; b) *Vogel's Textbook of Practical Organic Chemistry*, Longman Scientific & Technical, 5th edition, London, 1989, p. 220; c) For some improvements of the separation technique, *see*: D. S. Pedersen, C. Rosenbohm, *Synthesis,* **2001**, 2431-2434.

† D. D. Perrin, W. L. F. Armarego, *Purification of Laboratory Chemicals*, 3rd edition, Pergamon Press, **1988**.

EXPERIMENTAL PROCEDURES

The experimental procedures for the new AGF analogues are arranged in a natural order and follows the Scheme S1.

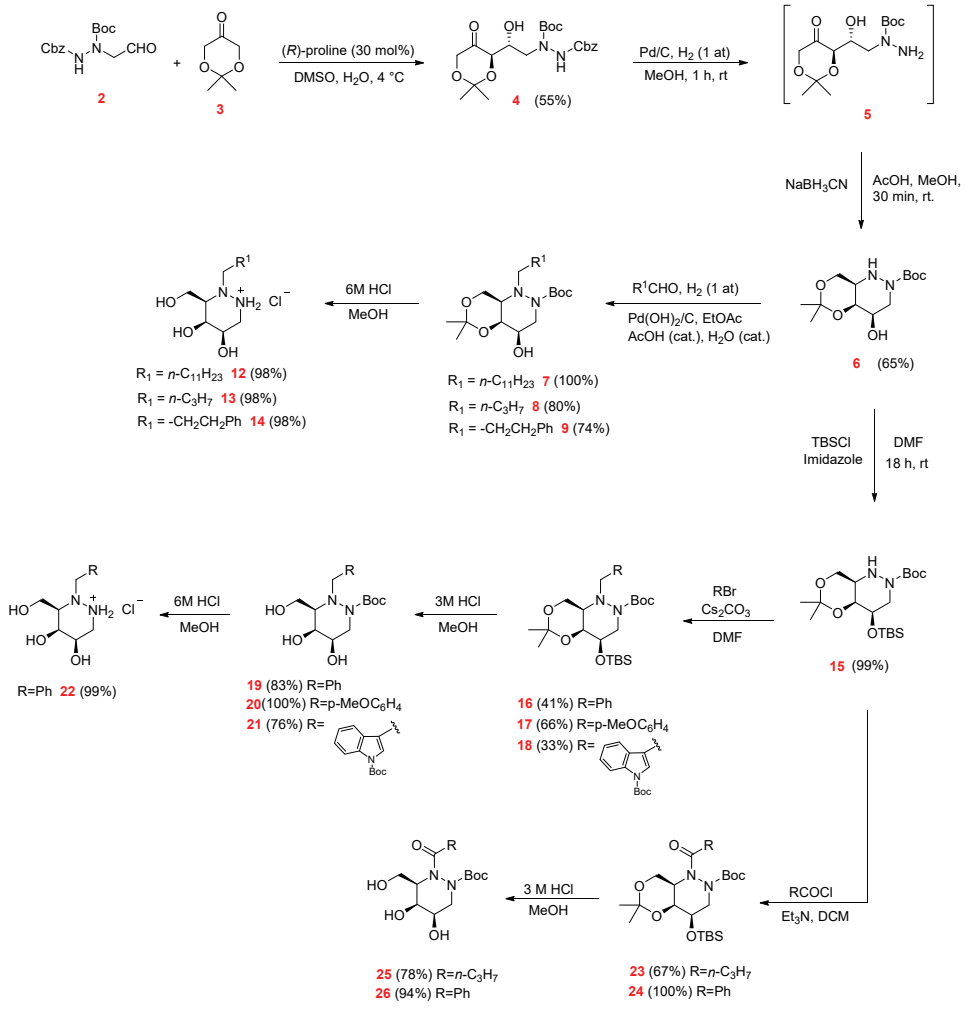

Scheme *S-1*

*2-Benzyl 1-(tert-butyl) 1-((R)-2-((R)-2,2-dimethyl-5-oxo-1,3-dioxan-4-yl)-2-hydroxyethyl)hydrazine-1,2-dicarboxylate (**4**)*

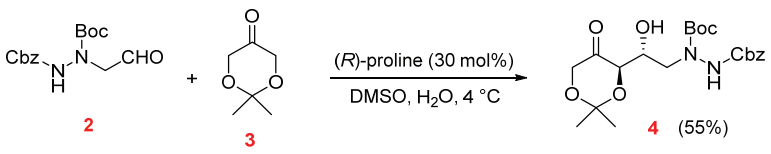

The freshly prepared aldehyde **2** (2.84 g; 9.22 mmol) was dissolved in DMSO (32 mL). The dioxanone **3** (3.20 g; 24.61 mmol; 2.67 eq) and (*R*)-proline (318 mg; 2.77 mmol; 30 mol%) were added. The mixture was stirred until homogeneous solution was formed. Water was added subsequently. The mixture was transferred to refrigerator and stirred for 3 days at 4 °C. The reaction mixture was diluted with EtOAc (100 mL), washed with water (4 x 50 mL) and brine, dried over anhydrous $MgSO_4$, filtered and concentrated under reduced pressure. The crude product was purified by dry-flash chromatography (benzene/ethyl acetate = 85:15), to afford 2.49 g (61%) of the pure aldol **4** as viscous mass. All spectral data are in accordance with the literature (J. Marjanovic Trajkovic, Z. Ferjancic, R. N. Saicic, *Tetrahedron* **73** (2017) 2629).

*tert-Butyl (4R,4aS,8aR)-4-hydroxy-6,6-dimethyltetrahydro-1H-[1,3]dioxino[5,4-c]pyridazine-2(3H)-carboxylate (**6**)*

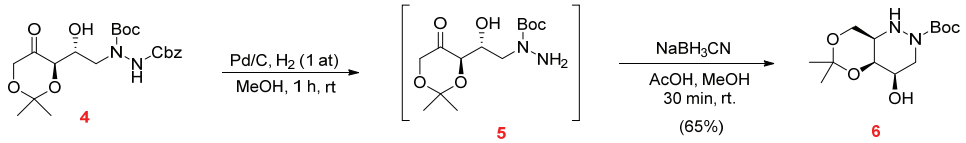

4 5 6

A mixture of **4** (500 mg; 0.114 mmol) and 10% Pd/C (100 mg; 0.094 mmol; 82 mol%) in methanol (30 mL) was stirred for 1 hour under a hydrogen atmosphere (1 atm). The mixture was filtered through celite and the filtrate was concentrated under reduced pressure. The residue was dissolved in MeOH (2 mL) and AcOH (8 mL) was added to the solution. The resulting mixture was stirred for 2 minutes and $NaBH_3CN$ (215 mg; 0.342 mmol; 3 eq) was added. Stirring was continued for 30 minutes at room temperature. The reaction mixture was diluted with DCM (50 mL) and neutralized with saturated $NaHCO_{3(aq)}$. Water layer was extracted two more times with DCM (2 x 50 mL). The combined organic layer was washed with brine, dried over anhydrous $MgSO_4$, filtered and concentrated on rotovap. The product was purified by dry-flash chromatography (ethyl acetate/petroleum ether/methanol = 76:20:4), to afford 213 mg (65%) of **6**, as a white solid. All spectral data are in accordance with the literture (J. Marjanovic Trajkovic, Z. Ferjancic, R. N. Saicic, *Tetrahedron* **73** (2017) 2629).

tert-Butyl (4R,4aS,8aR)-1-dodecyl-4-hydroxy-6,6-dimethyltetrahydro-1H-[1,3]dioxino[5,4-c]pyridazine-2(3H)-carboxylate (7)

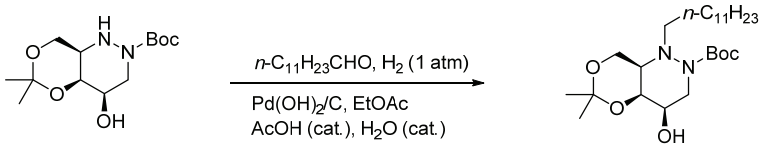

6 **7** (100%)

Compound **6** (10 mg; 0.035 mmol) and dodecyl aldehyde (33 mg; 0.179 mmol; 5.1 eq) were dissolved in EtOAc (500 µL) and water (6 µL) with catalytic amount of AcOH was added under argon atmosphere. 10% $Pd(OH)_2$ (10 mg; 0.007 mmol; 20 mol%) was added to the resulting solution, and the mixture was stirred under hydrogen atmosphere (1 atm) for 6 hours. The mixture was filtered through a pad of celite and the filtrate was concentrated under reduced pressure. The product was purified by column chromatography (petroleum ether/ethyl acetate = 1:1), to afford 16 mg (100%) of **7**, as a colorless film. Peaks in ^1H and ^{13}C NMR spectrum are broad and split, due to the presence of a *N*-Boc rotamers. ^1H NMR (400 MHz,

$CDCl_3$, δ): 4.13–3.60 (*m*, 4H), 3.19–2.60 (*m*, 3.5H), 2.34 (*t*, 0.5H, *J* = 7.6), 1.66–1.57 (*m*, 1H), 1.47, 1.45 and 1. 41 (3 x *bs*, 15H), 1.26 (*bs*, 20H), 0.88 (*t*, 3H, *J* = 6.7). ^{13}C NMR (100 MHz, $CDCl_3$, δ): 99.16, 80.10, 66.81, 65.74, 61.48, 54.17, 50.20, 31.89, 31.87, 29.64, 29.60, 29.56, 29.41, 29.32, 29.29, 29.22, 29.07, 28.31, 27.96, 27.13, 24.75, 22.65, 18.87, 14.08. Under the recording conditions, signal for one carbon could not be detected. HRMS (ESI-Orbitrap) *m/z*: $[M+H]^+$ calcd. for $C_{25}H_{49}N_2O_5$: 457.3636, found: 457.3629.

*tert-Butyl (4R,4aS,8aR)-1-butyl-4-hydroxy-6,6-dimethyltetrahydro-1H-[1,3]dioxino[5,4-c]pyridazine-2(3H)-carboxylate (**8**)*

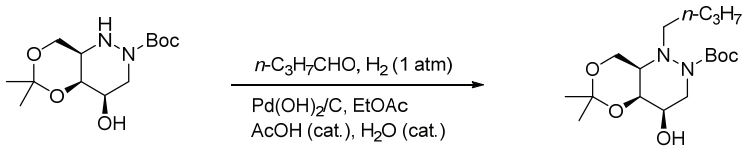

6 **8** (80%)

Compound **6** (10 mg; 0.035 mmol) and butyl aldehyde (31 μL; 0.347 mmol; 10 eq) were dissolved in EtOAc (500 μL) and water (6 μL) with catalytic amount of AcOH was added under argon atmosphere. To the resulting solution, 10% $Pd(OH)_2$ (10 mg; 0.007 mmol; 20 mol%) was added and the mixture was stirred under hydrogen atmosphere (1 atm) for 18 hours. The mixture was filtered through a pad of celite and the filtrate was concentrated under reduced pressure. The product was purified by column chromatography (petroleum ether/ethyl acetate = 1:1), to afford 10 mg (80%) of **8**, as a colourless film. Peaks in ^{1}H and ^{13}C NMR spectrum are broad and split, due to the presence of a *N*-Boc rotamers. ^{1}H NMR (400 MHz, $CDCl_3$, δ): 4.09–3.83 (*m*, 3H), 3.70–3.59 (*m*, 1H), 3.21–2.68 (*m*, 4H), 2.53–2.42 (*m*, 1H), 1.47, 1.44 and 1. 40 (3 x *bs*, 17H), 1.35–1.28 (*m*, 2H), 0.90 (*t*, 3H, *J* = 6.8). ^{13}C NMR (100 MHz, $CDCl_3$, δ): 99.29, 80.22, 67.00, 66.16, 61.72, 54.47, 50.01, 39.03, 30.18, 29.60, 28.33, 20.39, 19.05, 14.24. Under the recording conditions, signal for one carbon could not be detected. HRMS (ESI-Orbitrap) *m/z*: $[M+H]^+$ calcd. for $C_{17}H_{33}N_2O_5$: 345.2384, found: 345.2378.

*tert-Butyl (4R,4aS,8aR)-4-hydroxy-6,6-dimethyl-1-(3-phenylpropyl)tetrahydro-1H-[1,3]dioxino[5,4-c]pyridazine-2(3H)-carboxylate (**9**)*

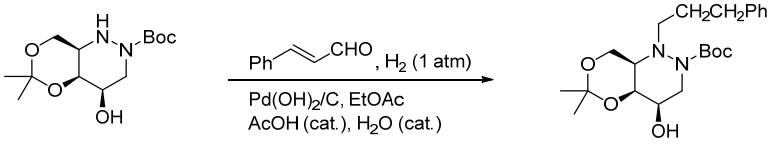

6 **9** (74%)

Compound **6** (20 mg; 0.069 mmol) and cinnamaldehyde (131 μL; 1.040 mmol; 15 eq) were dissolved in EtOAc (1000 μL) and water (12 μL) with catalytic amount of AcOH was added under argon atmosphere. To the resulting solution, 10% $Pd(OH)_2$ (30 mg; 0.021 mmol; 30 mol%) was added and the mixture was stirred under hydrogen atmosphere (1 atm) for 36 hours. The mixture was filtered through a pad of celite and the filtrate was concentrated under reduced pressure. The product was purified by column chromatography (petroleum ether/ethyl acetate = 1:1), to afford 21 mg (74%) of **9**, as a colorless film. Peaks in ^{1}H and ^{13}C NMR spectrum are broad and split, due to the presence of a *N*-Boc rotamers. ^{1}H NMR (400 MHz,

$CDCl_3$, δ): 7.28–7.18 (*m*, 4H), 7.15 (*t*, 1H, *J* = 7.0), 4.10–3.79 (*m*, 3H), 3.70–3.58 (*m*, 1H), 3.14 (*bs*, 2H), 3.03–2.81 (*m*, 3H), 2.68–2.58 (*m*, 1H), 2.51 (*d*, 1H, *J* = 8.6), 1.80–1.72 (*m*, 1H), 1.69–1.58 (*m*, 1H), 1.44 and 1. 37 (2 x *bs*, 15H). ^{13}C NMR (100 MHz, $CDCl_3$, δ): 142.71, 128.62, 128.30, 125.66, 99.34, 80.41, 67.01, 65.99, 61.59, 54.52, 49.55, 33.42, 33.35, 29.58, 29.53, 28.49, 18.98. Under the recording conditions, signal for one the quaternary carbon from Boc group could not be detected. HRMS (ESI-Orbitrap) *m/z*: $[M+H]^+$ calcd. for $C_{22}H_{35}N_2O_5$: 407.2540, found: 407.2534.

(3R,4S,5R)-2-Dodecyl-4,5-dihydroxy-3-(hydroxymethyl)hexahydropyridazin-1-ium chloride ***(12)***

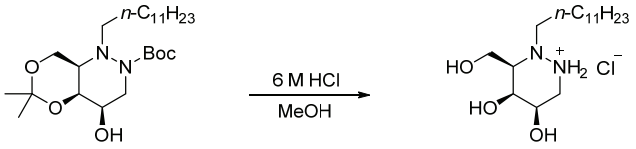

7 **12** (98%)

Compound **7** (12.5 mg; 0.027 mmol) was dissolved in MeOH (200 μL), and 6 M $HCl_{(aq)}$ (200 μL) was added. The resulting solution was stirred overnight at room temperature. The volatiles were removed on rotovap, to afford 9.5 mg (98%) of a pure hydrochloride salt **12** as a colourless film. ^{1}H NMR (400 MHz, D_2O, δ): 4.26–4.23 (*m*, 1H), 3.99–3.93 (*m*, 3H), 3.54–3.49 (*m*, 1H), 3.48–3.40 (*m*, 1H), 3.31–3.21 (*m*, 2H), 3.16 (*dd*, 1H, J_1 = 13.4, J_2 = 4.7), 1.84–1.73 (*m*, 2H), 1.35 and 1. 29 (2 x *bs*, 18H), 0.87 (*t*, 3H, *J* = 6.6). ^{13}C NMR (100 MHz, D_2O, δ): 66.94, 66.52, 64.92, 59.29, 53.77, 44.70, 31.78, 29.67, 29.60, 29.54, 29.47, 29.30, 29.06, 26.41, 22.99, 22.47, 13.70. HRMS (ESI-Orbitrap) *m/z*: $[M+H]^+$ calcd. for $C_{17}H_{37}N_2O_3$: 317.2799, found: 317.2795.

(3R,4S,5R)-2-Butyl-4,5-dihydroxy-3-(hydroxymethyl)hexahydropyridazin-1-ium chloride ***(13)***

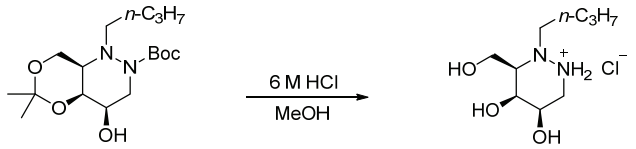

8 **13** (98%)

Compound **8** (9.5 mg; 0.029 mmol) was dissolved in MeOH (200 μL), and 6 M $HCl_{(aq)}$ (200 μL) was added. The resulting solution was stirred overnight at room temperature. The volatiles were removed on rotovap, to afford 6.8 mg (98%) of a pure hydrochloride salt **13** as a colorless film. ^{1}H NMR (400 MHz, D_2O, δ): 4. 26 (*bs*, 1H), 4.00–3.96 (*m*, 2H), 3.93 (*ddd*, 1H, J_1 = 10.4, J_2 = 5.0, J_3 = 2.9), 3.53–3.48 (*m*, 1H), 3.48–3.40 (*m*, 1H), 3.29 (*dd*, 1H, J_1 = 13.6, J_2 = 10.4), 3.30–3.21 (*m*, 1H), 3.18 (*dd*, 1H, J_1 = 13.6, J_2 = 5.0), 1.83–1.65 (*m*, 2H), 1.39 (*sx*, 2H, *J* = 7.4), 0.94 (*t*, 3H, *J* = 7.4). ^{13}C NMR (100 MHz, D_2O, δ): 67.08, 66.21, 65.02, 59.25, 53.79, 44.48, 24.25, 19.15, 12.69. HRMS (ESI-Orbitrap) *m/z*: $[M+H]^+$ calcd. for $C_9H_{21}N_2O_3$: 205.1547, found: 205.1545.

*(3R,4S,5R)-4,5-Dihydroxy-3-(hydroxymethyl)-2-(3-phenylpropyl)hexahydropyridazin-1-ium chloride (**14**)*

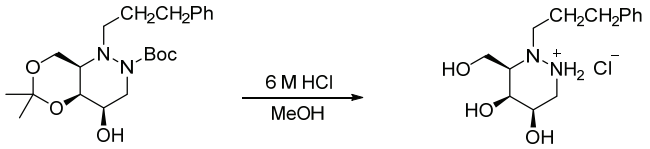

9 **14** (98%)

Compound **9** (20 mg; 0.049 mmol) was dissolved in MeOH (500 µL), and 6 M $HCl_{(aq)}$ (500 µL) was added. The resulting solution was stirred overnight at room temperature. The volatiles were removed on rotovap, to afford 14.6 mg (98%) of a pure hydrochloride salt **14** as a colorless film. ^{1}H NMR (400 MHz, D_2O, δ): 7.41–7.35 (*m*, 2H), 7.31–7.26 (*m*, 3H), 4.19 (bs, 1H), 3.92–3.84 (*m*, 3H), 3.45–3.35 (*m*, 2H), 3.27–3.19 (*m*, 2H), 3.15 (*dd*, 1H, J_1 = 13.6, J_2 = 5.0), 2.78–2.65 (*m*, 2H), 2.14–2.00 (*m*, 2H). ^{13}C NMR (100 MHz, D_2O, δ): 140.68, 128.67, 128.44, 126.36, 66.97, 65.93, 64.88, 59.17, 53.15, 44.59, 31.65, 24.06. HRMS (ESI-Orbitrap) *m/z*: $[M+H]^+$ calcd. for $C_{14}H_{23}N_2O_3$: 267.1703, found: 267.1699.

*tert-Butyl (4R,4aS,8aR)-4-((tert-butyldimethylsilyl)oxy)-6,6-dimethyltetrahydro-1H-[1,3]dioxino[5,4-c]pyridazine-2(3H)-carboxylate (**15**)*

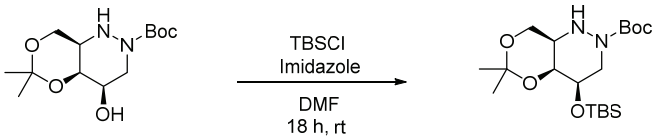

6 **15** (99%)

Compound **6** (304 mg; 1.0 mmol) and imidazole (137 mg; 2.0 mmol; 2 eq) were dissolved in DMF (1.5 mL) under argon atmosphere, and TBSCl (228 mg; 1.5 mmol; 1.5 eq) was subsequently added. The mixture was stirred overnight at room temperature. After the reaction completion, the mixture was diluted with EtOAc, washed with water, saturated $NaHCO3_{(aq)}$ and brine. Organic phase was dried over anhydrous $MgSO_4$, filtered and evaporated under reduced pressure. The residue was purified by dry-flash chromatography (benzene/ethyl acetate = 1:1), to yield 415 mg (99%) of **15**, as a white crystalline solid. ^{1}H NMR (400 MHz, $CDCl_3$, δ): 4.05 (*dd*, 1H, J_1 = 12.4, J_2 = 2.6), 4.01 (*d*, 1H, J = 1.9), 3.94 (*dd*, 1H, J_1 = 13.6, J_2 = 6.0), 3.90 (*d*, 1H, J = 13.0), 3.67 (*ddd*, 1H, J_1 = 10.8, J_2 = 4.9, J_3 = 3.1), 3.09 (*t*, 1H, J = 11.8), 2.64 (*s*, 1H), 1.48 (*s*, 9H), 1.45 (*s*, 3H), 1.43 (*s*, 3H), 0.90 (*s*, 9H), 0.10 (*s*, 6H). ^{13}C NMR (100 MHz, $CDCl_3$, δ): 155.41, 99.00, 80.57, 68.48, 67.86, 62.36, 52.33, 45.95, 29.73, 28.47, 25.93, 18.51, 18.42, -4.24, -4.41. HRMS (ESI-Orbitrap) *m/z*: $[M+H]^+$ calcd. for $C_{19}H_{39}N_2O_5Si$: 403.2623, found: 403.2620.

*tert-Butyl (4R,4aS,8aR)-1-benzyl-4-((tert-butyldimethylsilyl)oxy)-6,6-dimethyltetrahydro-1H-[1,3]dioxino[5,4-c]pyridazine-2(3H)-carboxylate (**16**)*

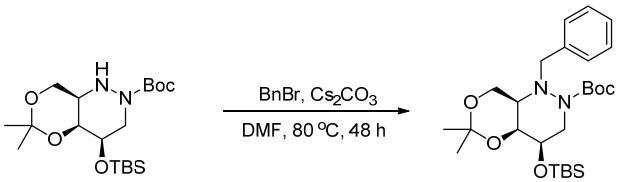

15 **16** (41%)

Compound **15** (25 mg; 0.060 mmol) was dissolved in DMF (1.5 mL) under argon atmosphere. Firstly, the Cs_2CO_3 (136 mg; 0.416 mmol; 7 eq) was added, followed by benzyl bromide (50 µL; 0.416 mmol; 7 eq). The mixture was stirred for 48 hours at 80 °C (full conversion was not achieved, even with prolonged reaction time). The mixture was diluted with Et_2O, washed with water, saturated $NH_4Cl_{(aq)}$ and brine. The organic phase was dried over anhydrous $MgSO_4$, filtered and evaporated under reduced pressure. The residue was purified by column chromatography (petroleum ether/ethyl acetate = 7:3), to afford 12 mg (41%) of **16**, as a colorless film, and 8.3 mg of the starting material **15**. Peaks in ^{1}H and ^{13}C NMR spectrum are broad and split, due to the presence of a *N*-Boc rotamers. ^{1}H NMR (400 MHz, $CDCl_3$, δ): 7.44–7.34 (*bs*, 2H), 7.28–7.26 (*bs*, 1H), 7.26–7.23 (*bs*, 1H), 7.22–7.16 (*m*, 1H), 4.54 (*d*, 1H, *J* = 14.5), 4.29–4.02 (*m*, 4H), 3.89–3.53 (*m*, 2H), 3.39–3.23 (*m*, 1H), 3.07–2.74 (*m*, 1H), 1.49 (*s*, 6H), 1.32–1.18 (*m*, 9H), 0.92 (*s*, 9H), 0.12 (*s*, 6H). ^{13}C NMR (100 MHz, $CDCl_3$, δ): 161.58, 139.36, 129.60, 127.88, 126.81, 99.22, 79.86, 68.56 (overlap of 2C), 62.01, 55.56, 29.84, 28.22, 26.07, 18.89, 18.54, -4.18, -4.45. Under the recording conditions, signal for two carbons could not be detected. HRMS (ESI-Orbitrap) *m/z*: $[M+Na]^+$ calcd. for $C_{26}H_{45}N_2NaO_5Si$: 515.2912, found: 515.2909.

*tert-Butyl (4R,4aS,8aR)-4-((tert-butyldimethylsilyl)oxy)-1-(4-methoxybenzyl)-6,6-dimethyltetrahydro-1H-[1,3]dioxino[5,4-c]pyridazine-2(3H)-carboxylate (**17**)*

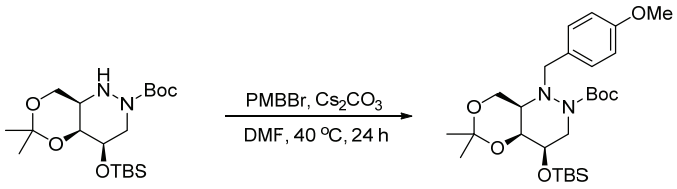

15 **17** (66%)

Substrate **15** (20 mg; 0.050 mmol) was dissolved in DMF (1 mL) under argon atmosphere. Firstly, the Cs_2CO_3 (81 mg; 0.248 mmol; 5 eq) was added, followed by PMB bromide (36 µL; 0.248 mmol; 5 eq). The mixture was stirred for 24 hours at 40 °C (full conversion was not achieved, even with prolonged reaction titme). The mixture was then diluted with Et_2O, washed with water, saturated $NH_4Cl_{(aq)}$ and brine. The organic phase was dried over anhydrous $MgSO_4$, filtered and evaporated under reduced pressure. The residue was purified by column chromatography (petroleum ether/ethyl acetate = 7:3), to afford 16.5 mg (66%) of **17**, as a colorless film. Peaks in ^{1}H and ^{13}C NMR spectrum are broad and split, due to the presence of a *N*-Boc rotamers. ^{1}H NMR (400 MHz, $CDCl_3$, δ): 7.34–7.26 (*m*, 2H), 6.80 (*d*, 2H, *J* = 8.0), 4.45 (b*d*, 1H, *J* = 13.8), 4.28–4.01 (*m*, 4H), 3.91–3.78 (*m*, 1H), 3.78 (*s*, 3H), 3.73–3.64 (*m*, 1H), 3.39–3.20 (*m*, 1H), 2.99–2.74 (*m*, 1H), 1.49 (*s*, 6H), 1.33–1.19 (*m*,

9H), 0.91 (*s*, 9H), 0.12 (*s*, 6H). ^{13}C NMR (100 MHz, $CDCl_3$, δ): 158.65, 130.36, 114.02, 113.32, 99.17, 77.36, 68.60 (overlap of 2C), 62.02, 55.41, 54.82 (overlap of 2C), 29.80, 28.23, 25.99, 18.81, 18.49, -4.20, -4.45. Under the recording conditions, signal for two carbons could not be detected. HRMS (ESI-Orbitrap) *m/z*: [M+H]+ calcd. for $C_{27}H_{47}N_2O_6Si$: 523.3198, found: 523.3198.

*tert-Butyl (4R,4aS,8aR)-1-((1-(tert-butoxycarbonyl)-1H-indol-3-yl)methyl)-4-((tert-butyldimethylsilyl)oxy)-6,6-dimethyltetrahydro-1H-[1,3]dioxino[5,4-c]pyridazine-2(3H)-carboxylate (**18**)*

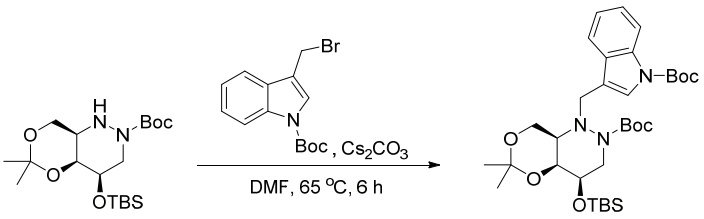

15 18 (32%)

Substrate **15** (50 mg; 0.124 mmol) was then dissolved in DMF (2 mL) under argon atmosphere. Firstly, the Cs_2CO_3 (404 mg; 1.242 mmol; 10 eq) was added, followed by *tert*-butyl 3-(bromomethyl)-1H-indole-1-carboxylate (347 mg; 1.118 mmol; 9 eq). The mixture was stirred for 6 hours at 65 °C (full conversion was not achieved, even with prolonged reaction time). The mixture was diluted with Et_2O, washed with water, saturated $NH_4Cl_{(aq)}$ and brine. The organic phase was dried over anhydrous $MgSO_4$, filtered and evaporated under reduced pressure. The residue was purified by column chromatography (benzene/ethyl acetate = 9:1), to afford 25 mg (32%) of **18**, as a colourless film. Peaks in ^{1}H and ^{13}C NMR spectrum are broad and split, due to the presence of a *N*-Boc rotamers. ^{1}H NMR (400 MHz, $CDCl_3$, δ): 8.17–8.09 (*m*, 1H), 7.70–7.64 (*m*, 1H), 7.29–7.24 (*m*, 2H), 7.20 (*t*, 1H, *J* = 7.4), 4.62 (b*d*, 1H, *J* = 14.1), 4.55–4.33 (*m*, 1H), 4.26–4.11 (*m*, 2H), 4.08 (*bs*, 1H), 3.97–3.51 (*m*, 2H), 3.31 (*t*, 1H, *J* = 12.0), 3.06–2.75 (*m*, 1H), 1.67 and 1.64 (2 x *s*, 10H), 1.52 (*bs*, 6H), 1.44–1.24 (*m*, 4H), , 0.91 (*bs*, 13H), 0.12 (*s*, 6H). ^{13}C NMR (100 MHz, $CDCl_3$, δ): 155.86, 149.91, 135.81, 124.12, 122.35, 118.24, 115.12, 99.25, 83.27, 68.63 (overlap of 2C), 62.29, 54.93, 46.08, 29.94, 28.34, 28.02, 25.98, 18.92, 18.48, -4.18, -4.46. Under the recording conditions, signals for three carbons could not be detected. Several peaks are missing due to overlap of N-Boc carbons. HRMS (ESI-Orbitrap) *m/z*: $[M+H]^+$ calcd. for $C_{33}H_{54}N_3O_7Si$: 632.3726, found: 632.3724.

*tert-Butyl (3R,4S,5R)-2-benzyl-4,5-dihydroxy-3-(hydroxymethyl)tetrahydropyridazine-1(2H)-carboxylate (**19**)*

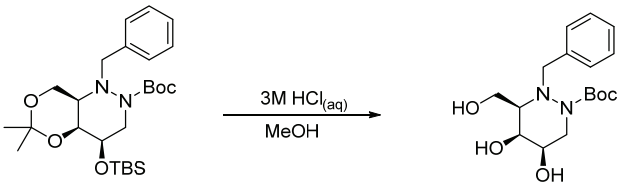

16 19 (83%)

Benzyl derivative **16** (12 mg; 0.025 mmol) was dissolved in MeOH (850 µL), and 3 M $HCl_{(aq)}$ (150 µL) was added. The resulting solution was stirred for 1 hour at room temperature. The mixture was neutralized with saturated $NaHCO_{3(aq)}$ and the volatiles were removed on rotovap. The resulting solid was suspended in EtOAc. The mixture was filtered through a pad of celite and the filtrate was concentrated under reduced pressure. The product was purified by column chromatography (EtOAc/EtOH 9:1), to afford 6.9 mg (83%) of a product **19** as a white foam. Peaks in ^{1}H and ^{13}C NMR spectrum are broad and split, due to the presence of a *N*-Boc rotamers. ^{1}H NMR (400 MHz, CD_3OD, δ): 7.35–7.06 (*m*, 5H), 4.11–3.75 (*m*, 6H), 3.58–3.50 (*m*, 1H), 3.45–3.39 (*m*, 1H), 3.05–2.94 (*m*, 1H), 1.26, 1.17 and 1.14 (3 x *s*, 9H). ^{13}C NMR (126 MHz, CD_3OD, δ) 158.78, 157.75, 138.72, 138.39, 130.96, 130.45, 129.27, 129.15, 128.78, 128.66, 128.50, 81.80, 68.59, 65.87, 64.88, 64.72, 60.07, 60.00, 57.94, 57.81, 45.42, 43.03, 28.44, 28.24.

*tert-Butyl (3R,4S,5R)-4,5-dihydroxy-3-(hydroxymethyl)-2-(4-methoxybenzyl)tetrahydropyridazine-1(2H)-carboxylate (**20**)*

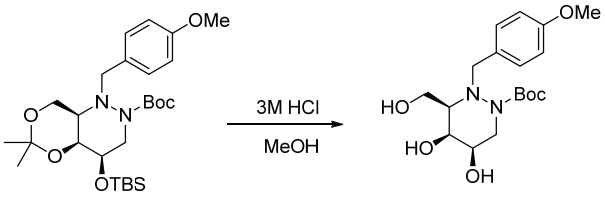

17 **20** (100%)

Compound **17** (16.5 mg; 0.032 mmol) was dissolved in MeOH (850 µL), and 3 M $HCl_{(aq)}$ (150 µL) was added. The resulting solution was stirred for 1 hour at room temperature. The mixture was neutralized with saturated $NaHCO_{3(aq)}$ and the volatiles were removed on rotovap. Resulting solid was suspended in EtOAc. The mixture was filtered through a pad of celite and the filtrate was concentrated under reduced pressure. The product was purified by column chromatography (EtOAc/MeOH 9:1), to afford 11.6 mg (100%) of a pure product **20** as a colorless film. Peaks in ^{1}H and ^{13}C NMR spectrum are broad and split, due to the presence of a *N*-Boc rotamers. ^{1}H NMR (400 MHz, CD_3OD, δ): 7.35–7.22 (*m*, 2H), 6.88–6.78 (*m*, 2H), 4.15–3.85 (*m*, 6H), 3.77, 3.76 and 3.75 (3 x *s*, 3H), 3.68–3.59 (*m*, 1H), 3.54–3.47 (*m*, 1H), 3.13–3.02 (*m*, 1H), 1.37, 1.29, 1.26, 1.24 and 1.22 (5 x *s*, 9H). ^{13}C NMR (100 MHz, CD_3OD, δ): 159.28, 156.34, 130.61, 130.21, 129.26, 128.88, 113.21, 113.09, 112.76, 80.30, 67.13, 67.10, 63.98, 63.40, 63.22, 62.89, 58.58, 58.55, 55.73, 55.62, 54.27, 54.21, 43.95, 41.53, 27.02, 26.82. HRMS (ESI-Orbitrap) *m/z*: $[M+H]^+$ calcd. for $C_{18}H_{29}N_2O_6$: 369.2020, found: 369.2018.

*tert-butyl 3-(((4R,5S,6R)-2-(tert-butoxycarbonyl)-4,5-dihydroxy-6-(hydroxymethyl)tetrahydropyridazin-1(2H)-yl)methyl)-1H-indole-1-carboxylate (**21**)*

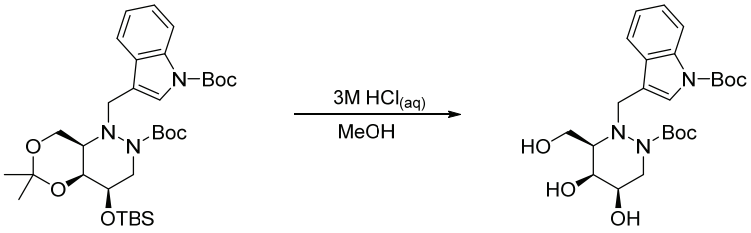

18 **21** (76%)

Compound **18** (21 mg; 0.033 mmol) was dissolved in MeOH (850 μL), and 3 M $HCl_{(aq)}$ (150 μL) was added. The resulting solution was stirred for 1 hour at room temperature. The mixture was neutralized with saturated $NaHCO_{3(aq)}$ and the volatiles were removed on rotovap. The resulting solid was suspended in EtOAc. The mixture was filtered through a pad of celite and the filtrate was concentrated under reduced pressure. The product was purified by column chromatography (EtOAc/MeOH 95:5), to afford 12.1 mg (76%) of a pure product **21** as a colorless film. Peaks in ^{1}H and ^{13}C NMR spectrum are broad and split, due to the presence of a *N*-Boc rotamers. ^{1}H NMR (400 MHz, CD_3OD, δ): 8.12–8.05 (*m*, 1H), 7.86 and 7.75 (2 x *d*, 1H, *J* = 7.7), 7.67 and 7.55 (2 x *s*, 1H), 7.33–7.20 (*m*, 2H), 4.35 (*d*, 0.7H, *J* = 13.4), 4.25–4.04 (*m*, 3.3H), 3.96–3.87 (*m*, 2H), 3.69–3.51 (*m*, 2H), 3.27–3.21 (*m*, 0.7H), 3.17–3.09 (*m*, 0.3H), 1.67, 1.66, 1.39 and 1.00 (4 x *s*, 18H). ^{13}C NMR (100 MHz, CD_3OD, δ): 157.93, 150.99, 137.12, 131.86, 126.18, 126.11, 125.54, 125.41, 123.82, 123.66, 121.05, 120.87, 118.45, 118.09, 116.27, 115.91, 84.98, 81.80, 81.74, 68.58, 68.53, 65.89, 64.95, 64.58, 63.91, 60.21, 59.91, 48.08, 45.44, 42.74, 28.46, 28.41, 28.37, 27.91. HRMS (ESI-Orbitrap) *m/z*: $[M+H]^+$ calcd. for $C_{24}H_{36}N_3O_7$: 478.2548, found: 478.2547.

*(3R,4S,5R)-2-Benzyl-4,5-dihydroxy-3-(hydroxymethyl)hexahydropyridazin-1-ium chloride (**22**)*

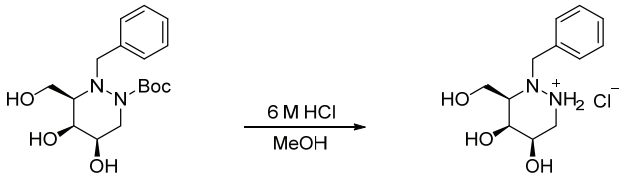

19 **22** (99%)

Compound **19** (6.9 mg; 0.020 mmol) was dissolved in MeOH (200 μL), and 6 M $HCl_{(aq)}$ (200 μL) was added. The resulting solution was stirred overnight at room temperature. The volatiles were removed on rotovap, to afford 5.5 mg (99%) of a pure hydrochloride salt **22** as a colourless film. ^{1}H NMR (400 MHz, D_2O, δ): 7.53–7.48 (*m*, 5H), 4.62 (*d*, 1H, *J* = 13.9), 4.24 (*t*, 1H, *J* = 2.6), 4.16 (*d*, 1H, *J* = 14.0), 4.11 (*dd*, 1H, J_1 = 12.7, J_2 = 5.6), 4.04 (*dd*, 1H, J_1 = 12.7, J_2 = 4.7), 3.98 (*ddd*, 1H, J_1 = 9.0, J_2 = 5.6, J_3 = 3.0), 3.41–3.35 (*m*, 1H), 3.27–3.17 (*m*, 2H). ^{13}C NMR (100 MHz, D_2O, δ): 131.03, 130.30, 129.50, 129.10, 66.61, 65.17, 64.43, 59.35, 57.19, 44.35. HRMS (ESI-Orbitrap) *m/z*: $[M+H]^+$ calcd. for $C_{12}H_{19}N_2O_3$: 239.1390, found: 239.1387.

*tert-Butyl (4R,4aS,8aR)-4-((tert-butyldimethylsilyl)oxy)-1-butyryl-6,6-dimethyltetrahydro-1H-[1,3]dioxino[5,4-c]pyridazine-2(3H)-carboxylate (**23**)*

15 **23** (67%)

Substrate **15** (22 mg; 0.055 mmol) was dissolved in DCM (800 µL) and Et_3N (38 µL; 0.275 mmol; 5 eq) was added under argon atmosphere. Butyryl chloride (23 µL; 0.220 mmol; 4 eq) was slowly added to the reaction mixture dropwise, at room temperature. The mixture was stirred for 30 minutes, upon which time the reaction was completed. The mixture was diluted with DCM and washed with saturated $NaHCO_{3(aq)}$, water and brine. The organic phase was dried over anhydrous $MgSO_4$, filtered and evaporated under reduced pressure. The residue was purified by column chromatography (petroleum ether/ethyl acetate = 75:25), to afford 17 mg (67%) of **23**, as a colorless film. Peaks in ^1H and ^{13}C NMR spectrum are broad and split, due to the presence of a *N*-Boc rotamers. ^1H NMR (400 MHz, $CDCl_3$, δ): 4.66 (*dd*, 0.38H, J_1 = 13.8, J_2 = 7.6), 4.34 (dd, 0.62H, J_1 = 10.0, J_2 = 5.3), 4.17 (*dd*, 0.62H, J_1 = 5.7, J_2 = 1.9), 4.12 (*dd*, 0.62H, J_1 = 5.8, J_2 = 1.8), 4.09–3.92 (*m*, 1.7H), 3.88–3.75 (*m*, 2.3H), 3.55 (*dd*, 0.38H, J_1 = 9.7, J_2 = 6.2), 3.43 (*dd*, 0.62H, J_1 = 11.0, J_2 = 7.2), 2.35–2.19 (*m*, 2H), 1.69–1.60 (*m*, 2H), 1.52 and 1.48 (2 x *s*, 9H), 1.41 and 1.36 (2 x *s*, 6H), 0.94 (*t*, 3H, *J* = 7.2), 0.90 and 0.87 (2 x *s*, 9H), 0.09, 0.07 and 0.06 (3 x *s*, 6H). ^{13}C NMR (100 MHz, $CDCl_3$, δ): 175.35, 175.26, 155.01, 154.59, 100.47, 98.95, 82.16, 81.97, 67.42, 66.79, 66.57, 66.49, 60.52, 58.98, 51.87, 49.48, 48.18, 46.81, 33.60, 33.58, 28.38, 27.38, 25.88, 25.79, 24.81, 22.88, 20.44, 18.38, 18.24, 18.15, 17.99, 14.10, 14.05, -4.49, -4.55, -4.58, -4.64. HRMS (ESI-Orbitrap) *m/z*: $[M+Na]^+$ calcd. for $C_{23}H_{44}N_2NaO_6Si$: 495.2861, found: 495.2871.

*tert-Butyl (4R,4aS,8aR)--benzoyl-4-((tert-butyldimethylsilyl)oxy)-6,6-dimethyltetrahydro-1H-[1,3]dioxino[5,4-c]pyridazine-2(3H)-carboxylate (**24**)*

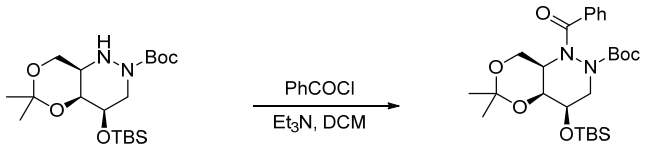

15 **24** (99%)

Compound **15** (40.3 mg; 0.10 mmol) was dissolved in DCM (800 µL) and Et_3N (35 µL; 0.25 mmol; 2.5 eq) was added under argon atmosphere. Benzoyl chloride (23 µL; 0.20 mmol; 2 eq) was slowly added to the reaction mixture dropwise, at room temperature. The mixture was stirred for 30 minutes, upon which time the reaction was completed. The mixture was diluted with DCM and washed with saturated $NaHCO_{3(aq)}$, water and brine. The organic phase was dried over anhydrous $MgSO_4$, filtered and evaporated under reduced pressure. The residue was purified by column chromatography (benzene/ethyl acetate = 85:15), to afford 50 mg (99%) of **24**, as a colorless film. Peaks in ^1H and ^{13}C NMR spectrum are broad and split, due to the presence of a *N*-Boc rotamers. ^1H NMR (400 MHz, $CDCl_3$, δ): 7.51–7.32 (*m*, 5H),

4.74–4.62 (*m*, 0.3H), 4.41–3.99 (*m*, 5.3H), 3.77 (*t*, 0.4H, *J* = 10.3), 3.57–3.43 (*m*, 1H), 1.46, 1.44, 1.38 and 1.36 (4 x *s*, 6H), 1.26 and 1.20 (2 x *s*, 9H), 0.93 and 0.91 (2 x *s*, 9H), 0.14 and 0.13 (2 x *s*, 6H). ^{13}C NMR (100 MHz, $CDCl_3$, δ): 171.66, 171.31, 154.37, 153.68, 134.05, 130.80, 130.17, 128.14, 127.84, 127.32, 126.66, 100.59, 99.16, 81.93, 81.85, 67.33, 66.90, 66.86, 66.72, 59.70, 58.86, 53.28, 51.30, 48.35, 47.30, 28.01, 27.87, 26.98, 25.90, 25.81, 24.52, 23.08, 20.77, 18.42, 18.27. HRMS (ESI-Orbitrap) *m/z*: $[M+Na]^+$ calcd. for $C_{26}H_{42}N_2NaO_6Si$: 529.2704, found: 529.2703.

*tert-Butyl (3R,4S,5R)-2-butyryl-4,5-dihydroxy-3-(hydroxymethyl)tetrahydropyridazine-1(2H)-carboxylate (**25**)*

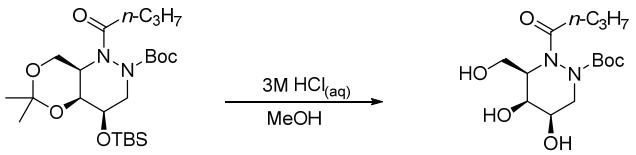

23 **25** (78%)

Compound **23** (15 mg; 0.032 mmol) was dissolved in MeOH (850 μL), and 3 M $HCl_{(aq)}$ (150 μL) was added. The resulting solution was stirred for 1 hour at room temperature. The mixture was neutralized with saturated $NaHCO_{3(aq)}$ and the volatiles were removed on rotovap. The resulting solid was suspended in EtOAc. The mixture was filtered through a pad of celite and the filtrate was concentrated under reduced pressure. The product was purified by column chromatography (EtOAc/MeOH 9:1), to afford 7.9 mg (78%) of a pure product **25** as a white foam. Peaks in ^{1}H and ^{13}C NMR spectrum are broad and split, due to the presence of a *N*-Boc rotamers. ^{1}H NMR (400 MHz, CD_3OD, δ): 4.92–4.87 (*m*, 0.75H), 4.74 (*dd*, 0.25H, J_1 = 11.6, J_2 = 5.7), 4.30 (*dd*, 0.32H, J_1 = 13.8, J_2 = 3.1), 4.22 (*dd*, 0.68H, J_1 = 14.2, J_2 = 2.7), 4.02 (*dd*, 0.74H, J_1 = 12.5, J_2 = 10.0), 3.91 (*d*, 0.5H, *J* = 5.7), 3.84–3.72 (*m*, 2.68H), 3.24 (*dd*, 0.68H, J_1 = 14.2, J_2 = 1.8), 3.17-3.10 (*m*, 0.32H), 2.53–2.23 (*m*, 2H), 1.70–1.57 (*m*, 2H), 1.53, 1.50, 1.49 and 1.44 (4 x *s*, 9H), 1.01–0.91 (*m*, 3H). ^{13}C NMR (400 MHz, CD_3OD, δ): 177.44, 177.35, 158.55, 156.43, 84.04, 83.41, 68.79, 68.67, 68.23, 68.07, 59.57, 59.16, 57.59, 57.50, 52.99, 50.53, 34.85, 34.73, 28.37, 28.33, 18.99, 18.92, 14.26, 14.15. HRMS (ESI-Orbitrap) *m/z*: $[M+Na]^+$ calcd. for $C_{14}H_{26}N_2NaO_6$: 341.1683, found: 341.1682.

*tert-Butyl (3R,4S,5R)-2-benzoyl-4,5-dihydroxy-3-(hydroxymethyl)tetrahydropyridazine-1(2H)-carboxylate (**26**)*

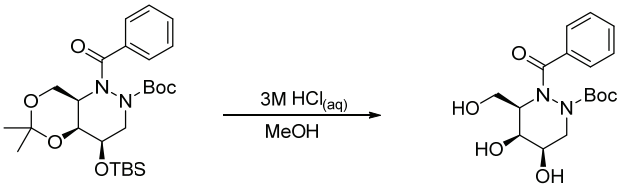

24 **26** (94%)

Compound **24** (50 mg; 0.099 mmol) was dissolved in MeOH (3.4 mL), and 3 M $HCl_{(aq)}$ (600 μL) was added. The resulting solution was stirred for 1 hour at room temperature. The mixture was neutralized with Et_3N (300 μL) and the volatiles were removed on rotovap. The resulting solid was subjected to column chromatography (EtOAc/EtOH 92:8), affording 32.7 mg (94%) of a pure product **26** as a colorless film. Peaks in ^{1}H and ^{13}C NMR spectrum are

broad and split, due to the presence of a *N*-Boc rotamers. ^{1}H NMR (400 MHz, CD_3OD, δ): 7.77–7.35 (*m*, 5H), 5.01–4.92 (*m*, 1H), 4.25 (*dd*, 0.5H, J_1 = 13.8, J_2 = 3.0), 4.18–3.83 (*m*, 4.5H), 3.24–3.13 (*m*, 1H), 1.62–1.24 (*m*, 9H). ^{13}C NMR (400 MHz, CD_3OD, δ): 131.42, 128.98, 128.20, 127.26, 83.71, 68.67, 68.31, 59.70, 59.30, 58.60, 53.25, 47.94, 28.21, 28.07. Under the recording conditions, no signal for two carbons could be detected. HRMS (ESI-Orbitrap) *m/z*: $[M+Na]^+$ calcd. for $C_{17}H_{24}N_2NaO_6$: 375.1527, found: 375.1516.

β-GLUCOSIDASE INHIBITION ASSAY FOR COMPOUNDS 12, 13, 14, 22, AGF AND CONDURITOL *β*-EPOXIDE

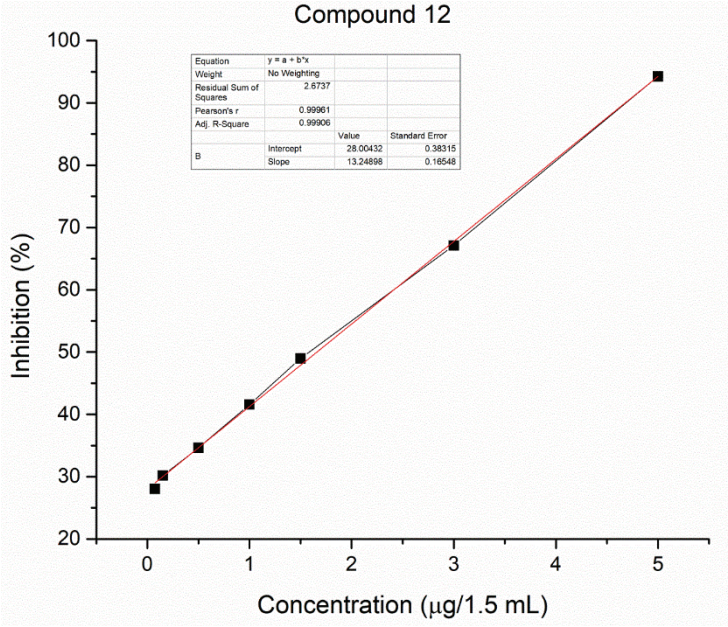

Figure *S-1*. Percentage of inhibition of *β*-glucosidase versus concentration of compound **12.**

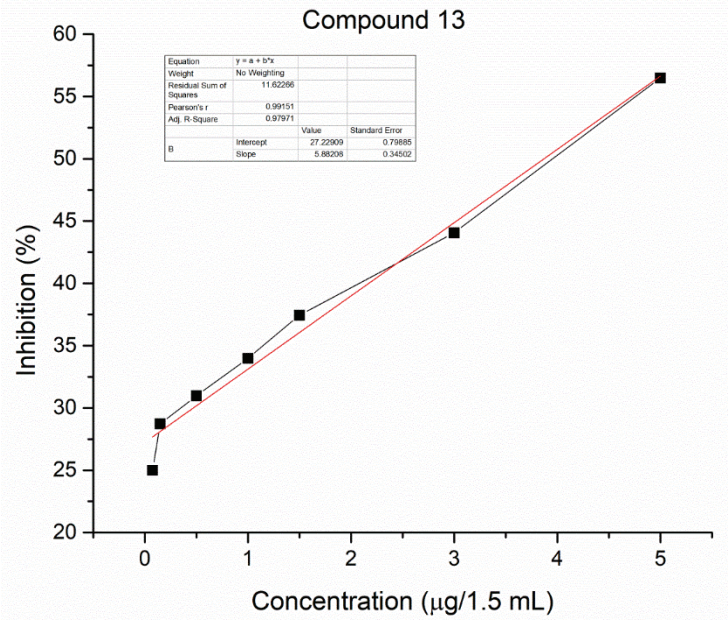

Figure *S-2*. Percentage of inhibition of *β*-glucosidase versus concentration of compound **13.**

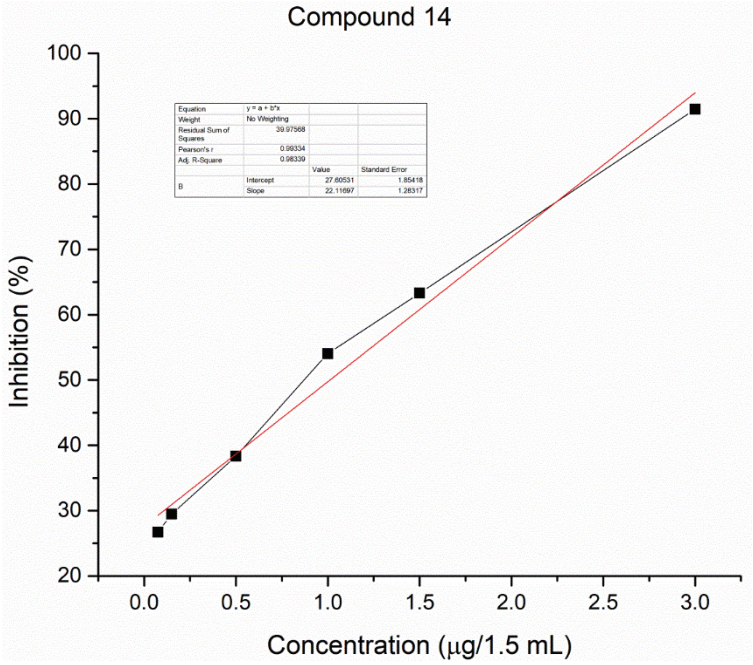

Figure *S-3*. Percentage of inhibition of *β*-glucosidase versus concentration of compound **14.**

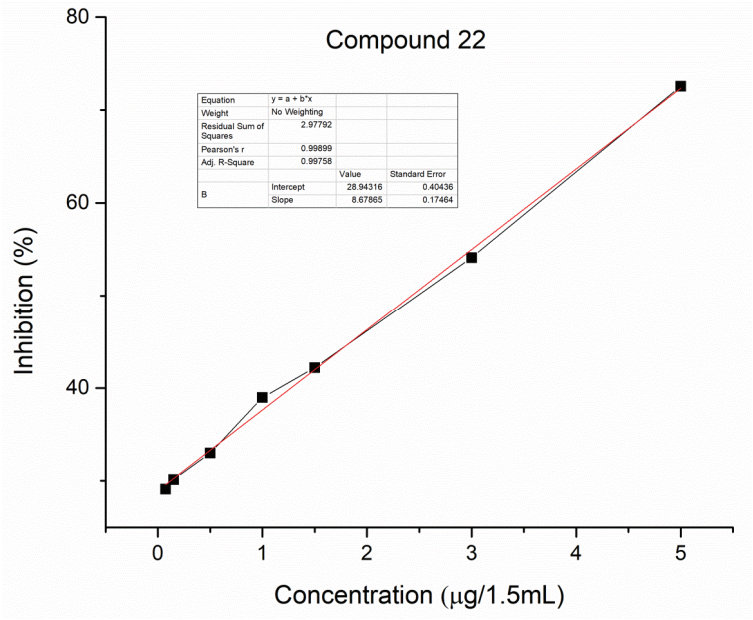

Figure *S-4*. Percentage of inhibition of *β*-glucosidase versus concentration of compound **22.**

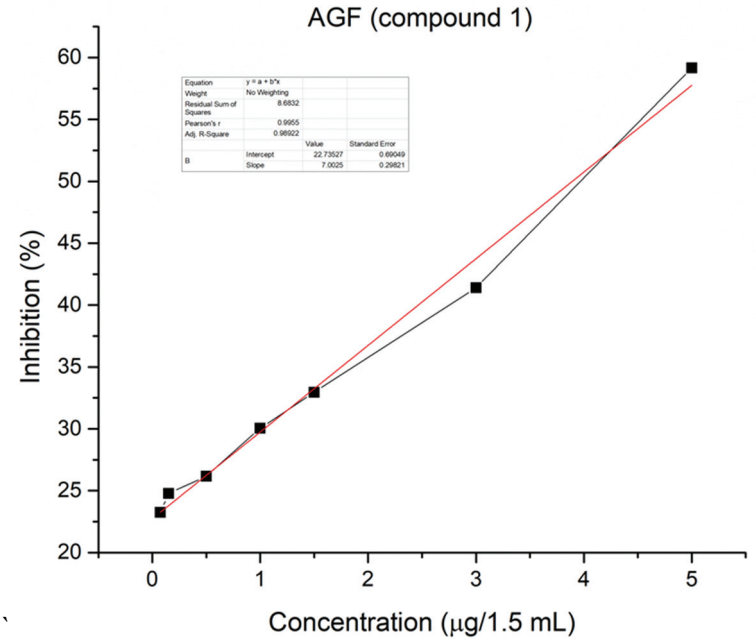

Figure *S-5*. Percentage of inhibition of *β*-glucosidase versus concentration of compound **AGF.**

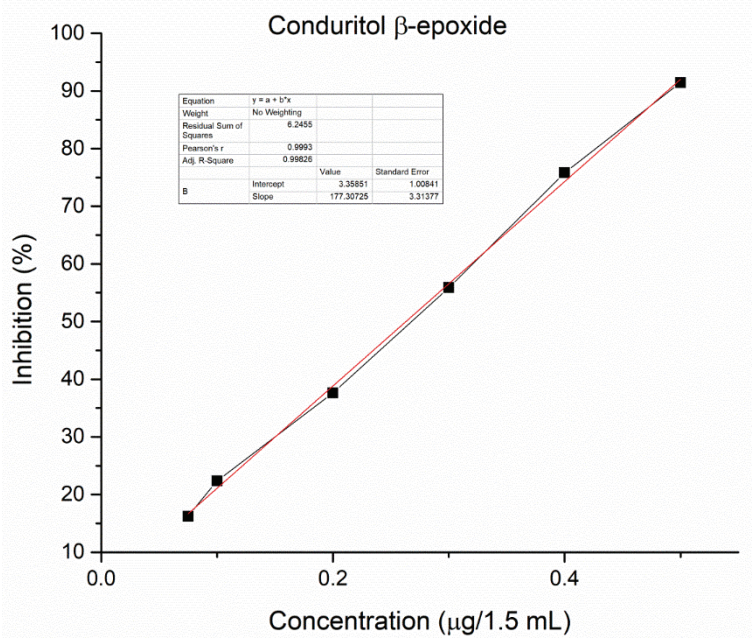

Figure *S-6*. Percentage of inhibition of *β*-glucosidase versus concentration of compound Conduritol *β*-epoxide.

LIGAND INTERACTIONS SCHEMES FOR COMPOUNDS 12, 13, 22 AND AGF

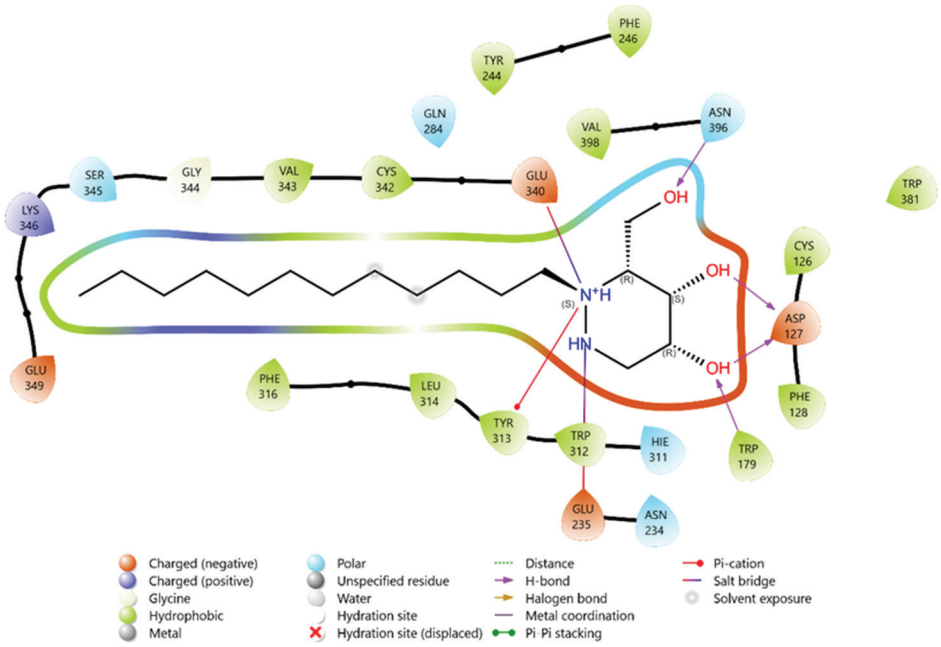

Figure ***S-7***. Ligand interactions for molecule **12** binded in *β*-glucosidase.

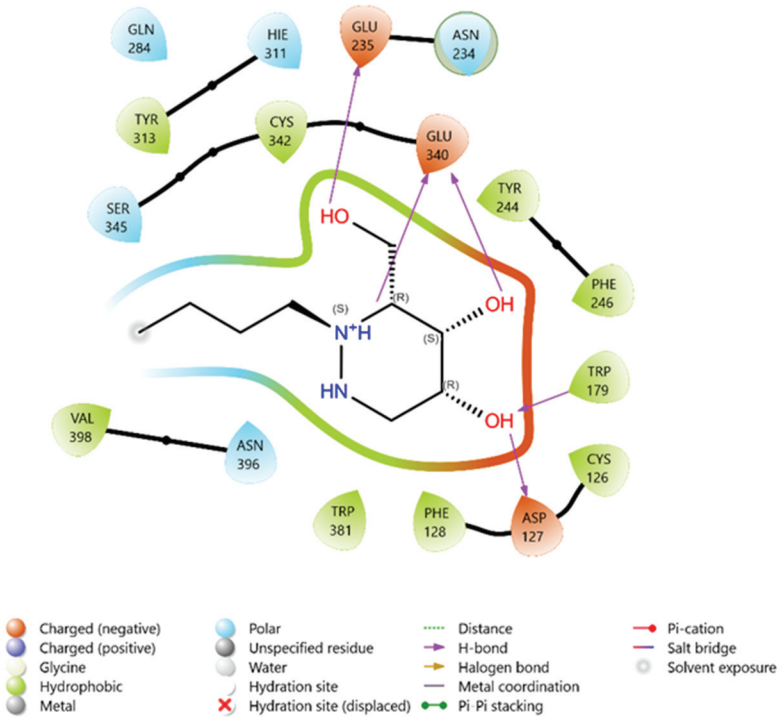

Figure *S-8*. Ligand interactions for molecule **13** binded in *β*-glucosidase.

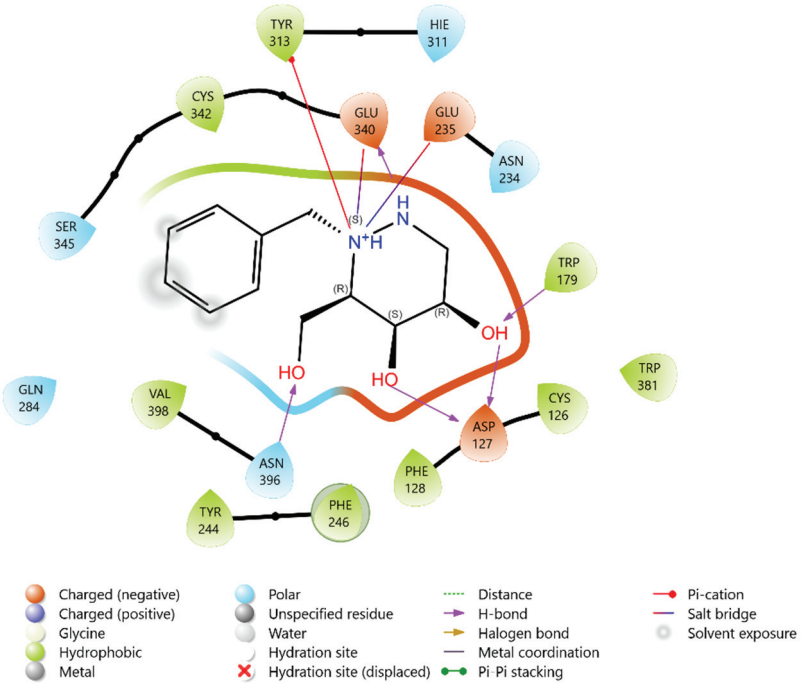

Figure *S-9*. Ligand interactions for molecule **22** binded in *β*-glucosidase.

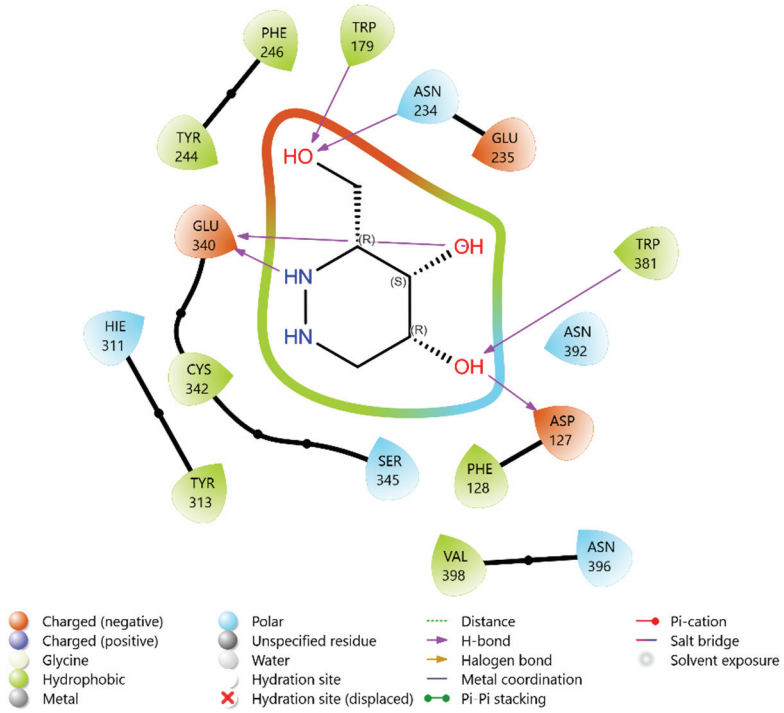

Figure *S-10*. Ligand interactions for molecule **AGF** binded in β-glucosidase.

COPIES OF NMR SPECTRA

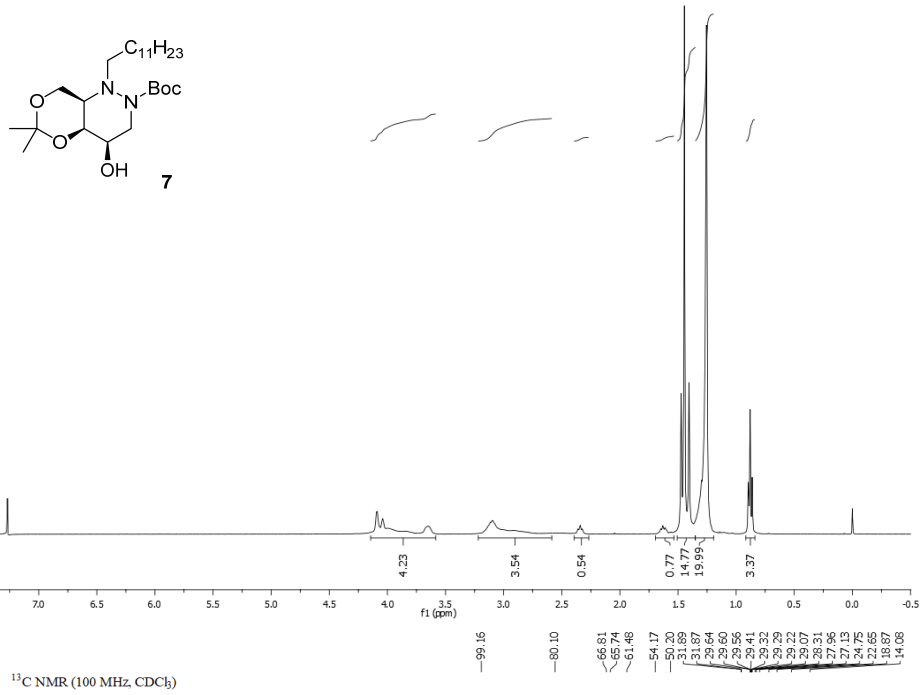

^{13}C NMR (100 MHz, $CDCl_3$)

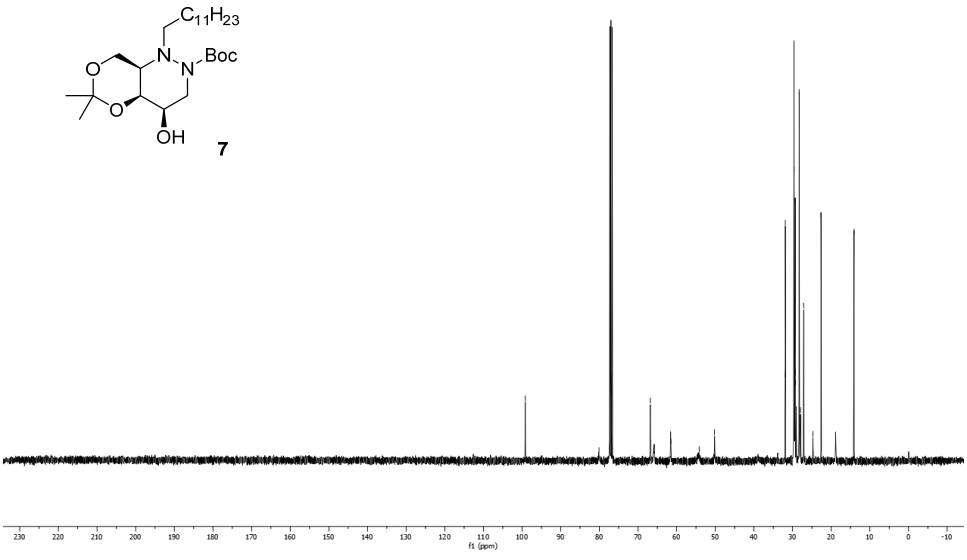

^{1}H NMR (400 MHz, $CDCl_3$)

8

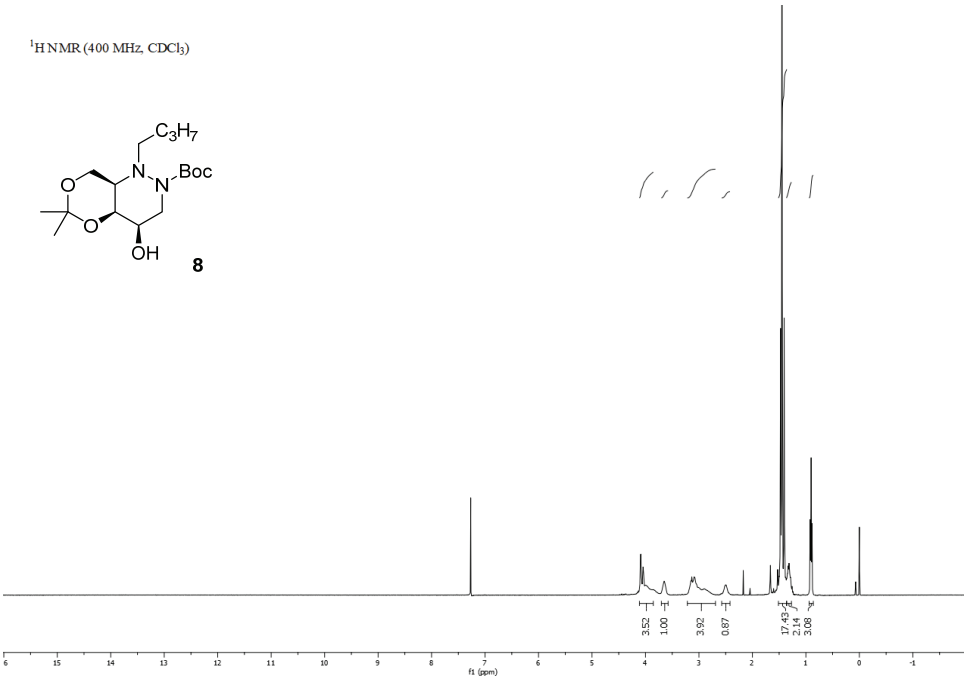

^{13}C NMR (100 MHz, $CDCl_3$)

8

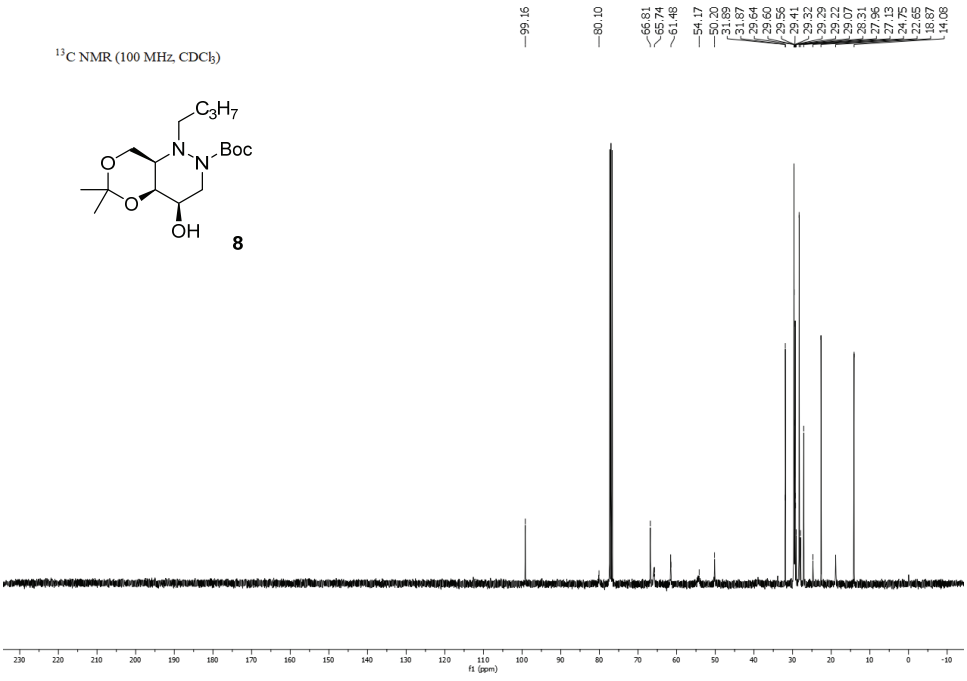

^{1}H NMR (400 MHz, $CDCl_3$)

9

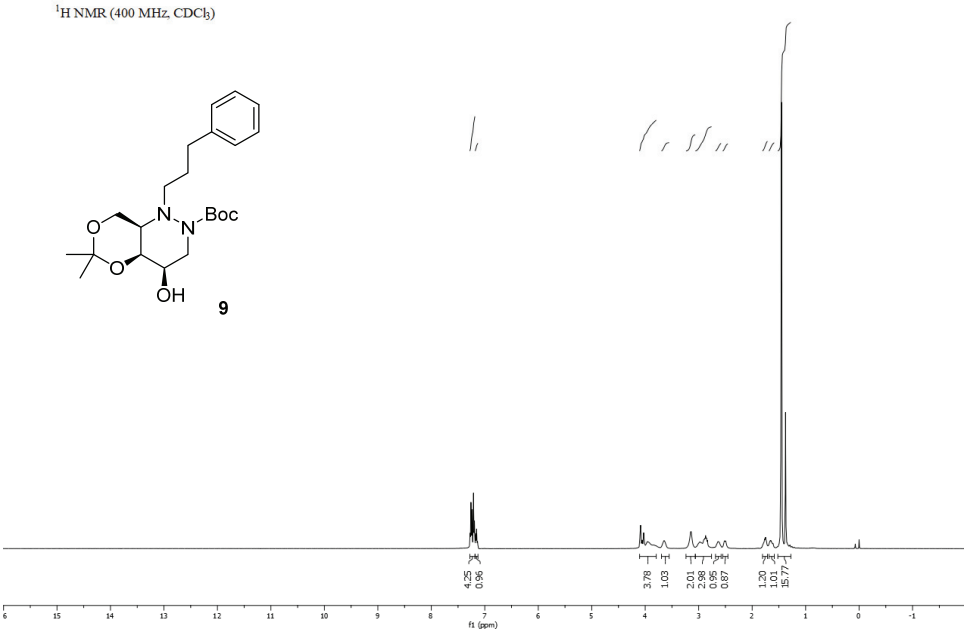

^{13}C NMR (100 MHz, $CDCl_3$)

9

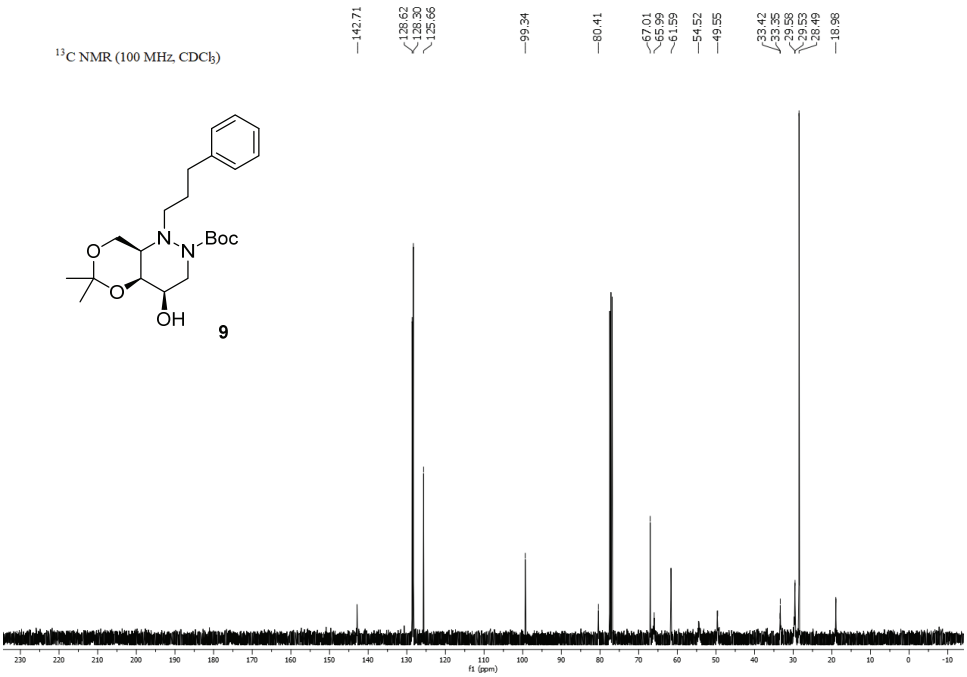

^{1}H NMR (400 MHz, D_2O)

12

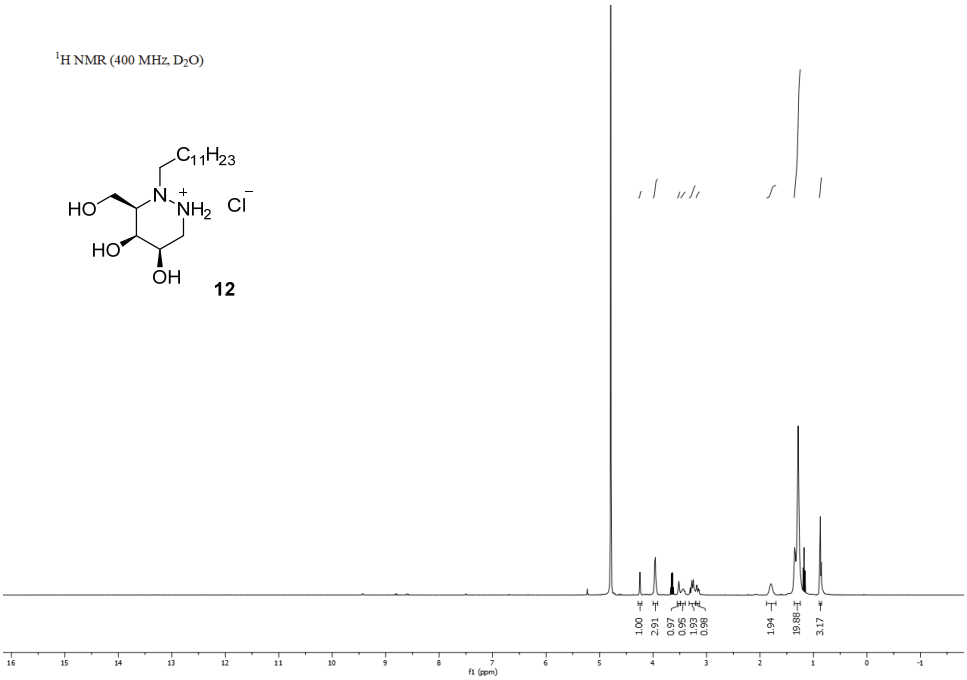

^{13}C NMR (100 MHz, D_2O)

12

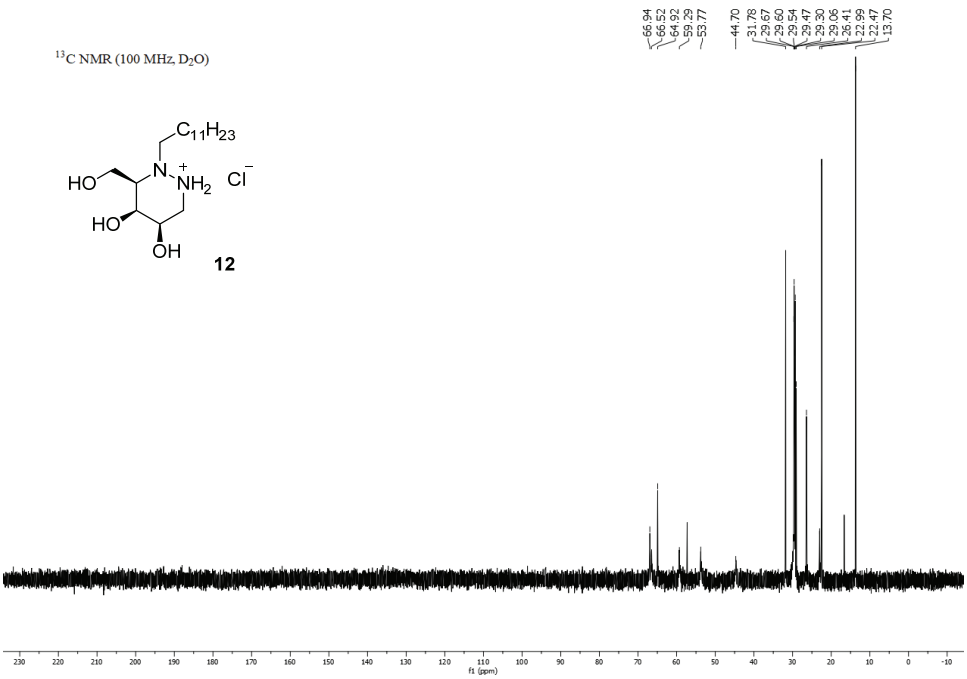

^{1}H NMR (400 MHz, D_2O)

13

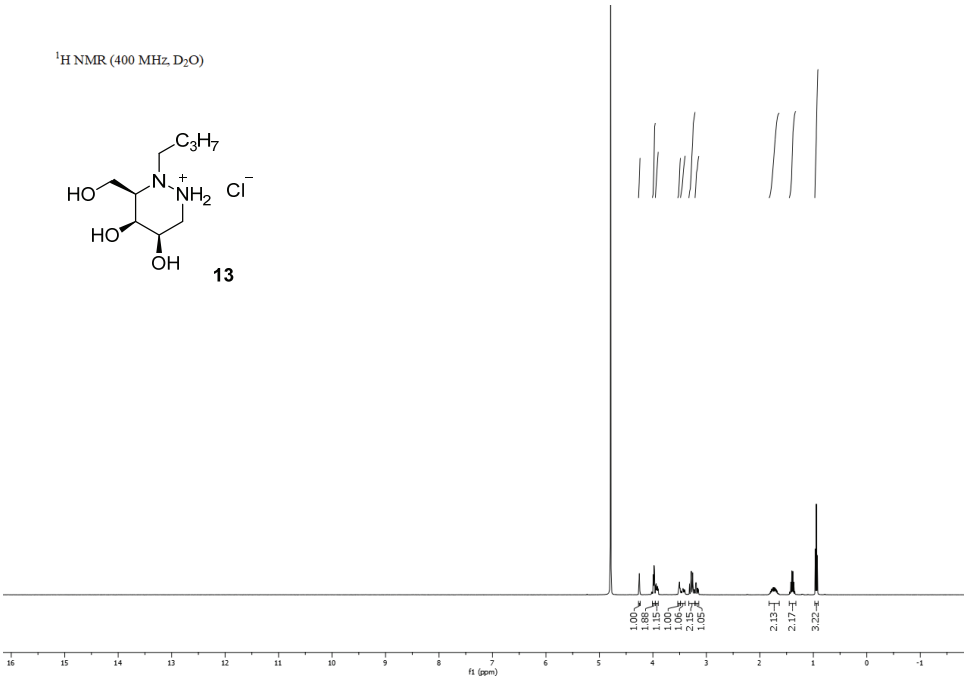

^{13}C NMR (100 MHz, D_2O)

13

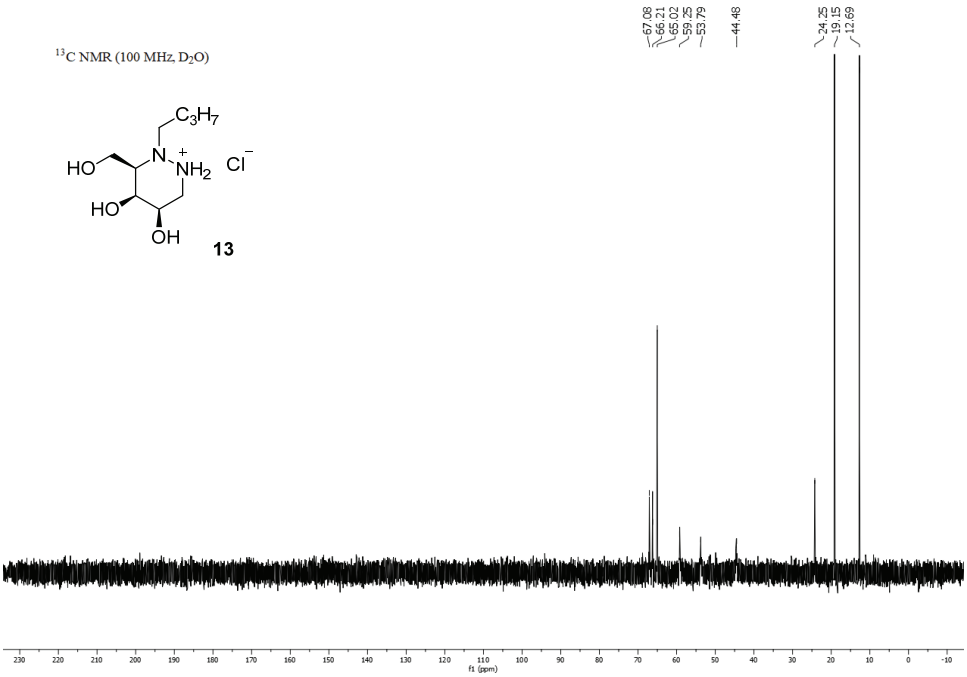

^{1}H NMR (400 MHz, D_2O)

14

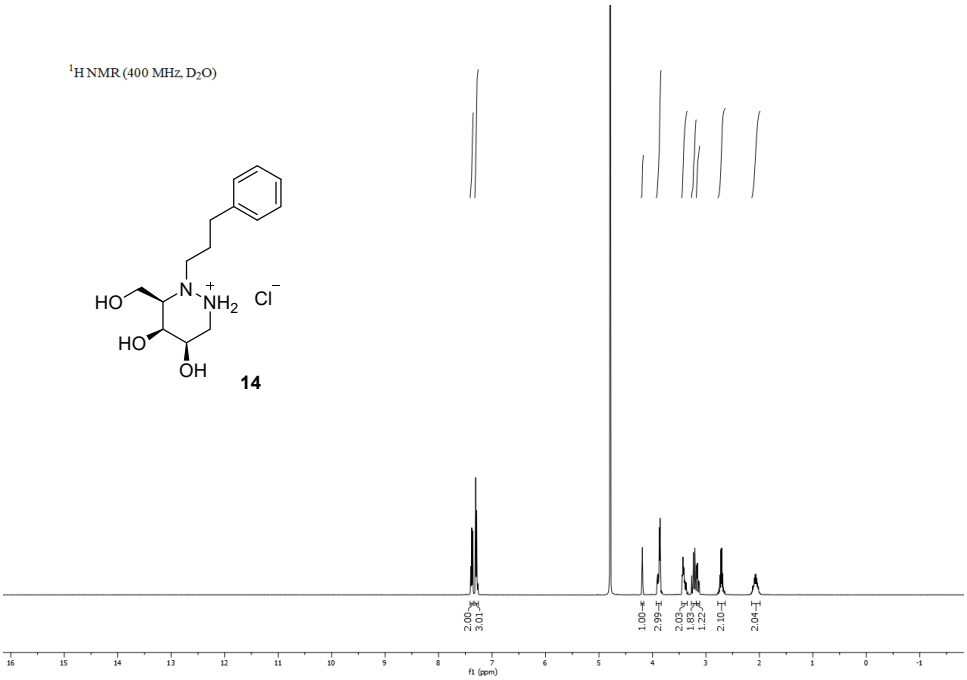

^{13}C NMR (100 MHz, D_2O)

14

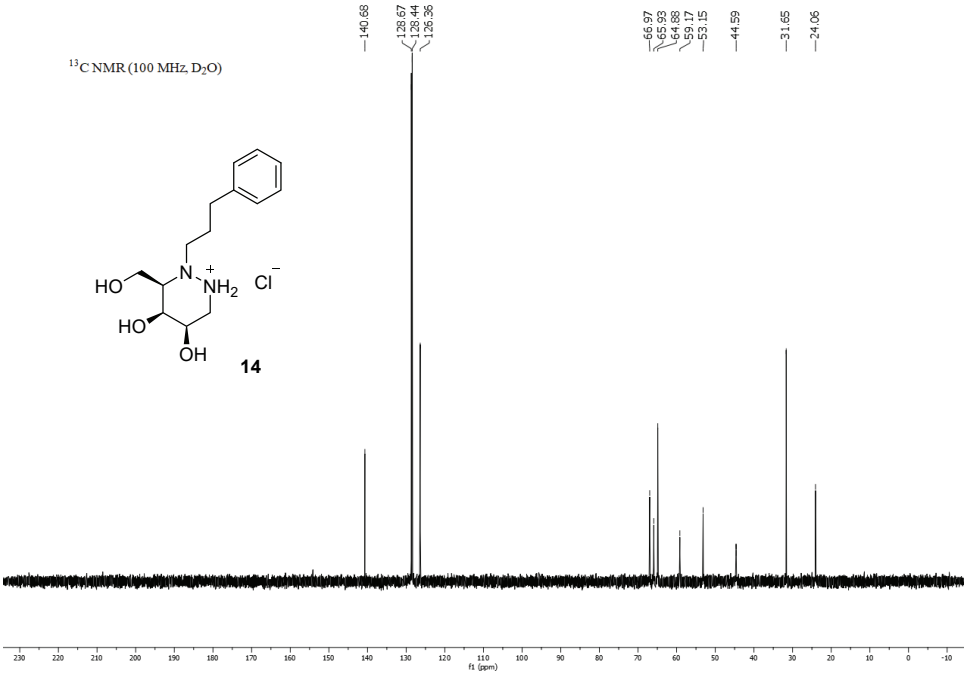

^{1}H NMR (400 MHz, $CDCl_3$)

15

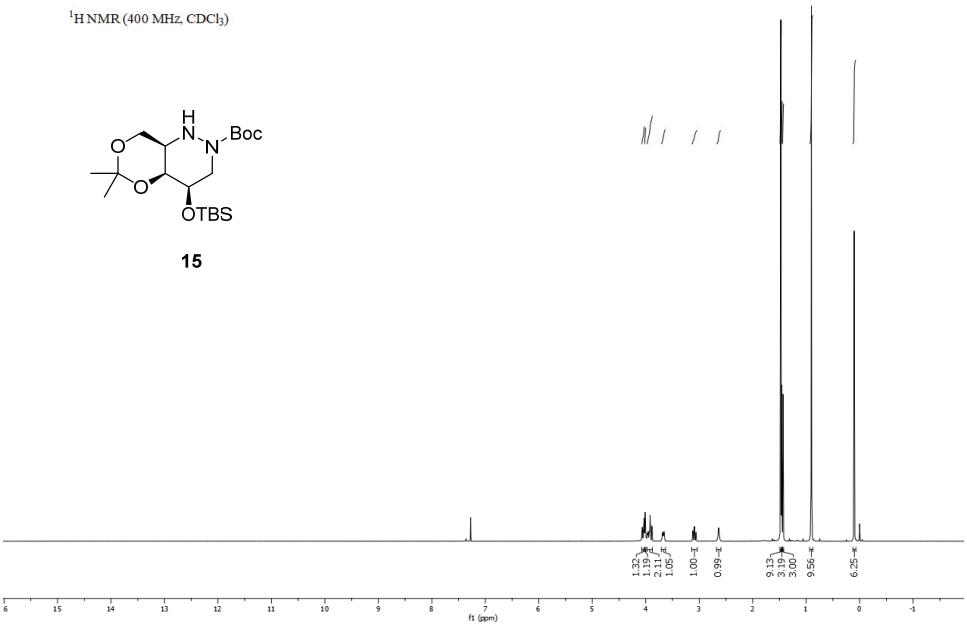

^{13}C NMR (100 MHz, $CDCl_3$)

15

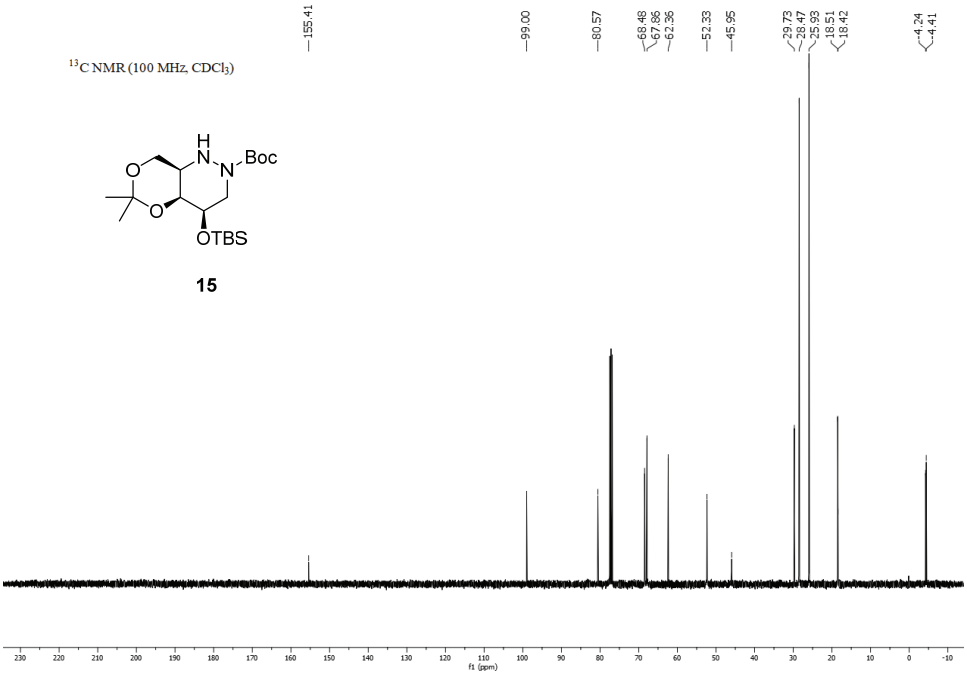

^{1}H NMR (400 MHz, $CDCl_3$)

16

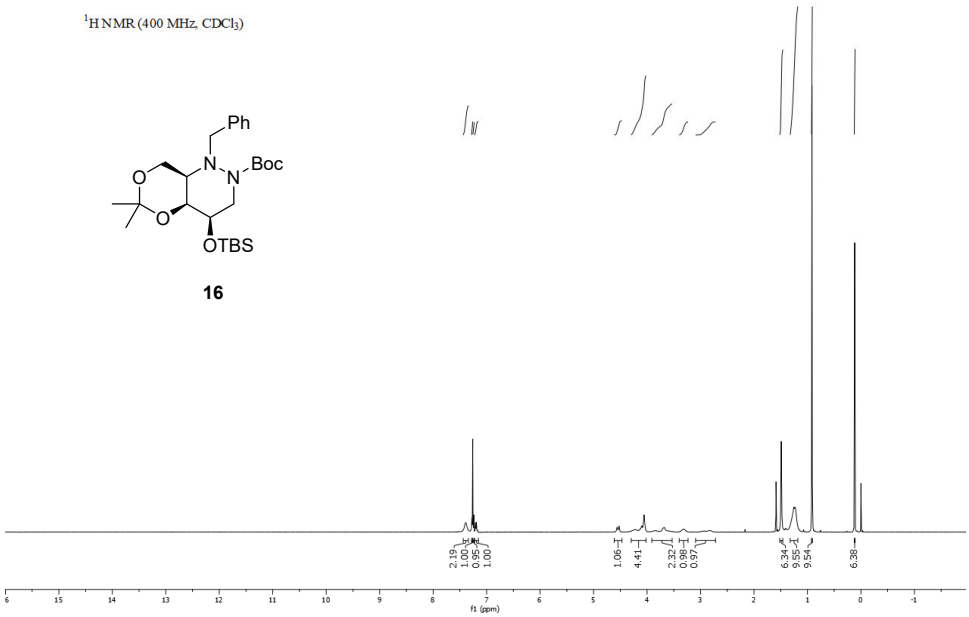

^{13}C NMR (100 MHz, $CDCl_3$)

16

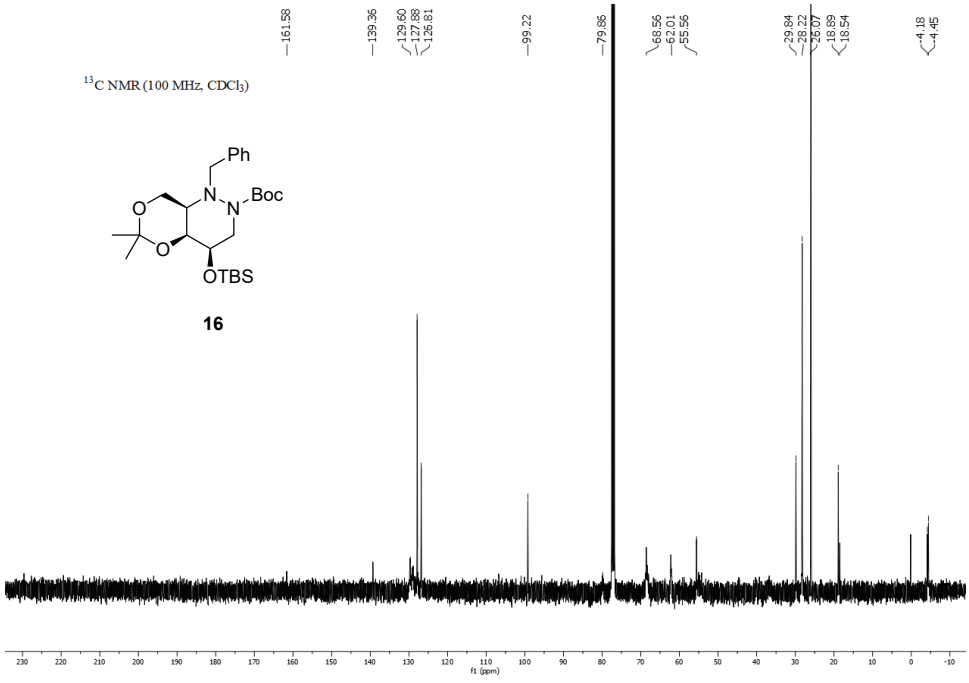

^{1}H NMR (400 MHz, $CDCl_3$)

17

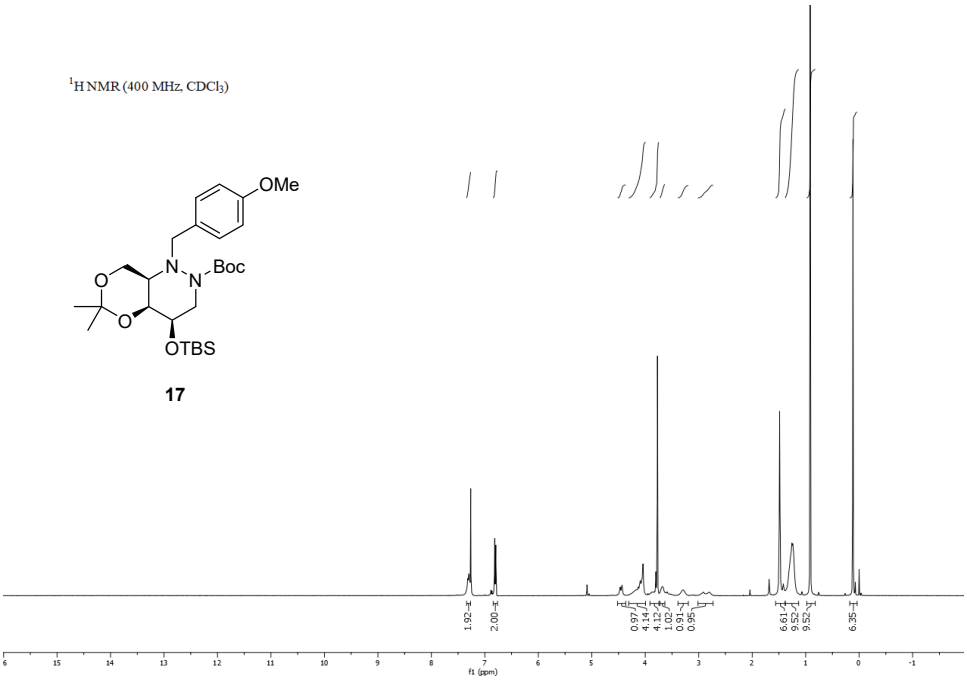

^{13}C NMR (100 MHz, $CDCl_3$)

17

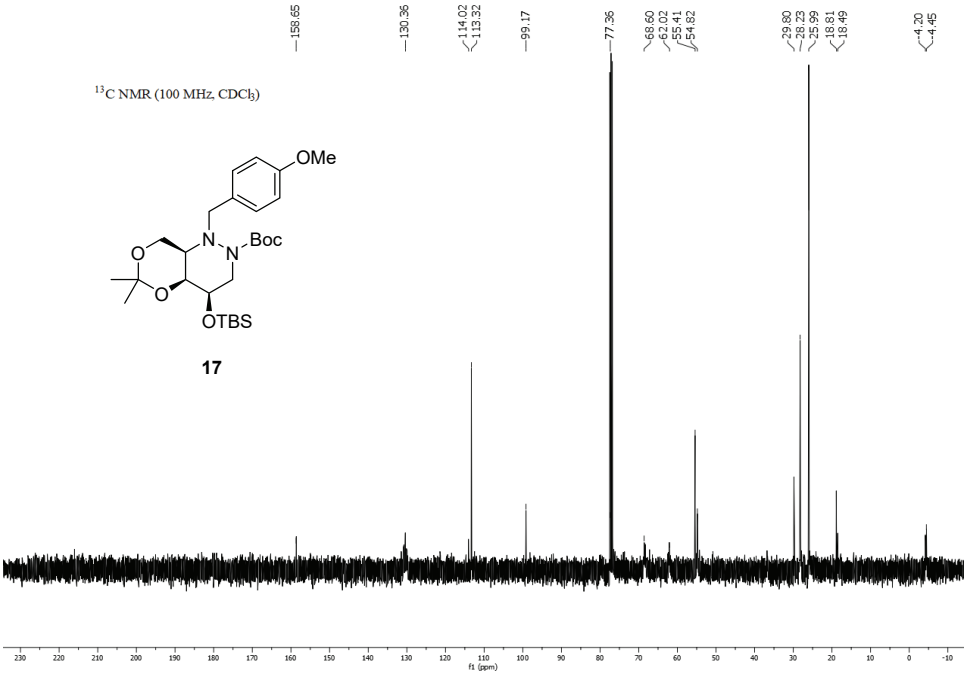

^{1}H NMR (400 MHz, $CDCl_3$)

18

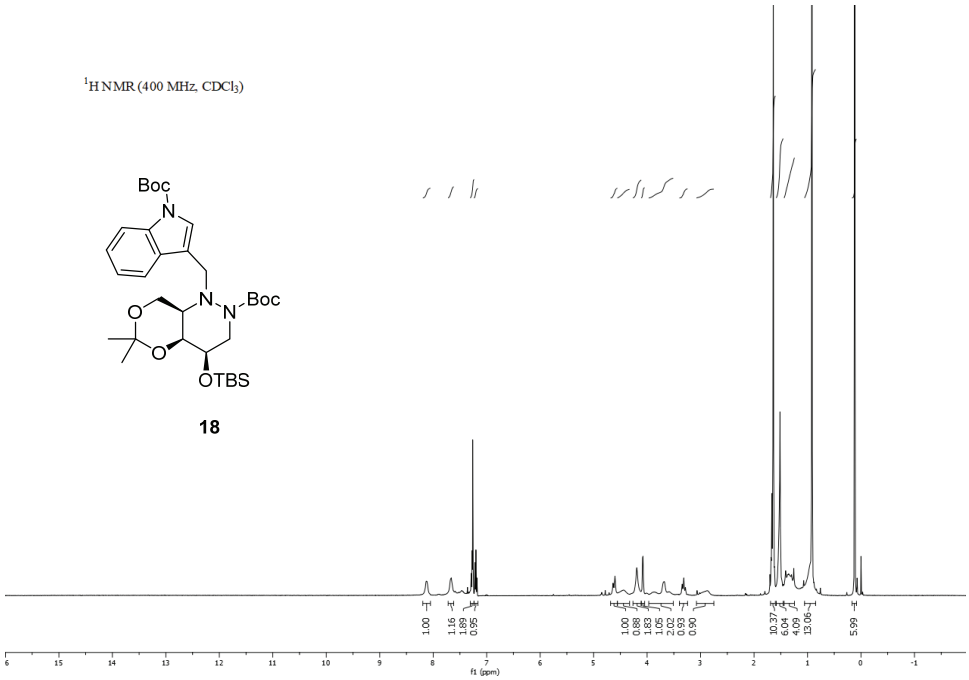

^{13}C NMR (100 MHz, $CDCl_3$)

18

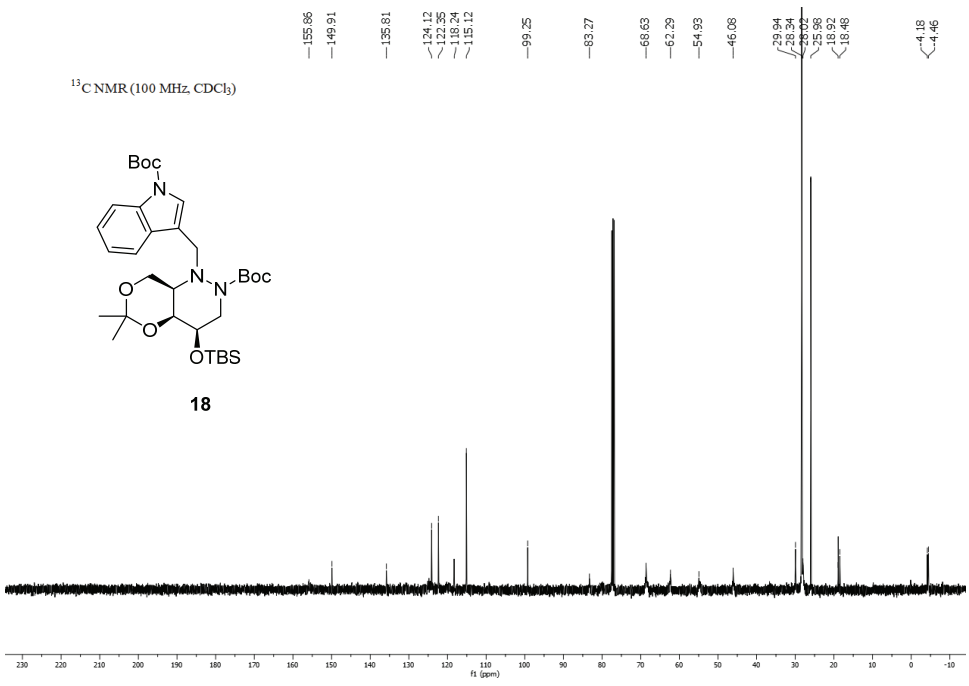

^{1}H NMR (400 MHz, CD_3OD)

19

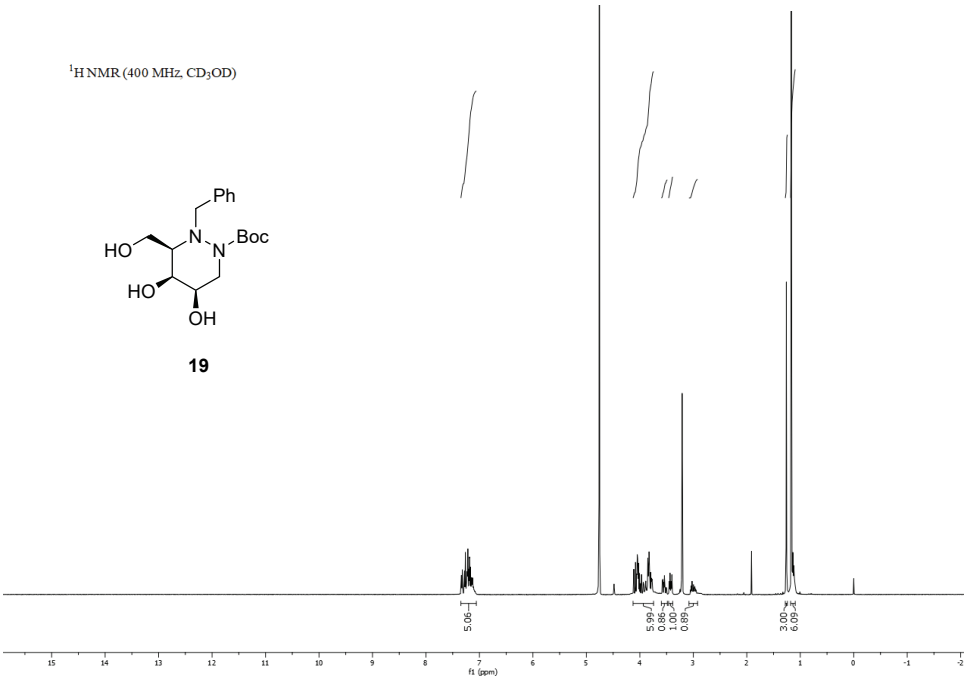

^{13}C NMR (100 MHz, CD_3OD)

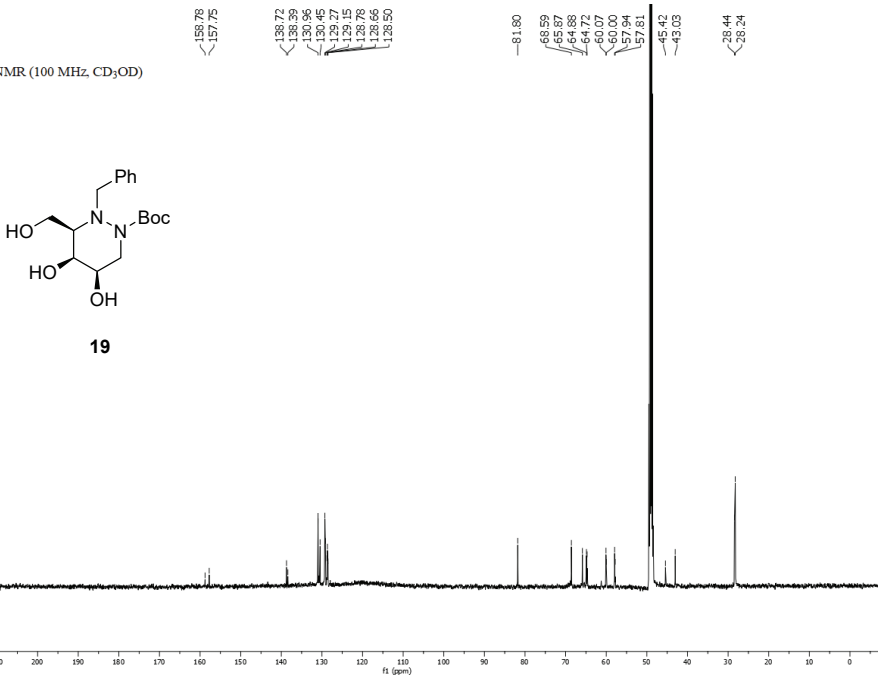

19

^{1}H NMR (400 MHz, CD_3OD)

20

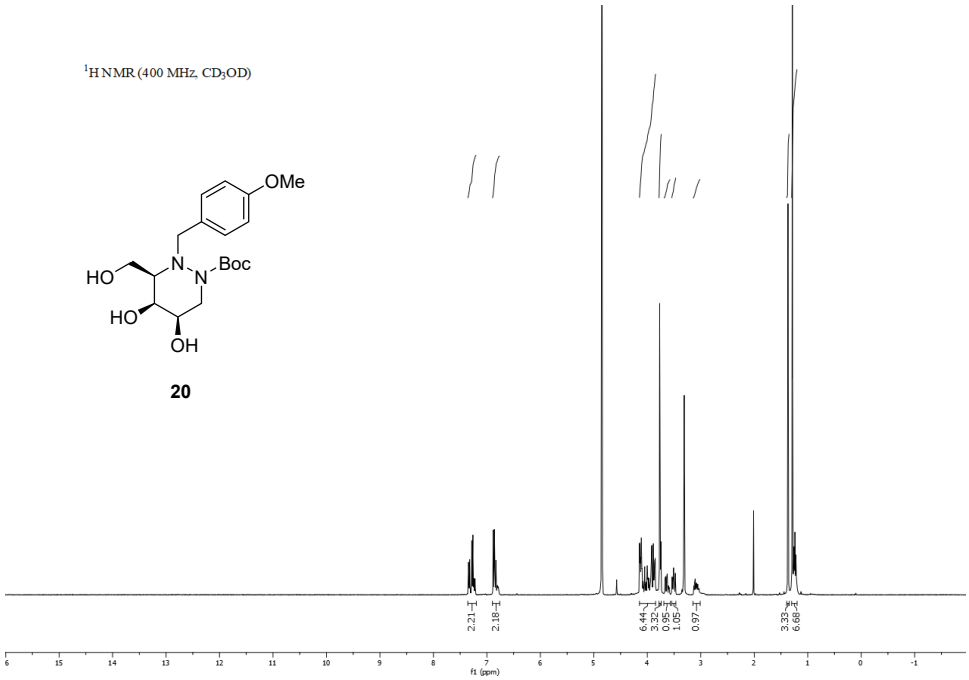

^{13}C NMR (100 MHz, CD_3OD)

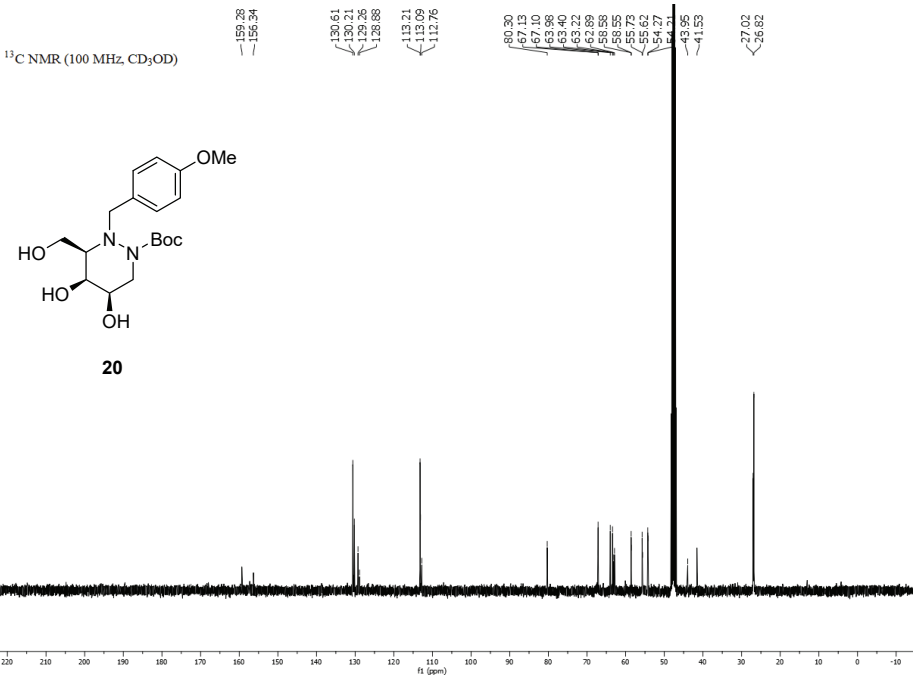

20

^{1}H NMR (400 MHz, CD_3OD)

21

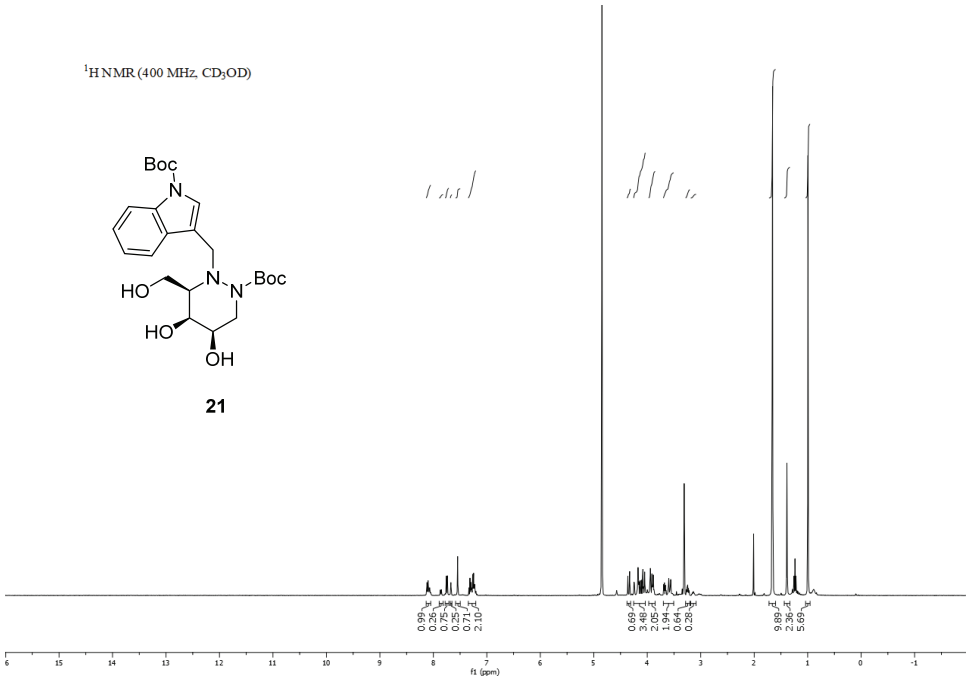

^{13}C NMR (100 MHz, CD_3OD)

21

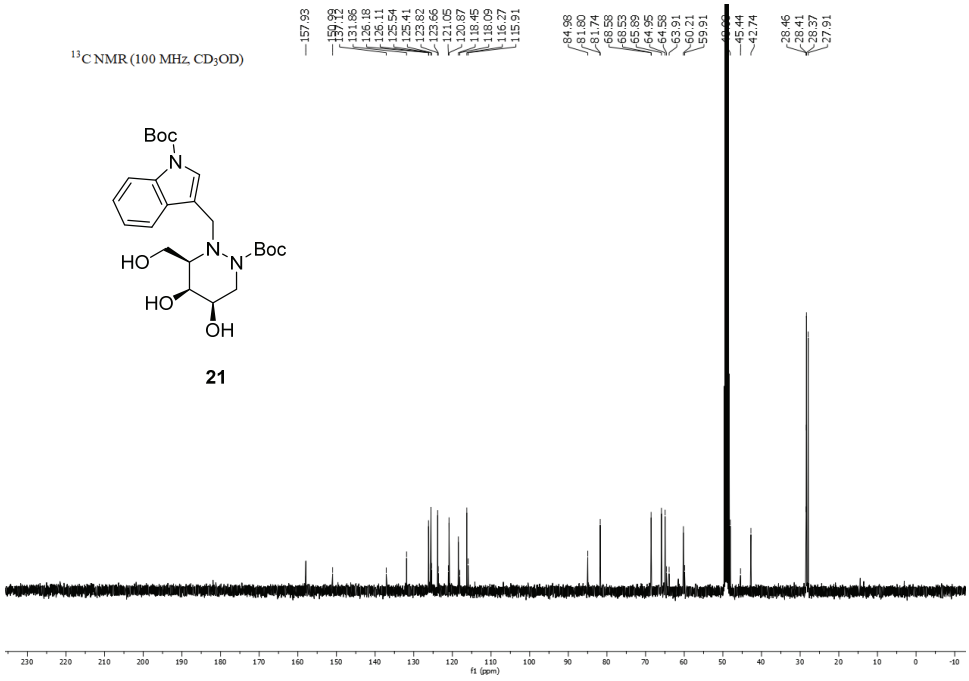

^{1}H NMR (400 MHz, D_2O)

22

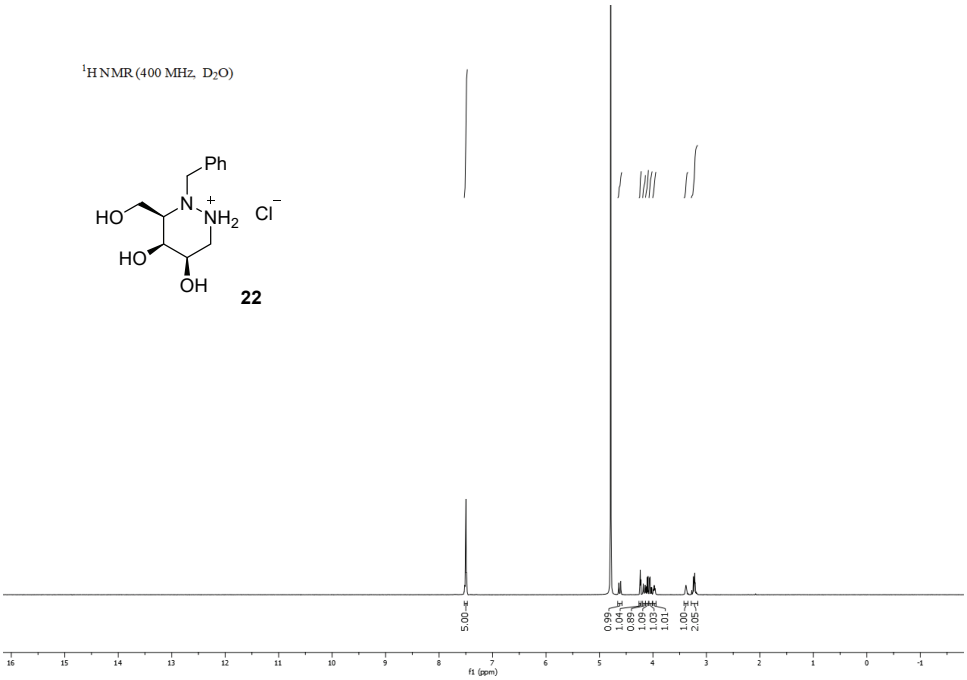

^{13}C NMR (100 MHz, D_2O)

22

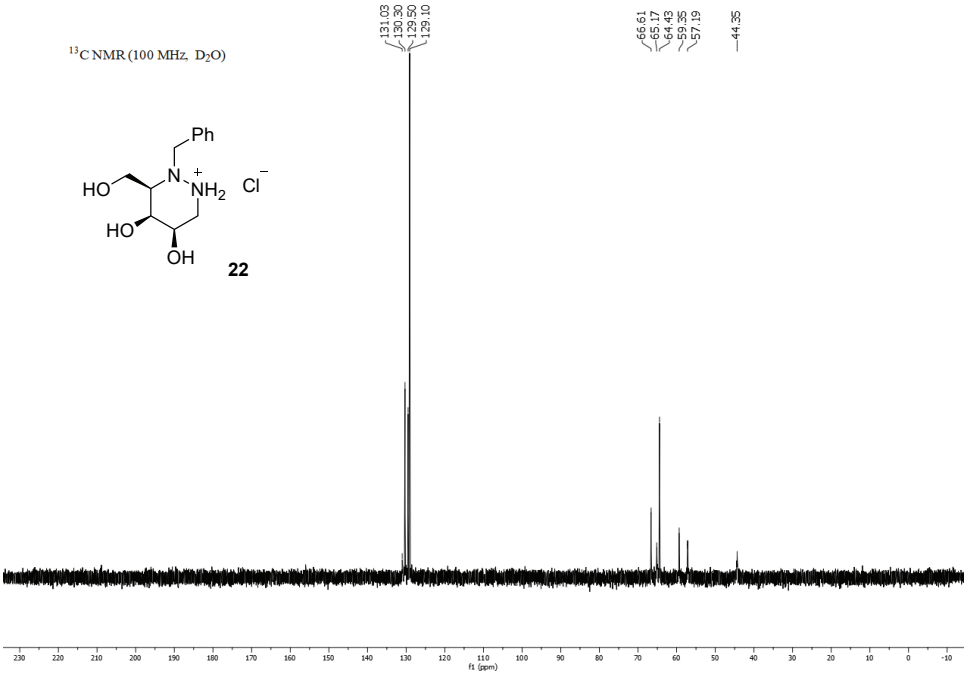

^{1}H NMR (400 MHz, $CDCl_3$)

23

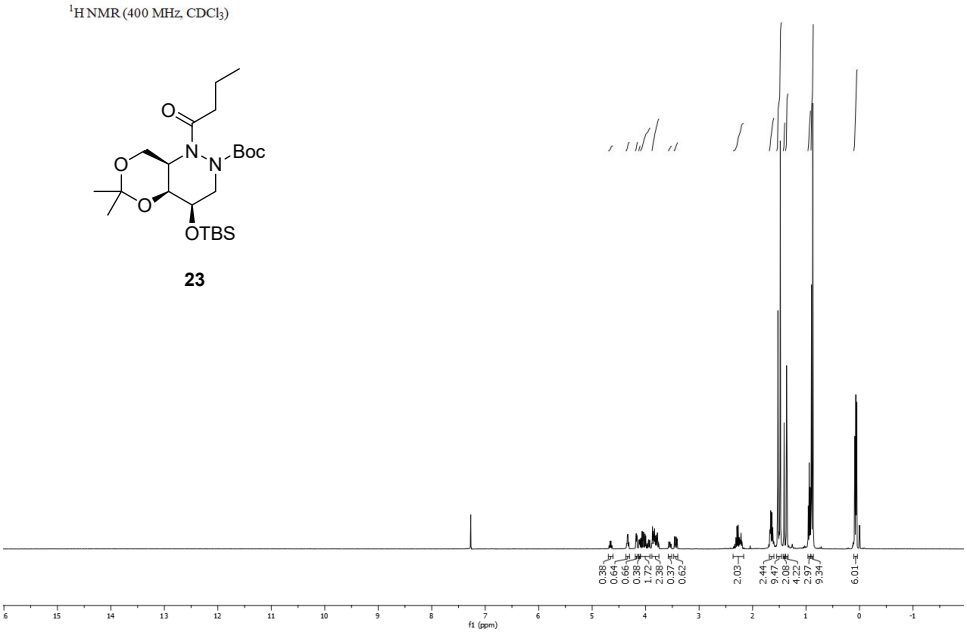

^{13}C NMR (100 MHz, $CDCl_3$)

23

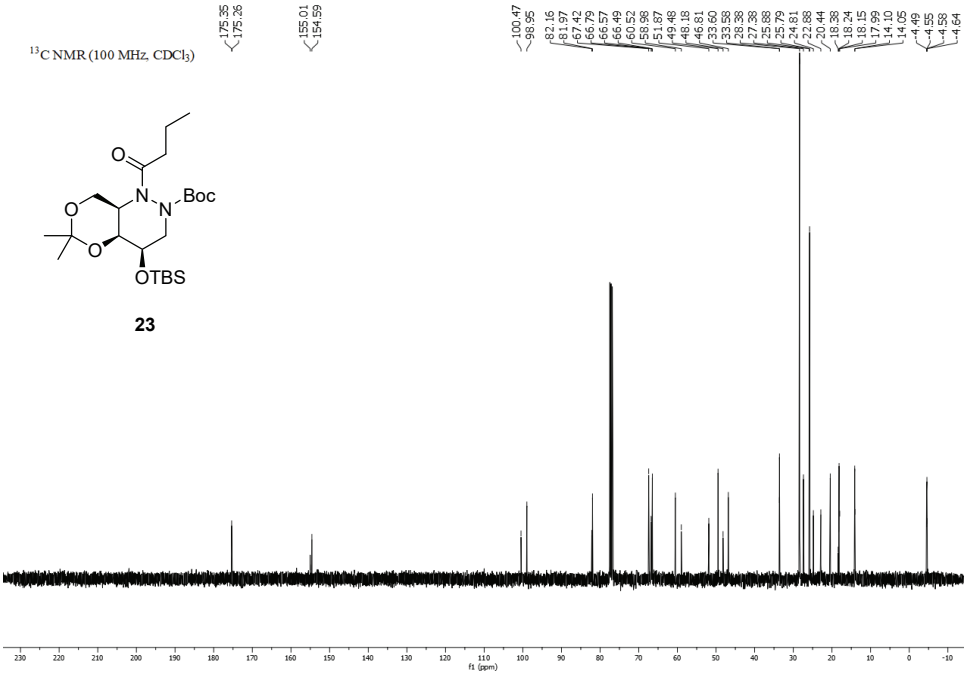

^{13}H NMR (400 MHz, $CDCl_3$)

24

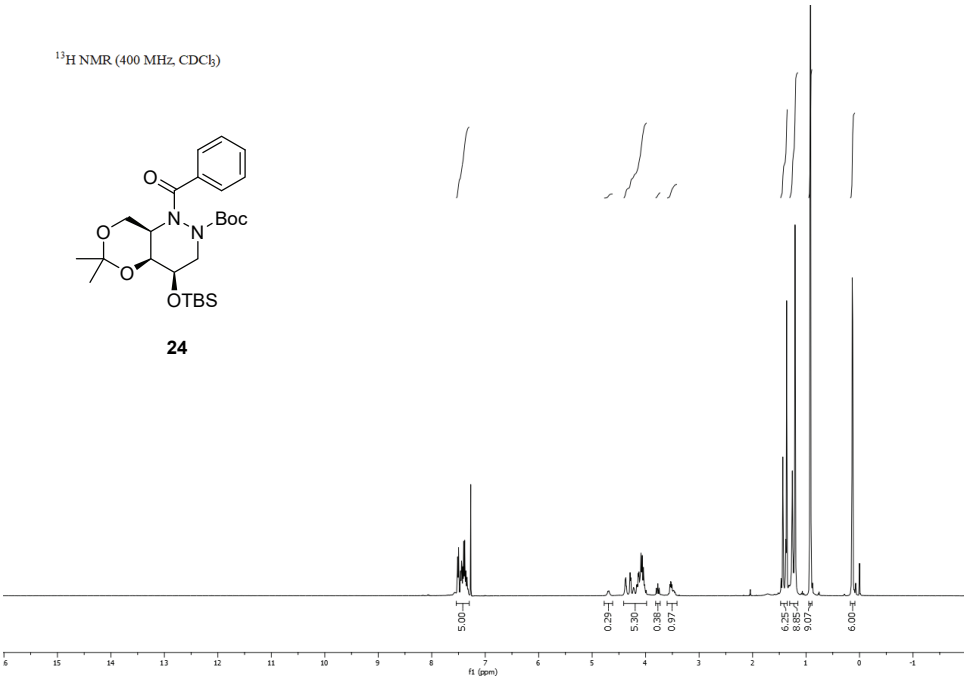

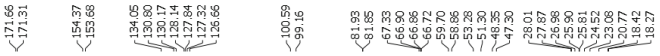

^{13}C NMR (100 MHz, $CDCl_3$)

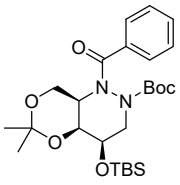

24

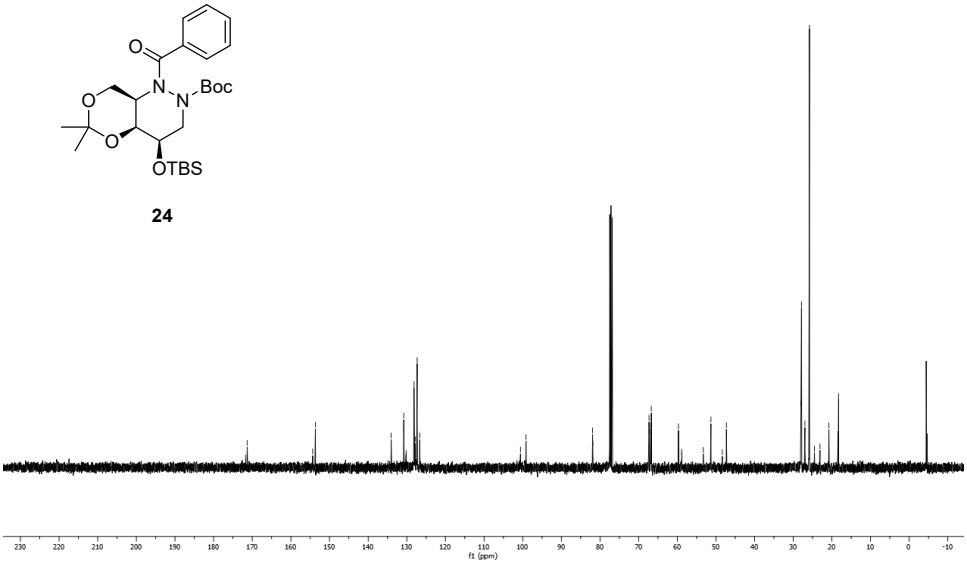

^{1}H NMR (400 MHz, CD_3OD)

25

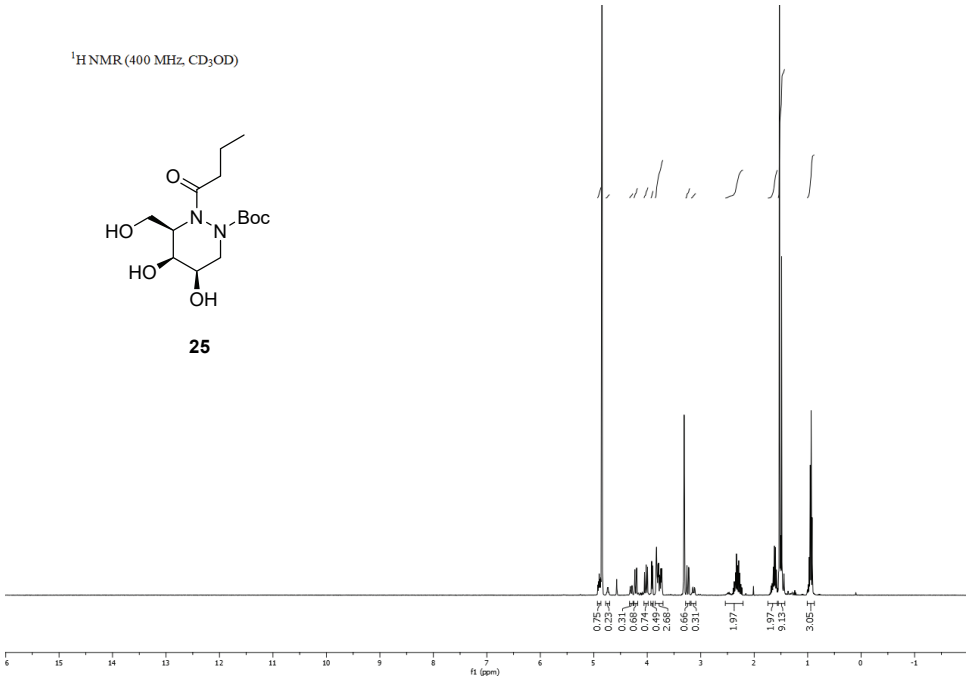

^{13}C NMR (100 MHz, CD_3OD)

25

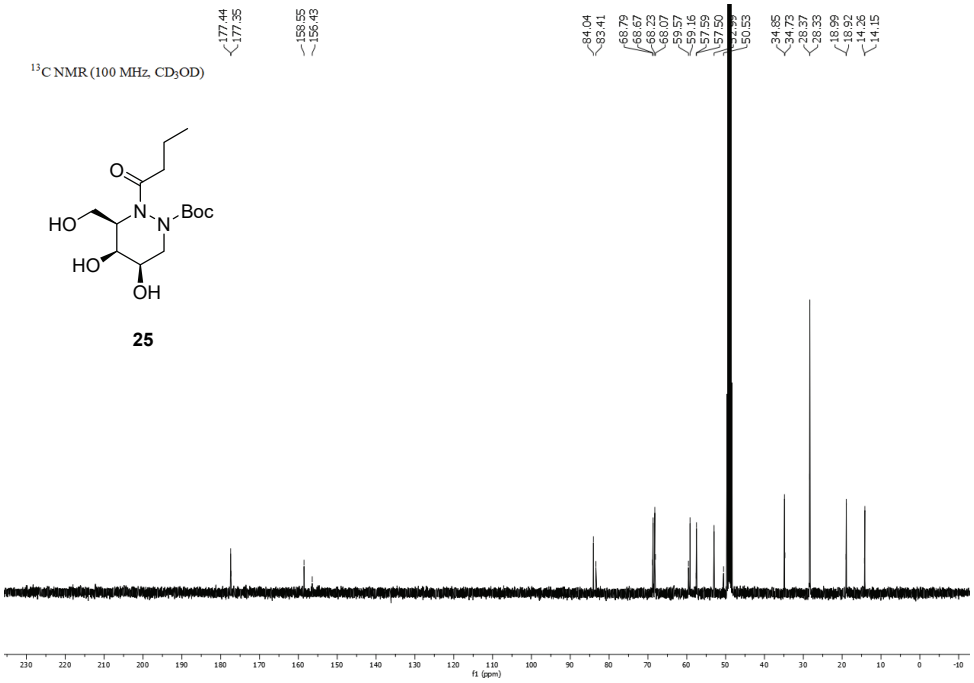

^{1}H NMR (400 MHz, CD_3OD)

26

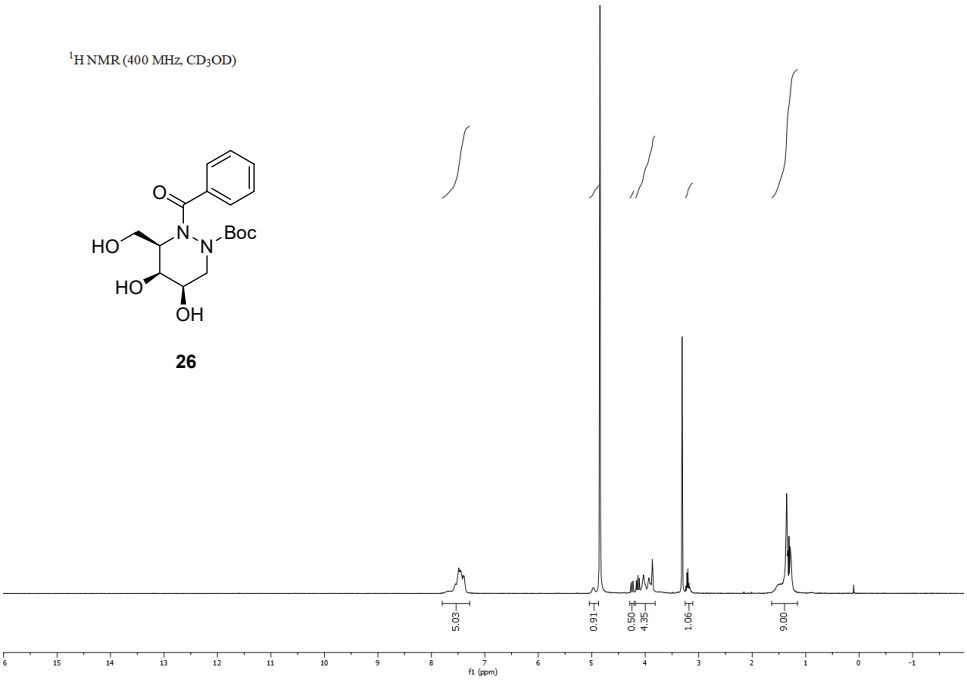

^{13}C NMR (100 MHz, CD_3OD)

26

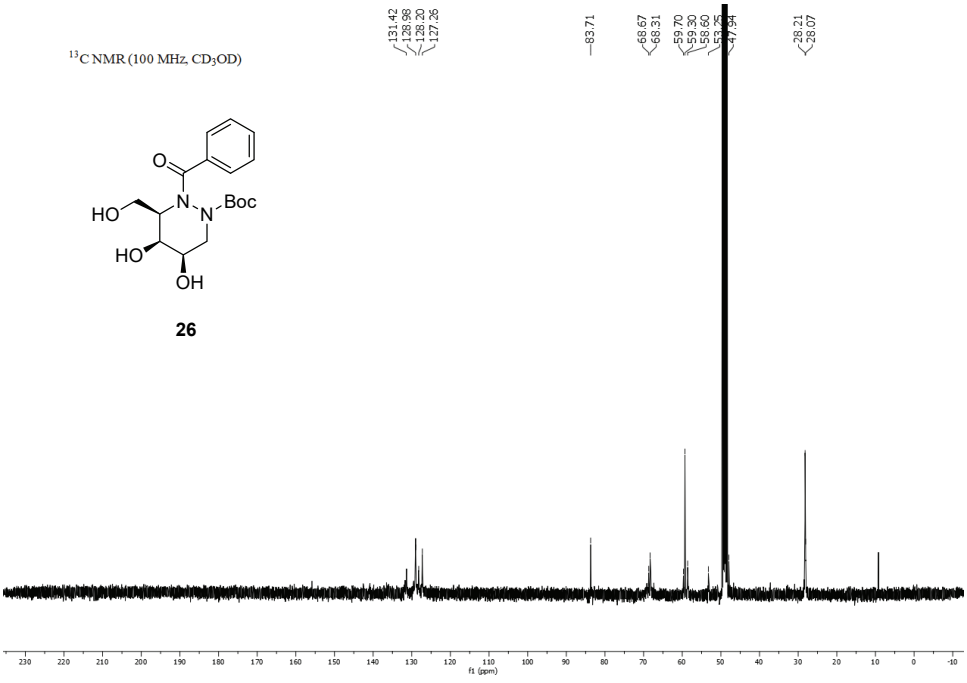

Journal of the Serbian Chemical Society
JSCS@tmf.bg.ac.rs • www.shd.org.rs/JSCS
J. Serb. Chem. Soc. *89* (10) 1269–1283 (2024)
JSCS–5786
Original scientific paper
Published 11 October, 2024

Immobilization of periodate-oxidized horseradish peroxidase by adsorption on sepiolite

NEVENA SURUDŽIĆ[1], MILOŠ SIMIĆ[2], MILICA CRNOGLAVAC POPOVIĆ[3], REYADH EL GAHWASH[3], MILICA SPASOJEVIĆ SAVKOVIĆ[4], RADIVOJE PRODANOVIĆ[3] and OLIVERA PRODANOVIĆ[1]*

[1]*University of Belgrade – Institute for Multidisciplinary Research, Kneza Višeslava 1, 11030 Belgrade, Serbia,* [2]*Center for New Technologies, 11000 Belgrade, Serbia,* [3]*University of Belgrade – Faculty of Chemistry, Studentski trg 12, 11000 Belgrade, Serbia and* [4]*University of Belgrade – Innovative Centre of the Faculty of Chemistry, Studentski trg 12, 11030 Belgrade, Serbia*

(Received 27 December 2023, revised 26 January, accepted 7 July 2024)

Abstract: Horseradish peroxidases (HRP), native and periodate-oxidized were immobilized onto sepiolite clay mineral by adsorption. Both peroxidases were adsorbed on this carrier in different quantities. Specific activity of immobilized enzymes was increased with increasing the amount of peroxidase added per gram of sepiolite. The highest specific activity was achieved when 15 mg of peroxidase was added per g of sepiolite. Also, periodate-oxidized enzymes showed similar specific activity as native ones. Stability studies (pH, thermal and operational stability) were conducted for both peroxidases. Residual specific activity of HRP immobilized onto sepiolite declined with an increase of incubation time at 65 °C. Oxidized-peroxidase lost 64 % of the initial activity, whereas native HRP dropped 92 % of its activity after 5 min of incubation at 65 °C. Reduction of the enzyme activity was observed with the temperature increase from 30 to 80 °C. pH profiles of native peroxidase immobilized onto sepiolite were higher in both acidic and basic regions compared to periodate-oxidized enzyme. Oxidized HRP was more successful in studies of operational stability, it retained 42 % of its activity after 4 consecutive cycles of pyrogallol oxidation, whereas native peroxidase kept only 11 % of the original activity.

Keywords: modified enzyme; specific activity; thermostability; reusability.

INTRODUCTION

Enzymes, as biological catalysts, have shown a large potential for application in various fields of industry such as pharmaceutical, chemical, paper, food and cosmetic industries, as well as in the production of detergents and textile.[1,2]

* Corresponding author. E-mail: oliverap@imsi.rs
https://doi.org/10.2298/JSC231227068S

Immobilization of enzymes on different support materials allows for a higher stability of enzyme, reduces an enzyme inactivation and prevents a product contamination.[3,4] Additionally, reusability and higher cost-effectiveness are accomplished by enzyme immobilization. It is important to stress that this method also allows for easy separation of the immobilized enzyme from the reaction mixture and, thus, its recovery. Different types of enzyme immobilization methods, such as adsorption, covalent binding, cross linking and entrapment, can be used.[5] Each of these methods has its own benefits and drawbacks. Adsorption implies binding between an enzyme and support *via* mostly weak bonds (van der Waals, electrostatic interactions and hydrogen bonds). This is a simple and cost-effective method; however, a leakage and inactivation of enzyme occur as common side effects. Covalent binding of an enzyme to a carrier provides strong linkage, thus preventing highly undesirable enzyme leakage.[5,6] Entrapment of an enzyme is a physical method which does not involve formation of covalent bonds between an enzyme and support, thereby increases the possibility of enzyme leakage.[7]

In order to be suitable in enzyme immobilization reactions criteria regardless of the enzyme immobilization type, carriers need to fulfil certain criteria, such as high surface area, high permeability and hydrophilicity, microbial, mechanical, chemical and thermal stability. Based on their chemical properties, carriers can be classified into two major groups: inorganic and organic.[8] First supports used for the enzyme immobilization were inorganic owning to their high mechanical strength, thermal stability and resistance to organic solvents. They are suitable for application in different fields of industry, whereas organic carriers, due to their high reactivity, have found greater application in laboratory conditions.

As a consequence of great abundance of naturally present clay minerals, their role in many fields of industry, as well as in the scientific research, increases.[9] Among them, the most commonly used are sepiolite, palygorskite, montmorillonite and kaolinite. Their availability, physicochemical properties and crystal structure allow for their potential applications in many different fields. These materials are economic and can be used without any additional modifications. Active groups presented on the surface of these materials (carboxyl, hydroxyl, thiol, amine groups) make them suitable for binding of many different enzymes in immobilization reactions.[9] Sepiolite ($Si_{12}O_{30}Mg_8(OH)_4(OH_2)_4{\cdot}nH_2O$), as a silicate clay mineral rich with magnesium, is characterized by a fibrous crystal structure, great specific surface area and active silanol groups on the external surface.[10] Each of these properties makes sepiolite an excellent candidate for adsorption reactions in many different areas. The world's sepiolite reserves are estimated to be about 8 million tons and the mine with the largest amount of sepiolite is located in Spain. Sepiolite often appears in two forms, α and β-sepiolite, differing in the crystal shape. α-sepiolite consists of a large bundle of fibrous crystals, whereas β-sepiolite comprises short and thin fibrous crystals. α-Sepiolite is abundant in

Tertiary rocks rich in phosphates, salts, zeolites, while *β*-sepiolite prevails in marine, lagoonal and pedogenic environments. Change in the nature and localization of functional groups on the surface of sepiolite alters mechanical properties of the whole molecule and therefore expands the range of areas in which it can be applied.[10]

Sepiolite has already been used as a carrier for various enzymes. Olshansky and co-workers immobilized by adsorption laccase derived from *Rhus vernicifera* on sepiolite and modified sepiolite (with Cu(II) and chitosan). The immobilized enzyme on unmodified Cu-chitosan- and chitosan-modified sepiolite has shown increased activity of 250, 700 and 500 % compared to the free form.[11] Alkaline phosphatase from the bovine intestinal mucous membrane was immobilized by sorption on Na-sepiolite. In a wide range of pH (from 5 to 11), the immobilized enzyme has shown substantially higher activity than the soluble enzyme. The authors have reported lower stability when storing at 30 °C and higher thermal denaturation of the immobilized alkaline phosphatase compared to its free form.[12] Sedaghat and co-workers immobilized alkaline phosphatase from calf intestinal mucous membrane on unmodified and modified sepiolite (with mono- and bilayer surfactant). The enzyme immobilized on sepiolite with the bilayer surfactant coverage has shown the most promising temperature and pH stability. Also, this immobilization system has shown the same activity as the free enzyme, whereas the enzyme immobilized on unmodified sepiolite and modified sepiolite with monolayer surfactant coverage has shown reduced activity by about 30 and 38 %.[13] Shirvani and coworkers have studied the adsorption of alkaline phosphatase on polygorskite and sepiolite. They found the enzyme activity loss after immobilization on these two carriers. However, higher resistance to a Cd inhibitory effect was achieved with immobilization.[14] Sepiolite and bentonite have been used as carriers for catalase, and an effect of immobilization on thermal, operational and storage stability has been studied. Compared to the free enzyme, immobilized catalase has shown improved properties, with the most promising thermal, operational, and storage stability achieved by immobilization on sepiolite.[15] Mortazavi and coworkers immobilized *α*-amylase from *Bacillus subtilis* and lipase from *Candida rugosa via* adsorption on modified Na-sepiolite. Lipase immobilized on modified sepiolite with hydrophobic properties and *α*-amylase immobilized on modified sepiolite with hydrophilic properties have shown improved thermal and storage stability, as well as reusability when compared to free enzyme.[16]

Peroxidases are enzymes that are capable of oxidizing phenolic compounds, the most frequent water pollutants, in the presence of hydrogen peroxide. This oxidation reaction results in the formation of water-insoluble polymeric aggregates, effortlessly eliminated from the aqueous phase by filtration or sedimentation. Among all enzymes from the group of peroxidases, horseradish peroxidase (HRP) has been the most commonly applied for this purpose.[17,18] A main issue in

using enzymes for water treatment is their inactivation, most probably caused by interactions between phenoxy radicals and the enzyme's active site.[19] This problem can be overcome by the enzyme immobilization.

In the present work, *β*-sepiolite clay mineral, obtained from a site near Obrenovac, was used for the first time as a carrier for immobilizing HRP (EC 1.11.7). Also, native HRP was, for the first time, immobilized by adsorption after periodate oxidation of the carbohydrate part of the protein molecule onto sepiolite. Activity, thermal and operational stability were tested to study the effect of enzyme modification by periodate oxidation on the activity and stability of sepiolite-adsorbed HRP.

EXPERIMENTAL

Materials

HRP (150–250 U mg^{-1}), pyrogallol used as a substrate for the peroxidase oxidation reaction and sodium periodate were purchased from Sigma–Aldrich. Hydrogen peroxide was obtained from AppliChem GmbH (Darmstadt, Germany). Sodium dihydrogen phosphate anhydrous and sodium acetate were purchased from Centrohem (Stara Pazova, Serbia) and Fluka (Buchs, Switzerland), respectively. Glycerol (from plant, for laboratory use) was purchased from Serva (Heidelberg, Germany).

Sepiolite

Sepiolite samples were collected near Obrenovac (Serbia) and milled with a pestle and mortar to the fineness of particles of 0.3 mm. Milled sepiolite was subsequently rinsed with distilled water and smaller particles were removed by fractional sedimentation. Procedure was repeated several times.

Oxidation of HRP

Oxidation of HRP was performed with the 5 mmol L^{-1} sodium periodate solution in sodium acetate buffer pH 5.0 (50 mmol L^{-1}) in the dark at 4 °C for 6 h. By adding glycerol to a final concentration of 0.2 vol. %, the oxidation reaction was stopped. Oxidized HRP was dialyzed overnight against sodium acetate buffer pH 5.

Immobilization of HRP onto sepiolite clay mineral

Sepiolite (0.1 g) was rinsed with 5 mL of sodium acetate buffer pH 5.0 (50 mmol L^{-1}) and incubated for 48 h with different amounts of native or oxidized HRP (1, 5, 15 and 25 mg g^{-1}) per g of clay mineral. Sepiolite with immobilized enzyme was subsequently rinsed with 2 mL of sodium acetate buffer pH 5.0 (0.1 mol L^{-1}) and stored in the same buffer at 4 °C until further use.

Washings were collected and used for determination of the unbound enzyme activity.

Activity studies of immobilized enzyme

Pyrogallol and hydrogen peroxide were used as substrates in an assay used to determine the peroxidase activity. Ten μL of enzyme dilution from the washings and 10 μL of H_2O_2 (9.7 mmol L^{-1}) were introduced into 1 mL of the pyrogallol solution (13 mmol L^{-1}) in sodium phosphate buffer pH 7 at room temperature. Absorbance was measured at 420 nm for 3 min using UV–Vis spectrophotometer (Shimadzu Corporation UV-2501PC, Japan). Value of the enzyme activity was calculated from the absorbance coefficient of purpurogallin (12 mg^{-1} cm^{-1}). The activity of immobilized enzyme was determined by introducing 9.0 mg of sepiolite with immobilized HRP and 30 μL of H_2O_2 into 3 mL of pyrogallol. Every 60 s aliquots were sampled from the mixture, filtrated and the absorbance at 420 nm was measured. One unit of enzyme activity

was defined as the amount of enzyme that produces 1 mg of purpurogallin in 20 s at 20 °C. The specific activity of enzyme was calculated per gram of dry weight of sepiolite. All measurements were done in triplicate.

Temperature stability kinetics of immobilized HRP

Temperature stability of native and periodate oxidized HRP and afterward immobilized onto sepiolite clay mineral (15 mg/g) was monitored at 65 °C for 5 and 30 min. An appropriate amount of the enzyme immobilized onto sepiolite was incubated in sodium phosphate buffer pH 7.0 (0.1 mol L^{-1}) at 65 °C a certain period of time. The immobilized enzyme was subsequently cooled down to room temperature. Residual specific activity of the immobilized enzyme was determined as described previously.

Activity measurements at different pH values

To monitor the enzymatic activity of immobilized HRP, a series of 0.1 mol L^{-1} phosphate––citrate buffers with pH values from 2.0 to 8.0 was used. In order to determine the enzyme stability at pH 9.0, sodium glycinate buffer (0.1 mol L^{-1}) was applied. According to the above-described procedure, relative activity of HRP immobilized onto sepiolite clay mineral was examined. Obtained results were afterwards normalized to the maximum activity at optimum pH, i.e. the relative activity, expressed as a percentage and presented.

Determination of thermostability of soluble and immobilized HRP

Thermostability of immobilized HRP at different temperatures (30, 40, 50, 60, 70 and 80 °C) was examined by incubating for 30 min of the enzyme immobilized on sepiolite in sodium phosphate buffer pH 7.0 (0.1 mol L^{-1}) at given temperatures. Subsequently, the immobilized enzyme was cooled down to room temperature and the relative activity was measured according to the procedure described above.

Reusability studies

Operational stability of immobilized peroxidase was determined by conducting pyrogallol oxidation in a batch reactor for several consecutive cycles at room temperature (25 °C). At the end of each cycle, sepiolite with the immobilized enzyme (native and oxidized) was rinsed couple of times with sodium phosphate buffer pH 7.0 (0.1 mol L^{-1}). This procedure was repeated several times with fresh aliquots of both substrates, pyrogallol and H_2O_2.

RESULTS AND DISCUSSION

Immobilization of an enzyme on different support materials provides the improved enzyme activity and stability at elevated temperatures, as well as satisfactory stability in organic solvents and at different pH values.[20] All of the above-mentioned facts allow for better reusability and longer storage stability, which is of great importance for potential applications. When naturally present clay minerals such as sepiolite or palygorskite are used for the enzyme immobilization, satisfactory results in terms of the enzyme activity and stability have been obtained. Shirvani and co-workers have studied adsorption of alkaline phosphatase on polygorskite and sepiolite. They found a loss of enzyme activity after immobilization on these two carriers. The enzyme lost 7.5–23.1 % and 9.8–28.8 % of its activity by immobilizing on polygorskite and sepiolite, respectively, depending on the substrate concentration. However, the immobilized enzymes have been substantially

more resistant to the inhibitory effect of Cd than the free enzyme.[14] Laccase derived from *Rhus vernicifera* immobilized by adsorption on sepiolite has shown an increased activity by 250 %.[11] Catalase immobilized on sepiolite has shown improved thermal, storage and operational stability in comparison to the free enzyme.[15]

In our research sepiolite was used as a carrier for the adsorption of HRP (native and periodate-oxidized, Fig. 1). Subsequently, the effect of immobilization on the stability (thermal, pH, *etc*.) of both native and oxidized enzymes was examined.

Fig. 1. Sepiolite clay mineral. The size of the particles was 50±20μm.

In order to perceive a difference in activity and stability of native and periodate-oxidized HRP, both immobilized onto sepiolite, obtained results are compared (Fig. 2). A formerly optimized method for hydrolases and invertase – the periodate method, involves binding to a support material through enzyme carbohydrate moiety previously subjected to oxidation with sodium periodate.[21–24]

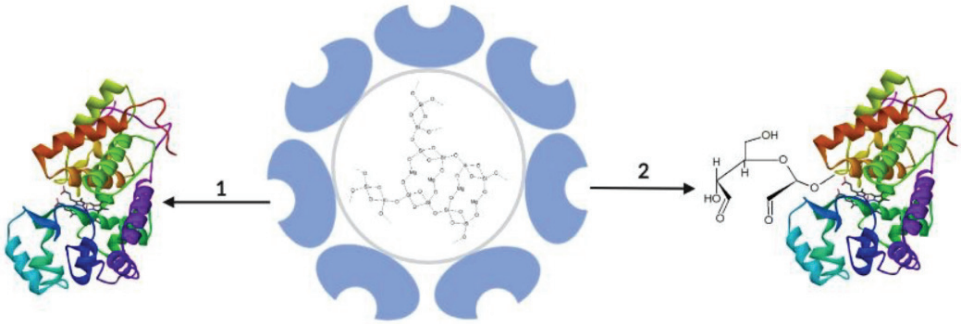

Fig. 2. Adsorption of HRP on sepiolite: 1) native and 2) oxidized enzyme.

Oxidation with sodium periodate creates aldehyde groups (Fig. 2) that could react with amino groups within the enzyme molecule leading to cross-linking and increase in adsorption efficiency and enzyme stability.

Different amounts of both native and periodate-oxidized enzyme are added per g of sepiolite (25, 15, 5 and 1 mg g^{-1}) and specific activities of immobilized

enzymes are calculated. When concerning native HRP immobilized onto sepiolite clay mineral, an increase in the amount of enzyme added per gram of the support results in enhanced specific activity of the immobilized enzyme (Fig. 3). Further growth in the amount of added enzyme leads to a decrease in the specific activity. The maximum enzyme specific activity is reached when the amount of 15 mg of peroxidase is immobilized per g of sepiolite. Different results are obtained when oxidized HRP was immobilized onto sepiolite. Specific activity increases with increasing the amount of enzyme added per gram of sepiolite. Compared to the oxidized enzyme, similar specific activities of native HRP are detected.

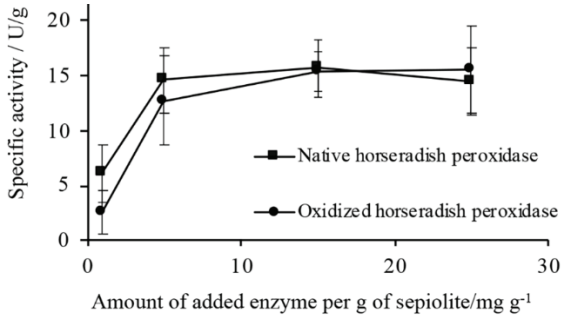

Fig. 3. Effect of the amount of added enzyme on the specific activity of immobilized HRP (native and oxidized). Standard error was calculated from triplicate measurements of the specific activity.

The obtained results for native and periodate-oxidized enzymes show that at 25 mg of the enzyme loading per g of sepiolite native peroxidase has the specific activity of 14.4 U g^{-1}, whereas oxidized HRP show 15.5 U g^{-1}. The trend is slightly different for other concentrations of the enzyme thus no general conclusions can be drawn. These findings are corroborated with results obtained by Öztürk *et al.* which have shown that excessive loadings of lipase onto sepiolite and montmorillonite clay minerals resulted in lower immobilization efficiency.[25] They have found that the optimal lipase content was 7.5 mg per g of both clay minerals. Higher amounts of the immobilized enzyme can lead to loss of the enzyme activity due to smaller accessibility of the enzyme to the substrate. Our study shows a rise of the specific activity with increasing the peroxidase loading onto sepiolite clay mineral up to 15 mg of enzyme per g of sepiolite for native peroxidase. Further increase in the enzyme loading does not lead to a significant change of the specific activity, which may be a result of burring of the active site with the excess of the enzyme, a steric hindrance on the access of the substrate, disarrangement of the three-dimensional structure of the enzyme or diffusional limitations.[13] With the increase in the amount of immobilized peroxidase, the specific activity of the periodate-oxidized enzyme raises, reaches a plateau and remains unaltered.

Thermostability

In order to examine how immobilization and periodate oxidation affect the thermostability of sepiolite adsorbed HRP, the enzymes immobilized in the amount of 15 mg per g of sepiolite was first incubated at 65 °C for different time periods (Fig. 4). Values of residual activities of native and periodate-oxidized HRPs show that more stable biocatalyst is the one previously oxidized with periodate. Periodate-oxidized enzyme preserves 36 % of residual activity after 5 min of incubation, whereas the native HRP retains only 8 % of residual activity. By increasing incubation time at 65 °C to 30 min the activity of both HRPs immobilized onto sepiolite substantially decreases to 6 % for periodate oxidized and 4 % for native HRP.

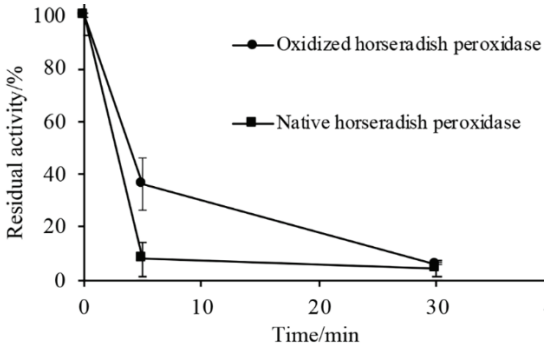

Fig. 4. Effect of incubation time at 65 °C on residual activities of native and periodate-oxidized HRPs immobilized onto sepiolite clay mineral by adding 15 mg of the enzyme per g of sepiolite.

Native peroxidase lost around 92 % of its initial activity after incubation at 65 °C for 5 min, whereas peroxidase oxidized with sodium periodate and immobilized onto sepiolite lost 64 % of the initial activity. Thus, periodate-oxidized HRP is more stable at elevated temperatures than native peroxidase immobilized onto sepiolite. Similar results have been obtained for catalase immobilized onto sepiolite and bentonite.[15] Sepiolite immobilized catalase retained 19.1 % of its initial activity at 65 °C after 1 h of incubation.

In further experiments for thermostability measurements, we have used a 30--min incubation period at different temperatures for different amounts of adsorbed enzyme.

The obtained results show the identical temperature stability for all used concentrations of immobilized enzymes at 40 °C. Data presented in Fig. 5 show dependence of incubation at different temperatures on the residual activity of oxidized HRP immobilized onto sepiolite, whereas results obtained for immobilized native peroxidase are not shown. The increase in the temperature from 40 to 80 °C, leads to the gradual decrease of the enzyme residual activity. At 60 °C periodate-oxid-

ized HRP retains almost 30 % of the initial activity. Further raise of temperature results in the decline of the activity by almost 20 %. These findings are corroborated with those reported for immobilized invertase.[26] Immobilized invertase preserved almost 85 % of its activity during incubation at 50 °C, whereas free invertase lost 50 % of the initial activity under the same conditions. After incubation at 70 °C, the free enzyme lost all activity, however immobilized invertase retained 80 % of its activity. Immobilization of HRP on perlite led to higher thermostability at 80 °C.[27] The immobilized enzyme retained 30 % of the initial activity after incubation at 80 °C for 20 min. Kim and co-workers immobilized HRP on fulvic acid-activated montmorillonite K-10. They compared the thermal stability of the immobilized and free enzyme and found the markedly higher relative activity of immobilized HRP over the relatively high-temperature range (75 % and around 55 % for immobilized and free HRP, respectively at 45 °C.[28] Zhang *et al.* found the activity loss of free HRP of around 18 % caused by increasing temperature from 20 to 60 °C, whereas the activity of hemin–histamine–montmorillonite conjugates increased by 3.6 times in the same temperature range.[29] The complete loss of the free enzyme activity at 70 °C as a consequence of protein denaturation has been reported in the literature.[30,31] Lower stability at higher temperatures may be due to loss of the heme group during incubation. Chattopadhyay *et al.* reported a drastic change in the overall secondary structure of the enzyme at 74 °C, associated with the complete release of the heme moiety from the enzyme.[32]

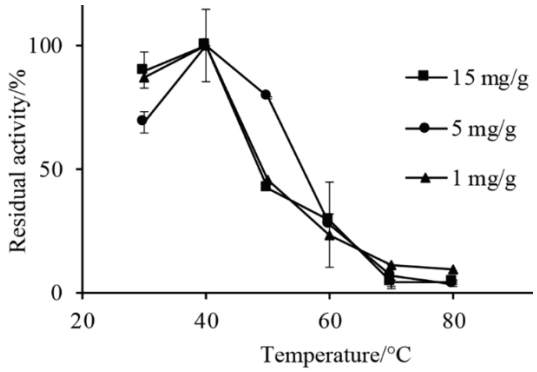

Fig. 5. Effect of incubation at different temperatures on the residual activity of periodate-oxidized HRP immobilized on sepiolite.

pH optimum

The change of pH values was monitored in the range from 2.0 to 9.0 for both native and HRP oxidized with sodium periodate and immobilized on the same carrier using 15 mg of the enzymes per gram of the sepiolite carrier (Fig. 6).

Both peroxidases show the same trend in terms of relative activities. The increase in pH values from acidic to basic leads to a gradual raise of relative act-

ivities until reaching the pH optimum (pH 7.0). Subsequently, the relative activities decline. The optimum pH values for both peroxidases (native and periodate-oxidized) overlap. The bell-shaped pH profiles demonstrate higher stabilities of sepiolite immobilized native peroxidase than periodate-oxidized HRP immobilized onto sepiolite in both acidic and basic regions. Optimum pH obtained in our study was corroborated with the study of Torabi *et al.*[23] Peroxidase immobilized onto perlite showed optimum at pH 7.0 and a wider pH range for native enzyme compared to immobilized peroxidase.[27] This effect is also observed in our study and can be explained by different behaviour of native enzyme in slightly acidic regions. The maximum activity of HRP immobilized on kaolin is at pH 5.0. As suggested by the authors, the enzyme binding at this pH allowed for the conservation of the catalytic function.[33] Liu *et al.* have shown that HRP immobilized on silane-modified ceramics showed higher acid-base stability than free HRP. Immobilized enzymes preserved their activity in a wide range of pH due to the reduced effect of pH alternation in the enzyme vicinity caused by the conditioning of the microenvironment. The maximum activity of immobilized enzyme was at pH 6 whereas that of free HRP was at pH 7.[34] Kim and co-workers have reported the optimal pH of free HRP and montmorillonite immobilized HRP of 8 and 9, respectively. This shift of the pH optimum to more alkaline conditions has been related to unequal H^+ displacement in the microenvironment around the immobilized enzyme, change in the microenvironment around the immobilized HRP towards a cationic environment, and separation of the enzyme from bulk as well as to the charge of clay. The immobilized enzyme has shown better activity than the free enzyme over a wide range of pH, which is attributed to the protection effect achieved by the stable binding to the inorganic carrier that restricts denaturation or unfolding of the enzyme due to sudden pH changes.[28] Sedaghat *et al.* have reported the dame pH optimum of free HRP and HRP immobilized on sepiolite, sepiolite with bilayer and monolayer surfactant coverage (pH 10) with the broader profile of the HRP immobilized on sepiolite with bilayer surfactant coverage.[13]

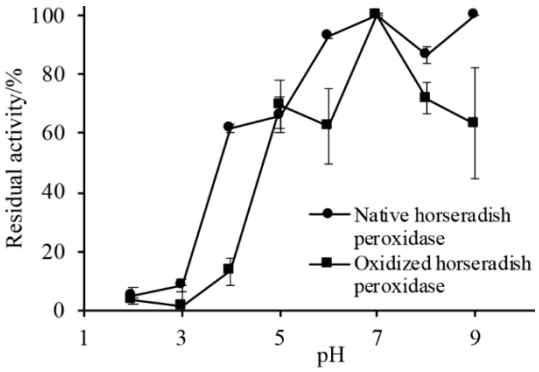

Fig. 6. Effect of pH on activities of native and oxidized HRP immobilized on sepiolite.

Operational stability and enzyme leakage

The same batch of immobilized enzymes (native and periodate-oxidized) is used in several consecutive cycles for pyrogallol oxidation to examine the operational stability. Residual activities of the immobilized enzymes are monitored for 4 cycles, with each cycle lasting 180 min. This time period was chosen based on our previous study showing that longer cycles provide higher amounts of solid oxidation products that block the pores of the carrier and, thus, the immobilized enzyme inside the pores, disabling its further catalytic activity.[35] Between two cycles sepiolites with immobilized HRP are rinsed several times with sodium phosphate buffer and subsequently used for another round of pyrogallol oxidation. The enzyme activity obtained in the first cycle is considered 100 %. When comparing values of residual activities for both native and oxidized HRP, especially at the concentration of 1 mg g^{-1} that we have shown in order to detect sooner leakage of the enzyme and loss of the activity, higher operational stability is achieved with the periodate-oxidized enzyme (Fig. 7). Native HRP retains only 11 % of its initial activity after 4 consecutive cycles of pyrogallol oxidation. HRP oxidized with sodium periodate and immobilized onto sepiolite shows better results in terms of the residual activity – after 4 cycles of pyrogallol oxidation it preserves 42 % of the initial activity. The operational stability of aldehyde dehydrogenase (ALDH) immobilized onto montmorillonite was monitored for several cycles.[24] The activity of the immobilized enzyme decreased by 20 % after each cycle, thus it dropped to barely 24 % by the end of the fifth cycle.

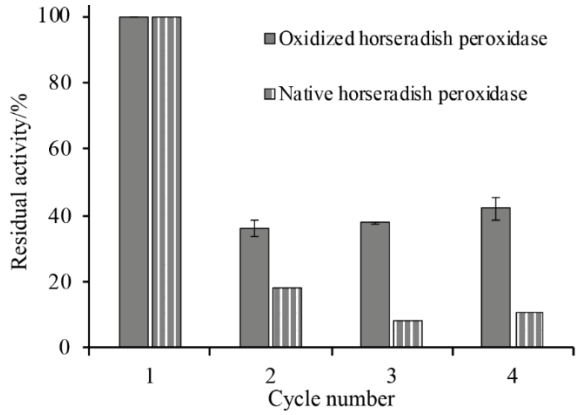

Fig. 7. Catalytic activity of native and oxidized HRP during repeated use.

Residual activities of different amounts of periodate-oxidized peroxidases immobilized per gram of sepiolite are shown on Fig. 8. After 4 cycles of repeated use in pyrogallol oxidation, the enzyme immobilized in the amount of 1 mg per g of sepiolite shows the most promising results regarding the residual activity. It

retains 42 % of the initial activity, whereas the enzyme immobilized in other concentrations shows slightly different results. Generally, the same trend is observed for all enzyme concentrations. An increase in the number of cycles leads to a decline of residual activities. Reduction of the specific activity after each cycle for lipase and *α*-amylase immobilized onto sepiolite has been reported in literature.[36] It has been addressed to either accumulation of water onto the sepiolite surface or enzyme inactivation. Inactivation of the enzyme, which results from blocking of the active site of the enzyme by radical products formed in oxidation reactions or the enzyme leakage from the carrier surface, can cause the activity loss during the repetitive use. In our study the periodate oxidation of HRP forms aldehyde groups and allows for cross-linking of HRP protein molecules during adsorption, thus decreasing the possibility of leakage and increasing the stability.

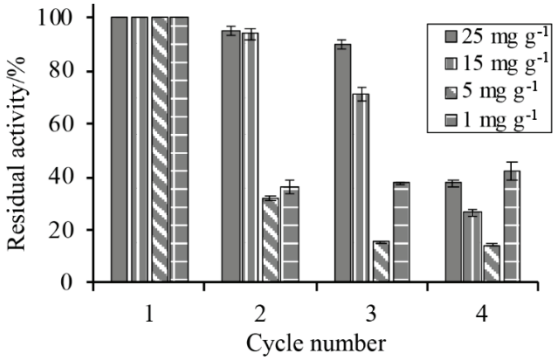

Fig. 8. Catalytic activity of periodate-oxidized HRP immobilized on sepiolite (different concentrations of the enzyme).

CONCLUSION

Sepiolite clay mineral was used for the immobilization of HRP. In order to determine whether difference in the binding affinity and stability of native and periodate-oxidized HRPs exists, several studies were performed with this enzyme for the first time. Effect of the amount of enzyme added per gram of sepiolite on the specific activity was examined. It was found that the specific activity raised with increasing the quantity of added enzyme. Fifteen mg of peroxidase per g of the carrier provided the maximum specific activity. Similar values of the specific activity were obtained for oxidized peroxidases in comparison to the native enzyme. Both native and oxidized HRP immobilized onto sepiolite were tested in various stability studies (pH, thermal and operational stability). Incubation of enzymes at 65 °C for an appropriate period of time showed increased stability at elevated temperatures for periodate oxidized HRP. Activity of immobilized peroxidases was also examined at various temperatures (30, 40, 50, 60, 70 and 80 °C). Obtained results showed gradual decrease of the enzyme stability and activity with increase-

ing temperature from 30 to 80 °C. The bell-shaped pH profiles were observed for both peroxidase (native and oxidized) immobilized onto sepiolite clay mineral. Operational stability was examined by using the same batch of immobilized enzymes for pyrogallol oxidation. Native HRP retained only 11 % of the initial activity after 4 consecutive cycles, whereas the oxidized enzyme preserved 42 % of the activity after the same number of cycles. All results indicate that periodate oxidation of HRP prior to adsorption on carriers such as sepiolite provided more stable immobilized enzyme probably as a result of formation of aldehyde groups that can cross-link enzyme molecules via amino groups and additionally stabilize adsorbed HRP. This method can generally apply for other catalytic glycoproteins.[22]

Acknowledgement. This work was financially supported by the Ministry of Education, Science and Technological Development of the Republic of Serbia (Grant No. 451-03-47/2023--01/200168, University of Belgrade – Faculty of Chemistry, Grant no. 451-03-47/2023-14/ /200288, Innovative Centre of the Faculty of Chemistry and Grant No. 451-03-47/2023-01/ /200053, University of Belgrade – Institute for Multidisciplinary Research).

И З В О Д

ИМОБИЛИЗАЦИЈА ПЕРЈОДАТНО ОКСИДОВАНЕ ПЕРОКСИДАЗЕ ИЗ РЕНА АДСОРПЦИЈОМ НА СЕПИОЛИТУ

НЕВЕНА СУРУЏИЋ[1], МИЛОШ СИМИЋ[2], МИЛИЦА ЦРНОГЛАВАЦ ПОПОВИЋ[3], REYADH EL GAHWASH[3], МИЛИЦА СПАСОЈЕВИЋ САВКОВИЋ[4], РАДИВОЈЕ ПРОДАНОВИЋ[3] и ОЛИВЕРА ПРОДАНОВИЋ[1]

[1]Универзитет у Београду – Институт за мултидисциплинарна истраживања, Кнеза Вишеслава 1, 11030 Београд, [2]Центар за нове технологије, 11000 Београд, [3]Универзитет у Београду – Хемијски факултет, Студентски трг 12, 11000 Београд и [4]Универзитет у Београду – Иновациони центар Хемијског факултета, Студентски трг 12, 11000 Београд

Пероксидазе из рена (HRP), нативна и оксидована перјодатом, су имобилизоване адсорпцијом на минерал глине сепиолита. Обе пероксидазе су адсорбоване на овом носачу у различитим количинама. Специфична активност имобилисаних ензима се повећава са повећањем количине додате пероксидазе по граму сепиолита. Највећа специфична активност је постигнута додавањем 15 mg пероксидазе по граму сепиолита. Поред тога установљено је и да перјодатно оксидовани ензими имају сличну специфичну активност као и нативни. За обе пероксидазе је одређена pH, термичка и оперативна стабилност. Установљено је да преостала специфична активност HRP имобилисане на сепиолит опада са повећањем времена инкубације на 65 °C. Оксидована пероксидаза је изгубила 64 % почетне активности, док је код нативне активности HRP опала за 92 % након 5 min инкубације на 65 °C. Са повећањем температуре од 30 до 80 °C смањује се активност ензима. И у киселом и у базном региону pH профил нативне пероксидазе имобилисане на сепиолиту је виши у поређењу са pH профилом перјодатно оксидованог ензима. Установљено је да је оперативна стабилност оксидоване HRP знатно боља него оперативна стабилност нативне пероксидазе. Перјодатно оксидована пероксидаза је задржала 42 % своје активности након 4 узастопна циклуса оксидације пирогалола, док је нативна задржала само 11 % првобитне активности.

(Примљено 27. децембра, ревидирано 26. јануара, прихваћено 7. јула 2024)

REFERENCES

1. C. L. B. Reis, E. Y. A. de Sousa, J. de F. Serpa, R. C. Oliveira, J. C. S. dos Santos, *Quim. Nova* **42** (2019) 768. (https://doi.org/10.21577/0100-4042.20170381)
2. S. Cantone, V. Ferrario, L. Corici, C. Ebert, D. Fattor, P. Spizzo, L. Gardossi, *Chem. Soc. Rev.* **42** (2013) 6262 (https://doi.org/10.1039/C3CS35464D)
3. D. M. Liu, J. Chen, Y. P. Shi, *TrAC – Trends Anal. Chem*. **102** (2018) 332 (https://doi.org/10.1016/j.trac.2018.03.011)
4. C. Garcia-Galan, Á. Berenguer-Murcia, R. Fernandez-Lafuente, R. C. Rodrigues, *Adv. Synth. Catal*. **353** (2011) 2885 (https://doi.org/10.1002/adsc.201100534)
5. Homaei, R. Sariri, F. Vianello, R. Stevanato, *J. Chem. Biol*. **6** (2013) 185 (http://dx.doi.org/10.1007/s12154-013-0102-9)
6. Brena, P. González-Pombo, F. Batista-Viera, *Immobilization of Enzymes and Cells: 3rd ed., Methods in Molecular Biology* **1051** (2013) 15 (https://doi.org/10.1007/978-1-62703-550-7_2)
7. Z. Ashkan, R. Hemmati, A. Homaei, A. Dinari, M. Jamlidoost, A. Tashakor, *Int. J. Biol. Macromol*. **168** (2020) 708 (https://doi.org/10.1016/j.ijbiomac.2020.11.127)
8. Homaei, in *Advances in Food Biotechnology*, R. V. Rai, Ed., John Wiley & Sons, Hoboken, NJ, 2015, p. 145 (https://doi.org/10.1002/9781118864463.ch09)
9. R. Ismail, K. H. Baek, *Int. J. Biol. Macromol*. **163** (2020) 1624 (https://doi.org/10.1016/j.ijbiomac.2020.09.021)
10. F. Largo, R. Haounati, S. Akhouairi, H. Ouachtak, R. El Haouti, A. El Guerdaoui, N. Hafid, D. M. F. Santos, F. Akbal, A. Kuleyin, A Jada, A. A. Addi, *J. Mol. Liq.* **318** (2020) 114247 (https://doi.org/10.1016/j.molliq.2020.114247)
11. Y. Olshansky, S. Masaphy, R. A. Root, G. Rytwo, *Appl. Clay Sci*. **152** (2018) 143 (https://doi.org/10.1016/j.clay.2017.11.006)
12. M. S. Carrasco, J. C. Rad, S. Gonzalez-Carcedo, *Biores. Technol*. **51** (1995) 175 (https://doi.org/10.1016/0960-8524(94)00115-H)
13. M. E. Sedaghat, M. Ghiaci, H. Aghaei, S. Soleimanian-Zad, *Appl. Clay Sci*. **46** (2009) 131 (https://doi.org/10.1016/j.clay.2009.07.021)
14. M. Shirvani, B. Khalili, M. Kalbasi, H. Shariatmadari, F. Nourbakhsh, *Clays Clay Miner*. **68** (2020) 287 (https://doi.org/10.1007/s42860-020-00066-w)
15. S. Cengiz, L. Çavaş, K. Yurdakoç, *Appl. Clay. Sci*. **65**–**66** (2012) 114 (https://doi.org/10.1016/j.clay.2012.06.004)
16. S. Mortazavi, H. Aghaei, *Int. J. Biol. Macromol*. **164** (2020) 1 (https://doi.org/10.1016/j.ijbiomac.2020.07.103)
17. N. Caza, J. K. Bewtra, N. Biswas, K. E. Taylor, *Water Res*. **33** (1999) 3012 (https://doi.org/10.1016/S0043-1354(98)00525-9)
18. F. Quintanilla-Guerrero, M. A. Duarte-Vázquez, B. E. García-Almendarez, R. Tinoco, R. Vazquez-Duhalt, C. Regalado, *Biores. Technol*. **99** (2008) 8605 (https://doi.org/10.1016/j.biortech.2008.04.031)
19. Alemzadeh, S. Nejati, *J. Haz. Mat.* **166** (2009) 1082 (https://doi.org/10.1016/j.jhazmat.2008.12.026)
20. N. Miletić, A. Nastasović, K. Loos, *Biores. Technol*. **115** (2012) 126 (https://doi.org/10.1016/j.biortech.2011.11.054)
21. Z. Knezevic, N. Milosavic, D. Bezbradica, *Biochem. Eng. J*. **30** (2006) 269 (https://doi.org/10.1016/j.bej.2006.05.009)
22. R. M. Prodanović, M. B. Simić, Z. M. Vujčić, *J. Serb. Chem. Soc*. **68** (2003) 819 (https://doi.org/10.2298/JSC0311819P)

23. N. Milosavić, R. Prodanović, S. Jovanović, Z. Vujčić, *Enzyme Microb. Technol*. **40** (2007) 1422 (https://doi.org/10.1016/j.enzmictec.2006.10.018)
24. R. Prodanović, S. Jovanović, Z. Vujčić, *Biotechnol. Lett*. **23** (2001) 1171 (https://doi.org/10.1023/A:1010560911400)
25. H. Öztürk, E. Pollet, V. Phalip, Y. Güvenilir, L. Avérous, *Polymers* **8** (2016) 416 (https://doi.org/10.3390/polym8120416)
26. H. N. Oztop, C. Hepokur, D. Saraydin, *J. Food Sci.* **74** (2009) N45 (https://doi.org/10.1111/j.1750-3841.2009.01302.x)
27. S. F. Torabi, K. Khajeh, S. Ghasempur, N. Ghaemi, S. O. R. Siadat, *J. Biotechnol*. **131** (2007) 111 (https://doi.org/10.1016/j.jbiotec.2007.04.015)
28. H. J. Kim, Y. Suma, S. H. Lee, J. A. Kim, H. S. Kim, *J. Mol. Catal., B* **83** (2012) 8 (https://doi.org/10.1016/j.molcatb.2012.06.012)
29. L. Zhang, C. Gu, J. Xiong, M. Yang, Y. Guo, *Sci. China Chem*. **58** (2015) 731 (https://doi.org/10.1007/s11426-014-5196-6)
30. M. Kurosawa, T. Itoh, Y. Kodera, A. Matsushima, M. Hiroto, H. Nishimura, Y. Inada, *Bioconjugate Chem*. **13** (2002) 167 (https://doi.org/10.1021/bc000133+)
31. J. Xiong, C. Hang, J. Gao, Y. Guo, C. Gu, *Chem. Eng. J*. **254** (2014) 276 (https://doi.org/10.1016/j.cej.2014.05.139)
32. K. Chattopadhyay, S. Mazumdar, *Biochemistry* **39** (2000) 263 (https://doi.org/10.1021/bi990729o)
33. N. Ž. Šekuljica, N. Ž. Prlainović, J. R. Jovanović, A. B. Stefanović, V. R. Djokić, D. Ž. Mijin, Z. D. Knežević-Jugović, *Bioprocess Biosyst. Eng*. **39** (2016) 461 (https://doi.org/10.1007/s00449-015-1529-x)
34. W. Liu, W. C. Wang, H. S. Li, X. Zhou, *Water Sci. Tech*. **63** (2011) 1621 (https://doi.org/10.2166/wst.2011.228)
35. N. Pantić, M. Spasojević, Ž. Stojanović, Đ. Veljović, J. Krstić, A. M. Balaž, R. Prodanović, O. Prodanović, *J. Polym. Environ*. **30** (2022) 3005 (https://doi.org/10.1007/s10924-021-02364-3)
36. S. Mortazavi, H. Aghaei, *Int. J. Biol. Macromol*. **164** (2020) 1 (https://doi.org/10.1016/j.ijbiomac.2020.07.103).

Journal of the Serbian Chemical Society
JSCS@tmf.bg.ac.rs • www.shd.org.rs/JSCS
J. Serb. Chem. Soc. *89* (10) 1285–1298 (2024)
JSCS–5787
Original scientific paper
Published 27 October, 2024

Synthesis of and theoretical research on some azine derivatives and investigation of their antimicrobial activities

SERTAN AYTAÇ*

Kırşehir Ahi Evran University, Kaman Vocational School, Department of Food Technology, 40300 Kaman, Kırşehir, Türkiye

(Received 17 August, revised 14 September, accepted 24 October 2023)

Abstract: This study includes experimental, theoretical and antimicrobial investigations on 1-(diphenylmethylene)-2-(4-methoxybenzylidene)hydrazine (**5**), 1-(3,5-dimethoxybenzylidene)-2-(diphenylmethylene)hydrazine (**6**) and 1-(diphenylmethylene)-2-(2,3,4-trimethoxybenzylidene)hydrazine (**7**). The structures of the compounds, synthesized by the microwave method, were determined by spectroscopic methods and elemental analysis. Conformational analysis, ground state structure, Fourier-transform infrared spectra (FT-IR) and nuclear magnetic resonance (NMR) spectra of the compounds were determined using density the functional theory (DFT) calculations in the theoretical research. Based on the B3LYP/6-31G(d,p) level, the conformers from the torsional barrier scanning were optimized. The B3LYP/6-311++G .(d,p) was used to determine the harmonic vibrational frequencies, potential energy distribution (PED), infrared intensities, and NMR chemical shifts of the most stable conformers. The experimental findings were compared with the theoretically expected spectral data. The antibacterial activity of the prepared compounds was tested *in vitro* against nine bacteria and one yeast species. The antimicrobial activity of the compounds was tested by minimum inhibitory concentration (*MIC*) and agar well diffusion method. Compound **7** showed good activity against the bacteria and yeast, while **5** and **6** showed no antimicrobial activity. Compound **7** showed zone of inhibition values in the range of 10–15 mm against *Klebsiella pneumonia, Pseudomonas aeruginosa* and *Salmonella typhimurium* The results indicated that compound **7** was effective against bacteria.

Keywords: heterocyclic compounds; microwave; microorganisms; DFT.

INTRODUCTION

Combating microorganisms that cause infections is of great importance for human health. For this purpose, there is increasing interest in the synthesis of new and effective antimicrobial agents.[1,2] The biological potential of hetero-

* Corresponding author. E-mail: saytac@ahievran.edu.tr
https://doi.org/10.2298/JSC230817081A

cyclic nitrogen-containing compounds against diverse bacteria has been documented.[3] There are many types of synthetic organic compounds with antimicrobial properties. Azines, sometimes called N–N-linked diimines (C=N-N=C), are among them and are 2,3-diaza analogues of 1,3-butadiene.[4] The conventional method for the synthesis of azines is the treatment of carbonyl compounds with hydrazine.[5] Several techniques for the preparation of these compounds under different conditions have been described in the literature, but most of them require high temperatures and complex catalysts.[6] In addition to the conventional synthesis technique, it has been reported that the synthesis of azines also employs microwave energy[7], ultrasonic radiation[8] and grinding[9] techniques. The short reaction time, low by-product formation, low solvent consumption and high efficiency are the most important advantages of these techniques over the classical technique.[10–12]

Azines are of great interest in organic synthesis, and they have important biological properties such as antibacterial, antifungal, antiviral, anticancer and antiinflammatory.[1] They are also good synthons for obtaining many pharmacologically interesting heterocyclic compounds such as pyrazoles, purines and pyrimidines.[6,13] They are an important agent for reducing the antimicrobial activities of common pathogenic bacteria such as *Bacillus subtilis*, *Streptococcus faecalis* and *Enterococcus faecalis*.[14,15]

The objective of the present study was to synthesize, characterize and theoretically analyse azine molecules and investigate their antimicrobial properties. For the first time, compounds **6** and **7** were synthesized using microwave irradiation, which is a fast, inexpensive, highly effective and environmentally friendly method.[12,16,17] Compound **5** has been reported in the literature. It is known from the literature that this compound was synthesized by the grinding method using 1-(diphenyl methylene) hydrazine and 4-methoxybenzaldehyde compounds.[6,18] However, in the present study for the re-synthesis of compound **5**, the microwave method was also used for the first time. Structures of compounds **5**–**7** were determined by NMR, FT-IR spectroscopy and elemental analysis techniques. The present study also includes the theoretical outcomes of a thorough investigation of the torsional barrier analysis, vibrational spectra, and NMR spectra of **5**–**7** using density functional theory (DFT) calculations. The antibacterial properties of **5–7** against selected microorganisms were examined applying the agar well diffusion and microdilution broth technique.

EXPERIMENTAL

General chemistry

All chemicals are commercially available and purchased from Merck and Sigma–Aldrich. Analytical-grade solvents were used without further purification. Reactions were performed *via* domestic microwave oven (Vestel MD 20 DB, 230 V-50 Hz, 900 W). Thin-layer chromatography (TLC) was employed to monitor the reactions. ^{1}H-NMR (400 MHz) and ^{13}C-NMR (100 MHz) spectra were recorded with a Varian spectrometer using $CDCl_3$. The FT-IR

spectra were recorded with a Perkin Elmer spectrophotometer in the range of 4000–600 cm^{-1}. A capillary melting device was used to determine melting points (Buchi 530). On a Leco CHNS-932 instrument, elemental analysis was carried out.

General synthesis of azines ***5****–****7***

Compounds **5**–**7** were synthesized according to the procedure described in the literature.[12,16,17] The general synthetic pathway is given Scheme 1.

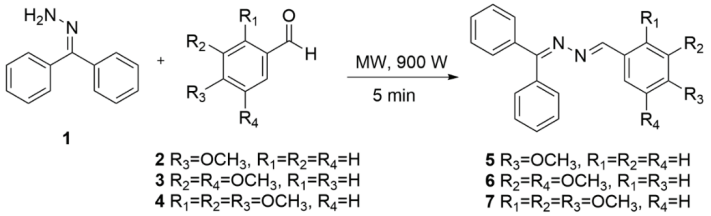

Scheme 1. The general synthetic pathway of azine derivatives.

Computational details

The software Gaussian 09 was used to carry out the DFT calculations.[19] In all calculations, the DFT/B3LYP functional was applied.[20-22] With the B3LYP functional, the basis sets 6-31G(d,p) and 6-311++G(d,p) were used. The 6-311++G(d,p) basis set was used in all other computations, whereas the conformer optimization was carried out on the 6-31G(d,p) basis set.[23]

Before beginning the computations of the other molecular characteristics of the system studied, the stable conformers of the molecular system must be identified. The conformational analysis must be completed first for these calculations. The software Spartan 08 is used to perform conformational analysis by examining the conformational distribution.[24] In this approach, calculations are performed using molecular mechanical methods, and then possible conformer structures are identified. In the present study, the Merck molecular force field (MMFF) method[25] was used for analysing conformational distribution. These conformers are then optimized using Gaussian 09.

The gauge independent atomic orbital (GIAO) approach was used to predict the theoretical NMR data of **5**–**7**. The IEF-PCM model was used for these calculations in chloroform solution. The predicted ^{1}H- and ^{13}C-NMR measurements were compared to the experimental results. This matching could help with more detailed identification and characterization of the compounds. Chemical shifts were measured from absolute isotropic magnetic shielding constants. This conversion was carried out using tetramethylsilane (TMS), which was employed as a standard.[26,27]

Conformational analysis and molecular structure

Fig. 1 shows the optimized molecular structure of compounds **5**–**7**. The bonds described for **1**–**3** in Fig. 2 were taken into consideration while performing the conformational analysis of **5**–**7**. Changing the dihedral angle in 10° steps from 0 to 360° allowed the potential energy surface (*PES*) scan to be performed on the dihedral angles around the bonds of C–OCH_3 (**1**), C-phenyl groups (**2**) and C–N-phenyl groups (**3**). According to the PES scan results in Fig. 1, the Spartan determined two conformers of **5**, six conformers of **6** and twelve conformers of **7**, using the MMFF.

These conformers were optimized by B3LYP/6-31G(d,p) level in Gaussian 09. The optimized geometric structure, optimized energies and relative energies of the conformers are given in Table I. These findings indicate that the first conformer (conformer-1) of **5**–**7** has the most stable molecular structure. Fig. 2 shows molecular structure and atomic numbering of the most stable geometries of **5**–**7**. All future calculations will be performed with these most stable conformers.

Conformers of compound **5**

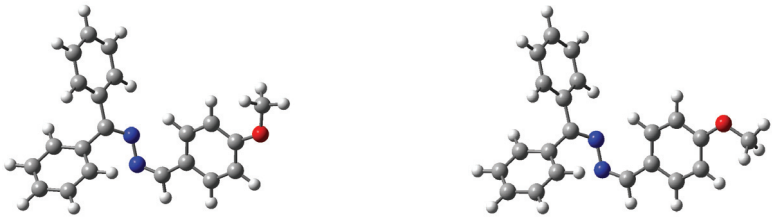

1 2

Conformers of compound **6**

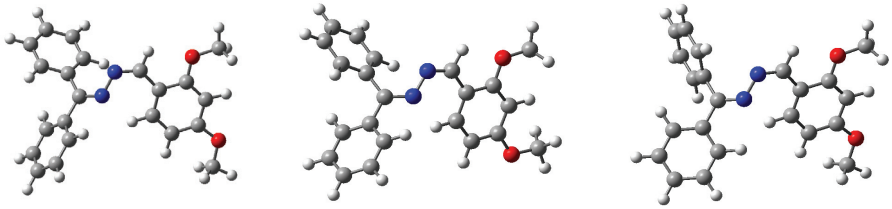

1 2 3

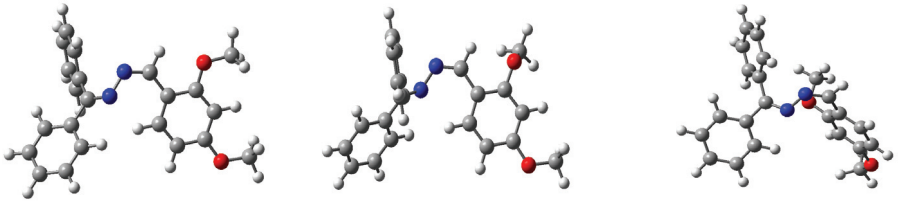

4 5 6

Conformers of compound **7**

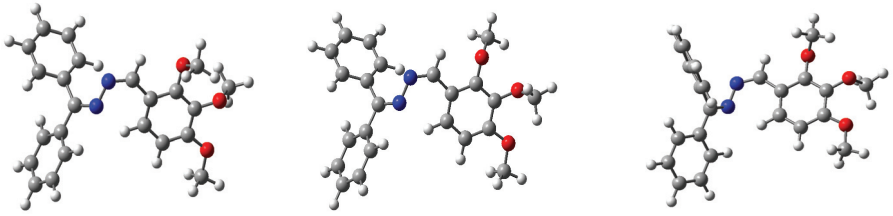

1 2 3

Fig. 1. Conformers of **5**–**7**.

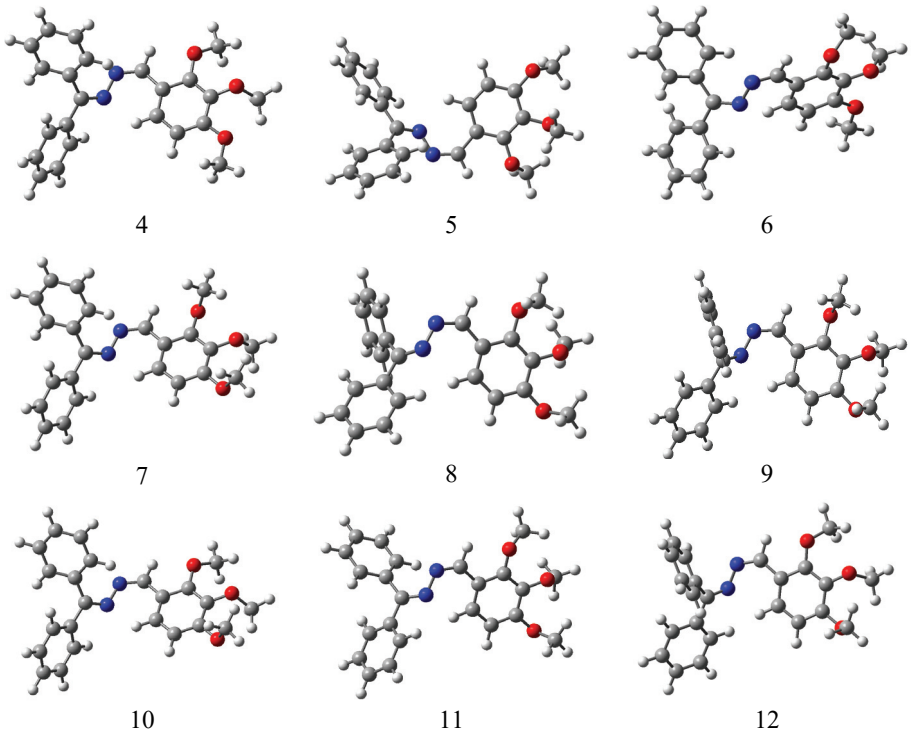

Fig. 1. (Continued).

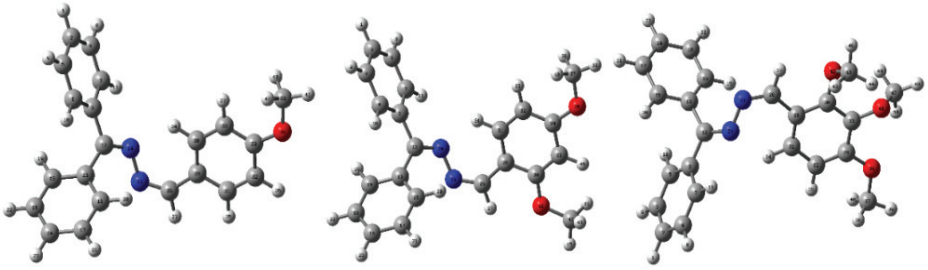

Fig. 2. Molecular structure and atomic numbering of the most stable geometries of **5**–**7**.

TABLE 1. Conformational analysis results of **5**–**7**

Compound		Opt. energy, a.u.	Rel. energy, kJ mol^{-1}	Pop. (298 K), %
5	Conformer–1	–995.779808398	0.00	55
	Conformer–2	–995.779618562	0.50	45
6	Conformer–1	–1110.30422576	0.00	68.56
	Conformer–2	–1110.30307700	3.02	20.30
	Conformer–3	–1110.30224177	5.21	8.38
	Conformer–4	–1110.30117394	8.01	2.71

TABLE 1. Conformational analysis results of **5**–**7**

Compound		Opt. energy, a.u.	Rel. energy, kJ mol^{-1}	Pop. (298 K), %
6	Conformer–6	–1110.29199733	32.10	0.00
	Conformer–5	–1110.29728690	18.22	0.04
7	Conformer–1	–1224.81524964	0.00	45.77
	Conformer–2	–1224.81502854	0.58	36.20
	Conformer–3	–1224.81319017	5.41	5.17
	Conformer–4	–1224.81292079	6.11	3.89
	Conformer–5	–1224.81263566	6.86	2.87
	Conformer–6	–1224.81257421	7.02	2.69
	Conformer–7	–1224.81241522	7.44	2.27
	Conformer–8	–1224.81077869	11.74	0.40
	Conformer–9	–1224.81072273	11.89	0.38
	Conformer–10	–1224.81009643	13.53	0.20
	Conformer–11	–1224.80974816	14.44	0.13
	Conformer–12	–1224.80812036	18.72	0.02

Antimicrobial activity

In the present study, the *in vitro* antimicrobial activities of several compounds were tested using agar well diffusion method and microdilution broth method. The *in vitro* antimicrobial activity of the compounds synthesized was assayed against nine bacterial strains and one yeast strain. These microorganisms were obtained from the Laboratory of Microbiology, Kırşehir Ahi Evran University, Kırşehir, Türkiye. The antimicrobial activities of **5**–**7** were determined according to the procedure described in the literature.[17] The antimicrobial results for the compounds and standard antibiotics and the *MIC* measurements of the new azine derivatives against the bacteria and yeast are presented.

RESULTS AND DISCUSSION

Chemistry

The compounds 1-(diphenylmethylene)-2-(4-methoxybenzylidene)hydrazine (**5**), 1-(3,5-dimethoxybenzylidene)-2-(diphenylmethylene)hydrazine (**6**) and 1-(diphenylmethylene)-2-(2,3,4-trimethoxybenzylidene)hydrazine (**7**) were prepared by the condensation of benzophenone hydrazone (**1**) with different aromatic aldehydes (**2**–**4**) at a ratio of (1:1) and exposure to microwave irradiation for 5 min.[12,16,17] The synthesized compounds' percentage yields were excellent (97, 96 and 97 %, respectively). In the experimental part, the physical properties of the compounds synthesized are described. The infrared spectra of the compounds confirm the presence of stretching of C=N bands at 1600–1660 cm^{-1} and the absence of carbonyl (C=O) at 1700 cm^{-1}, whereas NH has vanished or is hidden beneath the broad bands at 3450–3300 cm^{-1} in azines. In the ^{1}H-NMR spectrum of the compounds, the azomethine proton resonates as a singlet in the range of 8.30–8.76 ppm. All aromatic protons showed multiplet peaks in the range of 6.38–8.39 ppm. Additionally, the ^{13}C-NMR analysis of compounds **5**–**7** showed

that the carbon atoms in the H–C=N bond give signal at 159.30, 158.84 and 153.40 ppm, respectively.

Vibrational assignment

Compounds **5**–**7** have 42, 46 and 50 atoms, respectively. They have 120 (for **5**), 132 (for **6**), and 144 (for **7**) normal modes. Compounds **5**–**7** have C_1 symmetry. All basic vibrations are active in the FT-IR spectra. The frequencies calculated in the harmonic approximation were scaled to closely reproduce the experimental value. The frequencies calculated for the theory level B3LYP/6--311++G(d,p) were scaled to 0.960 in the high wavenumber region and 0.988 in the low wavenumber region (below 1800 cm^{-1}). The experimental and theoretical infrared spectra of compounds **5**–**7** are shown in Fig. 3. It is seen that both sets of spectral data almost completely overlap when the experimental FT-IR spectral data of compounds **5**–**7** are compared with those of the expected spectral data.[28,29]

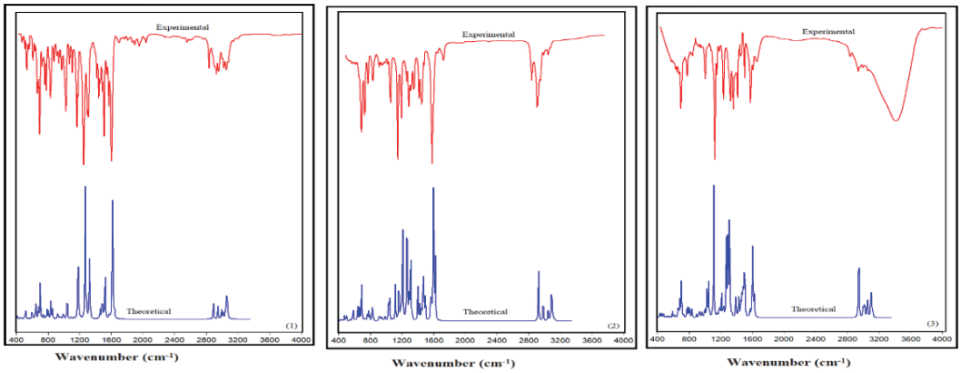

Fig. 3. The experimental and theoretical infrared spectra of **5**–**7**.

NMR spectra

Theoretical ^{1}H- and ^{13}C-NMR chemical shifts were estimated *via* the GIAO method using the B3LYP/6-311G++(d,p) level employing the optimized geometry of compounds **5**–**7**. Table II shows the experimental and computed chemical shifts for ^{1}H and ^{13}C nuclei. The experimental and theoretical ^{1}H- and ^{13}C--NMR spectra were observed in $CDCl_3$. The detected and expected NMR data for ^{1}H and ^{13}C nuclei are compared in Table II, which shows excellent agreement between the experimental ^{1}H- and ^{13}C-NMR data.

The GIAO approach was used to determine the theoretical ^{1}H- and ^{13}C--NMR chemical shifts of the **5**–**7**. In Table II, the detected and predicted NMR data for ^{1}H and ^{13}C nuclei are compared. The experimental ^{1}H- and ^{13}C-NMR spectra of **5**–**7** are given in Supplementary material to this paper.

TABLE II. Experimental and theoretical ^{1}H- and ^{13}C-NMR spectra of **5**–**7**

Compound **5**			Compound **6**			Compound **7**		
Atoms	Theo.	Exp.	Atoms	Theo.	Exp.	Atoms	Theo.	Exp.
C_{29}	168.5	166.02	C_{29}	170.1	166.27	C_{12}	164.6	166.18
C_{12}	165.1	161.86	C_{30}	167.4	160.86	C_{29}	163.7	158.56
C_{26}	155.1	159.30	C_{12}	163.7	158.84	C_{30}	162.3	
C_{3}	146.1		C_{26}	148.1		C_{26}	149.4	153.40
C_{13}	142.2		C_{3}	146.3		C_{33}	149.4	
C_{31}	139.3		C_{13}	142.2		C_{3}	146.2	
C_{30}	138.5	138.51	C_{31}	139.9	138.23	C_{13}	142.1	140.48
C_{16}	138.1		C_{16}	138.0	136.58	C_{15}	138.1	138.24
C_{6}	135.7	135.58	C_{6}	135.7	135.29	C_{6}	135.9	135.46
C_{2}	134.3		C_{2}	134.1		C_{2}	134.3	130.61
C_{14}	134.2	130.49	C_{14}	134.1		C_{14}	134.2	130.31
C_{15}	134.0	130.21	C_{15}	134.0	130.57	C_{16}	134.0	130.17
C_{7}	133.6	130.13	C_{7}	133.6	130.32	C_{31}	133.9	129.18
C_{4}	132.8	129.12	C_{4}	132.7	129.20	C_{7}	133.8	129.01
C_{5}	132.3	128.88	C_{18}	132.2	129.06	C_{4}	132.7	128.68
C_{18}	132.2	128.23	C_{5}	132.1	128.27	C_{17}	132.2	128.29
C_{17}	131.8	127.53	C_{17}	131.8	127.47	C_{5}	132.1	127.90
C_{28}	130.5	127.46	C_{28}	119.4		C_{18}	131.8	127.44
C_{32}	121.8		C_{32}	103.9	106.12	C_{28}	124.7	
C_{33}	112.8	114.16	C_{33}	101.6	103.42	C_{32}	109.1	105.44
C_{39}	55.06	55.37	C_{37}	55.22	55.41	C_{43}	61.72	60.94
H_{11}	8.66	8.59	C_{42}	55.15		C_{47}	60.10	56.07
H_{34}	8.59	7.84-7.72	H_{11}	8.60	8.51	C_{37}	55.21	
H_{27}	7.77		H_{34}	8.54	7.75	H_{11}	8.59	8.51
H_{8}	7.72	7.65	H_{27}	8.43		H_{27}	8.38	7.82-7.71
H_{1}	7.67		H_{8}	7.71	7.53-7.33	H_{34}	8.30	
H_{23}	7.64	7.56-7.35	H_{1}	7.68		H_{8}	7.70	7.49-7.35
H_{22}	7.62		H_{23}	7.66		H_{1}	7.69	
H_{21}	7.59		H_{22}	7.62		H_{23}	7.65	
H_{35}	7.59		H_{21}	7.54		H_{21}	7.62	
H_{9}	7.53		H_{9}	7.50		H_{22}	7.56	
H_{20}	7.46		H_{20}	7.43		H_{9}	7.51	
H_{19}	7.39		H_{19}	7.38		H_{19}	7.46	
H_{10}	7.30		H_{10}	7.27	6.85	H_{20}	7.39	
H_{36}	7.24	6.93	H_{46}	6.53		H_{10}	7.30	6.94
H_{37}	6.83		H_{35}	6.30	6.54	H_{35}	6.57	
H_{41}	4.04	3.86	H_{45}	4.18	3.79	H_{44}	4.61	3.91
H_{40}	3.68		H_{39}	4.00		H_{50}	4.21	
H_{42}	3.66		H_{43}	3.73		H_{39}	4.15	
			H_{44}	3.70		H_{46}	3.97	3.84
			H_{38}	3.66		H_{48}	3.94	
			H_{40}	3.64		H_{40}	3.70	
						H_{38}	3.64	
						H_{45}	3.47	
						H_{49}	3.47	

The C_{26} NMR chemical shift of each compound was calculated at 155.1 (**5**), 163.7 (**6**) and 149.4 ppm (**7**) by DFT method. Peaks experimentally measured as 3.86 (**5**), 3.79 (**6**) and 3.91 and 3.84 (**7**) ppm belonged to the proton of the methoxy groups. The proton peaks in the H–C=N group were reported in the ^{1}H-NMR spectra at 8.59 for **5** and 8.51 ppm for **6** and **7**. The chemical shift of H_{11} atoms was estimated by DFT calculations as 8.66 (**5**), 8.60 (**6**) and 8.59 ppm (**7**). The C_{26} peaks of each compound were measured experimentally in ^{13}C-NMR spectra at 159.3 (**5**), 158.84 (**6**) and 153.40 ppm (**7**). The C_{26} NMR chemical shift of each compound was calculated by DFT calculations at 155.1 (**5**), 163.7 (**6**) and 149.4 ppm (**7**). The peaks measured as 3.86 (**5**), 3.79 (**6**) 3.91 and 3.84 (**7**) ppm experimentally belong to the protons of the methoxy groups. The predicted ^{1}H-NMR chemical shift of each compound appeared in the 4.61–3.47 ppm region by DFT. The ^{13}C-NMR peaks were detected at 55.37 (**5**), 55.41 (**6**) and 60.94 and 56.07 ppm (**7**). The smallest ^{13}C-NMR chemical shift values were theoretically calculated for the metoxy group. For both ^{1}H- and ^{13}C-NMR, the theoretical and experimental values were apparently in good agreement. Except for the methoxy group, the predicted and experimental ^{13}C-NMR values all appeared to be over 100 ppm. The nitrogen atom, which displayed greater electronegative characteristics, was bound to carbon atoms that were more de-shielded.[30–33] Therefore, these atoms showed increased ^{13}C-NMR peaks than the others.

Frontier molecular orbital (FMO) analysis

Fig. 4 shows the plots for the **5**–**7**'s HOMO and LUMO. Red and green are used to represent the positive and negative phases, respectively. The HOMO and LUMO are distributed in all compounds. However, this distribution is not uniform. The HOMO is more concentrated on the pyridine group, whereas the LUMO is more concentrated on the phenyl and N–CH_3 groups.

B3LYP/6-311++G(d,p) theory was used to calculate the HOMO, LUMO, band gap energies and other molecular characteristics. Molecular characteristics such as ionization potential (I), electron affinity (A), electronegativity (A'), chemical potential (B), spherical hardness (S), spherical softness (S') and electrophilicity (B') were calculated using the formulae provided at the end of Table S-I of the Supplementary material.[34–36] Table S-I contains a list of these properties.

The literature indicates that a compound with lower reactivity and higher stability has a larger HOMO–LUMO gap. The values of the HOMO–LUMO gap calculated for compounds **5**–**7** were 4.083, 4.058 and 3.993 eV, respectively. The predicted η value of **5**–**7** was at 2.042, 2.029 and 1.997 eV, respectively. The σ value of the **5**–**7** compounds were determined at 0.245, 0.246 and 0.250 eV, respectively. As seen in Table S-I, the global hardness (η) of the compounds is greater than the global softness (σ). According to these results, the compounds are hard. A compound's characteristics vary according to its hardness or softness.

For instance, soft materials have a small energy gap compared to that of hard materials. Soft compounds are more easily polarized than hard ones. As a result, soft molecules are more biologically reactive than hard compounds.[34–36]

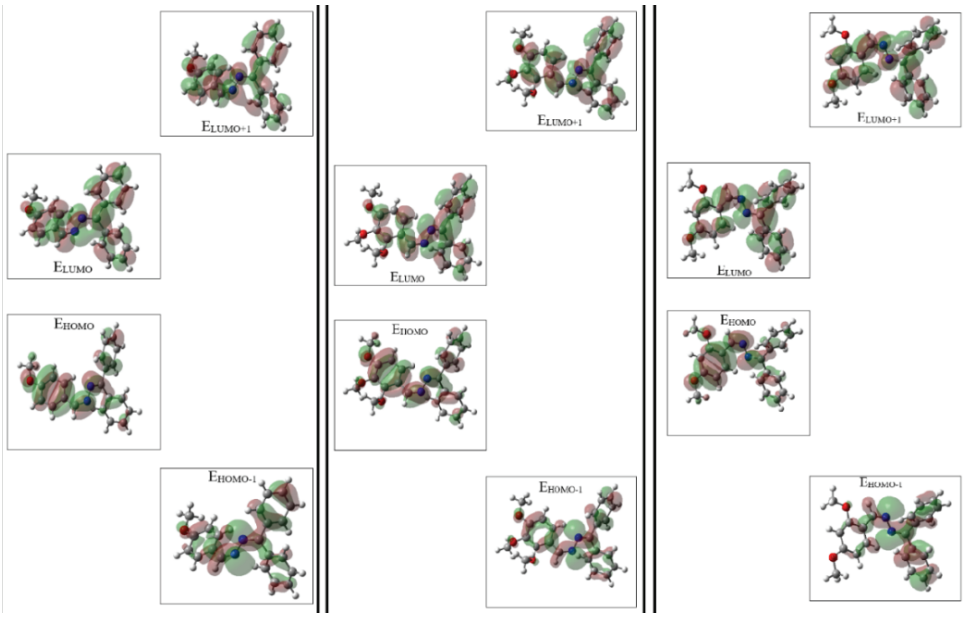

Fig. 4. HOMO and LUMO plots of the **5**–**7**.

Molecular electrostatic potential maps

A 3D plot of the molecular electrostatic potential (*MEP*) of compounds **5**–**7** is given in Fig. 5. Using the *MEP* diagram, it is simple to determine the compounds' reactive sites. Electron-deficient regions are depicted in blue, whereas electron-rich regions are depicted in red. The region around the nitrogen atom of the azine group and oxygen atom of the O–CH_3 groups was electron-rich (red) regions.[37–39]

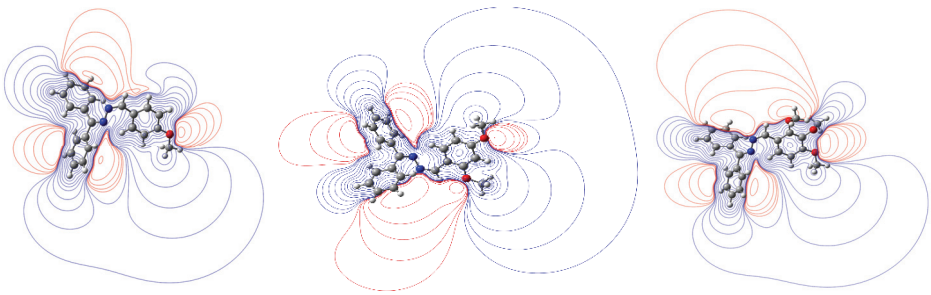

Fig. 5. Molecular electrostatic potential maps of compounds **5**–**7**.

Antimicrobial evaluation of the synthesized compounds

Using the micro-dilution and agar well diffusion methods, the compounds were examined for their antibacterial effects on nine bacteria and one yeast. Table III lists the antibacterial activity results for the compounds with minimal inhibitory concentrations (*MIC*) values and inhibition zone diameters (mm).

TABLE III. Antimicrobial evaluations of the synthesized compounds *MIC* (μg/mL) values and inhibition zone diameter (mm); concentration of compounds: 1000 μg/mL; –: *MIC* > 250 μg/mL; AMP: ampicilin; Cyclohex.: cycloheximide

Microorganism	*MIC*			Diameter of inhibition zone				
	5	**6**	**7**	**5**	**6**	**7**	AMP (10 μg)	Cyclohex.
L. monocytogenes ATCC 7644	–	–	–	–	–	–	10	–
S. aureus ATCC 25923	–	–	–	–	–	–	18	–
B. subtilis ATCC 6633	–	–	–	–	–	–	24	–
E. faecalis ATCC 29212	–	–	–	–	–	–	–	–
*K. pneumoni*ae ATCC 21541	–	–	7.81	–	–	15	18	–
P. aeruginosa ATCC 27853	–	–	7.81	–	–	15	18	–
S. dysenteriae ATCC 11835	–	–	–	–	–	–	20	–
S.typhimurium ATCC 14028	–	–	250	–	–	10	18	–
E. coli ATCC 25922	–	–	–	–	–	–	–	–
C. albicans ATCC 10231	–	–	–	–	–	–	–	18

According to this study, compound **7** showed good activity in the range of 7.81–250 μg/mL MIC values against *Klebsiella pneumoni*ae, *Pseudomonas aeruginosa* and *Salmonella typhimurium*. Compound **7** showed the zone of inhibition values in the range of 10–15 mm against *K. pneumoniae*, *P. aeruginosa* and *S. typhimurium.* Compound **7** showed activity of 250 μg/mL *MIC* against *S. typhimurium*. Compounds **5** and **6** did not show antimicrobial activity against the investigated bacteria and yeast (Table III). In 2011, Shams *et al.* reported that the *MIC* values of dyes and dye precursors against all microbial strains tested were generally in the range of 0.04–30.00 μg/mL, resulting in significant and potent antimicrobial activity.[40] The results obtained are similar to those published by Shams *et al.*

CONCLUSION

In the present study, a series of azine derivatives were synthesized in a short time with high yield by microwave method. NMR and FT-IR spectroscopy were used to verify the structures of the compounds prepared. Two conformers of **5**, six conformers of **6** and twelve conformers of **7** were determined using the PES scan result. The most stable conformers of the compounds were identified and then re-optimized for further calculations using the 6-311++G(d,p) basis set. There was perfect agreement between the experimental FT-IR, ^{1}H- and ^{13}C--NMR data and the theoretical data of the most stable isomer. Examination of the

antimicrobial screening data revealed that compounds **5** and **6** did not show antimicrobial activity against any of the bacterial strains and yeast. Compound 1-(diphenylmethylene)-2-(2,3,4-trimethoxybenzylidene)hydrazine (**7**) showed good activity in the range of 7.81–250 μg/mL *MIC* values against *K. pneumonia* ATCC 21541, *P. aeruginosa* ATCC 27853 and *S. typhimurium* ATCC 14028.

SUPPLEMENTARY MATERIAL

Additional data and information are available electronically at the pages of journal website: https://www.shd-pub.org.rs/index.php/JSCS/article/view/12551, or from the corresponding author on request.

Acknowledgements. I would like to express my gratitude to Prof. Dr. Yusuf Erdoğdu, Prof. Dr. Belgin Erdem and all of the other scholars who made significant contributions to the theoretical and microbiological investigations.

ИЗВОД

СИНТЕЗА И ТЕОРИЈСКО ПРОУЧАВАЊЕ НЕКИХ АЗИНСКИХ ДЕРИВАТА И ИСТРАЖИВАЊЕ ЊИХОВИХ АНТИМИКРОБНИХ ДЕЈСТАВА

SERTAN AYTAÇ

Kırşehir Ahi Evran University, Kaman Vocational School, Department of Food Technology, 40300 Kaman, Kırşehir, Türkiye

Ова студија укључује експериментална, теоријска, и антимикробна истраживања 1-(дифенилметилен)-2-(4-метоксибензилиден)хидразина (**5**), 1-(3,5-диметоксибензилиден)-2-(дифенилметилен)хидразина (**6**) и 1-(дифенилметилен)-2-(2,3,4-триметоксибензилиден)хидразина (**7**). Структуре једињења синтетисаних микроталасном методом, одређене су спектроскопским методама и елементалном анализом. Конформациона анализа, структура основног стања, FT-IR и NMR спектри једињења су израчунати користећи теорију функционала густине (DFT) у теоријском истраживању. На нивоу B3LYP/6-31G(d,p), оптимизовани су конформери, због торзионе баријере. B3LYP/6-311++G (d,p) је коришћен за одређивање хармонијских вибрационих фреквенци, расподеле потенцијалне енергије (PED), IR интензитета и NMR хемијских помака најстабилнијих конформера. Експериментални налази упоређени су са теоријски очекиваним спектралним подацима. Антибактеријска активност припремљених једињења тестирана је *in vitro* на девет бактерија и једној врсти квасца. Антимикробна активност једињења тестирана је преко минималне инхибирајуће концентрације (*MIC*) методом дифузије у бунарићима агара. Једињење **7** је показало добру активност против бактерија и квасца, док **5** и **6** нису показали антимикробну активност. Једињење **7** показало је вредности зоне инхибирања у распону од 10–15 mm према *Klebsiella pneumonia, Pseudomonas aeruginosa* и *Salmonella typhimurium*. Према резултатима, једињење **7** је од испитаних најефикасније против бактерија.

(Примљено 17. Августа, ревидирано 14. Септембр,; прихваћено 24. октобра 2023)

REFERENCES

1. D. Amariucai-Mantu, V. Mangalagiu, I. Bejan, A. Aricu, II. Mangalagiu, *Pharmaceutics* **2** (2022) 2026 (https://doi.org/10.3390/pharmaceutics14102026)

2. M. F. N. N. Carvalho, *Antibiotics* **11** (2022) 337 (https://doi.org/10.3390/antibiotics11030337)
3. A. S. Salman, N. A. Mahmoud, A. Abdel-Aziem, M. A. Mohamed, D. M. Elsisi, *Int. J. Org. Chem*. **5** (2015) 81 (https://doi.org/10.4236/ijoc.2015.52010)
4. S. Kulaksızoglu, C. Gökçe, R. Gup, *Turk. J. Chem.* **36** (2002) 717 (https://doi.org/10.3906/kim-1110-3)
5. S. P. Simeonov, V. B. Kurteva, R. P. Bontchev, *Bulg. Chem. Commun*. **40** (2008) 409 (http://www.bcc.bas.bg/bcc_volumes/Volume_40_Number_4_2008/Volume_40_Number_4_2008_PDF/BCC_v40_n4.pdf#page=39)
6. B. Krishnakumar, M. Swaminathan, *Catal. Commun.* **16** (2011) 50 (https://doi.org/10.1016/j.molcata.2011.08.026)
7. H. Loghmani-Khouzani, M. M. M. Sadeghi, J. Safari, M. S. Abdorrezaie, M. Jafarpisheh, *J. Chem. Research* **2** (2001) 80 (https://doi.org/10.3184/030823401103169036)
8. K. Venkatesan, V. S. V. Satyanarayana, A. Sivakumar, *J. Chin. Chem. Soc*. **58** (2011) 583 (https://doi.org/10.1002/jccs.201190091)
9. A. Y. Vibhute, S. S. Mokle, Y. S. Nalwar, Y. B. Vibhute, V. M. Gurav, *Bull. Catal. Soc. India* **8** (2009) 164 (https://www.researchgate.net/profile/Shyam-Mokle/publication/257656004_An_Efficient_and_Operationally_Simple_Synthesis_of_Some_New_Schiff_Bases_Using_Grinding_Technique/links/00463525af8a3c66e6000000/An-Efficient-and-Operationally-Simple-Synthesis-of-Some-New-Schiff-Bases-Using-Grinding-Technique.pdf)
10. W. A. A. Arafa, R. M. Shaker, *ARKIVOC* (iii) (2016) 187 (http://dx.doi.org/10.3998/ark.5550190.p009.464)
11. A. Rammohan, J. S. Reddy, G. Sravya, C. N. Rao, G. V. Zyryanov, *Environ. Chem. Lett*. **18** (2002) 433 (https://doi.org/10.1007/s10311-019-00959-w)
12. S. Aytaç, *JIST* **11** (2021) 2979 (https://doi.org/10.21597/jist.976184)
13. Safari, S. Gandomi-Ravandi, *Synth. Commun.* **41** (2011) 645 (https://doi.org/10.1080/00397911003629523)
14. J. Jayabharathi, V. Thanikachalam, A. Thangamani, M. Padmavathy, *Med. Chem. Res.* **16** (2007) 266 (https://doi.org/10.1007/s00044-007-9029-4)
15. A. Zieba, Z. P. Czuba, W. Krol, *Acta Pol. Pharm.* **69** (2012) 1149 (https://www.ptfarm.pl/pub/File/Acta_Poloniae/2012/6/1149.pdf)
16. H. Çelik, A. Babagil, *Int. J. Second. Metab.* **6** (2019) 38 (https://doi.org/10.21448/ijsm.479108)
17. M. Ayaz, O. Gundogdu, S. Aytac, B. Erdem, H. Ciftci, Y. Erdogdu, *J. Mol. Struct.* **1269** (2022) 133791 (https://doi.org/10.1016/j.molstruc.2022.133791)
18. K. Ravi, B. Krishnakumar, M. Swaminathan, *Int. Sch. Res. Notices* (2012) 595868 (https://doi.org/10.5402/2012/595868)
19. *Gaussian 16, Revision B.01*, Gaussian, Inc., Wallingford, CT, 2016
20. C. Lee, W. Yang, R.G. Parr, *Phys. Rev*., *B* **37** (1988) 785 (https://doi.org/10.1103/physrevb.37.785)
21. A. D. Becke, *Phys. Rev., A* **38** (1988) 3098 (https://doi.org/10.1103/PhysRevA.38.3098)
22. A. D. Becke, *J. Chem. Phys*. **98** (1993) 5648 (https://doi.org/10.1063/1.464913)
23. D. Sajan, Y. Erdogdu, T. Kuruvilla, I. H. Joe, *J. Mol. Struct*. **983** (2010) 12 (https://doi.org/10.1016/j.molstruc.2010.08.003)
24. *Spartan 08*, Wavefunction Inc., Irvine, CA, 2008 (ISBN978-1-890661-38-4)
25. T. A. Halgren, *J. Comput. Chem.* **17** (1996) 490 (https://doi.org/10.1002/(SICI)1096-987X(199604)17:5/6<490::AID-JCC1>3.0.CO;2-P)

26. Y. Erdogdu, Ö. Dereli, D. Sajan L. Joseph, O. Ünsalan, M. T. Güllüoğlu, *Mol. Simul.* **38** (2012) 315 (https://doi.org/10.1080/08927022.2011.632416)
27. S. Saglam, A. Disli, Y. Erdogdu, M. K. Marchewka, N. Kanagathara, B. Bay, *Spectrochim. Acta, A.* **135** (2015)1011 (https://doi.org/10.1016/j.saa.2014.07.071)
28. A. Borba, M. Albrecht, A. G. Zavaglia, L. Lapinski, M. J. Nowak, M. A. Suhmb, R. Fausto, *Phys. Chem. Chem. Phys*. **10** (2008) 7010 (https://doi.org/10.1039/B810002K)
29. A. Atilgan, S. Yurdakul, Y. Erdogdu, M. T. Gulluoglu, *J. Mol. Struct*. **1161** (2018) 55 (https://doi.org/10.1016/j.molstruc.2018.01.080)
30. Y. Erdogdu, S. Saglam, M. T. Gulluoglu, Spectrochim. *Acta, A* **146** (2015) 88 (https://dx.doi.org/10.1016/j.saa.2015.03.031)
31. M. Yilmaz, B. Aydin, O. Dogan, O. Dereli, *J. Mol. Struct.* **1128** (2017) 345 (https://doi.org/10.1016/j.molstruc.2016.08.067)
32. E. K. Sarıkaya, S. Bahçeli. D. Varkal, O. Dereli, *J. Mol. Struct.* **1141** (2017) 44 (https://doi.org/10.1016/j.molstruc.2017.03.088)
33. Y. Erdogdu, Ş. Yurdakul, S. Badoglu, M.T. Güllüoğlu, *J. Mol. Struct.* **1184** (2019) 364 (https://doi.org/10.1016/j.molstruc.2019.02.016)
34. S. Chandra, H. Saleem, Y. Erdogdu, S. Subashchandrabose, A. R. Krishnan, M. T. Güllüoğlu, *J. Mol. Struct.* **998** (2011) 69 (https://doi.org/10.1016/j.molstruc.2011.05.014)
35. S. Çelik, M. Alp, S. Yurdakul, *Spectrosc. Lett.* **53** (2020) 234 (https://doi.org/10.1080/00387010.2020.1734840)
36. S. Çelik, S. Yurdakul, B. Erdem, *Inorg. Chem. Commun*. **131** (2021)108760 (https://doi.org/10.1016/j.inoche.2021.108760)
37. Ö. Dereli, Y. Erdogdu, M. T. Gulluoglu, E. Türkkan, A. Özmen, N. Sundaraganesan, *J. Mol. Struct.* **1012** (2012) 168 (https://doi.org/10.1016/j.molstruc.2012.01.003)
38. L. Joseph, D. Sajan, R. Reshmy, B. S. A. Sasi, Y. Erdogdu, K. K. Thomas, *Spectrochim. Acta, A* **99** (2012) 234 (https://doi.org/10.1016/j.saa.2012.07.084)
39. N. R. Babu, S. Subashchandrabose, M. S. A. Padusha, H. Saleem, Y. Erdogdu, *Spectrochim. Acta, A* **120** (2014) 314 (https://doi.org/10.1016/j.saa.2013.09.089)
40. H. Z. Shams, R. M. Mohareb, M. H. Helal, A. E-S. Mahmoud, *Molecules* **16** (2011) 6271 (https://doi.org/10.3390/molecules16086271).

Journal of the Serbian Chemical Society
JSCS@tmf.bg.ac.rs • www.shd.org.rs/JSCS
J. Serb. Chem. Soc. 89 (10) S338–S344 (2024) *Supplementary material*

SUPPLEMENTARY MATERIAL TO

Synthesis of and theoretical research on some azine derivatives and investigation of their antimicrobial activities

SERTAN AYTAÇ*

Kırşehir Ahi Evran University, Kaman Vocational School, Department of Food Technology, 40300 Kaman, Kırşehir, Türkiye

J. Serb. Chem. Soc. 89 (10) (2024) 1285–1298

CONTENTS

Spectroscopic Data of Main Compounds S339-S340
TABLE S1. HOMO, LUMO, HOMO-LUMO gap and selected molecular properties of **5**, **6,** and **7** S341
NMR Spectra of Maın Compounds S342-S344

* Corresponding author. E-mail: saytac@ahievran.edu.tr

SPECTROSCOPIC DATA OF MAIN COMPOUNDS

*1-(diphenylmethylene)-2-(4-methoxybenzylidene)hydrazine (**5**)*

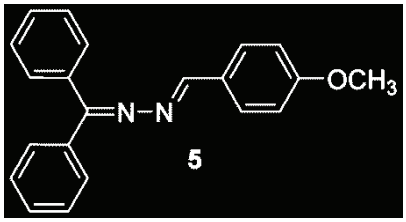

Yield: 97%, yellow solid, m.p. 95-96 °C. R_f: 0.66 (Ethyl acetate/P.Ether, 1:4)
^{1}H NMR (400 MHz, $CDCl_3$) δ 8.59 (s, 1H), 7.84-7.72 (m, 2H), 7.65 (d, *J* = 8.8 Hz, 2H), 7.56-7.35 (m, 8H), 6.93 (d, *J* = 8.8 Hz, 2H), 3.86 (s, 3H).
^{13}C NMR (100 MHz, $CDCl_3$) δ 166.02, 161.86, 159.30, 138.51, 135.58, 130.49, 130.21, 130.13, 129.12, 128.88, 128.23, 127.53, 127.46, 114.16, 55.37.
FT-IR (cm^{-1}): 1605 (HC=N), 1567 (C=N), 1511, 1491, 1443, 1413, 1301, 1252.
Elemental Anal.Calcd. for $C_{21}H_{18}N_2O$ C, 80.23; H, 5.77; N, 8.91 Found C, 80.36; H, 5.42; N,8.93.

*1-(3,5-dimethoxybenzylidene)-2-(diphenylmethylene)hydrazine (**6**):*

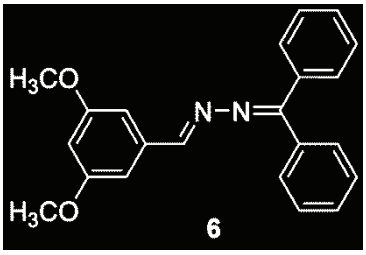

Yield: 96%, yellow solid, m.p. 86-87 °C.
^{1}H NMR (400 MHz, $CDCl_3$) δ 8.51 (s, 1H), 7.75 (dd, *J* = 8.2, 1.3 Hz, 2H), 7.53 – 7.33 (m, 8H), 6.85 (d, *J* = 2.3 Hz, 2H), 6.54 (t, *J* = 2.3 Hz, 1H), 3.79 (s, 6H).
^{13}C NMR (100 MHz, $CDCl_3$) δ 166.27, 160.86, 158.84, 138.23, 136.58, 135.29, 130.57, 130.32, 129.20, 129.06, 128.27, 127.47, 106.12, 103.42, 55.41.
FT-IR (cm^{-1}): 1590 (HC=N), 1456, 1425, 1356, 1297, 1202.
Elemental Anal.Calcd. for $C_{22}H_{20}N_2O_2$ C, 76.72; H, 5.85; N, 8.13; Found: C, 76.79; H, 5.78; N, 8.10.

1-(diphenylmethylene)-2-(2,3,4-trimethoxybenzylidene)hydrazine (7):

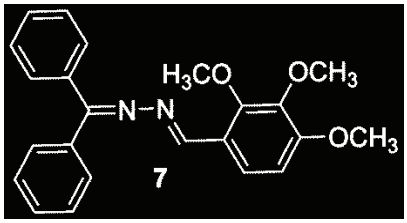

Yield: 97%, yellow solid, m.p. 70-72 °C.

^{1}H NMR (400 MHz, $CDCl_3$) δ 8.51 (s, 1H), 7.82-7.71 (m, 2H), 7.49-7.35 (m, 8H), 6.94 (s, 2H), 3.91 (s, 3H), 3.84 (s, 6H, 2xOCH_3).

^{13}C NMR (100 MHz, $CDCl_3$) δ 166.18, 158.56, 153.40, 140.48, 138.24, 135.46, 130.61, 130.31, 130.17, 129.18, 129.01, 128.68, 128.29, 127.90, 127.44, 105.44, 60.94, 56.07 (2C).

FT-IR (cm^{-1}): 1574 (C=N), 1502 (C=C aromatic), 1461, 1414, 1359 (C-N), 1126.

Elemental Anal. Calcd. for $C_{23}H_{22}N_2O_3$ C, 73.78; H, 5.92; N, 7.48 Found: C, 73.34; H, 5.58; N, 7.76.

TABLE S-I. HOMO, LUMO, HOMO-LUMO gap and selected molecular properties of **5**, **6,** and **7**

		Energy (eV)		Energy gap (eV)	Ionization Potential (I) (eV)	Electron affinity (A) (eV)	Global Hardness (η) (eV)	Electronegativity (χ) (eV)	Chemical potential (μ) (eV)	Global Softness (σ) $(eV)^{-1}$	Global electrophilicity (ω) (eV)
	HOMO	-5.987	$\Delta E_{HOMO-LUMO}$	4.083	5.987	1.904	2.042	3.946	-3.946	0.245	3.813
	LUMO	-1.904									
5	HOMO-1	-6.088	$\Delta E_{(H-1)-(L+1)}$	5.131	6.088	0.956	2.566	3.522	-3.522	0.195	2.418
	LUMO+1	-0.956									
	HOMO	-5.922	$\Delta E_{HOMO-LUMO}$	4.058	5.922	1.864	2.029	3.893	-3.893	0.246	3.735
	LUMO	-1.864									
6	HOMO-1	-5.992	$\Delta E_{(H-1)-(L+1)}$	5.069	5.992	0.923	2.535	3.457	-3.457	0.197	2.358
	LUMO+1	-0.923									
	HOMO	-5.791	$\Delta E_{HOMO-LUMO}$	3.993	5.791	1.797	1.997	3.794	-3.794	0.250	3.604
	LUMO	-1.797									
7	HOMO-1	-5.791	$\Delta E_{(H-1)-(L+1)}$	4.902	5.791	0.888	2.451	3.339	-3.339	0.204	2.275
	LUMO+1	-0.888									

$I = -E_{HOMO}$, $A = -E_{LUMO}$, $\eta = ((I-A))/2$, $\chi = ((I+A))/2$, $\mu = (-(I+A))/2$, $\sigma = 1/2\eta$, $\omega = \mu^2/2\eta$

NMR SPECTRA OF MAIN COMPOUNDS

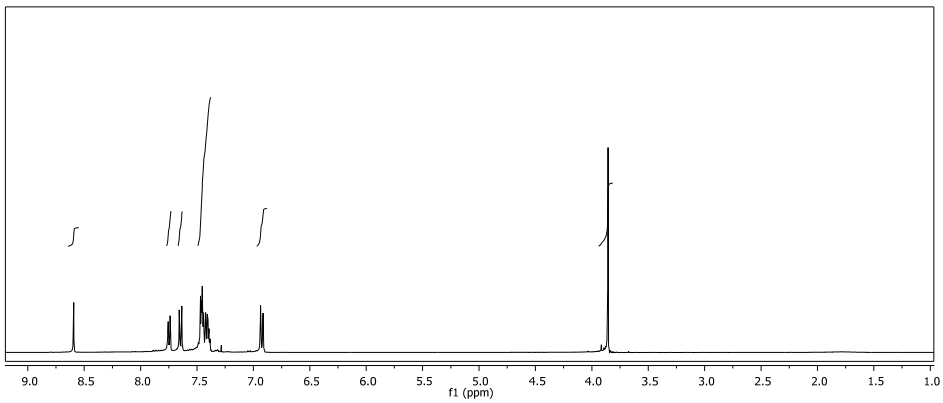

Figure S-1. ^{1}H NMR spectrum of 1-(diphenylmethylene)-2-(4-methoxybenzylidene)hydrazine (**5**) in $CDCl_3$

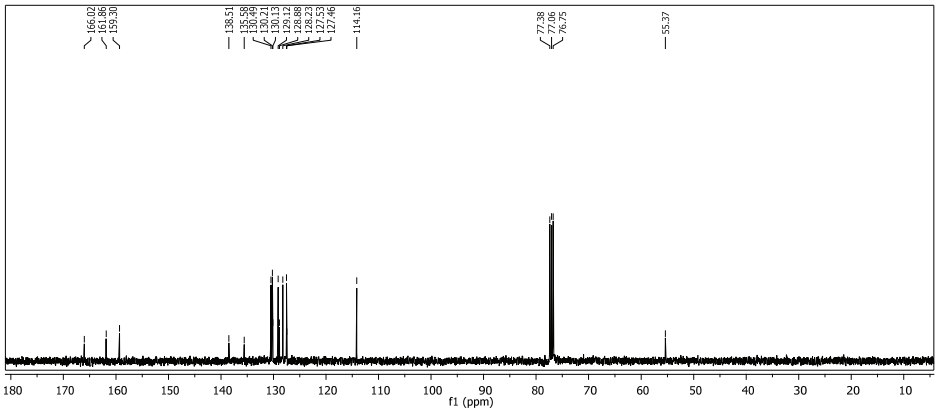

Figure S-2. ^{13}C NMR spectrum of 1-(diphenylmethylene)-2-(4-methoxybenzylidene)hydrazine (**5**) in $CDCl_3$

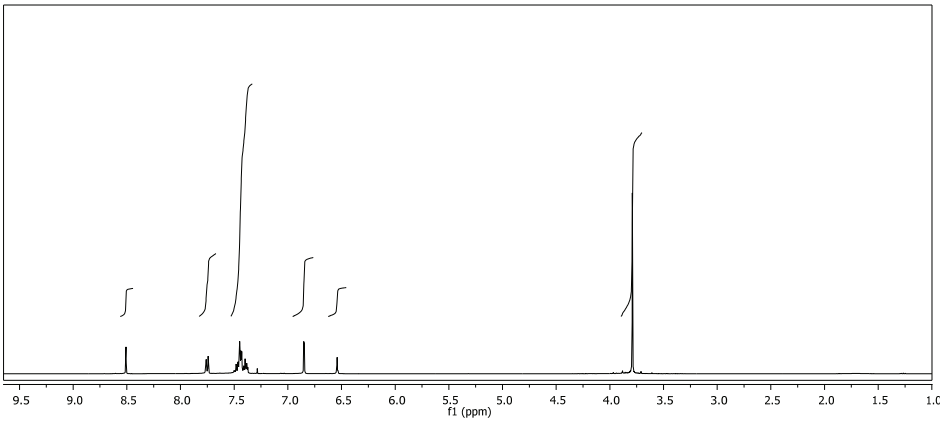

Figure S-3. ^{1}H NMR spectrum of 1-(3,5-dimethoxybenzylidene)-2-(diphenylmethylene)hydrazine (**6**) in $CDCl_3$

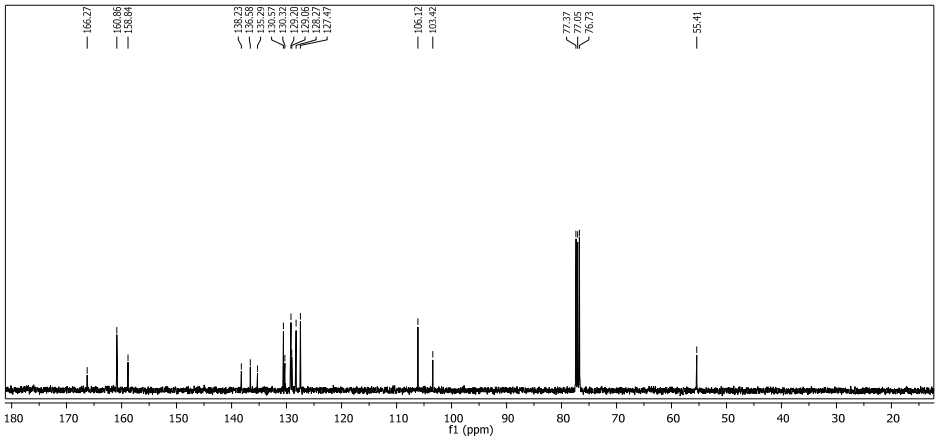

Figure S-4. ^{13}C NMR spectrum of 1-(3,5-dimethoxybenzylidene)-2-(diphenylmethylene)hydrazine (**6**) in $CDCl_3$

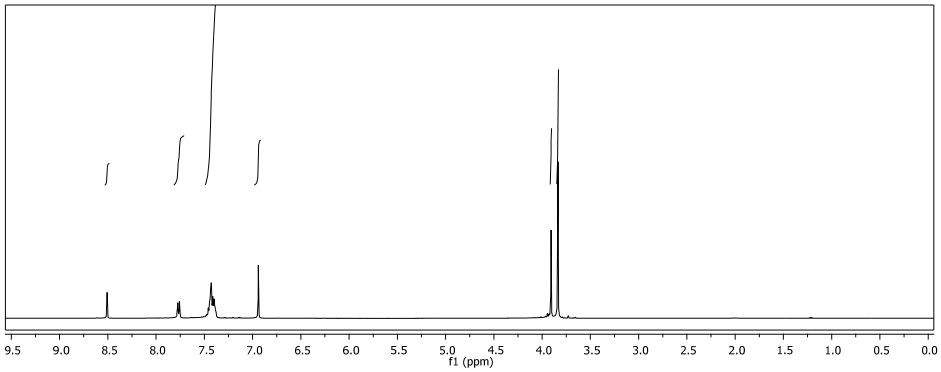

Figure S-5. ^{1}H NMR spectrum of 1-(diphenylmethylene)-2-(2,3,4-trimethoxybenzylidene)hydrazine (**7**) in $CDCl_3$

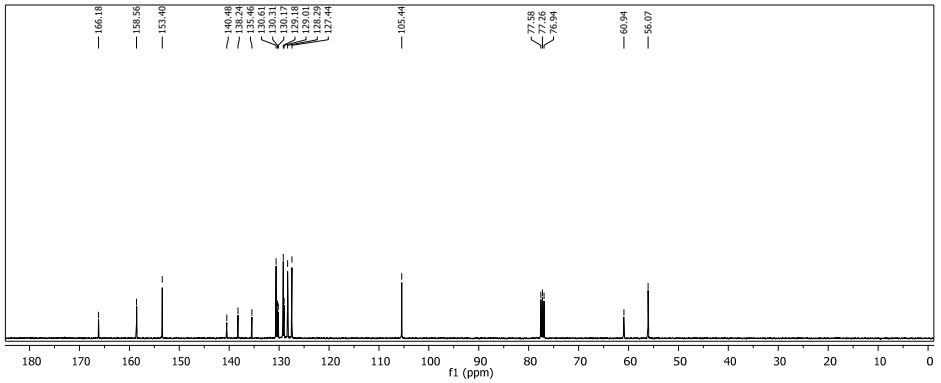

Figure S-6. ^{13}C NMR spectrum of 1-(diphenylmethylene)-2-(2,3,4-trimethoxybenzylidene)hydrazine (**7**) in $CDCl_3$

Journal of the Serbian Chemical Society
JSCS@tmf.bg.ac.rs • www.shd.org.rs/JSCS
J. Serb. Chem. Soc. *89* (10) 1299–1309 (2024)
JSCS–5788
Original scientific paper
Published 29 October, 2024

Mathematical approaches to a method of semiconductor materials films synthesis type $A^{II}B^{VI}$ for photosensitive structures used in alternative energy

RUSLANA R. GUMINILOVYCH*, PAVLO Y. SHAPOVAL, MARTYN A. SOZANSKYI, VITALII Y. STADNIK and LILIYA R. DEVA

Lviv Polytechnic National University, 12, S. Bandera str., 79013 Lviv, Ukraine

(Received 25 October, revised 15 November 2023, accepted 1 January 2024)

Abstract: The scientific direction of the synthesis of CdS and CdSe thin films by the method of chemical surface deposition (CSD) using the aqueous solutions of cadmium-containing salts: chloride, nitrate, sulphate, acetate and iodide has been developed. A mathematical model of the CSD process of CdS and CdSe thin films was developed to improve the efficiency of experiments and reduce costs. The model makes it possible to determine the concentration of reagents, the duration, and the CSD temperature, which are necessary to obtain films of a specified thickness. The optimization of chemical deposition parameters of film-type semiconductor materials has been carried out. Based on the mathematical model, the optimal synthesis conditions were the following: the concentration of cadmium-source salt – 0.01 mol/L, chalcogenizer – 1.0 mol/L or 0.1 mol/L in the case of thiourea or sodium selenosulphate, respectively; the temperature: 70 °C and the duration of 3 min. The mathematical dependence of the experimental studies results of the metal ions content in thin-film solar cells for the effective direct conversion of solar radiation into electrical energy was proposed taking errors into account.

Keywords: thin films; chemical surface deposition; solar cells.

INTRODUCTION

Now in the public consciousness, there is a growing conviction that the energy of the future should be based on the large-scale use of solar energy, and in its various manifestations. The bet on solar energy should be seen not only as a win-win situation, but in the long term as one of the best choices for humanity. We will consider the possibilities of converting solar energy into electrical energy using semiconductor solar photocells in retrospective and prospective terms. These devices appear to be quite mature scientifically and technologically today to be

* Corresponding author. E-mail: guminilovych@gmail.com
https://doi.org/10.2298/JSC231023001G

regarded as the technical basis for the large-scale solar power of the future. Photovoltaic converters of solar energy occupy a special place among the alternative and the renewable energy sources.

Solar PV cells are a very real technically and cost-effective alternative to fossil fuels in several applications. The solar cell can directly convert solar radiation into electricity without the use of any moving mechanisms. Due to this, the service life of solar generators is quite long. Photovoltaic systems have proven themselves well since the beginning of the industrial application of photovoltaic cells.

Improving the photoconversion efficiency by increasing the short-circuit current in solar cells with a CdS or CdSe buffer layer requires a decrease in losses because of the optical absorption of photons with energies $h\nu < 2.4$ eV, which can be achieved by minimizing the thickness of cadmium sulphide and cadmium selenide films to optimal sizes. Therefore, the studies of the deposition process of CdS and CdSe thin films with the given photoelectric properties for the creation based on them of thin-film solar cells are of considerable practical interest.

The search for new approaches to obtain the films of $A^{II}B^{VI}$ semiconductor materials, in particular CdS and CdSe films, will solve the problems of reducing the cost of photosensitive elements, a comprehensive study of the electrophysical properties of film-type semiconductor materials and the structures based on them, as well as the development of new methods for their implementation. The prospect of this direction is justified by the fact that, despite numerous studies, semiconductor photosensitive structures based on cadmium sulphide and cadmium selenide thin films are widely used in thin-film solar cells for the efficient direct conversion of solar radiation into electrical energy.[1,2] The industrial introduction of such elements and the use of solar modules in alternative energy is hindered by the high cost of their manufacture, and, accordingly, the high cost of electricity produced by them. The manufacturing cost can be significantly reduced if the method for obtaining thin films is simple and will not require the use of high temperatures and expensive initial materials.

The operation of thin-film elements is based on a Cd (S, Se)/CdTe or Cd (S, Se)/Si heterojunction, and their parameters and technical characteristics are determined by the properties of thin films and the conditions for making the heterojunctions. Therefore, the development of the synthesis basis of CdS and CdSe continuous semiconductor thin films from aqueous solutions using a simple and reproducible method that must satisfy the economic and environmental aspects of production and must ensure high quality of the material is an important and actual scientific problem.[3] The use of mathematical modelling for the decrease of the film manufacturing cost and the increase of its production amount was not observed in the scientific research in this field, which can open a new approach to economical, and environmentally friendlier semiconductor synthesis in terms of decreasing the

amount of by-products formation and the increase of the effectiveness of reactants conversion.

To obtain a high-quality mathematical model, it is essential to gather a substantial amount of experimental data related to the nature of the initial agents, concentration, synthesis temperature and duration, as well as film thickness.

To acquire this data, the following steps are necessary:

1. Choose the synthesis technique, initial substances, and synthesis conditions.
2. Produce several thin film samples.
3. Determine their thickness, optical, and morphological properties.
4. Establish relationships between these properties.

Chemical surface deposition (CSD)

To achieve the goals of this research, first of all, it was necessary to choose the film synthesis technique because the number of factors which should be used for the mathematical modelling and the quality of the film directly depends on the process which lay in its base. For this reason, we decided to use the chemical surface deposition technique since it requires the minimum amount of reactants, and this method is ideal for the production of thin films over large areas at temperatures <100 °C, which is one of the main requirements for the mass use of solar energy. The technology of chemical deposition of semiconductor films consists of the deposition of a solution containing metal ions and a source of sulphur or selenium ions onto a substrate. The deposition of CdS thin films from aqueous solutions is a reaction between cadmium salts and thiourea in an alkaline medium.[4,5] To obtain high-quality cadmium coatings, it is necessary to use well-water-soluble cadmium sources, which will be cheap and would not provide any additions, which may cause the formation of other undesirable by-products. For this purpose, it perfectly fits some simple cadmium salts. Preferably, the most used are $CdSO_4$, CdI_2, $Cd(NO_3)_2$, $Cd(CH_3COO)_2$ and $CdCl_2$. Thiourea is used as a sulphur-containing agent in the sulphide deposition reactions since it has a high affinity for metal cations and decomposes at low temperatures. The deposition process can be described by two mechanisms: homogeneous and heterogeneous.[6]

The homogeneous mechanism presupposes the formation of a coating of colloidal CdS particles, which are formed in solution and consist of several stages:

1. Dissociation of ammonium hydroxide:

$$NH_4^+ + OH^- \rightarrow NH_3 + H_2O \quad (1)$$

In an alkaline medium due to the interaction of Cd^{2+} with OH^- is the possible formation of an undesirable product – $Cd(OH)_2$:[4,5]

$$Cd^{2+} + 2OH^- \rightarrow Cd(OH)_2 \downarrow \quad (2)$$

2. Hydrolysis of thiourea, $(NH_2)_2CS$, with the formation of sulphides:

$$(NH_2)_2CS + H_2O \rightarrow HS^- + H^+ + (NH_2)_2CO \quad (3)$$

$$HS^- + OH^- \rightarrow S^{2-} + H_2O \quad (4)$$

3. Formation of the final product:

$$Cd^{2+} + S^{2-} \rightarrow CdS\downarrow \quad (5)$$

According to the heterogeneous mechanism of CdS thin films, the deposition from aqueous solutions passes through the stage of $[Cd(NH_3)_4]^{2+}$ formation, which reduces the overall reaction rate and prevents the formation of $Cd(OH)_2$.[7] The formed cadmium tetraamine ion interacts with sulphides, which are formed by hydrolysis of thiourea (Eqs. (3) and (4)):

$$Cd^{2+} + 4NH_4OH \rightarrow Cd[(NH_3)_4]^{2+} + 4H_2O \quad (6)$$

$$Cd[(NH_3)_4]^{2+} + S^{2-} \rightarrow CdS\downarrow + 4NH_3 \quad (7)$$

In general:

$$Cd[(NH_3)_4]^{2+} + (NH_2)_2CS + OH^- \rightarrow CdS\downarrow + 4NH_3 + H^+ + (NH_2)_2CO \quad (8)$$

The deposition of sulphide films from thiourea coordination compounds has several chemical features.

Depending on the salt nature and the composition of the solution different coordination forms may dominate, moreover together with the thiourea molecules the anions Cl^-, Br^- and I^- may enter the complex inner sphere under certain conditions with SO_4^{2-}. Thus, the nearest environment of cadmium atoms can be sulphur, halogen and oxygen atoms, moreover, during thermal destruction, some of the Cd–Hal or Cd–O bonds are stored and defects $Hal_S^{\bullet}$ and $O_S^{\bullet}$ are formed in the sulphide lattice.[8]

The orientation of thiourea complexes occurs on the active centres of its surface at the interaction with the substrate. Complex particles capable of interacting with the active centres of the substrate are the link that provides the binding of sulphide to the substrate. The nature of this interaction also determines the nature of film adhesion.

In the case of cadmium sulphide deposition on quartz or glass substrates, the active centres are silanol groups (≡Si–OH), which interact with halide or hydroxyl mixed complexes. As a result of this interaction, the oxygen bridges of the Cd–O–Si type are formed.[9] This explains the good adhesion of cadmium sulphide films obtained from thiourea coordination compounds to glass substrates.

CSD technology allows to obtain of thin films by using the sample surface as a heat source. The surface tension of the solution ensures that the volume of liquid used is minimized. The combination of the heat delivery method to the surface and

a small volume of the solution leads to the high utilization of cadmium and its compounds.

Summarizing the above it can be argued that due to the several disadvantages of the described methods for obtaining compounds of the $A^{II}B^{VI}$ group, the search for more efficient, cost-effective technologies is relevant. In this aspect, the CSD method of thin semiconductor films is of considerable interest. This is indicated by numerous publications and research studies conducted by us.

The process of chemical surface deposition was carried out at room temperature by dosed application of the working solution on a pre-prepared surface of an optically homogeneous glass plate (18 mm×22 mm). The plates with the working solution were placed on a preliminarily thermostated surface to ensure uniform heating. The surface tension of the solution ensures that the volume of the reaction mixture is minimized and its retention on the substrate at the CSD method.

The film deposition occurs by heterogeneous nucleation of the compound on the substrate surface during heat transfer to the solution (Fig. 1). The heterogeneous nucleation is preferred over homogeneous fallout due to the thermal stimulation of chemical activity on a warmer growth surface. As a result, a high proportion of cadmium from the solution in the film is obtained and it depends on the substrate heteroepitaxial growth of the film. The heat outflow from the solution to the environment helps to maintain favourable conditions for the heterogeneous growth of the film over the period required for the film deposition. After heating the glass plate was taken away, and the surface was washed with a stream of distilled water and dried in air.

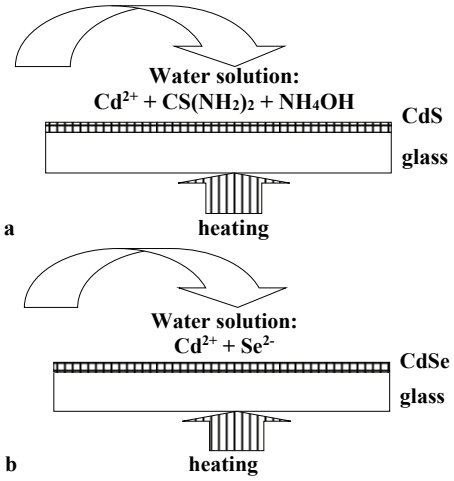

Fig. 1. The scheme of obtaining thin films (a – CdS; b – CdSe).

The freshly prepared aqueous solutions of cadmium salts were used to obtain CdS and CdSe thin films by CSD: $Cd(CH_3COO)_2$, $CdSO_4$, $CdCl_2$, $Cd(NO_3)_2$,

CdI_2. The solutions composition and the corresponding concentrations are given in Tables I and II.

TABLE I. Composition and solutions concentrations for CdS films

Salt	*c*(cadmium salt) mol/L	*c*($CS(NH_2)_2$) mol/L	*c*(NH_4OH) mol/L	Temperature °C
$Cd(CH_3COO)_2$ $CdCl_2$ CdI_2 $CdSO_4$ $Cd(NO_3)_2$	0.01–0.05	0.5–1.5	1.8	50.0–90.0

TABLE II. Composition and solutions concentrations for CdSe films

Salt	*c*(cadmium salt) mol/L	*c*(Na_2SeSO_3) mol/L	Temperature °C
$Cd(CH_3COO)_2$ $CdCl_2$ CdI_2 $CdSO_4$ $Cd(NO_3)_2$	0.01–0.05	0.1–0.4	50.0–90.0

CSD allows to obtain the films with structural, optical and electrical parameters that are not inferior to the films prepared by other methods. Also, CSD makes it possible to control film growth, maintain accurate process parameters, and dynamically change conditions to obtain homogeneous continuous films of a given thickness. This reduces the amount of waste and the volume of solutions containing cadmium ions eliminates mixing. The equipment used is affordable and does not require the use of high temperatures and pressures, which reduces energy consumption and simplifies and reduces the cost of technology.

EXPERIMENTAL

A mathematical model of the film's deposition process was developed based on the experiments for more efficiency and reduction of costs for its organization following existing techniques.[10-12]

Factors selected:

– x_1 – concentration of starting cadmium–containing salt, c_1, mol/L;
– x_2 – concentration of thiourea or sodium selenosulfate, c_2, mol/L;
– x_3 – process temperature, T, °C;
– x_4 – deposition time, t, min.

All chemicals used in the experiments were of high-purity grade (Se, $Cd(CH_3COO)_2$, $CdSO_4$, $CdCl_2$, $Cd(NO_3)_2$, CdI_2, Alfa Aesar GmbH) and of analytical grade (NH_4OH, $(NH_2)_2CS$, Na_2SO_3, Sfera Sim Ltd.) or were freshly synthesized before the experiment (Na_2SeSO_3).

Table III gives data on the factor levels and variation intervals. A planning matrix for full factorial experiment (FFE 3^{10}) was compiled for the maximum detection influence of factors

on the response function taking into account the effect of factors interaction. Since four factors are at 3 levels and we need to carry out 81 experiments, it is advisable to build a central compositional rotatable plan of the 2nd order (CCRP), see Table IV. The response function is the content of cadmium ions in the experimentally obtained thin films samples – y.

TABLE III. Factors levels and variations intervals

The factor name	Coded designation	Factors level					Variations interval
		–2	–1	0	+1	+2	
c_1 – concentration of starting cadmium-containing salt, mol/L	x_1	0.01	0.02	0.03	0.04	0.05	0.01
c_2 – concentration of thiourea, mol/L	x_2	0.50	0.75	1.00	1.25	1.50	0.25
T – temperature, °C	x_3	50	60	70	80	90	10
t – time, min	x_4	1	2	3	4	5	1

TABLE IV. Central compositional rotatable plan of the 2nd order

No.	x_0	x_1	x_2	x_3	x_4	x_1x_2	x_1x_3	x_1x_4	x_2x_3	x_2x_4	x_3x_4	x_1^2	x_2^2	x_3^2	x_4^2	y_1	y_2	y_{cp}
1	1	–1	–1	–1	–1	1	1	1	1	1	1	1	1	1	1	0.5461	0.5457	0.5459
2	1	1	–1	–1	–1	–1	–1	–1	1	1	1	1	1	1	1	1.7991	1.7985	1.7988
3	1	–1	1	–1	–1	–1	1	1	–1	–1	1	1	1	1	1	1.3801	1.3807	1.3804
4	1	1	1	–1	–1	1	–1	–1	–1	–1	1	1	1	1	1	1.8431	1.8436	1.8434
5	1	–1	–1	1	–1	1	–1	1	–1	1	–1	1	1	1	1	2.9211	2.9217	2.9214
6	1	1	–1	1	–1	–1	1	–1	–1	1	–1	1	1	1	1	4.5695	4.5705	4.5700
7	1	–1	1	1	–1	–1	–1	1	1	–1	–1	1	1	1	1	2.4828	2.4836	2.4832
8	1	1	1	1	–1	1	1	–1	1	–1	–1	1	1	1	1	2.8713	2.8723	2.8718
9	1	–1	–1	–1	1	1	1	–1	1	–1	–1	1	1	1	1	1.6245	1.6239	1.6242
10	1	1	–1	–1	1	–1	–1	1	1	–1	–1	1	1	1	1	5.2207	5.2203	5.2205
11	1	–1	1	–1	1	–1	1	–1	–1	1	–1	1	1	1	1	2.5233	2.5238	2.5236
12	1	1	1	–1	1	1	–1	1	–1	1	–1	1	1	1	1	4.5049	4.5059	4.5054
13	1	–1	–1	1	1	1	–1	–1	–1	–1	1	1	1	1	1	4.3119	4.3129	4.3124
14	1	1	–1	1	1	–1	1	1	–1	–1	1	1	1	1	1	4.6616	4.6608	4.6612
15	1	–1	1	1	1	–1	–1	–1	1	1	1	1	1	1	1	2.6176	2.6184	2.6180
16	1	1	1	1	1	1	1	1	1	1	1	1	1	1	1	3.8286	3.8294	3.8290
17	1	–2	0	0	0	0	0	0	0	0	0	4	0	0	0	0.7649	0.7639	0.7644
18	1	2	0	0	0	0	0	0	0	0	0	4	0	0	0	4.8556	4.8548	4.8552
19	1	0	–2	0	0	0	0	0	0	0	0	0	4	0	0	3.6848	3.6842	3.6845
20	1	0	2	0	0	0	0	0	0	0	0	0	4	0	0	2.3208	2.3212	2.3210
21	1	0	0	–2	0	0	0	0	0	0	0	0	0	4	0	1.1612	1.1604	1.1608
22	1	0	0	2	0	0	0	0	0	0	0	0	0	4	0	2.8301	2.8294	2.8298
23	1	0	0	0	–2	0	0	0	0	0	0	0	0	0	4	2.9131	2.9125	2.9128
24	1	0	0	0	2	0	0	0	0	0	0	0	0	0	4	2.0433	2.0443	2.0438
25	1	0	0	0	0	0	0	0	0	0	0	0	0	0	0	2.6346	2.6338	2.6342
26	1	0	0	0	0	0	0	0	0	0	0	0	0	0	0	2.6156	2.6146	2.6151
27	1	0	0	0	0	0	0	0	0	0	0	0	0	0	0	2.6065	2.6061	2.6063
28	1	0	0	0	0	0	0	0	0	0	0	0	0	0	0	2.6518	2.6528	2.6523
29	1	0	0	0	0	0	0	0	0	0	0	0	0	0	0	2.6159	2.6151	2.6155
30	1	0	0	0	0	0	0	0	0	0	0	0	0	0	0	2.6242	2.6248	2.6245
31	1	0	0	0	0	0	0	0	0	0	0	0	0	0	0	2.6471	2.6475	2.6473

The experiments were randomized in time, and each experiment, according to the planning matrix of Table IV, was repeated twice.

RESULTS AND DISCUSSION

The processing of the measurement results was carried out by the well-known methods of mathematical statistics brought to scientific research.[13–15] Each experiment was accompanied by the occurrence of errors, *i.e.*, by the reproducibility errors. Each experiment was carried out several times to assess reproducibility, so a series of parallel experiments were organized. Evaluation of the experiments' reproducibility was reduced in order to determine the dispersion of experiments' reproducibility.

Also, the randomization of experiments was carried out to eliminate systematic errors, when drawing up a plan of a matrix of the experiment. The experiments were carried out in a random sequence, which was established using a table of random numbers.

During the experiments, each of them was carried out twice, under the same conditions, in order to estimate the errors. During each experiment, the values of the averaged optimization parameters were obtained. The details are given in Supplementary material to this paper.

In order to check the adequacy and compatibility of the calculated mathematical model with the experimental results of thin film synthesis, the Fig. 2 was plotted.

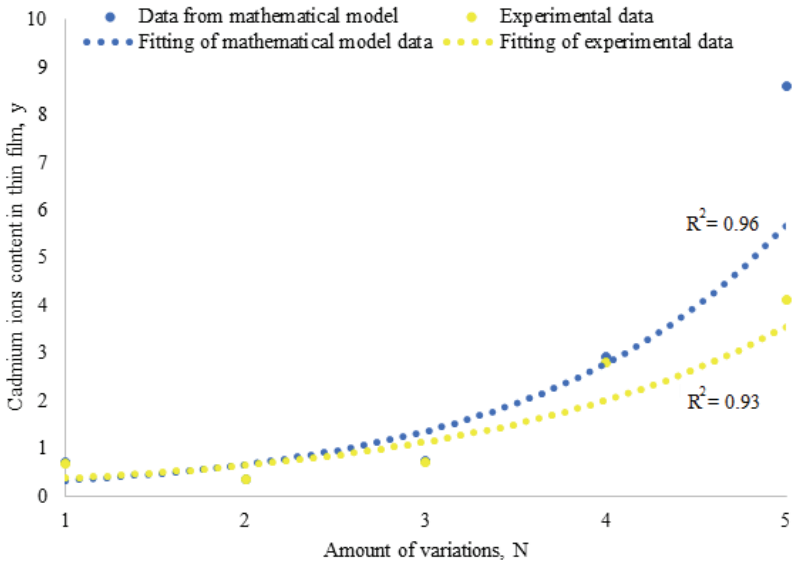

Fig. 2. Comparison of the results of mathematical modelling and experimental synthesis of thin film.

By comparing the R^2 factors of both dependencies, it is evident that the calculated mathematical model is appropriate, as the experimental data align closely with the values predicted by the model.

Based on the analysis of regression coefficients, it can be stated:

– a significant effect on the behaviour of the response function is exerted by the factor x_1 (concentration of the initial cadmium containing salt, mol/L), x_3 (process temperature, T, °C), and x_4 (deposition time, t, min), while the factor x_2 (concentration of thiourea, mol/L) does not have such a significant effect;

– numerical increase in the concentration of the initial cadmium containing salt; the process temperature and the deposition time lead to an increase in the response function and an increase in the concentration of thiourea - to its decrease.

As the regression equation shows, an increase in the 1st, 3rd and 4th factor leads to an increase in the response function, and an increase in the 2nd factor leads to its decrease.

Based on the results of experimental studies of the content of cadmium ions (Table S-II of the Supplementary material), a nomogram is constructed.[17]

It was established that the optimum conditions, selected based on the model and confirmed according to the held experiments under which films with the highest cadmium content were produced, are:

– concentration of initial cadmium-containing salt – 0.01 mol/L;
– thiourea concentration – 1 mol/L;
– sodium selenosulfate concentration – 0.1 mol/L;
– process temperature – 70 °C;
– deposition time – 3 min.[4,5,7,18–21]

CONCLUSION

The scientific basics for synthesizing CdS and CdSe semiconductor thin films from the aqueous solutions of cadmium-containing salts has been established through mathematical modelling of this process. An important scientific problem of great practical importance has been solved: the optimal conditions for the synthesis of CdS and CdSe thin films by the method of chemical surface deposition using the aqueous solutions of cadmium-containing salts: chloride, nitrate, sulphate, acetate and iodide have been determined. The influence of the nature of the initial salt, process temperature, deposition duration and the concentrations of salts, thiourea and sodium selenosulphate were studied. A mathematical model of chemical surface deposition of CdS and CdSe thin films as the effective photoconverters of solar radiation has been developed. The use of chemically deposited semiconductor materials of the $A^{II}B^{VI}$ type significantly reduces the cost and simplifies the process of creating solar cells, which can become the basis for the mass production of solar cells and solar battery modules. The adequacy of the obtained mathematical model was checked by Fisher's and Cochran's criteria. The optimal

synthesis conditions by means of the mathematical calculations were the following: the cadmium-source salt – 0.01 mol/L; the chalcogenizer – 1.0 or 0.1 mol/L in the chase of thiourea or sodium selenosulphate, respectively; the temperature – 70 °C and the duration of 3 min.

SUPPLEMENTARY MATERIAL

Additional data and information are available electronically at the pages of journal website: https://www.shd-pub.org.rs/index.php/JSCS/article/view/12637, or from the corresponding author on request.

ИЗВОД

МАТЕМАТИЧКИ ПРИСТУП МЕТОДИ СИНТЕЗЕ ПОЛУПРОВОДНИЧКИХ МАТЕРИЈАЛА ФИЛМОВА ТИПА $A^{II}B^{VI}$ ЗА ФОТООСЕТЉИВЕ СТРУКТУРЕ КОЈЕ СЕ КОРИСТЕ ЗА АЛТЕРНАТИВНУ ЕНЕРГИЈУ

RUSLANA R. GUMINILOVYCH, PAVLO Y. SHAPOVAL, MARTYN A. SOZANSKYI, VITALII Y. STADNIK и LILIYA R. DEVA

Lviv Polytechnic National University, 12, S. Bandera str., 79013 Lviv, Ukraine

Развијена је научна смерница за синтезу танких филмова CdS и CdSe методом хемијског површинског наношења (CSD), коришћењем раствора са солима које садрже кадмијум: хлорид, нитрат, сулфат, ацетат и јодид. Да би се појачала ефикасност експеримента и смањили трошкови, развијен је математички модел за CSD процес за CdS и CdSe танке филмове. Модел омогућава одређивање концентрације реагенаса, трајање и температуру CSD, који су потребни за добијање филмова одређене дебљине. Спроведена је оптимизација параметара хемијске депозиције филмастог полупроводничког материјала. На основу математичког модела, оптимални услови за синтезу су следећи: концентрација кадмијумове соли – 0,01 mol/L, халкогенизатор – 1,0 mol/L, односно 0.1 mol/L у случају тиоурее или натријум-селеносулфата; температура – 70 °C, и трајање 3 min. Узимајући у обзир грешке, предложена је математичка зависност резултата експерименталних проучавања од садржаја металних јона у танком филму соларних ћелија за ефикасну директну конверзију сунчевог зрачења у електричну енергију.

(Примљено 17. октобра, ревидирано 15. новембра 2023, прихваћено 1. јануара 2024)

REFERENCES

1. J.P. Espinós, A.I. Martín-Concepción, C. Mansilla, F. Yubero, A.R. González-Elipe, *J. Vac. Sci. Technol., A* **24**(4), 919 (https://doi.org/10.1116/1.2198868)
2. S. Ahmad, M. Ganaie, S. Islam, M. S. Khan, K. Asokan. M. Zulfequar, *Int. J. Phys. Astronomy* **2** (2014) 79 (http://ijpanet.com/journals/ijpa/Vol_2_No_2_June_2014/5.pdf)
3. J. A. Heredia-Cancino, K. J. Mendoza-Peña, H. J. Higuera-Valenzuela, M. B. Anahí Soto, R. Ochoa-Landín, S. J. Castillo, *Coatings* **12** (2022) 1691 (https://doi.org/10.3390/coatings12111691)
4. M.A. Sozanskyi, P.Y. Shapoval, R.R. Guminilovych, M.M. Laruk, Y.Y. Yatchychyn, *Pytannya khimiyi ta khimichnoyi tekhnolohiyi* **2** (2019) 39 (http://dx.doi.org/10.32434/0321-4095-2019-123-2-39-46)
5. M.A. Sozanskyi, P.Y. Shapoval, T.B. Gnativ, R.R. Guminilovych, V.E. Stadnik, M.M. Laruk, *Zhurnal nano- ta elektronnoyi fizyky* **14** (2022) 05026 (https://doi.org/10.21272/jnep.14(5).05026)

6. L. Holland, *Vacuum deposition of thin films*, Chapman & Hall, London, 1963 (https://www.biblio.com/book/vacuum-deposition-thin-films-holland-l/d/514215367)
7. P. Shapoval, R. Guminilovych, I. Yatchyshyn, *Chem. Chem. Technol*. **7** (2013) 345 (https://doi.org/10.23939/chcht07.03.345)
8. L. Maissel, R. Glang, *Handbook of Thin Film Technology*, McGraw Hill Book Company, New York, 1970 (https://studizba.com/files/show/djvu/1942-1-maysel-l--spravochnik--tehnologiya.html)
9. K.L. Chopra, *Thin Film Phenomena*, McGraw Hill Book Company, New York, 1969 (https://catalog.library.vanderbilt.edu/discovery/fulldisplay/alma991016722269703276/01VAN_INST:vanui)
10. Y.P. Adler, Y.V. Markova, Y.V. Granovskiy, *Planirovaniye eksperimenta pri poiske optimal'nykh usloviy*, Nauka, Moskow, 1976 (http://libarch.nmu.org.ua/handle/GenofondUA/66249)
11. M.A. Sozanskyi, P.Y. Shapoval, R.R. Guminilovych, V.E. Stadnik, Y.Y. Yatchyshyn, *Funct. Mater.* **27** (2020) 396 (https://doi.org/10.15407/fm27.02.396)
12. M. Solovyov, *Osnovy naukovykh doslidzhen'*, Sentr uchbovoyi literatury, Kyiv, 2007 (http://moodle.nati.org.ua/mod/resource/view.php?id=15288)
13. M. Dorozhovets′, *Opratsyuvannya rezul'tativ vymiryuvan'*, Publishing house of the Lviv Polytechnic National University, Lviv, 2007 (https://www.twirpx.com/file/416989/)
14. R. Guminilovych, P. Shapoval, I. Yatchyshyn, V. Kusnezh, H. Il'chuk, M. Sozanskiy, *Chem. Metals Alloys* **7** (2013), 345 (http://publications.lnu.edu.ua/chemetal/ejournal12/CMA0241.pdf)
15. G.S. Rozenberga, D.B. Gelashvili, *Problemy ekologicheskogo eksperimenta (planirovaniye i analiz nablyudeniy)*, Kassandra, Tol'yatti, 2008 (https://www.twirpx.link/file/1123431/)
16. M.S. Vinarskiy, M.V. Lur'ye. Planirovaniye eksperimenta v tekhnologicheskikh issledovaniyakh, Tekhnika, Kyiv, Ukraine, 1975 (https://rusneb.ru/catalog/002676_000027_IRKNB-RU_%D0%98%D0%9E%D0%93%D0%A3%D0%9D%D0%91_HOBBIT_6_%D0%92+48-000000-038773/)
17. R. Guminilovych, P. Shapoval, I. Yatchyshyn, S. Shapoval, *Chem. Chem. Technol*. **9** (2015) 287 (https://doi.org/10.23939/chcht09.03.287)
18. M. Sozanskyi, V. Stadnik, R. Chaykivska, R. Guminilovych, P. Shapoval, I. Yatchychyn, *Chem. Chem. Technol*. **11** (2017) 445 (https://doi.org/10.23939/chcht11.04.445)
19. R.R. Huminilovych, P.Y. Shapoval, Y.Y. Yatchyshyn, V.E. Stadnik, M.A. Sozanskyi, *Chem.Technol. Applic. Substances* **2** (2019) 1 (https://doi.org/10.23939/ctas2019.01.001)
20. G.A. Il'Chuk, I.V. Kurilo, V.V. Kus'Nezh, R.Y. Petrus', P.I. Shapoval, R.R. Guminilovich, M.V. Partyka, S.V. Tokarev, *Inorg. Mater*. **50** (2014) 762 (https://doi.org/10.1134/S0020168514080093)
21. A.I. Kashuba, H.A. Ilchuk, B. Andriyevsky, R.Y. Petrus, I.V. Semkiv, R.R. Guminilovych, *Mol. Crys. Liquid Cryst*. **751** (2022) 41 (https://doi.org/10.1080/15421406.2022.2073527).

Journal of the Serbian Chemical Society
JSCS@tmf.bg.ac.rs • www.shd.org.rs/JSCS
J. Serb. Chem. Soc. 89 (10) S345–S352 (2024) *Supplementary material*

SUPPLEMENTARY MATERIAL TO

Mathematical approaches to a method of semiconductor materials films synthesis type $A^{II}B^{VI}$ for photosensitive structures used in alternative energy

RUSLANA R. GUMINILOVYCH*, PAVLO Y. SHAPOVAL, MARTYN A. SOZANSKYI, VITALII Y. STADNIK and LILIYA R. DEVA

Lviv Polytechnic National University, 12, S. Bandera str., 79013 Lviv, Ukraine

J. Serb. Chem. Soc. 89 (10) (2024) 1299–1309

The deviation of the result of any experiments from the arithmetic mean indicates the variability of parallel experiments. A variance can be used to measure this variability:

$$s^2 = \frac{\sum_1^n (y_i - y_{cp})^2}{n-1}, \quad \text{(S-1)}$$

where $(n - 1)$ – the number of degrees of liberty, which is 1 less than the number of experiments.

The quadratic error is determined:

$$s = \sqrt{\frac{\sum_1^n (y_i - y_{cp})^2}{n-1}} \quad \text{(S-2)}$$

Fisher's criterion F was used to check the homogeneity of variances, which is equal to the ratio of the larger variance s^2_{max} to the smaller variance s^2_{min}:

$$F = \frac{s^2_{max}}{s^2_{min}}. \quad \text{(S-3)}$$

Further, the obtained value of F was compared with the tabular value of Fisher's criterion F_{tabl}. If the tabular value is lower than the value obtained from the experiment, then this dispersion is inhomogeneous and additional verification of the measurement results is required.

For inhomogeneous dispersions, as well as for the certainty of the dispersion homogeneity, the Cochran criterion G was used.

The results of processing experimental data are presented in Table S-I.

Fisher's criterion:

$$F = \frac{0.00000100}{0.00000016} = 6.25. \quad \text{(S-4)}$$

* Corresponding author. E-mail: saytac@ahievran.edu.tr

TABLE S-I. Determination of errors in the study of cadmium ions content

S^2_u x 10^4	0.44	57.46	0.27	4.16	214.92	3.61	0.18	0.55
$x_3x_4y_{CP}$	0.55	1.80	1.38	1.84	-2.92	-4.57	-2.48	-2.87
$x_2x_4y_{CP}$	0.55	1.80	-1.38	-1.84	2.92	4.57	-2.48	-2.87
$x_2x_3y_{CP}$	0.55	1.80	-1.38	-1.84	-2.92	-4.57	2.48	2.87
$x_1x_4y_{CP}$	0.55	-1.80	1.38	-1.84	2.92	-4.57	2.48	-2.87
$x_1x_3y_{CP}$	0.55	-1.80	1.38	-1.84	-2.92	4.57	-2.48	2.87
$x_1x_2y_{CP}$	0.55	-1.80	-1.38	1.84	2.92	-4.57	-2.48	2.87
x_4y_{CP}	-0.55	-1.80	-1.38	-1.84	-2.92	-4.57	-2.48	-2.87
x_3y_{CP}	-0.55	-1.80	-1.38	-1.84	2.92	4.57	2.48	2.87
x_2y_{CP}	-0.55	-1.80	1.38	1.84	-2.92	-4.57	2.48	2.87
x_1y_{CP}	-0.55	1.80	-1.38	1.84	-2.92	4.57	-2.48	2.87
$\Sigma x_i^2 y_{CP}$	2.18	7.20	5.52	7.37	11.69	18.28	9.93	11.49
$x_4^2y_{CP}$	0.55	1.80	1.38	1.84	2.92	4.57	2.48	2.87
$x_3^2y_{CP}$	0.55	1.80	1.38	1.84	2.92	4.57	2.48	2.87
$x_2^2y_{CP}$	0.55	1.80	1.38	1.84	2.92	4.57	2.48	2.87
$x_1^2y_{CP}$	0.55	1.80	1.38	1.84	2.92	4.57	2.48	2.87
y_{CP}	0.5459	1.7988	1.3804	1.8434	2.9214	4.57	2.4832	2.8718
x_4	2	2	2	2	2	2	2	2
x_3	60	60	60	60	80	80	80	80
x_2	0.75	0.75	1.25	1.25	0.75	0.75	1.25	1.25
x_1	0.02	0.04	0.02	0.04	0.02	0.04	0.02	0.04
№	1	2	3	4	5	6	7	8

0.03	135.96	0.02	14.36	14.14	0.77	4.80	2.99	0.67	
-1.62	-5.22	-2.52	-4.51	4.31	4.66	2.62	3.83	0.00	
-1.62	-5.22	2.52	4.51	-4.31	-4.66	2.62	3.83	0.00	
1.62	5.22	-2.52	-4.51	-4.31	-4.66	2.62	3.83	0.00	
-1.62	5.22	-2.52	4.51	-4.31	4.66	-2.62	3.83	0.00	
1.62	-5.22	2.52	-4.51	-4.31	4.66	-2.62	3.83	0.00	
1.62	-5.22	-2.52	4.51	4.31	-4.66	-2.62	3.83	0.00	
1.62	5.22	2.52	4.51	4.31	4.66	2.62	3.83	0.00	
-1.62	-5.22	-2.52	-4.51	4.31	4.66	2.62	3.83	0.00	
-1.62	-5.22	2.52	4.51	-4.31	-4.66	2.62	3.83	0.00	
-1.62	5.22	-2.52	4.51	-4.31	-4.66	-2.62	3.83	-1.53	
6.50	20.88	10.09	18.02	17.25	18.64	10.47	15.32	3.06	
1.62	5.22	2.52	4.51	4.31	4.66	2.62	3.83	0.00	
1.62	5.22	2.52	4.51	4.31	4.66	2.62	3.83	0.00	
1.62	5.22	2.52	4.51	4.31	4.66	2.62	3.83	0.00	
1.62	5.22	2.52	4.51	4.31	4.66	2.62	3.83	3.06	
1.6242	5.2205	2.5236	4.5054	4.3124	4.6612	2.618	3.829	0.7644	
4	4	4	4	4	4	4	4	3	
60	60	60	60	80	80	80	80	70	
0.75	0.75	1.25	1.25	0.75	0.75	1.25	1.25	1.00	
0.02	0.04	0.02	0.04	0.02	0.04	0.02	0.04	0.01	
9	10	11	12	13	14	15	16	17	

0.90	32.95	3.03	0.01	1.72	3.39	0.81	0.67	2.69	
0.00	0.00	0.00	0.00	0.00	0.00	0.00	0.00	0.00	
0.00	0.00	0.00	0.00	0.00	0.00	0.00	0.00	0.00	
0.00	0.00	0.00	0.00	0.00	0.00	0.00	0.00	0.00	
0.00	0.00	0.00	0.00	0.00	0.00	0.00	0.00	0.00	
0.00	0.00	0.00	0.00	0.00	0.00	0.00	0.00	0.00	
0.00	0.00	0.00	0.00	0.00	0.00	0.00	0.00	0.00	
0.00	0.00	0.00	-2.32	5.66	-5.83	4.09	0.00	0.00	
0.00	-7.37	4.64	0.00	0.00	0.00	0.00	0.00	0.00	
9.71	0.00	0.00	0.00	0.00	0.00	0.00	0.00	0.00	
19.42	14.74	9.28	4.64	11.32	11.65	8.18	0.00	0.00	
0.00	0.00	0.00	0.00	0.00	0.00	0.00	0.00	0.00	
0.00	0.00	0.00	4.64	11.32	0.00	0.00	0.00	0.00	
0.00	14.74	9.28	0.00	0.00	0.00	0.00	0.00	0.00	
19.42	0.00	0.00	0.00	0.00	0.00	0.00	0.00	0.00	
4.8552	3.6845	2.321	1.1608	2.8298	2.9128	2.0438	2.6342	2.6151	
3	3	3	3	3	1	5	3	3	
70	70	70	50	90	70	70	70	70	
1.00	0.50	1.50	1.00	1.00	1.00	1.00	1.00	1.00	
0.05	0.03	0.03	0.03	0.03	0.03	0.03	0.03	0.03	
18	19	20	21	22	23	24	25	26	

0.67	2.76	0.64	18.32	5.57
0.00	0.00	0.00	0.00	0.00
0.00	0.00	0.00	0.00	0.00
0.00	0.00	0.00	0.00	0.00
0.00	0.00	0.00	0.00	0.00
0.00	0.00	0.00	0.00	0.00
0.00	0.00	0.00	0.00	0.00
0.00	0.00	0.00	0.00	0.00
0.00	0.00	0.00	0.00	0.00
0.00	0.00	0.00	0.00	0.00
0.00	0.00	0.00	0.00	0.00
0.00	0.00	0.00	0.00	0.00
0.00	0.00	0.00	0.00	0.00
0.00	0.00	0.00	0.00	0.00
0.00	0.00	0.00	0.00	0.00
0.00	0.00	0.00	0.00	0.00
2.6063	2.6523	2.6155	2.6245	2.6473
3	3	3	3	3
70	70	70	70	70
1.00	1.00	1.00	1.00	1.00
0.03	0.03	0.03	0.03	0.03
27	28	29	30	31

The value of the Fisher criterion for the significance level 0.05 was taken from the corresponding table: $F_{tabl} = 19$.

Comparing the data obtained from the experiments and the tabular value of Fisher's criterion 6.25 <19 it can be seen that the tabular value is greater than the experimental one. But to be sure, Cochran's criterion was used:

$$G = \frac{s_{max}^2}{\sum_1^N s_i^2 \frac{0.00000100}{0.00001743}}. \tag{S-5}$$

From the corresponding table for the number of degrees of freedom $f = n - 1 = 3$ and the number of experiments $N = 31$, $G_{tabl} = 0.2113$ is taken for a significance level of 0.05.

Since the tabular value of the Cochran criterion is greater than the experimental 0.0574 < 0.2113, the homogeneity of the dispersion is confirmed.

After checking for homogeneity, the variance is averaged and the following formula is used:

$$s^2(y) = \frac{\sum_1^N \sum_1^n (y_i - y_{cp})}{N(n-1)}. \tag{S-6}$$

Therefore, the reproducibility variance is equal:

$$s^2(y) = \frac{0.00001743}{31(4-1)} = 1.8742 \cdot 10^{-7}. \quad \text{(S-7)}$$

The reliability of the results of experimental measurements of the content of cadmium ions was checked for adequacy according to the corresponding Fisher and Cochran criteria outside the confidence interval $\alpha = 0.95$.

Since the homogeneity of the variance has been confirmed, it is possible to average the variance and use the formula (S-5):

$$s^2(y) = \frac{\sum_1^N \sum_1^n (y_i - y_{cp})^2}{N(n-1)} = \frac{1.27 \cdot 10^{-11}}{31 \cdot (4-1)} = 1.36 \cdot 10^{-13} \quad \text{(S-8)}$$

Regression coefficients were determined by formulas:

$$b_0 = \frac{A}{n}\left[2\lambda^2(k+2)\sum_{u=1}^n y_u - 2\lambda c \sum_{i=1}^k \sum_{u=1}^n x_{iu}^2 y_u\right], \quad \text{(S-9)}$$

$$b_i = \frac{c}{n}\sum_{u=1}^n x_{iu} y_u \quad \text{(S-10)}$$

$$b_{ij} = \frac{c^2}{n\lambda}\sum_{u=1}^n x_{iu} x_{ju} y_u \quad \text{(S-11)}$$

$$b_u = \frac{A}{n}\left\{\begin{array}{c} c^2[(k+2)\lambda - k]\sum_{u=1}^n x_{iu}^2 y_u + \\ +c^2(I-\lambda)\sum_{i=1}^k \sum_{u=1}^n x_{iu}^2 y_u - 2\lambda c \sum_{u=1}^n y_u \end{array}\right\} \quad \text{(S-12)}$$

In these formulas, the following designations are accepted:

$c = \frac{n}{\sum_{u=1}^n x_{iu}^2}$; $\lambda = \frac{n2^k}{\left(\sum_{u=1}^n x_{iu}\right)^2}$ - for a plan whose core is a full factorial experiment; $\lambda = \frac{n2^{k-1}}{\left(\sum_{u=1}^n x_{iu}\right)^2}$ - for a plan whose core is a semi replicaton of a full factorial experiment; $A = \frac{1}{2\lambda[(k+2)\lambda - k]}$.

As can be seen from the above formulas, the influence of the plan core structure on the values of the regression coefficients is taken into account by the value of λ. If formulas (S-9) - (S-12) calculate all the values that depend on the plan structure, they can be written as:

$$b_0 = \delta_0^{/} \sum_{u=1}^n y_u - \delta_0^{//} \sum_{u=1}^n \sum_{i=1}^k x_{iu}^2 y_u \quad \text{(S-13)}$$

$$b_i = \delta_i \sum_{u=1}^n x_{iu} y_u \quad \text{(S-14)}$$

$$b_{ij} = \delta_{ij} \sum_{u=1}^n x_{iu} x_{ju} y_u \quad \text{(S-15)}$$

$$b_{ll} = \delta_u^{/} \sum_{u=1}^n x_{iu}^2 y_u + \delta_{il}^{//} \sum_{i=1}^k \sum_{u=1}^n x_{iu}^2 y_u - \delta_{ll}^{///} \sum_{u=1}^n y_u \quad \text{(S-16)}$$

The values of δ included in formulas (S-13) - (S-16) can be taken from Table S-I. The data given in the tables provide everything for the construction of rotatable plans and minimize the calculations required to obtain the regression coefficients.[16]

The following model is accepted:

$$y_i = b_0 + b_1x_1 + b_2x_2 + b_3x_3 + b_4x_4 + b_{12}x_1x_2 + b_{13}x_1x_3 + b_{14}x_1x_4 + b_{23}x_2x_3 + b_{24}x_2x_4 + b_{34}x_3x_4 + x_1^2 + x_2^2 + x_3^2 + x_4^2 \quad \text{(S-17)}$$

After calculating the regression coefficients, you can write the regression equation:

$$y = (9.00 - 0.91x_4) + (-2.13 + 0.01x_4)p + (0.10 + 0.03x_4)p^2 \quad \text{(S-18)}$$

where: $p = (-23.76 + 0.36x_3) + (13.43 - 0.13x_3)t + (-1.39 + 0.01x_3)t^2$; $t = (2.82 - 0.97x_2) + (-24.98 - 0.54x_2)x_1 + (882.14 - 214.29x_2)x_1^2$; x_1, x_2, x_3 and x_4 – coded designations from Table S-II.

TABLE S-II. Data for calculating regression coefficients in second-order rotatable planning

The plan core	b_0		b_i	b_{ij}	b_{ii}		
	δ_0'	δ_0''	δ_i	δ_{ij}	δ_{ii}'	δ_{ii}''	δ_{ii}'''
2^2	0.200000	0.100000	0.125000	0.250000	0.125000	0.018750	0.100000
2^3	0.166338	0.056791	0.073224	0.125000	0.062500	0.006889	0.056791
2^4	0.142857	0.035714	0.041667	0.062500	0.031250	0.003720	0.035714
2^{4-1}	0.150091	0.034091	0.041667	0.062500	0.031250	0.002841	0.034091
2^5	0.099982	0.019392	0.023088	0.031346	0.015666	0.001523	0.019392
2^{6-1}	0.110749	0.018738	0.023087	0.031250	0.015625	0.001217	0.018738
2^6	0.066653	0.010553	0.012499	0.015833	0.007914	0.000681	0.010553
2^{7-1}	0.070312	0.009766	0.012500	0.015625	0.007812	0.000489	0.009766
2^7	0.047611	0.006428	0.006656	0.008089	0.004044	0.000418	0.006428

The regression coefficients show how strongly the factor affects the optimization parameter and how a change in the factor will affect the change in the response function.

It is necessary to hold statistical estimates by obtaining a polynomial model. This procedure, described earlier, remains unchanged when experimenting with a rotatable plan. The difference is that the regression coefficients are determined with different variances, which are calculated using the following formulas:

$$s_{b_0}^2 = \frac{2A\lambda^2(k+2)}{n} s_y^2 \quad \text{(S-19)}$$

$$s_{b_i}^2 = \frac{c}{n} s_y^2 \quad \text{(S-20)}$$

$$s_{b_{ll}}^2 = \frac{A[(k+2)\lambda-(k-1)]c^2}{n} s_y^2 \quad \text{(S-21)}$$

$$s_{b_{il}}^2 = \frac{c^2}{n\lambda} s_y^2 \quad \text{(S-22)}$$

Formulas (S-19) - (S-22) can be rewritten as: $s_{b_0}^2 = \gamma_0 s_y^2$; $s_{b_{il}}^2 = \gamma_{il} s_y^2$; $s_{b_i}^2 = \gamma_i s_y^2$; $s_{b_{ij}}^2 = \gamma_{ij} s_y^2$.

The corresponding values of γ are summarized in Table S-III.[16]

Experimental error in rotatable planning can be determined by:

$$s_0^2 = \frac{\sum_{u=1}^{n_0}(y_{0u} - \overline{y_0})^2}{n_0 - 1} \quad \text{(S-23)}$$

The numerator of the expression (S-23) is the residual sum of squares in the centre of the plan:

$$s_0 = \sum_{u=1}^{n_0}(y_{0_u} - \overline{y_0})^2 \quad \text{(S-24)}$$

It is obvious from expression (S-23) that this sum is associated with the number of degrees of freedom $f_0 = n_0 - 1$. The total residual sum of squares of the plan:

$$s_{\text{заг}} = \sum_{u=1}^{n}(y_u - y_{u_{\text{розр}}})^2 \quad \text{(S-25)}$$

with the number of liberty degrees $f_{заг} = n - \frac{(k+2)(k+1)}{2}$.

TABLE S-III. Data for determining the variances of regression coefficients in rotatable planning of the second-order

The plan core	γ_0	γ_i	γ_{ii}	γ_{li}
2^2	0.2000	0.1250	0.2500	0.1250
2^3	0.1663	0.0732	0.1250	0.0625
2^4	0.1429	0.0417	0.0625	0.0312
2^{5-1}	0.1591	0.0417	0.0625	0.0312
2^5	0.1000	0.0231	0.03125	0.0157
2^{6-1}	0.1107	0.0231	0.03125	0.0156
2^6	0.0667	0.0125	0.0158	0.0079
2^{7-1}	0.0703	0.0125	0.0156	0.0078
2^7	0.0476	0.0067	0.0081	0.0040

The variance of the adequacy of the model is characterized by the sum

$$s_{ад} = s_{заг} - s_0 \quad \text{(S-26)}$$

with the number of liberty degrees

$$f_{ад} = n - \frac{(k+2)(k+1)}{2} - (n_0 - 1) \quad \text{(S-27)}$$

Dispersion of adequacy $s_{ад}^2 = \frac{s_{ад}}{f_{ад}}$.

The adequacy of the model is checked by Fisher's criterion:

$$F = \frac{s_{ад}^2}{s_0^2}. \quad \text{(S-28)}$$

The coefficient will be significant if its absolute value is greater than the possible error. Since it was established that all factors are significant using the above formulas, we could proceed to the analysis of research the results and the construction of a nomogram, and obtain an empirical formula.

Journal of the Serbian Chemical Society
JSCS@tmf.bg.ac.rs • www.shd.org.rs/JSCS
J. Serb. Chem. Soc. *89* (10) 1311–1321 (2024)
JSCS–5789
Original scientific paper
Published 2 November, 2024

Molecular dynamics modelling of the structural, dynamic and dielectric properties of the LiF–ethylene carbonate energy storage system at various temperatures

SANAA RABII, AYOUB LAHMIDI, SAMIR CHTITA, MHAMMED EL KOUALI, MOHAMMED TALBI and ABDELKBIR ERROUGUI*

Laboratory of Analytical and Molecular Chemistry, Faculty of Sciences Ben M'Sick, Hassan II University of Casablanca, Morocco

(Received 5 February, revised 21 March, accepted 16 June 2024)

Abstract: Lithium-ion batteries (LIBs) play a vital role in advancing the hybrid industry, especially in electric vehicles, as clean and sustainable electrochemical energy sources. However, the prevalent use of organic solvents in the liquid electrolytes of these energy storage systems raises environmental concerns. In this study, we investigated the impact of a polar aprotic solvent, ethylene carbonate (EC), on the structural, dynamic and dielectric properties of the LiF electrolyte using molecular dynamics simulations. By employing the CHARMM 36 force field, our goal was to comprehend the various physicochemical phenomena occurring in this electrolytic system across different temperatures within the saturation region. The structural properties were analyzed through the computation of the radial distribution function (*RDF*) for various pairs, while the dynamic and dielectric behaviors were elucidated by simulating the self-diffusion coefficient (D) and the dielectric constant (ε).

Keywords: molecular dynamics; energy storage; solvation phenomenon; lithium fluoride; ethylene carbonate; lithium-ion batteries.

INTRODUCTION

Energy storage is at the heart of today's challenges because it is an essential element for the evolution towards a more sustainable, reliable, and profitable energy future.[1] It modulates energy production and consumption by reducing waste and storing excess energy when available, releasing it during periods of higher demand.[2] This capability proves particularly useful in compensating for the intermittency or fluctuation of renewable energy production, thereby meeting a constant demand.[3] Various forms of energy, including thermal, chemical, mechanical and electrical energy.[4,5] Energy storage technologies are diverse and

* Corresponding author. E-mail: Abdelkbir.errougui@univh2c.ma
https://doi.org/10.2298/JSC240205061R

encompass batteries, systems such as flywheels, springs, gravity energy storage systems and pumped hydraulic storage.[6]

Rechargeable lithium-ion batteries (LIBs) stand out as one of the most versatile battery systems, exhibiting significant improvements in energy density and efficiency. They find wide applications in electronic devices, such as laptops and mobile phones, and are crucial for storing the energy required to power electric vehicles.[7–12] Furthermore, the performance of rechargeable lithium batteries is strongly influenced by the nature of the chosen electrolyte and the understanding of the different mechanisms at play within the electrolyte solution in the presence of an organic solvent. Presently, new materials utilized as cathodes or anodes necessitate solvate electrolytes to ensure the highest possible conductivity and ion mobility between electrodes.[13,14]

The objective of this study is to use the molecular dynamics approach to simulate the structural, dynamic and dielectric behavior of the LiF–ethylene carbonate (EC) system, and then understanding the effect of temperature on the solvation mechanism of Li^+ and F^- in the presence of an organic aprotic solvent namely EC widely used in lithium battery technology, it can also be used in other applications as plasticizer and precursor of vinylene carbonate, and it is present in fibers, plastics, surface coatings, and dyes.[15,16]

The present article is a continuation of our previous work focused on molecular simulations.[17–19] Literature analysis has shown that this LiF–EC energy storage system is very little studied, especially in the temperature range from 313.15 to 373.15 K, which is the subject of our simulations using the molecular dynamics approach.

COMPUTATIONAL DETAILS

The molecular dynamics (MD) simulations approach is one of the powerful and appropriate methods to study the properties of the LiF–EC energy storage system due to its precision, its ability to provide a detailed understanding of molecular interactions, its flexibility, its numerous applications, and its capacity for validation through experimentation. The GROMACS--2020-6 software package was employed to conduct radial distribution function (RDF), self-diffusion coefficient and dielectric constant calculations, allowing for the extraction of the structural, dynamic and dielectric properties of this system over a wide range of temperatures.[20,21] In this work, all simulations were performed using the CHARMM force field.[22,23]

The values of the charges and intermolecular interactions between the solvent molecules, Li^+ and F^- are described with the Lennard–Jones (LJ) parameters (Table I). The Ewald summation method was used to calculate electrostatic interactions.[24,25]

After the optimization process, the following dynamics simulation procedures are performed, NVT equilibration was executed to control the temperature for this system using Nose––Hoover thermostat.[26,27] After that, NPT equilibration was done using Parrinello–Rahman barostat[28] at 1 bar for 60 ns. All these simulations were conducted with a time-step of 1 fs.

The simulation was conducted with 803 EC solvent molecules, and the concentration of the system is 0.9 M LiF salt, corresponding to 68 Li^+ and 68 F^- in a simulation box of (5×5×5) nm^3, with temperatures ranging from 313.15 to 373.15 K.

In addition, our previous research[29,30] elaborates on the theoretical and mathematical approaches employed to analyze all properties calculated in this work.

TABLE I. Lennard–Jones and electrostatic parameters for the EC solvent[31]; O_1: oxygen of ethylene carbonate cycle, C_1: carbon of ethylene carbonate cycle, O_2: Oxygen of carbonyl group, C_2: carbone of carbonyl group

Element	q(e)	σ_{LJ} / nm	ε_{LJ} / kJ/mol
Li^+	+1.000	0.2311	0.0097
F^-	–1.000	0.2513	0.5648
O_1	–0.4684	0.3153	0.6363
C_1	0.0330	0.3875	0.2301
O_2	0.6452	0.3029	0.5021
C_2	1.0996	0.3563	0.4602
H	0.1041	0.2351	0.0920

RESULTS AND DISCUSSION

Thermodynamics and solvation properties

The structural properties of the electrolytic system involving lithium fluoride dissolved in the aprotic solvent ethylene carbonate (EC) were determined through molecular simulation. This was achieved by calculating the radial distribution function (*RDF*), which evaluates the structural behavior of various pairs: ion–ion, ion–solvent and solvent–solvent. The interatomic distance and the degree of coordination were also calculated. Table II presents the solvation's structural and thermodynamic properties for this electrolytic system at different temperatures ranging from 313.15 to 373.15 K.

TABLE II. Simulation values of thermodynamics and structural properties of LiF–EC energy storage system at various temperatures

LiF–EC system for 0.9 M	1	2	3	4	5	6	Reference
Temperature, K	313.15	323.15	333.15	343.15	353.15	373.15	–
Volume, nm^3	96.704	97.499	98.203	99.039	99.883	101.446	–
Density, 10^3 kg m^{-3}	1.244	1.234	1.225	1.215	1.204	1.186	1.320 for EC[32]
E_{kin} / 10^3 kJ mol^{-1}	27.705	28.591	29.476	30.363	31.247	33.015	–
$r_{max(Li-O2)}$ / nm	0.19	0.19	0.19	0.19	0.19	0.19	0.19[32]
Coordination number (CN_{Li-O2})	1.81	1.67	1.57	1.48	1.33	1.29	–
$r_{max(F-H)}$ / nm	0.25	0.25	0.25	0.25	0.25	0.25	–
Coordination number (CN_{F-H})	2.48	2.45	2.36	2.23	2.13	2.10	–
$r_{max(Li-F)}$ / nm	0.18	0.18	0.18	0.18	0.18	0.18	0.17[34]
Coordination number (CN_{LiF})	2.23	2.59	2.66	2.83	3.14	3.19	–
$r_{max(O2-H)}$ / nm	0.20	0.20	0.20	0.20	0.20	0.20	0.28[32]
$r_{max(O2-O2)}$ / nm	0.38	0.38	0.38	0.38	0.38	0.38	0.39[32]

Fig. 1 illustrates that the density of the LiF–EC electrolyte system decreases as the temperature increases, with values ranging between 1.244 and 1.186 g cm^{-3}. Additionally, our molecular simulation results follow the same trend observed by

Chang *et al.* for the pure aprotic solvent EC.[32] Indeed, the observed difference is mainly due to the effect of adding the LiF electrolyte, which generates mutual interactions between the aprotic polar solvent (EC) and the ions (Li^+ and F^-) present in the electrolyte solution, leading to a noticeable decrease in density. In Fig. 2, the microstructure formed by organic solvent molecules is analyzed. The *RDF*s variation as a function of the interatomic distance for O–O in ethylene carbonate exhibits multiple peaks. The first layer, situated at a distance of 0.38 nm, indicates a maximization of intramolecular dipole interactions. The intensity decreases with rising temperature due to thermal agitation.[32,35]

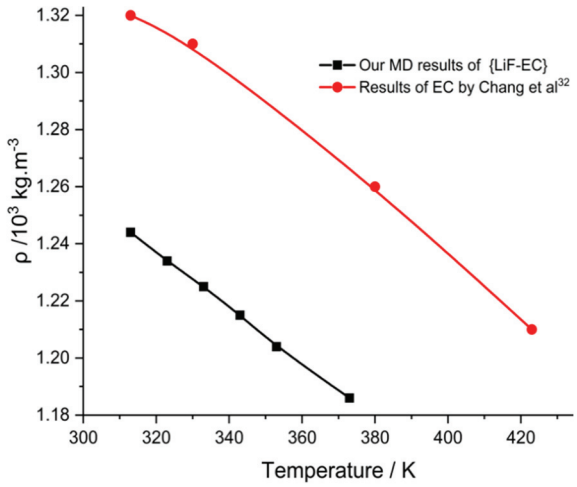

Fig. 1. Density simulations for the LiF–EC system at different temperatures.

Fig. 3 depicts the *RDF* for O_2–H. The temperature-disrupting effect is evident, showing a single peak at a distance of 0.20 nm. This interatomic distance is shorter compared to that found between O_2–O_2, suggesting that carbonyl oxygen has a preference for association with hydrogen atoms due to the attraction between O_2–H.[32,36]

Analysis of Fig. 4 reveals a prominent peak at a distance of 0.19 nm, suggesting a coordination number between 1.81 and 1.29 EC molecules around Li^+. This value is lower than those reported in classical simulations by Skarmoutsos *et al.*,[37] Smith and Borodin[38] and other theoretical studies.[39–41] Experimental studies generally indicate a coordination number of lithium between 4 and 5 in the presence of EC, with the highest value observed so far being $CN = 7$ in 1 M of $LiClO_4$ by Castriota *et al.*[42] Additionally, we found that lithium completes its coordination with F^- which compete with the oxygen of the carbonyl due to their high electronegativity. The absence of an acidic proton in the aprotic solvent, such as EC,

facilitates the penetration of fluoride. Consequently, lithium manages to complete its coordination with 5 species (2 EC molecules, and 3 F^-).

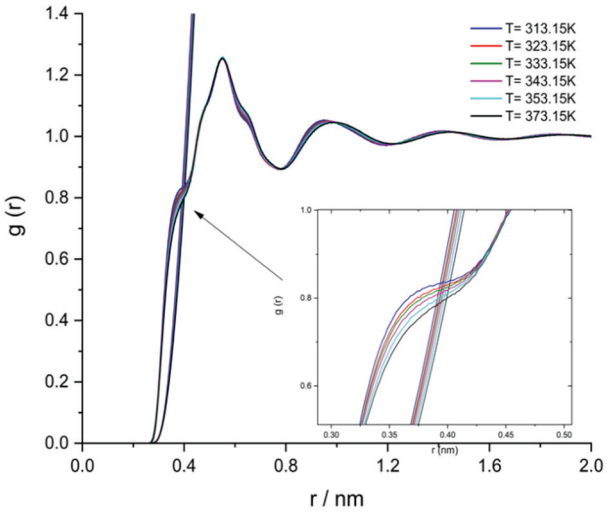

Fig. 2. Evolution of the $g_{O2\text{-}O2}(r)$ functions at different temperatures.

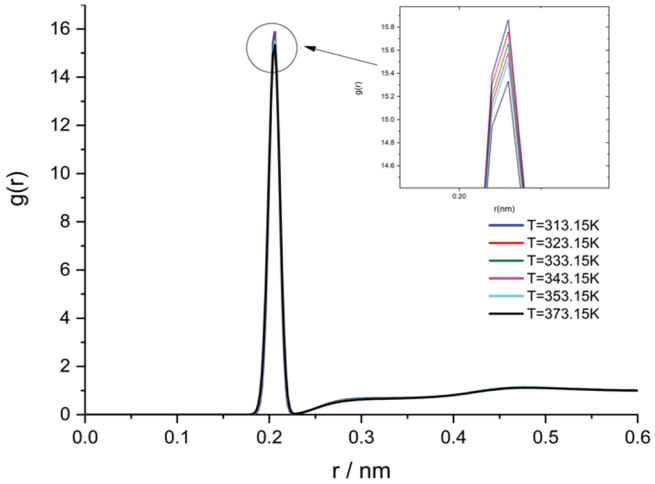

Fig. 3. Evolution of the $g_{O2\text{-}H}(r)$ functions at different temperatures.

Moreover, the distribution of F–H bonds is depicted in Fig. 5. This curve illustrates that F^- is predominantly surrounded by two hydrogen shells of EC molecules. The first shell, located at 0.25 nm, is broad and intense, resulting from the mutual polarizability of F^- and the solvent. Notably, there is no contribution to the solvation of the anions through hydrogen bonding, as the aprotic polar solvent's nature exclusively favors the solvation of Li^+. Consequently, F^- remains free and

unsolvated in the solution due to the absence of an acidic hydrogen atom. Additionally, the distribution of the F–H network undergoes significant degradation due to thermal agitation evolution, as observed by Castriota, Armand and Parker *et al.*[42–44]

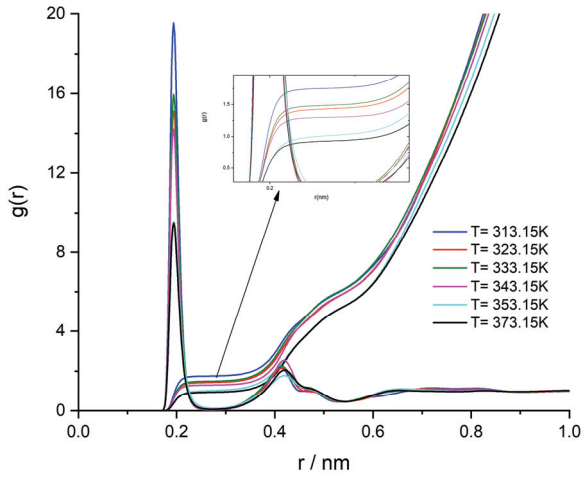

Fig. 4. Variation of the $g_{Li\text{-}O2}(r)$ functions at various temperatures.

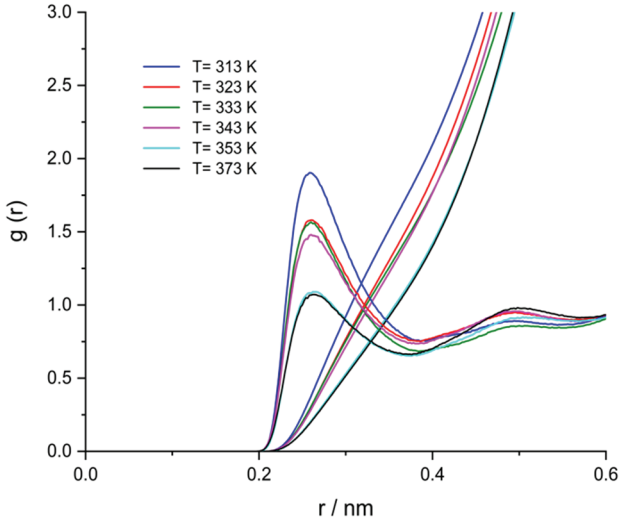

Fig. 5. Variation of the $g_{F\text{-}H}(r)$ functions at various temperatures.

The analysis of Fig. 6 reveals that the solvation process of the LiF electrolyte in the presence of an aprotic solvent primarily occurs in the form of pairs of contact ions. This process is evidently influenced by temperature evolution; specifically, an increase in temperature results in heightened intensity of *RDF* functions. This

is substantiated by the presence of a major and more intense peak at a distance of 0.18 nm, corresponding to the formation of a substantial number of contact ion pairs (CIP) in the electrolyte.[34] Consequently, this leads to the creation of successive shells formed by F^- around Li^+, attributed to the freedom of the anion and the aprotic polar behavior of the solvent, suggesting robust interactions between non-ionized ions, influenced by the solvent's polarity.

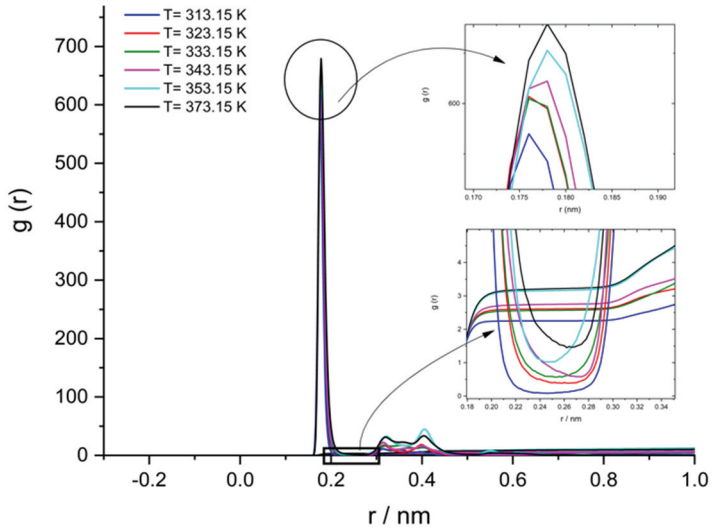

Fig. 6. Variation of the $g_{Li\text{-}F}(r)$ functions at various temperatures.

Moreover, our findings indicate that Li^+ is surrounded by 2.32 up to 3.19 F^-. This coordination variation is significantly impacted by thermal agitation, electronegativity difference in Li–F, as well as the size and charge, particularly of the fluorides.[45,46]

Dynamics and dielectric properties

In this study, we investigated the transport and dielectric properties of the electrolytic system LiF–EC at various temperatures for a concentration of 0.9 M using molecular dynamics simulations, as summarized in Table III.

TABLE III. Simulation results for the dynamical and dielectric properties of EC, Li^+ and F^- at various temperatures – the self-diffusion coefficient (10^{-9} m^2/s)

Temperature, K	DEC–LiF	DEC	DLi+	DF−	ε
313.15	0.202±0.002	0.206±0.002	0.046±0.004	0.050±0.003	59.67±0.34
323.15	0.287±0.003	0.293±0.003	0.057±0.017	0.071±0.022	54.88±0.43
333.15	0.364±0.003	0.372±0.003	0.055±0.003	0.069±0.005	56.03±0.59
343.15	0.451±0.006	0.459±0.007	0.092±0.004	0.126±0.005	58.52±0.24
353.15	0.628±0.009	0.641±0.007	0.113±0.075	0.116±0.074	61.82±0.48
373.15	0.812±0.005	0.829±0.007	0.139±0.071	0.145±0.067	57.20±0.07

The analysis of Fig. 7 illustrates that the self-diffusion coefficient increases with the evolution of the temperature. In addition, Li^+ and F^- move with almost the same speed during the simulation time, suggesting that this relative mobility is mainly due to the strong electrostatic interactions, the difference in electronegativity between the two ions ($\eta_{Li-F} = 3$), the size of the ions, and also the polar and aprotic nature of the solvent. These factors favor the formation of contact ion pairs and the reduction of ion–solvent interactions.[32,47,48]

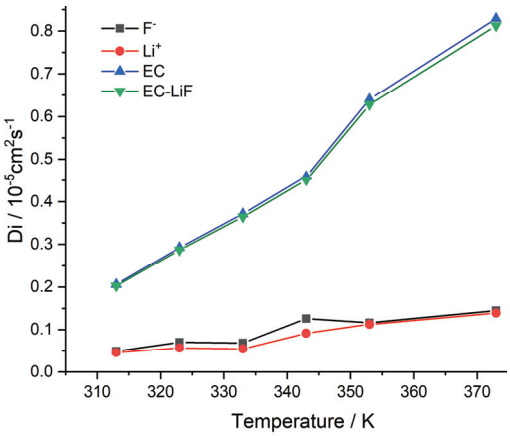

Fig. 7. Self-diffusion coefficients variation of the EC solvent, lithium and fluoride ions in the LiF–EC storage energetic system as a function of temperature.

Fig. 8 reveals that the temperature evolution influences the dielectric behavior of the electrolytic system; indeed, the dielectric constant decreases with an increase in temperature. Additionally, we observed a significant decrease in the dielectric constant of the pure solvent, dropping from 89.78 to 59.67 at $T = 313$ K.[49] This phenomenon can be explained by the disruptive effect of the LiF on the pure EC solvent. Furthermore, Parida *et al.* reported a similar behavior during the study of the energy system $LiPF_6$–EC.[33]

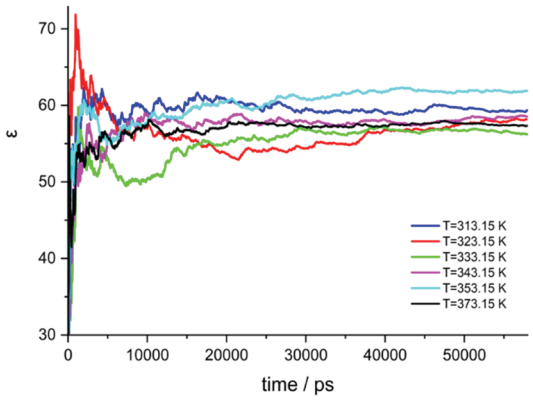

Fig. 8. Dielectric constant of the LiF–EC system at various temperatures.

CONCLUSION

In this study, we employed the molecular dynamics approach to simulate new structural, dynamic and dielectric properties of the innovative energy storage system LiF–ethylene carbonate, an electrolyte system with an ionic composition widely employed in lithium-ion battery technology. Specific algorithms were implemented based on the choice of a CHARMM force field, enabling the description of various ion–ion, ion–solvent and solvent–solvent interactions. The influence of temperature on structural behavior was assessed using the radial distribution function (*RDF*), which involved calculating the interatomic distance and coordination of various pairs within the solvation shells.

Furthermore, this scientific approach allowed us to enhance our understanding of different interactions and molecular mechanisms inherent in such an innovative energy storage system extensively used in rechargeable lithium battery technology. Temperature also plays a significant role in influencing the mobility and dielectric behavior of the current system, with its self-diffusion coefficient increasing as the temperature rises. Notably, the solvent was found to have a minimal impact on ion diffusion. The molecular simulation results obtained will offer valuable information for designing new materials and improving our comprehension of the processes governing this type of electrolytic energy storage systems.

ИЗВОД

МОДЕЛОВАЊЕ СТРУКТУРНИХ, ДИНАМИЧКИХ И ДИЕЛЕКТРИЧНИХ СВОЈСТАВА СИСТЕМА LiF–ЕТИЛЕН-КАРБОНАТ ЗА СКЛАДИШТЕЊЕ ЕНЕРГИЈЕ МОЛЕКУЛСКОМ ДИНАМИКОМ НА РАЗЛИЧИТИМ ТЕМПЕРАТУРАМА

SANAA RABII, AYOUB LAHMIDI, SAMIR CHTITA, MHAMMED EL KOUALI, MOHAMMED TALBI и ABDELKBIR ERROUGUI

Laboratory of Analytical and Molecular Chemistry, Faculty of Sciences Ben M'Sick, Hassan II University of Casablanca, Morocco

Литијум-јонске батерије играју важну улогу у развоју индустрије хибрида, посебно у случају електричних возила, као чисти и одрживи електрохемијски извори енергије. Међутим, преовлађујућа употреба органских растварача у течним електролитима ових система за складиштење енергије изазива забринутост за животну средину. У овом раду, испитиван је утицај поларног апротичног растварача, етилен-карбоната, на структурна, динамичка и диелектрична својства LiF електролита применом симулација молекулске динамике. Применом CHARMM 36 поља сила, циљ је био да се објасне различити физичкохемијски феномени који се јављају у овом електролитичком систему на различитим температурама у области засићења. Структурне особине су анализиране кроз прорачуне радијалне дистрибуционе функције за различите парове, док су динамичко и дилектрично понашање разјашњени симулацијама коефицијента самодифузије и диелектричне константе.

(Примљено 5. Фебруара, ревидирано 21. марта, прихваћено 16. јуна 2024)

REFERENCES

1. I. Hadjipaschalis, A. Poullikkas, V. Efthimiou, *Renew. Sust. Energy Rev.* **13** (2009) 1513 (https://doi.org/10.1016/j.rser.2008.09.028)

2. A. Kusko, J. Dedad, *IEEE Ind. Appl. Mag.* **13** (2007) 66 (https://doi.org/10.1109/MIA.2007.4283511)
3. T. M. I. Mahlia, T. J. Saktisahdan, A. Jannifar, M. H. Hasan, H. S. C. Matseelar, *Renew. Sust. Energy Rev.* **33** (2014) 532 (https://doi.org/10.1016/j.rser.2014.01.068)
4. H. Ibrahim, A. Ilinc, in *Energy Storage – Technologies and Applications*, A. Zobaa, Ed., InTech, Rijeka, 2013 (https://doi.org/10.5772/52220)
5. D. Lefebvre, F. H. Tezel, *Renew. Sust. Energy Rev.* **67** (2017) 116 (https://doi.org/10.1016/j.rser.2016.08.019)
6. S. Hameer, J. L. Van Niekerk, *Int. J. Energy Res.* **39** (2015) 1179 (https://doi.org/10.1002/er.3294)
7. S. Chen, C. Niu, H. Lee, Q. Li, L. Yu, W. Xu, J.-G. Zhang, E. J. Dufek, M. S. Whittingham, S. Meng, J. Xiao, J. Liu, *Joule* **3** (2019) 1094 (https://doi.org/10.1016/j.joule.2019.02.004)
8. O. Salihoglu, R. Demir-Cakan, *J. Electrochem. Soc.* **164** (2017) A2948 (https://doi.org/10.1149/2.0271713jes)
9. X.-B. Cheng, C. Yan, J.-Q. Huang, P. Li, L. Zhu, L. Zhao, Y. Zhang, W. Zhu, S.-T. Yang, Q. Zhang, *Energy Storage Mater.* **6** (2017) 18 (https://doi.org/10.1016/j.ensm.2016.09.003)
10. H. Li, *Joule* **3** (2019) 911 (https://doi.org/10.1016/j.joule.2019.03.028)
11. C. Niu, H. Lee, S. Chen, Q. Li, J. Du, W. Xu, J.-G. Zhang, M. S. Whittingham, J. Xiao, J. Liu, *Nat. Energy* **4** (2019) 551 (https://doi.org/10.1038/s41560-019-0390-6)
12. J. Y. Hwang, S. J. Park, C. S. Yoon, Y. K. Sun, *Energy Environ. Sci.* **12** (2019) 2174 (https://doi.org/10.1039/C9EE00716D)
13. A. Arslanargin, A. Powers, T. L. Beck, S. W. Rick, *J. Phys. Chem. B* **120** (2016) 1497 (https://doi.org/10.1021/acs.jpcb.5b06891)
14. X. You, M. I. Chaudhari, S. B. Rempe, L. R. Pratt, *J. Phys. Chem., B* **120** (2016) 1849 (https://doi.org/10.1021/acs.jpcb.5b09561)
15. X. Li, G. Cheruvally, J. K. Kim, J. W. Choi, J.-H. Ahn, K. W. Kim, H. J. Ahn, *J. Power Sources* **167** (2007) 491 (https://doi.org/10.1016/j.jpowsour.2007.02.032)
16. L. Long, S. Wang, M. Xiao, Y. Meng, *J. Mater. Chem., A* **4** (2016) 10038 (https://doi.org/10.1039/C6TA02621D)
17. A. Errougui, M. Talbi, M. Kouali, *J. E3S Web Conf.* **297** (2021) 01009 (https://doi.org/10.1051/e3sconf/202129701009)
18. A. Errougui, A. Lahmidi, S. Chtita, M. El Kouali, M. Talbi, *J. Solution Chem.* **52** (2023) 176 (https://doi.org/10.1007/s10953-022-01222-7)
19. A. Lahmidi, S. Rabii, S. Chtita, M. E. Kouali, M. Talbi, A. Errougui, *Chem. Phys. Impact* **8** (2024) 100400 (https://doi.org/10.1016/j.chphi.2023.100400)
20. B. Hess, C. Kutzner, D. Van Der Spoel, E. Lindahl, *J. Chem. Theory Comput.* **4** (2008) 435 (https://doi.org/10.1021/ct700301q)
21. M. J. Abraham, T. Murtola, R. Schulz, S. Páll, J. C. Smith, B. Hess, E. Lindahl, *SoftwareX* **1**–**2** (2015) 19 (https://doi.org/10.1016/j.softx.2015.06.001)
22. B. R. Brooks, C. L. Brooks, A. D. Mackerell, L. Nilsson, R. J. Petrella, B. Roux, Y. Won, G. Archontis, C. Bartels, S. Boresch, A. Caflisch, L. Caves, Q. Cui, A. R. Dinner, M. Feig, S. Fischer, J. Gao, M. Hodoscek, W. Im, K. Kuczera, T. Lazaridis, J. Ma, V. Ovchinnikov, E. Paci, R. W. Pastor, C. B. Post, J. Z. Pu, M. Schaefer, B. Tidor, R. M. Venable, H. L. Woodcock, X. Wu, W. Yang, D. M. York, M. Karplus, *J. Comput. Chem*. **30** (2009) 1545 (https://doi.org/10.1002/jcc.21287)
23. P. Bjelkmar, P. Larsson, M. A. Cuendet, B. Hess, E. Lindahl, *J. Chem. Theory Comput.* **6** (2010) 459 (https://doi.org/10.1021/ct900549r)

24. T. Darden, D. York, L. Pedersen, *J. Phys. Chem.* **98** (1993) 10089 (https://doi.org/10.1063/1.464397)
25. U. Essmann, L. Perera, M. L. Berkowitz, T. Darden, H. Lee, L. G. Pedersen, *J. Phys. Chem.* **103** (1995) 8577 (https://doi.org/10.1063/1.470117)
26. M. Parrinello, A. Rahman, *J. Appl. Phys.* **52** (1981) 7182 (https://doi.org/10.1063/1.328693)
27. S. Nosé, *Mol. Phys.* **52** (1984) 255 (https://doi.org/10.1080/00268978400101201)
28. W. G. Hoover, *Phys. Rev., A* **31** (1985) 1695 (https://doi.org/10.1103/PhysRevA.31.1695)
29. A. Errougui, M. Talbi, M. El Kouali, *Egypt. J. Chem.* **65** (2022) 1 (https://doi.org/10.21608/ejchem.2021.67302.3453)
30. A. Lahmidi, S. Rabii, A. Errougui, S. Chtita, M. E. Kouali, M. Talbi, *J. Serb. Chem. Soc.* **89** (2024) 877 (https://doi.org/10.2298/JSC231106003L)
31. D. Ward, R. Jones, J. Templeton, K. Reyes, M. Kane, *ECS Trans.* **61** (2014) 181 (https://doi.org/10.1149/06127.0181ecst)
32. T.-M. Chang, L. X. Dang, *J. Phys. Chem.* **147** (2017) 161709 (https://doi.org/10.1063/1.4991565)
33. R. Parida, S. Pahari, M. Jana, *J. Power Sources* **521** (2022) 230962 (https://doi.org/10.1016/j.jpowsour.2021.230962)
34. B. Ravikumar, M. Mynam, S. Repaka, B. Rai, *J. Mol. Liq.* **338** (2021) 116613 (https://doi.org/10.1016/j.molliq.2021.116613)
35. J.-C. Soetens, C. Millot, B. Maigret, I. Bakó, *J. Mol. Liq.* **92** (2001) 201 (https://doi.org/10.1016/S0167-7322(01)00192-1)
36. L. B. Silva, & L. C. G. Freitas, *J. Mol. Struct: Theochem* **806** (2007) 23 (https://doi.org/10.1016/j.theochem.2006.10.014)
37. I. Skarmoutsos, V. Ponnuchamy, V. Vetere, S. Mossa, *J. Phys. Chem., C* **119** (2015) 4502–4515 (https://doi.org/10.1021/jp511132c)
38. O. Borodin, G. D. Smith, *J. Phys. Chem., B* **110** (2006) 4971 (https://doi.org/10.1021/jp056249q)
39. O. Borodin, G. D. Smith, *J. Phys. Chem., B* **113** (2009) 1763 (https://doi.org/10.1021/jp809614h)
40. P. Ganesh, D. Jiang, P. R. C. Kent, *J. Phys. Chem., B* **115** (2011) 3085 (https://doi.org/10.1021/jp2003529)
41. K. Leung, C. M. Tenney, *J. Phys. Chem., C* **117** (2013) 24224 (https://doi.org/10.1021/jp408974k)
42. M. Castriota, E. Cazzanelli, I. Nicotera, L. Coppola, C. Oliviero, G. A. Ranieri, *J. Phys. Chem.* **118** (2003) 5537 (https://doi.org/10.1063/1.1528190)
43. M. Armand, P. Touzain, *Mater. Sci. Eng.* **31** (1977) 319 (https://doi.org/10.1016/0025-5416(77)90052-0)
44. A. J. Parker, *Q. Rev. Chem. Soc.* **16** (1962) 163 (https://doi.org/10.1039/QR9621600163)
45. J. Jones, M. Anouti, M. Caillon-Caravanier, P. Willmann, D. Lemordant, *Fluid Phase Equilib.* **285** (2009) 62 (https://doi.org/10.1016/j.fluid.2009.07.020)
46. S. Wang, Z. Tan, L. Sun, S. Xiao, W.Hu, H. Deng, *J. Mol. Liq.* **369** (2023) 120833 (https://doi.org/10.1016/j.molliq.2022.120833)
47. X. You, M. I. Chaudhari, S. B. Rempe, L. R. Pratt, *J. Phys. Chem., B* **120** (2016) 1849 (https://doi.org/10.1021/acs.jpcb.5b09561)
48. A. Rodriguez, S. T. Lam, M. Hu, *ACS Appl. Mater. Interfaces* **13** (2021) 55367 (https://doi.org/10.1021/acsami.1c17942)
49. R. Payne, I. E. Theodorou, *J. Phys. Chem.* **76** (1927) 2892 (https://doi.org/10.1021/j100664a019).

Journal of the Serbian Chemical Society
JSCS@tmf.bg.ac.rs • www.shd.org.rs/JSCS
J. Serb. Chem. Soc. *89* (10) 1323–1336 (2024)
JSCS–5790
Original scientific paper
Published 3 September, 2024

Electrical, optical and structural characterization of interfaces containing poly(3-alkylthiophenes) (P3ATs) and polydiphenylamine on ITO/TiO_2: Interaction between P3ATs polymeric segments and TiO_2

MAYARA MASAE KUBOTA[1], RICARDO VIGNOTO FERNANDES[2] and HENRIQUE DE SANTANA[1]*

[1]*Departamento de Química, CCE, Universidade Estadual de Londrina, Londrina, PR 86051-990, Brazil and* [2]*Departamento de Física, CCE, Universidade Estadual de Londrina, Londrina, PR 86051-990, Brazil*

(Received 25 November 2023, revised 24 January, accepted 3 March 2024)

Abstract: With the aim of studying the use of conjugated polymers poly(3--methylthiophene) (P3MT), poly(3-hexylthiophene) (P3HT) and polydiphenylamine (PDPA) in order to produce the active layer of inverted organic solar cells forming the interface with TiO_2 and also to help shed light on the optical and electronic properties applied to develop this technology, the interfaces between films containing P3MT, P3HT and PDPA on the indium tin oxide (ITO) electrode were electrochemically prepared, after chemically depositing a film of TiO_2. The systems under investigation were designated ITO/TiO_2/P3MT, ITO/TiO_2/PDPA/P3MT, ITO/TiO_2/PDPA, ITO/TiO_2/P3HT and ITO/TiO_2/PDPA/P3HT and characterized by Raman techniques (spectroscopy and microscopy), electrochemical impedance spectroscopy (EIS) and photoluminescence (PL). In this study, the aromatic, semiquinone and quinone segments in the polymer matrices of P3ATs and PDPA at these interfaces were monitored and characterized by comparison with films of their homopolymers by means of Raman spectroscopy and EIS. The Raman imaging demonstrates that the P3MT film can be incorporated into the titanium oxide crystalline lattice. The systems containing P3MT or P3HT were found to strongly interact with the TiO_2, stabilizing the P3AT radical cation segments and the presence of PDPA destabilized this interaction. These findings were complemented by the low-temperature (15 K) PL spectra, revealing a reduction in the intensity and displacement of the band associated with the radical cation emission, observed in the absence of TiO_2 in the system under investigation.

Keywords: film incorporated; interaction; Raman; EIS; organic photovoltaic cells.

* Corresponding author. E-mail: hensan@uel.br
https://doi.org/10.2298/JSC231125024K

INTRODUCTION

Over the last few decades, the attempts have been made to incorporate organic solar cells as a possible renewable, clean, sustainable and low-cost energy source.[1,2] In this context, the organic semiconductor polymers play a central role, since they exhibit a number of advantages over inorganic materials, *i.e.*, they are low-cost, lightweight and flexible.[1] However, despite the numerous advantages of these polymers, they are still not commercially available because they are still not very efficient in terms of solar energy conversion into electrical energy. For this reason, it is of key importance to study and characterize new materials to make up the photoactive lay of the device in order to improve the energy conversion rate.[1–4]

Most solar cells based on conjugated polymers are manufactured using conventional architecture, designed in layers made up of a transparent conducting substrate (ITO), a hole-transporting layer (anode), a photoactive layer containing an electron donor polymer, a photoactive layer containing an electron donor polymer and electron acceptor compound and a metal electrode with high work function to improve electron transportation (cathode). However, in this configuration some compounds such as poly(3,4-ethylenodioxithiophene) : poly(styrene sulfonate), generally used in the anode, cause instability at the interface of the photoactive layer due to ITO corrosion.[1,2] To improve the interface stability and prevent device degradation, one alternative would be to use an inverted configuration in which the ITO acts as the cathode and a high work function metal as the anode, affording greater device stability.[1–3] The use of a thin layer of TiO_2 as an electron selective layer is very effective in inverted solar cells.[2]

For the photoactive layer, the polymer mix system currently under investigation is based on P3HT and fullerene [6,6]-phenyl-C_{61}-butyric acid methyl ester (PCBM). This polymer mix boosted efficiency by up to 5 % and interfaces incorporating this material have been fairly well investigated in order to improve its properties. The use of optical and spectroscopic techniques in the structural characterization of these systems has helped to improve our understanding of the emission and charge transporting processes.[2,5–7]

The studies aimed at the structural characterization using Raman spectroscopy and EIS on systems containing PDPA, P3HT and P3MT to form the active layer on platinum and ITO and their comparison with the monomer structures have shown variations in charge transfer resistance processes and linked them to the equilibrium displacements among aromatic, radical cation and dication segments along the polymer matrix of the materials produced.[8]

With the aim of evaluating the interfaces forming the active layer and examine whether their properties are suitable for the inverted organic solar cell applications, ITO/TiO_2/P3MT, ITO/TiO_2/PDPA/P3MT, ITO/TiO_2/PDPA, ITO/TiO_2/

/P3HT and ITO/TiO_2/PDPA/P3HT systems were prepared using chemical and electrochemical techniques and characterized by Raman spectroscopy, EIS and PL.

EXPERIMENTAL

Reagents

3-hexylthiophene monomer ($C_{10}H_{16}S$), 3-methylthiophene (C_5H_6S) and diphenylamine ($(C_6H_5)_2NH$) were supplied by Sigma–Aldrich and used as received. The support electrolyte was lithium perchlorate ($LiClO_4$, 99 % pure; AcrosOrganics) and the solvent was acetonitrile (ACN, high-performance liquid chromatography (HPLC) grade, 99.5 % pure; JT Baker).

Electrochemical synthesis and cyclic voltammetry

PDPA was synthesized by cyclic voltammetry, varying the potential between 0.60 and 1.20 V in steps of 100 mV s^{-1} in a solution of 0.10 mol L^{-1} DPA in $LiClO_4$–ACN onto ITO electrodes for 50 cycles at 22 °C. The electrode incorporating the PDPA film was removed at a potential of 1.2 V and kept at ambient temperature.

P3HT and P3MT films were synthesized electrochemically by chronoamperometry, applying the potentials of 1.80 and 1.65 V to the P3HT and P3MT, respectively, in a solution of 3-hexylthiophene and 3-methylthiophene monomers at concentrations of 0.04 and 0.035 mol L^{-1} in $LiClO_4$–ACN respectively. The temperature was kept constant at 22 °C during the synthesis. The electrode with P3HT and P3MT films were removed from the solution at a potential of 1.65 or 1.80 V and kept at ambient temperature.

To prepare a layer of P3HT on the substrate/PDPA interphase, PDPA was initially synthesized on the substrate and the P3HT or P3MT films subsequently synthesized on this material under the aforementioned synthesis conditions. After the deposition on the electrodes, the films were kept at ambient temperature pending characterization after the analysis times stated herein had elapsed.

Both chronoamperometry and cyclic voltammetry were performed using a potentiostat/ /galvanostat (Autolab PGSTAT 302 N) coupled to a microcomputer running NOVA 1.8 software. The auxiliary electrode was a platinum plate of an area of 0.50 cm^2. The potentials were determined with reference to Ag/AgCl in a Luggin capillary in a 0.10 mol L^{-1} solution of lithium perchlorate in acetonitrile ($LiClO_4$–ACN).

Synthesis of TiO_2 films

The TiO_2 sol was synthesized using a method described by Hoffmann *et al.*[9] and Nazeeruddin *et al.*[10] A solution consisting of 0.39 mL NH_4OH, 0.34 mL H_2O_2, 10 mL H_2O and 0.70 g TiO_2 was dispersed in a 25 mL beaker and the gel formed was heated to 75 °C under magnetic agitation for 2 h. To increase the gel fluidity, three drops of Triton X-100 and seven drops of acetylacetone were added to the solution. The TiO_2 thin film was prepared using a painter's method on 1.2 cm^2 of Ti. It was dried at 100 for 10 min and calcined at 500 °C for 2 h. The films were then cooled to ambient temperature.

Raman spectroscopy and microscopy

Ex situ Raman spectra were obtained using a portable Raman spectrometer (Advantage532®, DeltaNu) excited at 532 nm, with a resolution of 8 cm^{-1}. DeltaNu NuSpec software and baseline resources were used to remove background fluorescence.

Raman imaging was obtained using an alpha300+ WITec® confocal Raman microscope system (excitation at 532 nm), with a ZEISS 50× lens.

Electrochemical impedance spectroscopy (EIS)

The impedance diagrams were obtained using a potentiostat (AutoLab PGSTAT 302 N) with the FRAM32 impedance module and varying the frequency from 100 kHz to 0.01 Hz. The open circuit stabilization potentials (E_{OC}) were reached when the E_{OC} remained constant (±5 mV) for 30 min, the time necessary to reach the stationary state.

Photoluminescence (PL)

PL measurements were taken in a helium closed-cycle cryostat at a temperature of 15 K. A 15 mW, 405 nm laser was used (Laserline, FDA Laser Power supply). The emissions from the sample were captured using a 5.5 cm lens and two colour filters (Schott GG435 and Edmund GG435). The detection was done by an Ocean Optics USB4000 mini-spectrometer.

RESULTS AND DISCUSSION

To monitor the polymer matrix in terms of thiophene, aromatic and quinone rings (radical cation and dication segments) were stabilized at the interfaces between the TiO_2 and P3HT or P3MT, *i.e.*, at the ITO/TiO_2/P3HT and ITO/ /TiO_2/P3MT interfaces and we obtained *ex situ* Raman spectra of these systems at different times after the electrochemical synthesis.

Fig. 1 shows the Raman spectra for the ITO/TiO_2/P3HT system obtained at different post-synthesis times. After the synthesis (Fig. 1a) we observed low intensity bands at 1373 cm^{-1} characteristic of C–C stretching of the ring and around 1450 cm^{-1} characteristic of symmetric C=C stretching of the thiophene ring.[11] As time progressed the latter band was displaced from 1450–1454 cm^{-1} and the spectrum exhibited an improved signal/noise ratio.

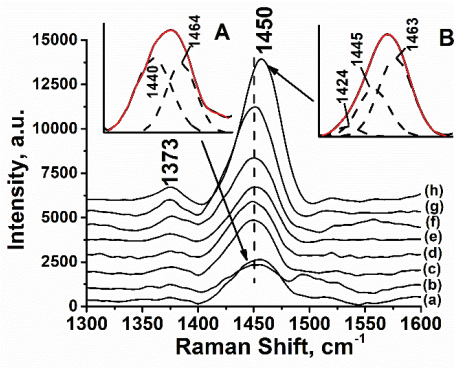

Fig. 1. Raman spectrum of the ITO/TiO_2/P3HT system. Post-synthesis times of: a) 0, b) 1, c) 5, d) 10, e) 15, f) 24, g) 30 and h) 97 h were applied at excitation radiation of 532 nm. Inset: deconvoluted Raman spectra of the ITO/TiO_2/ /P3HT system after: A) 0 and B) 97 h.

The elongated band centred at 1450 cm^{-1} is associated with the contributing radical cation, dication and aromatic segments of the thiophene ring, which coexisted in the polymer matrix of the P3HT after electrochemical synthesis.[12,13] However, this involved deconvoluting this band in order to observe the presence of each of these segments.

As shown in th inset A of Fig. 1, shortly after the synthesis of the ITO/TiO_2/ /P3HT system, the deconvolution is accompanied by bands at 1440 and 1464 cm^{-1},

respectively, associated with the dication and radical cation segments of the thiophene ring. Inset B shows that after keeping the film under ambient conditions for 97 h, the deconvolution enabled us to observe the frequencies at 1424, 1445 and 1463 cm^{-1}, respectively, related to the aromatic, dication and radical cation segments of the thiophene ring.[8] The deconvolution of the band associated with the radical cation segment was intensified by the deconvolution compared to the system shortly after synthesis.

These findings can be compared to those obtained by Kubota *et al*.,[8] in which, under the same electrochemical synthesis conditions, the deposition of P3HT on the ITO conductive substrate was observed. At this interface, the stabilization of the radical cation was not as pronounced as at the interface with TiO_2, leading us to conclude that the TiO_2 interacts more strongly with the polymer material in order to stabilize the radical cation segments of the P3HT.

To complement the results obtained using Raman spectroscopy, the impedance magnitude and the Bode-phase diagrams were plotted based on the data obtained by EIS for the ITO/TiO_2 and ITO/TiO_2/P3HT systems in 0.100 mol L^{-1} $LiClO_4$–ACN. EIS measurements were taken at an open circuit potential (OCP) and monitored at the same post-synthesis times as those applied to the Raman spectra after deposition of the film on the ITO/TiO_2 electrode. The intensity magnitude diagram is a piece of data that should be plotted together with the Bode--phase diagram to support the latter results; thus, only Bode-phase's data were commented on.

Fig. 2a and b show the impedance magnitude and the Bode-phase diagrams plotted for the ITO/TiO_2/P3HT system. The low-frequency phase maxima were observed at around 0.02, 0.04 and 0.08 Hz (Fig. 2b) and related to the charge transfer processes at the interface. In the study carried out by Kubota *et al*.,[8] EIS measurements over time showed that, at times of up to 5 h, the two phase maximum at low and high frequencies were observed and became unstable after this time had elapsed. The elongated phase maximum at high frequency was predominant, indicating the stability of the dication segment after 48 h had elapsed.

In the results obtained in the presence of TiO_2, the low-frequency phase maximum could indicate that the charge transfer by conduction is primarily polaronic. However, instability in the system was observed, mainly after 1, 10 and 24 h, with a drastic reduction in the intensity of the phase angle at ~0.02 Hz. This effect resulted in more intense phase angles at frequencies of ~0.04 and ~0.08 Hz, probably due to a drop in the contribution of radical cation segments compared to the dication segments, thus increasing the bipolaronic conduction of the material.[5] This natural deprotonation effect, involving the equilibrium between the number of radical cation and dication segments in the polymer matrix, could be considered responsible for the instability observed. However, due to the possibility of a strong interaction between TiO_2 and the P3HT system, the radical cation

segments could be primarily undergoing restabilization after a period of 30 h, as observed by the predominance of the stabilized phase maximum at low frequency (~0.02 Hz). Therefore, this result could be considered contingent on those previously obtained by the Raman spectra and that show higher intensity in the band associated with the radical cation segments on the same timescale.

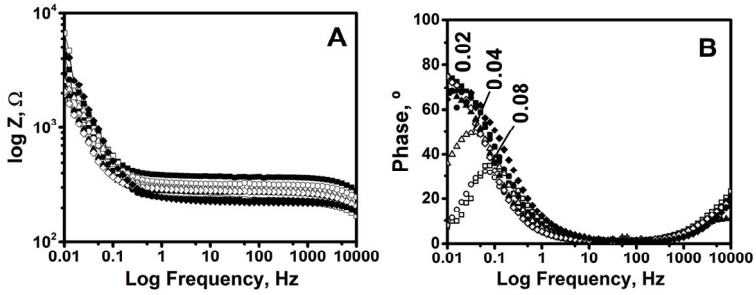

Fig. 2. a) Impedance magnitude and b) Bode-phase diagrams at open circuit potential and constant temperature of 22 °C for the ITO/TiO_2/P3HT system. Post-synthesis analysis times were: 0 (solid square), 1 (empty square), 5 (solid circle), 10 (empty circle), 15 (solid triangle), 24 (empty triangle), 30 (empty lozenge) and 97 h (solid lozenge) after electrochemical synthesis.

To confirm the results obtained previously, the diagrams of the impedance magnitude (Fig. S-1A of the Supplementary material to this paper) and the phase angle as a function of the frequency (Fig. S-1B) of the ITO/TiO_2 system were presented.

Fig. S-1B shows the Bode-phase diagram plotted for the ITO/TiO_2 system, showing the presence of a low-frequency phase maximum around 0.13 Hz and a high-frequency phase maximum around 14.70 Hz. This result indicates that the low-frequency phase maximum of TiO_2 has a strong interaction with the low-frequency phase maximum of P3MT, since in the ITO/P3MT system there are two phases, one in the low and one in the high frequency, however, in the ITO/TiO_2/ /P3MT system there is only the appearance of the low-frequency phase maximum, indicating the high amount of cation radical as seen in the data obtained by the Raman and IES techniques.

Fig. 3 shows the Raman spectra for the ITO/TiO_2/P3MT system, obtained at different time intervals. After synthesis, the Raman spectrum shows the characteristic frequencies of the P3MT thiophene ring at 1204 cm^{-1}, attributed to the C–C interring stretching, at 1335 cm^{-1} attributed to symmetric inter-ring C–C stretching, the band at 1423 cm^{-1}, generally attributed to symmetric C=C stretching of the thiophene ring and the band at 1518 cm^{-1} characteristic of asymmetric C=C stretching of the thiophene ring.[14]

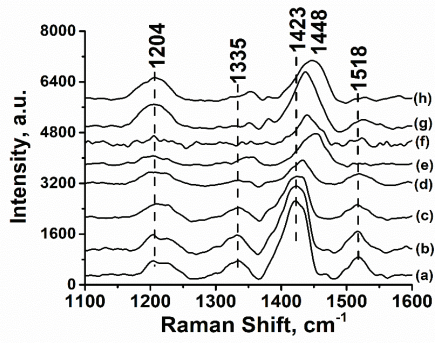

Fig. 3. Raman spectra for the ITO/TiO_2/P3MT system. Post-synthesis analysis times were: a) 0, b) 1, c) 5 d) 10, e) 15, f) 24, g) 30 and h) 97 h at excitation of 532 nm.

These results are comparable to those in De Lima *et al*.,[8] in which, under the same electrochemical synthesis conditions, P3MT deposition on ITO was investigated. After synthesis, the frequencies were observed at 1205, 1331, 1480 and 1515 cm^{-1}. Of these bands, only the band at 1480 cm^{-1}, attributed to the radical cation segment of the P3MT, was observed at 1423 cm^{-1} in the spectrum for the system containing TiO_2 at the interface with P3MT.

After 15 h, the band at 1423 cm^{-1} was shifted to 1448 cm^{-1}, quite close to that observed by De Lima *et al*.,[7] and after 15 h to 1457 cm^{-1}.

The unconventional position of the band at 1423 cm^{-1} in the spectrum obtained for the recently synthesized ITO/TiO_2/P3MT, which is usually observed at approximately 1440 cm^{-1}, could indicate that the radical cation segments of the P3MT interact more strongly with the TiO_2 than observed at the interface with the P3HT. It can also be seen that the blue coloration film of the P3MT, deposited initially on the surface of the TiO_2, underwent an alteration as time progressed and was incorporated into the TiO_2 crystalline structure.

In the spectra obtained after 15 h, the band at 1423 cm^{-1} begins to undergo a slight shift and after 97 h is positioned at 1448 cm^{-1}. Because of this strong interaction between P3MT and TiO_2 and incorporation into the TiO_2 crystalline structure, the displacement observed indicates the presence of the radical cation segment in the polymer matrix, even after 97 h.

This result shows that the TiO_2 contributes to the formation of the radical cation segment compared to previous studies,[7] where it boosts the dication segment in the P3MT polymer matrix rather than the radical cation segment.

Figs. 4a shows the impedance magnitude and Fig. 4b Bode-phase diagrams plotted for the ITO/TiO_2/P3MT system. The low-frequency phase maxima were observed at around 0.02, 0.04 and 0.06 Hz (Fig. 4b) at the analysis times. As shown previously for the system containing P3HT, there was a partial shift of the frequency at 0.02 to those at ~0.04 and ~0.06 Hz.

As shown by the Raman spectroscopy, there was a strong interaction between the P3MT and the TiO_2 as time progressed. It must be the change of the

phase angles observed, indicating that the conduction charge-transfer process is primarily polaronic.

After 15 h, the radical cation is stabilized in the P3MT polymer matrix, confirming the results previously obtained by the Raman spectra.

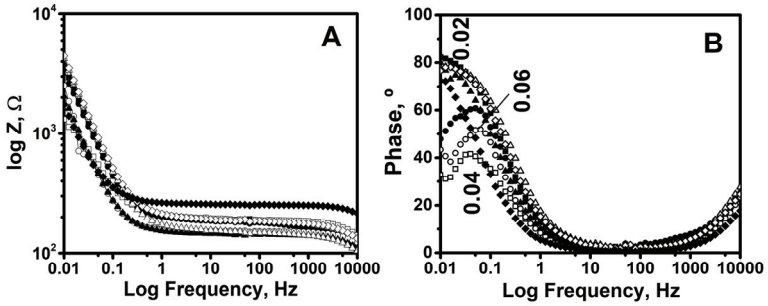

Fig. 4. a) Impedance magnitude and b) Bode-Phase diagrams at open circuit potential and constant temperature of 22 °C for the ITO/TiO_2/P3MT system. Post-synthesis analysis times were: 0 (solid square), 1 (empty square), 5 (solid circle), 10 (empty circle), 15 (solid triangle), 24 (empty triangle), 30 (empty lozenge) and 97 h (solid lozenge), after electrochemical synthesis.

Considering the need to verify the dispersion of the polymeric material on substrate surface and its incorporation into the porous structure of TiO_2, a Raman imaging was obtained from the real imaging (Fig. 5a) obtained from the confocal microscope. Filters to the TiO_2 and P3MT characteristic bands at 1448 and 1423 cm^{-1}, respectively, were used to generate a Raman imaging (Fig. 5b) of the film in the determined area (*x* and *y* axes). It was observed that regions with the accumulation of P3MT occur in the red region and in the blue region solid TiO_2 predominates. Likewise, the imaging of the thickness (*z* axis) of the ITO/TiO_2/ /P3MT system was obtained (Fig. 5c), where it was observed that the accumulation of P3MT occur in the red region and in the blue region TiO_2 predominates, demonstrate that the P3MT film can incorporate into the titanium oxide crystalline lattice, as previously discussed.

With the aim of modifying the effect of including P3ATs films, which underwent rearrangement in the TiO_2 crystalline structure after the deposition on TiO_2, these films at the ITO/TiO_2/PDPA interface were studied, given that the PDPA was previously examined as an inducer phase to promote the stabilization of the radical cation segments in the P3ATs polymer matrix.[8,13]

Fig. S-2 of the Supplementary material shows the Raman spectra for the ITO/TiO_2/PDPA system, obtained at different times. After synthesis and up to 97 h, there was a predominance of the bands characteristic of the PDPA radical cation at 1202, 1320 and 1530 cm^{-1}, respectively attributed to the C–H angular deformation, the interring C–C stretching and the C–N stretching. Similarly, the

elongated band characteristic of the aromatic ring at 1607 cm^{-1}, attributed to the C–C stretching of the PDPA aromatic ring, persisted at the analysis times.[15]

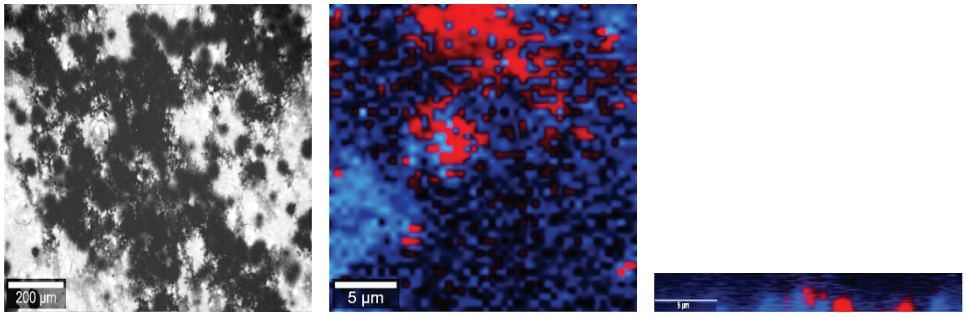

a) b) c)

Fig. 5. Raman imaging of the ITO/TiO_2/P3MT system obtained from the confocal microscopy: a) real, b) surface and c) thickness imaging. Red regions – P3MT accumulation occurs and blue region – solid TiO_2 predominates.

According to the work of De Santana *et al.*,[15] the radical cation segments exhibit an elongated absorption band between 450 and 490 nm in the UV–Vis spectra, so that the spectrum excited at 532 nm undergoes the Raman resonance intensification. Thus, the bands observed at 1202, 1320 and 1530 cm^{-1} remained intense in the spectrum. In this study, we considered the feasibility of deconvoluting the elongated band characteristic of the aromatic ring at 1607 cm^{-1} and using it to show the relative quantities of dication, aromatic and radical cation segments present in the polymer matrix.

As shown in insets A and B of Fig. S-2, the deconvolution of the elongated band at 1607 cm^{-1} in the recently-synthesized system and after 97 h exhibited the dication, the aromatic and the radical cation segments at 1590/1562–1599, 1608 and 1621–1624 cm^{-1}, respectively.[8]

These findings are comparable with those of Kubota *et al.*,[8] in which, given the same electrochemical synthesis conditions, the deposition of PDPA onto the ITO was examined. The deconvolution of the band at 1608 cm^{-1} after a period of 97 h boosted the formation of the radical cation segment, in contrast to our findings, which showed a boost in the dication segment of the film's polymer matrix, due to the presence of TiO_2 at the interface with the PDPA.

Fig. S-3 of the Supplementary materialshows the Raman spectra at different times after the electrochemical synthesis of the layered ITO/TiO_2/PDPA/P3HT system.

The spectrum after synthesis (Fig. S-3a) exhibited the bands related respectively to the PDPA radical cation and aromatic segments at 1202, 1322 and 1527 cm^{-1}, *i.e.*, 1608 cm^{-1} and an elongated, low-intensity band at 1455 cm^{-1}, characteristic of symmetric C=C stretching of the P3HT thiophene ring.

At the different post-synthesis times, the band at 1455 cm^{-1} exhibited some variations in frequency and intensity and was more intense after 97 h. In order to understand better the behaviour of this band at 1455 cm^{-1}, this region was deconvoluted. Inset A of Fig. S-3 shows that, soon after the deposition, the frequencies showed the aromatic, the dication and the radical cation segments of the thiophene ring, respectively, at 1442, 1458 and 1478 cm^{-1}, as in the work of Kubota *et al.*[8] These observed shifts could probably be explained by the strong interactions between the charged layers of the PDPA and P3HT over the TiO_2. After 97 h, the deconvolution (Fig. S-3, inset B) revealed frequencies at 1440 and 1457 cm^{-1} related to the aromatic and dication segments of the P3HT, respectively, confirming that as time progressed the dication and the aromatic segments of this system were stabilized.

Fig. S-4 of the Supplementary materialis a Bode-phase diagram for the ITO/ /TiO_2/PDPA/P3HT system, revealing the phases at low and high frequency around 0.02, 0.05 and 100 Hz, relating to charge-transfer processes at the interfaces.

In the work of Kubota *et al.*,[8] EIS on the ITO/PDPA/P3HT system showed high instability at the analysis time, with a predominance of the elongated phase at high frequencies, indicating the stability of the dication segment. In the results obtained in the presence of TiO_2 and PDPA at the interface with P3HT, the low-frequency phase maximum at ~0.02 Hz, as shown previously for the ITO/TiO_2/ /P3HT system, alternates by ~0.05 Hz. As time progressed, the interaction of the P3HT with TiO_2 changed the phase angle as observed, indicating that the polaronic conduction charge-transfer process could be in progress. However, after 15 h, we also observed a high-frequency phase at 100 Hz, indicating a tendency to stabilize the dication segment, as observed in the Raman spectra.

Fig. S-5 of the Supplementary material shows the Raman spectra at various analysis times after the electrochemical synthesis of the ITO/TiO_2/PDPA/P3MT systems, prepared by layering. A discussion of these results must include the comparison with the work of De Lima *et al.*,[7] in which deposition of P3MT onto ITO was investigated under the same electrochemical synthesis conditions. After the synthesis, the frequencies at 1204/1322 and 1526/1607 cm^{-1} were observed, related respectively to the radical cation and the aromatic segments of the PDPA and a band at 1472 cm^{-1} characteristic of P3MT thiophene ring radical cation segments.

After 10 h, the band at 1472 cm^{-1} was shifted to 1458 cm^{-1} and a similar result was observed by De Lima *et al.*,[7] although the shift was to 1457 cm^{-1}.

The band at 1472 cm^{-1} could indicate that the radical cation segments of P3MT did not strongly interact with the TiO_2, as observed in the ITO/TiO_2/P3MT system. On the other hand, this result shows that the P3MT at the interface with TiO_2 in the presence of PDPA was not favourable to the formation of the radical cation segment, as observed in a previous study by De Lima *et al.*,[7] in which the

dication segment of the P3MT polymer matrix was responsible for the band observed at 1458 cm^{-1}.

Fig. S-6 of the Supplementary material is the Bode-phase diagram for the ITO/TiO_2/PDPA/P3MT system, revealing the presence of low-frequency phase maximum around ~0.02 and ~0.05 Hz relating to the charge transfer processes at the interface.

The system as a whole exhibited high instability at the analysis time, alternating between the low-frequency phase maximum at ~0.01 Hz and the phase maximum at ~0.05 Hz, indicating a problem with stabilization of the polaronic phase in the presence of PDPA at the interface of P3MT with TiO_2. This result could also indicate a tendency to destabilize the radical cation segment in the presence of PDPA, as observed in the Raman spectra, with a predominance of spectra for bands associated with the dication.

With the aim of investigating emission associated with the radical cation segments at the polymer interface as prepared in the presence of TiO_2, photoluminescence (PL) spectra of these materials were obtained at low temperature (15 K). Next, these results were compared to the emission behaviour observed previously for P3ATs,[6] in order to confirm the results obtained by Raman spectroscopy and EIS, in which the radical cation segments present in P3ATs were observed to interact with the TiO_2.

For the Pt/P3MT system, Bento *et al*.[6] observed that the PL spectrum at 15 K exhibited a band at 476 nm and a shadow around 507 nm, attributed to the mixed chains formed by the aromatic and the quinone segments,[16] and an intense band at 680 nm, present only at low temperature, which was associated with the boosted radical cation segments in the polymer matrix at this temperature compared to the PL spectra for the Pt/P3MT system at liquid nitrogen temperature (77 K) and at 298 K.

Fig. 6 shows the PL spectra at 15 K for the ITO/TiO_2/P3MT and ITO/TiO_2/ /P3HT systems under the same conditions of excitation and recording as the PL spectra previously obtained by Bento *et al.*[6]

After the deconvolution of the elongated band obtained, the emissions were observed in the PL spectra at 491, 524 and 562 nm for the ITO/TiO_2/P3MT system and at 496, 524 and 554 nm for the ITO/TiO_2/P3HT interface. Comparing the results obtained herein for the interfaces in the presence of TiO_2 with the work of Bento *et al.*,[6] it can be inferred that the band observed at 562 nm at the TiO_2 interface with P3MT and the band at 554 nm for interfaces with P3HT could be related to the radical cation emission. This result confirms that there is an interaction between the radical cation segments of P3ATs and TiO_2, based on the drop in the intensity of the bands related to the radical cation and the shifts observed.

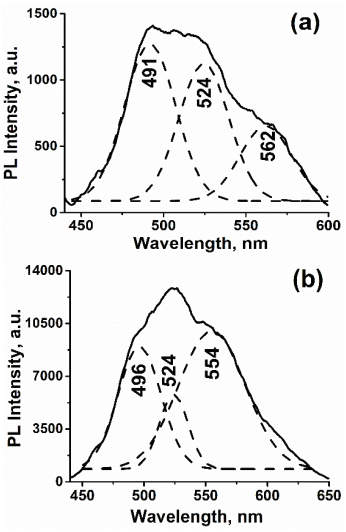

Fig. 6. PL spectra after deconvolution, obtained at a temperature of 15 K for the following systems: a) ITO/ /TiO_2/P3MT and b) ITO/TiO_2/P3HT.

CONCLUSION

In this study, we were able to observe the behaviour of the systems under investigation in the presence of TiO_2 and how the compounds involved behave over time at the synthesized interfaces. The presence of TiO_2 was found to result in a strong interaction among P3ATs, causing the radical cation segment to stabilize in the P3MT and P3HT polymer matrices P3HT, with good results at the post-synthesis analysis times.

After applying EIS and Raman spectroscopy to the systems under investigation, it was possible to monitor the segments present in these systems. The interface most favourable to the radical cation segment stabilization was the ITO/TiO_2/P3MT system. This system interacted most strongly with TiO_2 and combined with its crystalline structure, as well as producing an unprecedented result, not previously investigated. The radical cation was observed to stabilize in the polymer matrix, even after 97 h. The systems containing PDPA were observed to destabilize the interaction between the TiO_2 and P3ATs, to the detriment of radical cation segments at the active layer interface.

Comparing this result with those obtained by the confocal Raman technique, it was observed that the TiO_2, even though it is in excess in some regions on surface of the film formed after the deposition of the P3MT, it still coats it, even if in smaller quantities, therefore, the EIS measurements for the systems containing the P3ATs do not suffer interference from the TiO_2.

The PL results were in agreement with those obtained by Raman techniques and EIS, allowing us to recognize the interaction between the radical cation segments and TiO_2.

We consider the interfaces investigated herein to be the promising candidates for the formation of the active layer in inverted organic solar cells.

SUPPLEMENTARY MATERIAL

Additional data and information are available electronically at the pages of journal website: https://www.shd-pub.org.rs/index.php/JSCS/article/view/12701, or from the corresponding author on request.

Acknowledgments. We would like to express our appreciation to the Spectroscopy Laboratory (SPEC) at the PROPPG/UEL Multiuser Center. We would also like to thank the National Council for Scientific and Technological Development for its support.

ИЗВОД

ЕЛЕКТРИЧНА, ОПТИЧКА И СТРУКТУРНА КАРАКТЕРИЗАЦИЈА МЕЂУФАЗНИХ ОБЛАСТИ КОЈА САДРЖЕ ПОЛИ(3-АЛКИЛТИОФЕНЕ) (P3AT) И ПОЛИДИФЕНИЛАМИН НА ITO/TiO_2: ИНТЕРАКЦИЈА ИЗМЕЂУ ПОЛИМЕРНИХ СЕГМЕНАТА P3AT И TiO_2

MAYARA MASAE KUBOTA[1], RICARDO VIGNOTO FERNANDES[2] и HENRIQUE DE SANTANA[1]

[1]*Departamento de Química, CCE, Universidade Estadual de Londrina, Londrina, PR 86051-990, Brazil и* [2]*Departamento de Física, CCE, Universidade Estadual de Londrina, Londrina, PR 86051-990, Brazil*

У циљу испитивања могуће употребе коњугованих полимера поли(3-метилтиофена) (P3MT), поли(3-хексилтиофена) (P3HT) и полидифениламина (PDPA) за састављање активног слоја инвертованих органских соларних ћелија које формирају међуфазну област са TiO_2, а такође и да би се допринело разјашњењу која су оптичка и електронска својства активног слоја потребна за развој ове технологије, електрохемијски су направљене међуфазне области између филмова који садрже P3MT, P3HT и PDPA на индиум-калај-оксид електроди (ITO) након што је на њега хемијски исталожен филм TiO_2. Системи који су испитивани означени су као ITO/ /TiO_2/P3MT, ITO/TiO_2/PDPA//P3MT, ITO/TiO_2/PDPA, ITO/TiO_2/P3HT и ITO/TiO_2/ /PDPA/P3HT и карактерисани Рамановим техникама (спектроскопија и микроскопија), спектроскопијом електрохемијске импеданције (EIS) и фотолуминисценцијом (PL). У овој студији су ароматични, семихинонски и хинонски сегменти у полимерним матрицама P3AT и PDPA на наведеним границама фаза карактерисани помоћу Раманове спектроскопије и EIS и поређени са филмовима њихових хомополимера. Раманове технике показују да се филм P3MT може уградити у кристалну решетку TiO_2. Утврђено је да системи који садрже P3MT или P3HT остварују јаку интеракцију са TiO_2 стабилишући сегменте катјонских радикала P3AT, док присуство PDPA дестабилизује ову интеракцију. Приказани резултати, допуњени нискотемпературним (15 K) PL спектром, показали су смањење интензитета и померај траке повезане с емисијом катјонских радикала, што је запажено када у испитиваном систему није био присутан TiO_2.

(Примљено 25. новембра 2023, ревидирано 24. јануара, прихваћено 3. марта 2024)

REFERENCES

1. M. Abdallaoui, N. Sengouga, A. Chala, A. F. Meftah, A. M. Meftah, *Opt. Mater.* **105** (2020) 109916 (https://doi.org/10.1016/j.optmat.2020.109916)
2. S. K. Hau, H.-L. Yip, A. K.-Y. Jen, *Polym. Rev.* **50** (2010) 474 (https://doi.org/10.1080/15583724.2010.515764)

3. D. W. Zhao, S. T. Tan, L. Ke, P. Liu, A. K. K. Kyaw, X. W. Sun, G. Q. Lo, D. L. Kwong, *Sol. Energy Mater. Sol. Cells* **94** (2010) 985 (https://doi.org/10.1016/j.solmat.2010.02.010)
4. C. J. Brabec, *Sol. Energy Mater. Sol. Cells* **83** (2004) 273 (https://doi.org/10.1016/j.solmat.2004.02.030)
5. A. D. Batista, W. Renzi, J. L. Duarte, H. De Santana, *J. Electron. Mater.* **47** (2018) 6403 (https://doi.org/10.1007/s11664-019-07268-6)
6. D. C. Bento, E. C. R. Maia, T. N. M. Cervantes, R. V. Fernandes, E. Di Mauro, E. Laureto, M. A. T. Da Silva, J. L. Duarte, I. F. L. Dias, H. De Santana, *Synth. Met.* **162** (2012) 2433 (https://doi.org/10.1016/j.synthmet.2012.12.006)
7. J. H. C. De Lima, D. F. Valezi, A. D. Batista, D. C. Bento, H. De Santana, *J. Mater. Sci.: Mater. Electron.* **29** (2018) 6511 (https://doi.org/10.1007/s10854-018-8633-z)
8. M. M. Kubota, H. De Santana, *J. Electron. Mater.* **50** (2021) 1167 (https://doi.org/10.1007/s11664-020-08685-8)
9. M.R. Hoffmann, S.T. Martin, W.Y. Choi, D.W. Bahnemann, *Chem. Rev.* **95** (1995) 69 (https://doi.org/10.1021/cr00033a004)
10. M.K. Nazeeruddin, A. Kay, I. Rodício, R. Humphry-Baker, E. Muller, P. Liska, N. Vlachopoulos, M. Grätzel, *J. Am. Chem. Soc.* **115** (1993) 6382 (https://doi.org/10.1021/ja00067a063)
11. S. Quillard, G. Louarn, J. P. Buisson, S. Lefrant, J. Masters, A. G. MacDiarmid, *Synth. Met.* **50** (1992) 525 (https://doi.org/10.1016/0379-6779(92)90208-Z)
12. X. Feng, X. Wang, *Thin Solid Films* **519** (2011) 5700 (https://doi.org/10.1016/j.tsf.2011.03.043)
13. M. Baibarac, M. Lapkowski, A. Pron, S. Lefrant, I. Baltog, *J. Raman Spectrosc.* **29** (1998) 825 (https://doi.org/10.1002/(SICI)1097-4555(199809)29:9<825::AID-JRS309>3.0.CO;2-2)
14. G. Louarn, J. Y. Mevellec, J. P. Buisson, S. Lefrant, *Synth. Met.* **55-57** (1993) 587 (https://doi.org/10.1016/0379-6779(93)90996-A)
15. H. De Santana, M. L. A. Temperini, J. C. Rubim, *J. Electroanal. Chem.* **356** (1993) 145 (https://doi.org/10.1016/0022-0728(93)80516-K)
16. E. M. Therézio, J. L. Duarte, E. Laureto, E. Di Mauro, I. F. L. Dias, A. Marletta, H. De Santana, *J. Phys. Org. Chem.* **24** (2011) 640 (https://doi.org/10.1002/poc.1802).

Journal of the Serbian Chemical Society
JSCS@tmf.bg.ac.rs • www.shd.org.rs/JSCS
J. Serb. Chem. Soc. *89* (10) S353–S356 (2024) *Supplementary material*

SUPPLEMENTARY MATERIAL TO

Electrical, optical and structural characterization of interfaces containing poly(3-alkylthiophenes) (P3ATs) and polydiphenylamine on ITO/TiO_2: Interaction between P3ATs polymeric segments and TiO_2

MAYARA MASAE KUBOTA[1], RICARDO VIGNOTO FERNANDES[2] and HENRIQUE DE SANTANA[1]*

[1]*Departamento de Química, CCE, Universidade Estadual de Londrina, Londrina, PR 86051-990, Brazil and* [2]*Departamento de Física, CCE, Universidade Estadual de Londrina, Londrina, PR 86051-990, Brazil*

J. Serb. Chem. Soc. *89* (10) (2024) 1323–1336

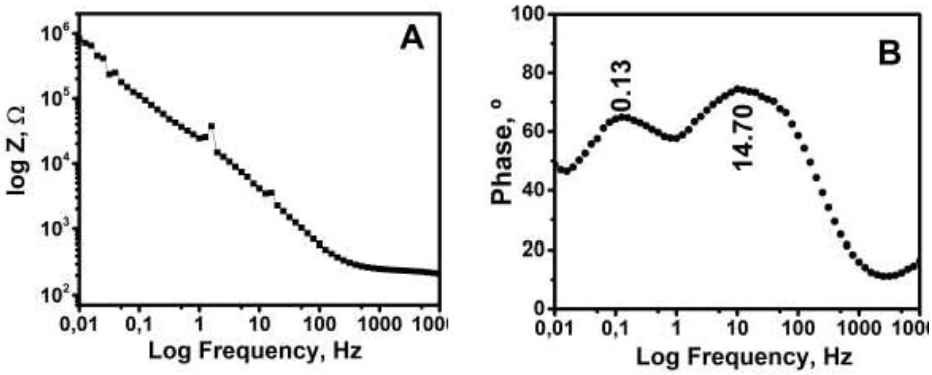

Fig. S-1. Impedance magnitude (A) and Bode-Phase (B) diagrams at open-circuit potential and constant temperature of 22 ºC for the ITO/TiO_2 system.

* Corresponding author. E-mail: hensan@uel.br

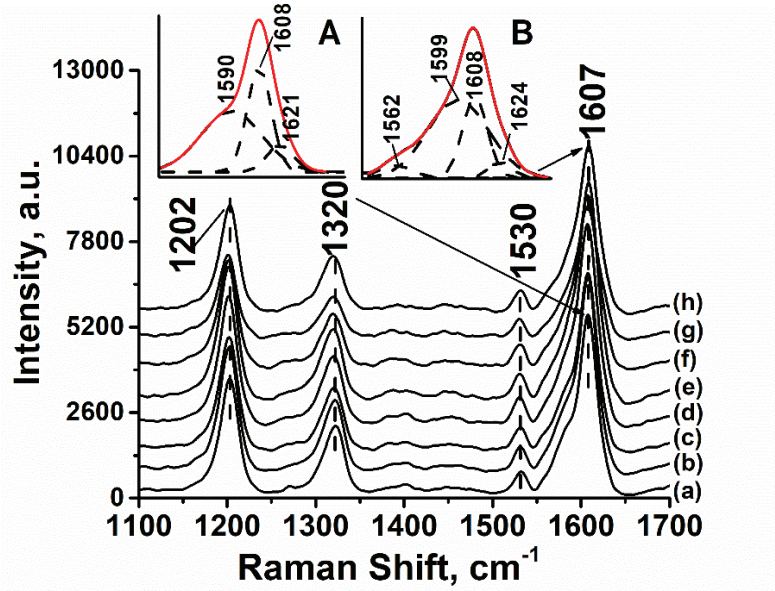

Fig. S-2. Raman spectra of the ITO/TiO_2/PDPA system. Post-synthesis analysis times were a) 0 h, b) 1 h, c)5 h, d) 10 h, e) 15 h, f) 24 h, g) 30 h and h) 97 h at excitation of 532 nm. Insert 5. Deconvoluted Raman spectra for the ITO/TiO_2/PDPA system after A) 0 h and B) 97 h.

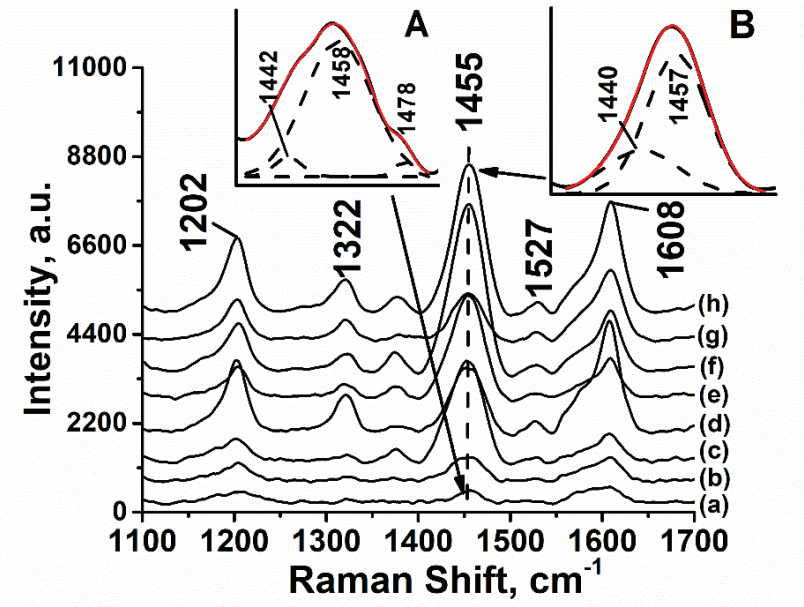

Fig. S-3. Raman spectra of the ITO/TiO_2/PDPA/P3HT system. Post-synthesis analysis times were a) 0 h, b)1 h, c) 5 h, d) 10 h, e) 15 h, f) 24 h, g) 30 h and h) 97 h, at excitation of 532 nm. Insert 6. Deconvoluted spectra for the ITO/TiO_2/PDPA/P3HT after A) 0 h and B) 97 h.

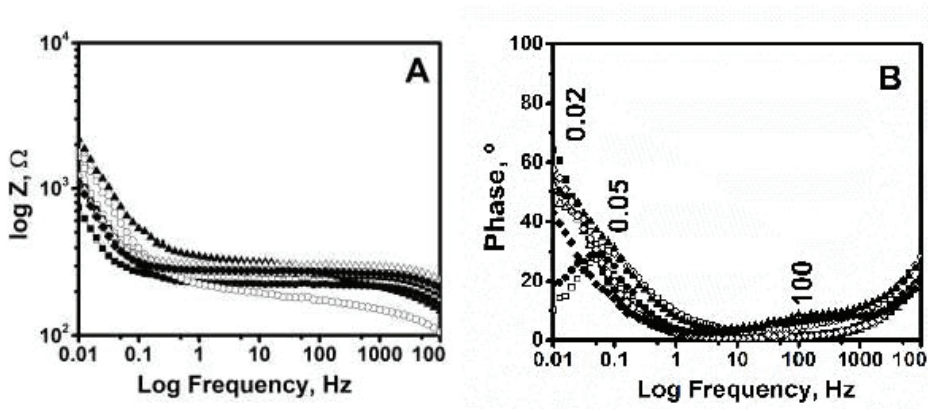

Fig. S-4. Impedance magnitude (A) and Bode-Phase (B) diagrams at open-circuit potential and constant temperature of 22 ºC for the ITO/TiO_2/PDPA/P3HT system. Post-synthesis analysis times were a) 0 h (solid square), b) 1 h (empty square), c) 5 h (solid circle), d) 10 h (empty circle), e) 15 h (solid triangle), f) 24 h (empty triangle), g) 30 h (empty lozenge) and h) 97 h (solid lozenge), after electrochemical synthesis.

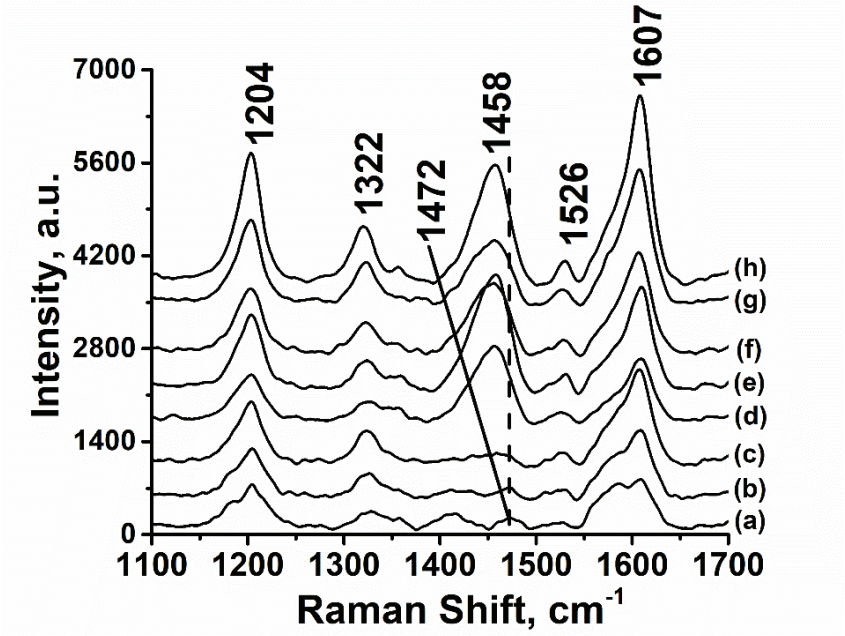

Fig. S-5. Raman spectra of the ITO/TiO_2/PDPA/P3MT system. Post-synthesis analysis times were a) 0 h, b) 1 h, c) 5 h, d) 10 h, e) 15 h, f) 24 h, g) 30 h and h) 97 h, at excitation of 532 nm.

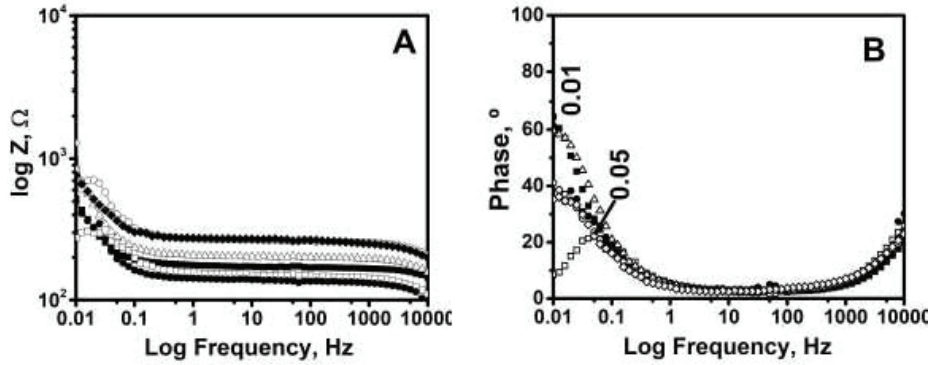

Fig. S-6. Impedance magnitude (A) and Bode-Phase (B) diagrams at open-circuit potential and constant temperature of 22 ºC for the ITO/TiO_2/PDPA/P3MT system. Post-synthesis analysis time were a) 0 h (solid square), b) 1 h (empty square), c) 5 h (solid circle), d) 10 h (empty circle), e) 15 h (solid triangle), f) 24 h (empty triangle) and g) 30 h (empty lozenge), after electrochemical synthesis.

Journal of the Serbian Chemical Society
JSCS@tmf.bg.ac.rs • www.shd.org.rs/JSCS
J. Serb. Chem. Soc. *89* (10) 1337–1351 (2024)
JSCS–5791
Original scientific paper
Published 2 November, 2024

Dispersive liquid–liquid microextraction for determining urinary muconic acid as benzene biological indicator

ABOLFAZL MOGHADASI[1,2], SAEED YOUSEFINEJAD[3]*, ESMAEEL SOLEIMANI[2]**, SAJJAD TAGHVAEI[4] and SAEED JAFAI[2]

[1]*Student Research Committee, Shiraz University of Medical Sciences, Shiraz, Iran,* [2]*Department of Occupational Health Engineering, School of Health, Shiraz University of Medical Sciences, Shiraz, Iran,* [3]*Research Center for Health Sciences, Institute of Health, Department of Occupational Health Engineering, School of Health, Shiraz University of Medical Sciences, Shiraz, Iran and* [4]*Department of Mechanical Engineering, Shiraz University, Shiraz, 71936-16548, Iran*

(Received 25 January, revised 5 April, accepted 7 July 2024)

Abstract: The monitoring of occupational exposure to chemicals is essential for assessing the workplace. In the case of hazardous and carcinogenic chemicals, such as benzene, occupational monitoring becomes even more crucial. *Trans*,*trans*-muconic acid (*t*,*t*-MA) is one of the benzene urinary metabolites. Pretreatment methods for *t*,*t*-MA generally include liquid–liquid extraction and solid–phase extraction. Using dispersive liquid–liquid microextraction (DLLME) during sample preparation and extraction can reduce extraction costs and environmental impacts. Furthermore, the process is cost-effective and easy to operate. This study is aimed to develop, optimize, and validate an analytical method for measuring *t*,*t*-MA concentration in urine matrix through DLLME combined with high-performance liquid chromatography. In this method, five variables including pH, the volume of the extractant and the disperser, salt content and the time of centrifugation were optimized using the response surface methodology with a central composite design approach and experimental data. The proposed DLLME was successfully applied to real samples of exposed workers to benzene with extraction efficiencies from 95.8 to 102.4 %. The optimum conditions were pH 8, extractant solvent, 300 µL, disperser solvent, 300 µL, salt, 3.4 % and centrifuge, 3 min. According to the result of this study, the proposed DLLME approach can be effectively applied to the biomonitoring of individuals exposed to benzene.

Keywords: biomonitoring; DLLME; HPLC; central composite design; exposure assessment.

* Corresponding authors. E-mail: (*)yousefinejad.s@gmail.com; (**)esoleimani61@gmail.com
https://doi.org/10.2298/JSC240125066M

INTRODUCTION

As part of the occupational exposure assessment, monitoring occupational exposure to chemicals is necessary.[1] It is important to consider all routes of exposure during this monitoring, including inhalation, ingestion and skin.[2] The occupational monitoring becomes more important when toxic and carcinogenic chemicals are involved, such as benzene.[3] Both the United States Environmental Protection Agency (US-EPA) and the International Agency for Research on Cancer (IARC) have confirmed that benzene is carcinogenic (a class I carcinogen).[4,5] People who have been exposed to benzene acutely may experience central nervous system depression.[6] On the other hand, long-term exposure to benzene may result in anemia, leukemia and immune system alterations.[7] Benzene is present in a wide range of petroleum products, including motor fuel and solvents, in the workplace, in the general environment and at home.[8] Furthermore, both active smokers and second-hand smokers are at risk of exposure to benzene through cigarettes.[9]

Two methods are used to monitor the occupational exposure to benzene: air monitoring and biological monitoring.[10,11] As part of air monitoring, benzene concentrations in breathing air are measured. Comparatively, biological monitoring assesses the amount of benzene entering the body via various routes such as inhalation, skin and digestion.[5,11] Through its metabolites, such as trans, trans muconic acid (*t*,*t*-MA), benzene can be eliminated from the body.[9,12] According to studies, there is a significant correlation between exposure to low levels of benzene (lower than 1 ppm) and urinary *t*,*t*-MA levels.[13] Moreover, some organizations and countries consider urinary *t*,*t*-MA as a benzene biological indicator, including the American Conference of Governmental Industrial Hygienists (ACGIH) and the Occupational Safety and Health Administration (OSHA).[14]

Liquid–liquid extraction (LLE) and solid–phase extraction (SPE) are often used as pretreatments of *t*,*t*-MA.[15,16] These treatments can lead to the separation of *t*,*t*-MA from the urine matrix, which makes its analysis easier.[17] In general, SPE is more effective than LLE.[5] However, SPE is relatively expensive and requires the preparation of columns.[18] By reducing the amount of solvent and maximizing its effectiveness, liquid–liquid microextraction (LLME) can be effectively employed to extract urinary *t*,*t*-MA.[15,19] In addition, recent research has focused on developing more efficient, environmentally friendly and miniaturized methods using microextractions.[16,20] In addition to simplifying the sample preparation and reducing the amount of solvent used, the microextraction techniques can also reduce extraction costs and the impact on the environment.[21]

Due to its high efficiency and rapidity, dispersive liquid–liquid microextraction (DLLME) would be applied for the preconcentration of aqueous samples. DLLME has been employed for the analysis of analytes such as phthalate esters, and bisphenol A.[19] When an extractant is injected and dispersed rapidly in an aqueous solution, tiny droplets of the extract disperse. This increases the contact

surface of the analyte in the sample matrix by extractant solvent. Consequently, the efficiency of extraction will be enhanced, and a large quantity of analytes can be collected rapidly. Additionally, this process is easy to operate and cost-effective.

Rismanchian *et al.* developed a partitioned dispersive liquid–liquid microextraction (PDLLME) method based on chloroform extraction for the extraction of urinary *t*,*t*-MA.[22] It consists of a two-stage procedure in which tetrahydrofuran is mixed with chloroform followed by centrifuging and drying using nitrogen flow. The metabolite is then prepared for injection into HPLC by resolving it in methanol. Despite all its advantages, this method has some limitations, such as a long extraction time, the use of solvents in relatively high amounts, and the use of tetrahydrofuran, which is highly volatile. Therefore, this study was designed to develop a dispersive liquid–liquid microextraction method that is simpler, requires fewer solvents, and uses a solvent with lower volatility.

The purpose of this study was to develop a valid method using DLLME and high-performance liquid chromatography (HPLC) for the extraction of *t*,*t*-MA from urine matrix. The biological monitoring of individuals exposed to benzene was successfully performed using the proposed method.

EXPERIMENTAL

Reagents and solutions

Hydrochloric acid (HCl, 37 %, Merck), chloroform (CHCl, Merck), *t*,*t*-MA (Sigma–Aldrich) analytical grades were used. Acetonitrile (CH_3CN) in liquid chromatography grade (Merck), methanol (CH_3OH) in gas chromatography grade (Merck), and NaCl (purity > 99 %, Sigma Aldrich) were used in the suggested microextraction/chromatographic method as well.

Purified deionized water was produced by a Direct-Q 3UV Millipore system (Molsheim, France).

Apparatus

The chromatographic analysis was carried out using an HPLC system (HPLC, Knauer, Smartline system 1000, Berlin, Germany) coupled with a UV detector (Knauer, 2000) at 274 nm. A C18 analytical column was used to separate the analyte (Knauer, Eurospher 100-5, 150 mm×4.6 mm). The utilized mobile phase was a mixed solvent containing acetic acid (1 %) and methanol with a volume ratio of 70:30 with a flow rate of 1.0 ml/min for elution. A 100 µl Hamilton syringe was used for injecting the sample into a 20 µL stainless steel injection loop. For pH measurement, a Metrohm 827 pH-meter (Metrohm, Switzerland) was used. Organic solvents were separated from sample solutions using a Hettich EBA 20 centrifuge.

Experimental design

The DLLME efficiency could be affected by a variety of factors, including solution pH, percentage of salt, the quantity of both dispersers and extractants and the centrifuge time. Analytes solubility, sample matrix surface area, and interactions between the sample matrix and the extraction could be affected by these parameters. By optimizing each parameter, the efficiency of the extraction can be maximized. Thus, determining the optimal conditions for experiments is an essential step in the extraction process. The optimisation of the extraction process parameters can be achieved through experimental design. Using an experimental design method, time is saved, efficiency is improved, parameter interactions are investigated, and errors are

reduced with fewer runs. In addition, experimental design methods can be used to optimize process parameters systematically and cost-effectively.

Central composite design (CCD) has been used to link polynomial models with experimental data utilizing response surface methodology (RSM). This approach enables researchers to identify the optimal combination of input parameters and to understand the interactions between them. RSM is an approach to modelling the relationships between a response variable and a set of predictor variables. RSM is used when there is interest in understanding how the response variable responds to changes in the predictor variables and for the response optimization. CCD is an efficient and cost-effective way to gain deeper insight into the system behaviour and to optimize the design.

A CCD with five variables and five levels was used in this study. The variables included pH (*A*), the quantity of the extractant (*B*, µL), the volume of the disperser (*C*, µL), the amount of salt (*D*, %), and the centrifugation time (*E*, min). The utilized factors and their levels are summarized in Table I.

TABLE I. The central composite design matrix and responses

Variable	Level			Star points (α = 2.0)	
	Low (–1)	Central (0)	High (+1)	$-\alpha$	$+\alpha$
Extractant solvent volume, µl	100	150	200	50	250
Disperser solvent volume, µl	200	300	400	100	500
Salt amount ,%	2	4	6	0	8
Centrifuge time, min	2	3	4	1	5
pH	4	6	8	2	10

Standard solutions and calibration curve

A stock solution of 100 ppm of *t*,*t*-MA was prepared by dissolving *t*,*t*-MA in a mixture of deionized water and methanol (1:4 volume ratio). The stock was diluted five times, then the standard solutions were prepared from the 20 ppm solution (used for spiked urine samples and calibration curve). Urine samples of non-smokers and healthy volunteers who were not occupationally exposed to benzene were used for the calibration curve. To reduce and remove coarse suspended particles and molecules, the samples were centrifuged (5000 rpm; 10 min), then filtered through a membrane (pore size = 0.45 µm) and were diluted 1:2. After finding the optimal conditions using CCD, seven urine samples were prepared and analysed in the optimum conditions for calibration curves, including non-spiked urine and six spiked samples (2, 1, 0.5, 0.1, 0.05 and 0.01 ppm).

DLLME procedure

According to the proposed extraction method, Fig. 1 illustrates the DLLME procedure schematically. To minimize the matrix effect, urine was centrifuged (10 min, 5000 rpm). 2 mL of urine was diluted 1:2 with deionized water. A stepwise addition of HCl and NaOH solution was applied to adjust the sample pH (pH 8). The urine was then injected with 300 µL of chloroform. Next, the salt concentration was adjusted by the required percentage of NaCl (3.4 %), and gently shaking the solution. Afterward, 300 µL of dispersive (acetonitrile) was added, which resulted in a cloudy solution. The cloudy solution remained stable for approximately 10 min. Finally, the cloudy solution was centrifuged at 4000 rpm for 4 min. The extracted phase was separated from the bottom of the solution using the syringe and then injected into the HPLC for further analysis.

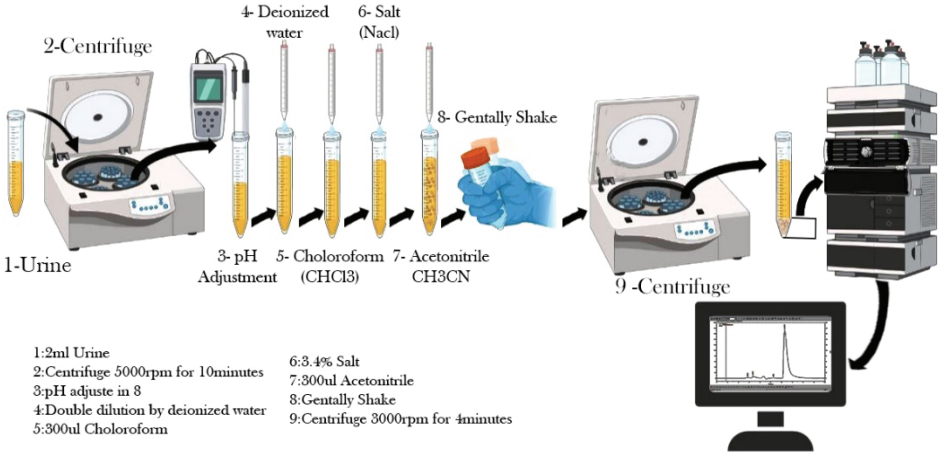

Fig. 1. Schematic procedure for the utilized DLLME technique for determination of *t*,*t*-MA.

Collection of real samples

Urine samples were collected from four occupationally exposed workers from Petrochemical company at end-of-shift. All samples were analysed within a week. The samples were stored at –20 °C before analysis. All procedures associated with the collection of urine samples and human participation conformed to the relevant regulations and the Helsinki Declaration's ethical principles. Shiraz University of Medical Sciences Ethics Committee approved this study.

RESULTS AND DISCUSSION

Selection of extraction and dispersive solvents

Two extractants including carbon tetrachloride and chloroform, and three dispersants including acetonitrile, methanol and acetone were used as potential solvents for extraction of urinary *t*,*t*-MA. Both extractants were tested with all dispersers. In addition, all possible experiments were carried out under three pH conditions: pH 2, 7 and 10. For each experiment, 2 ml of centrifuged urine was diluted 1:2 with deionized water. The urine was treated with 100 µL of extractant and a dispersive solvent. It was observed that the extractant phase was separated from the urine phase without centrifugation. Ultimately, the extractant/dispersive couple that produced the most effective extraction efficiency and the separation of the organic phase within the shortest possible time was chosen as the extraction and dispersive solvent.

In different conditions, carbon tetrachloride made two phases between 15–50 min with three dispersants. The result showed that the organic phase separation using carbon tetrachloride and acetonitrile at pH 10 was obtained at 14 min, while using carbon tetrachloride and methanol at pH 7separation time was 75 min. It is emphasized that the separation without centrifugation is possible for application in automated separation in future studies. In addition, in various conditions, the separation of organic phase from urine were observed using chloroform with three dis-

persants in times longer than 60 min. Finally, chloroform was chosen as the extractant and acetonitrile as the dispersant.

Optimization variables; RSM-CCD

As shown in Table S-I (Supplementary material to this paper), the experimental runs were ordered randomly in the CCD matrix to prevent uncontrolled variables. The CCD matrix was used to ensure that all experimental runs in the suggested DLLME were conducted in an unbiased manner. This ensured that the results of the experiment were not influenced by external factors which can be a guarantee for the application of the method. The results of the experiment were then analysed to determine the variable's effect on the peak area of the extracted *t*,*t*-MA as the outcome of model. Following the collection of responses associated with each run (Table S-I), the quadratic polynomial model was fitted based on the ANOVA analysis results. A backward elimination variable method was used to establish a reined model and to eliminate factors or interaction variables with non--significant *p*-values (> 0.1) and the final results are as follows:

$$\text{Peak Area} = 192.5428 + (1.554873A) + (0.544503B) + (-5.74414C) + \\ + (-73.9784\times\text{D}) + (-232.203E) + (-0.00577AB) + (-0.08685-) + \\ (0.532968\times\text{B}\times\text{E}) + (2.733038CD) + (10.83993CE) + (20.52228DE) \quad (1)$$

To confirm the capability of the obtained linear regression model (MLR), Fisher's statistical test (F-test) was employed. In the model (Eq. (1)), the *F*-value (41.17) was higher than the critical *F*-value in the required degree of freedom, which shows its significance. The results of the Fisher's statistical test indicated that the multiple linear regression model was statistically significant. Therefore, the model can be used to predict the outcome of the experiment.

To confirm the validity of MLR models obtained for this suggested DLLME, a non-significant lack of fit (*LOF*) is another critical criterion to consider. According to the current model, the *F*-value of *LOF* was 0.4875, indicating that it was not significant. Moreover, it indicates that the proposed MLR is free of pure errors. The squared regression coefficients of MLR model were calculated for the evaluation of overall fitness and predictive ability, such as the calibration R^2 (R^2_{cal}), adjusted R^2 (R^2_{adj}) and prediction R^2 (R^2_{pred}). This showed that the model was able to accurately predict the peak area of *t*,*t*-MA after applying the microextraction based on the given inputs.

As can be seen in Tables II and S-II of the Supplementary material, R^2_{cal} demonstrates the proposed CCD model successfully models 92.8 % of the data. Its goodness of fit was confirmed by an R^2_{adj} that was greater than 0.8. The R^2_{pred} (0.807) and the R^2_{adj} (0.894) were consistent. An indication that the prediction ability is very good is the closeness between R^2_{pred} and R^2_{adj} with a difference of less than 0.2.[23] The degree of precision is another statistic used to measure signal-

-to-noise (*S*/*N*). A precision greater than 4 is considered acceptable and based on Tables II and S-II, a signal-to-noise ratio of 18.54 is considered appropriate.[19]

TABLE II. Analysis of variance (ANOVA), summary statistics of the quadratic model – statistical parameters of the MLR model, in the current microextraction study

Std. Dev.	6.723	R^2	0.970
Mean	45.068	R^2_{adi}	0.946
C.V., %	14.917	R^2_{pred}	0.831
PRESS	3570.196	Adeq. Precision	22.585

It is evident from all the above metrics that the factors and interactions included in the suggested MLR model are sufficiently correlated. The peak area is used as the response value of the *t*,*t*-MA recovery derived from DLLME. Based on the plot in Fig. 2a, it can be seen that the predicted peak area is in good agreement with the experimental peak area values, which indicates the ability of the proposed model to make accurate predictions. Using the residual value (the difference between actual and predicted response) is a criterion for determining the applicability domain of an MLR. A narrow range for the studentized residual of the outcome model is shown in Fig. 2b, demonstrating its reliability.[24] Furthermore, all residual values are scattered randomly on either side of the zero line, indicating that there has been no systematic error.[25]

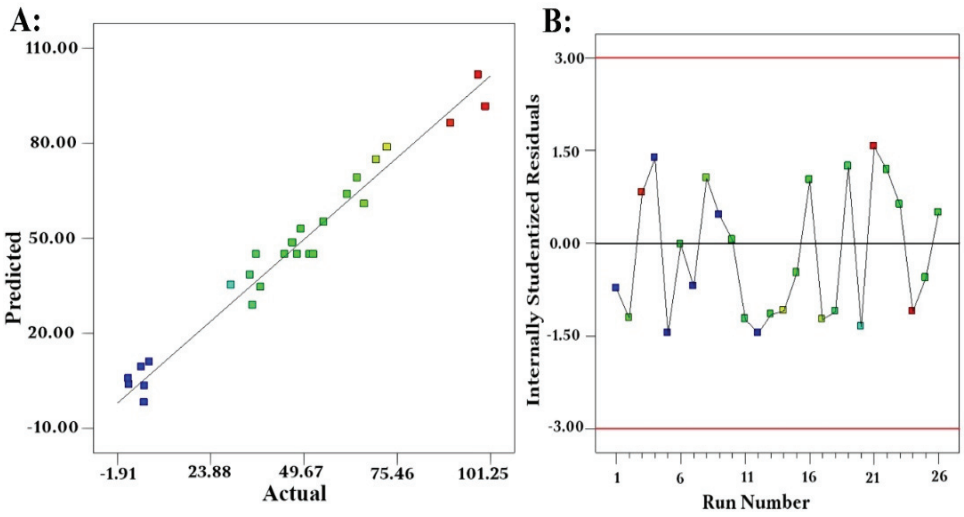

Fig. 2. The internally studentized residuals *vs*. the performed runs (A); and the predicted value vs. actual response (B).

MLR model includes some interaction terms, such as the interaction between *AC*, *AE*, *CD* and *CE*, as shown in Eq. (1). Three-dimensional (3D) response surface plots have been used to describe the mixed effects of factors in between-factors-

-interaction terms and to determine optimal values for the independent parameters in the suggested DLLME. Additionally, these curves are useful in identifying possible interactions between two independent variables to provide information about the maximum responses.

In Fig. 3A, it is demonstrated that the matrix pH and the disperser volume simultaneously affect the response (peak area of *t*,*t*-MA). pH plays an important role in all extraction techniques involving basic or acidic analytes. Several experiments were conducted to investigate the effect of pH on *t*,*t*-MA extraction from the sample solutions (Table III). As can be seen in Fig. 3a, the maximum response was observed by increasing the pH and volume of the disperser solvent. It is therefore necessary to increase the pH of the sample to achieve the highest extraction rate. The maximum response was observed at pH 6.

Fig. 3B illustrates the effect of different amounts of dispersive and extraction on the extraction of *t*,*t*-MA. To determine whether the quantity of disperser affects the response level, a variety of examinations were designed, using the acetonitrile volumes ranging from 100 to 500 μL(Table II). The maximum response (peak area) was achieved when acetonitrile value was increased. Various tests have been conducted with various quantities of chloroform ranging from 50 to 250 μL to determine the impact of the volume of extractant solvent (Table II). As a result of these tests, which can be seen in Fig. 3B, increasing both dispersing and extractant solvents provided increasing the *t*,*t*-MA peak area.

Based on the variations in salt versus pH (Fig. 3C), it appears that increasing pH led to increase in the efficiency of the suggested DLLME and consequently increased *t*,*t*-MA peak area. However, the increasing salt percentage has no significant effect on the analyte signal when compared with pH.

Fig. 3D shows the interaction between centrifuge time and extractant solvent volume. Assuming that the metabolite concentration, the salt amount, and the volume of dispersive solvent were constant, increasing the extractant solvent needs a decrease in the centrifuge time to reach an enhancement in the peak area of metabolite. In other word, by the addition of extractant solvent, increasing the centrifuge time showed negative effect on the extraction efficiency (Fig. 3D).

As shown in Fig. 3E, increasing the centrifugation time can decrease the microextraction efficiency in higher amount of salt. Thus, it can be suggested that simultaneously increasing the salt amount and centrifugation time has a negative effect on the peak area.

The change in the peak area in different amounts of pH and centrifugation time is represented in Fig. 3F. In lower pH values, increasing the centrifuge time can decrease the peak areas of the metabolite and microextraction efficiency. On the other hand, at higher values of pH, increasing centrifuge time can lead to higher peak areas.

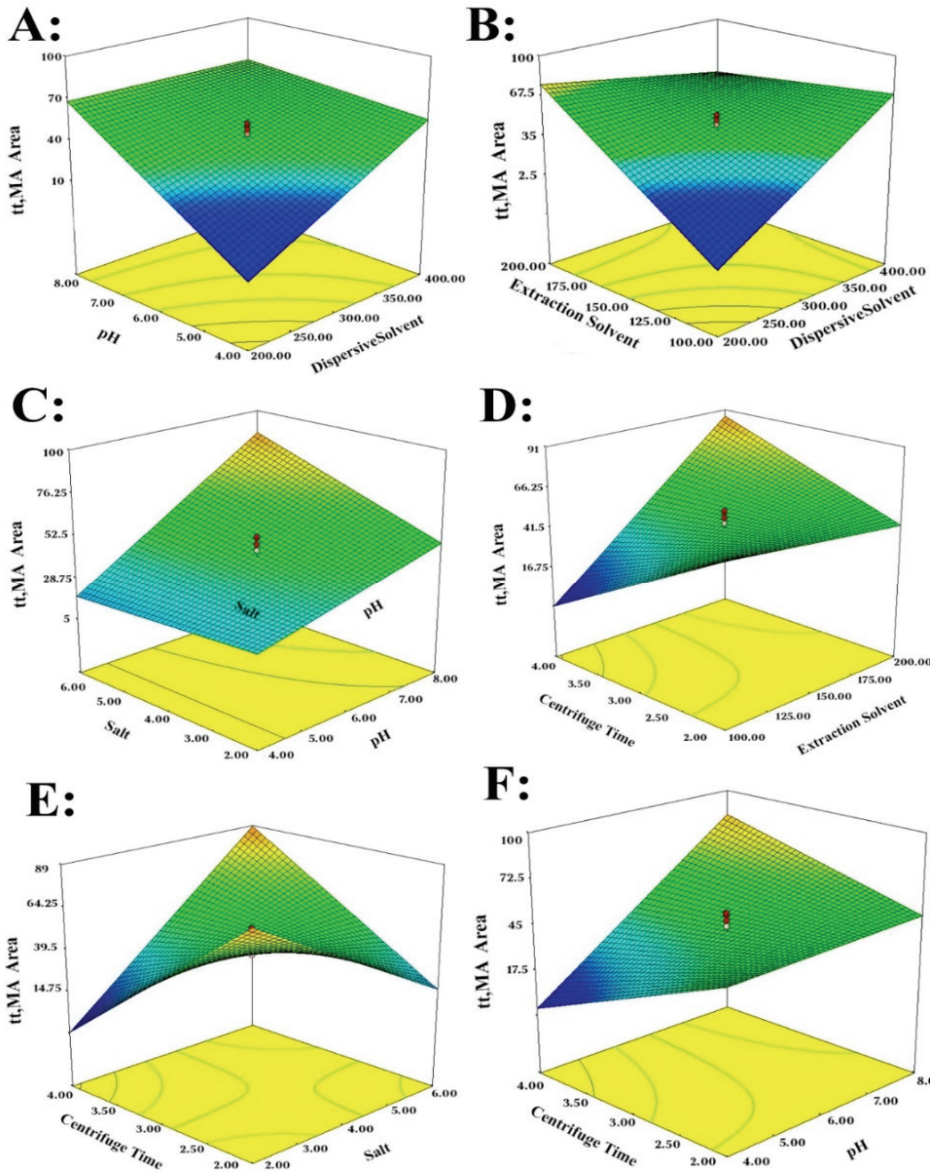

Fig. 3. Three-dimensional response surface plots of between-factor interaction terms.

TABLE III. Analytical characteristics of the method

Correlation coefficient (r^2)	0.9996
LDR, μL/ml	0.008–5.0
LOD, μg/ml	0.0024
LOQ, μg/ml	0.008
Calibration equation	$y = 2\times10^6x + 474423$

Optimum conditions

As given above, the statistical analysis of the suggested MLR model showed the validity of the proposed DLLME and thus can be applied to find the optimum conditions. For the determination of the optimal experimental conditions for the extraction of *t*,*t*-MA, the simplex optimization was applied. As shown in Table S--III (Supplementary material), the optimum conditions were as follows: pH 8, extractant solvent volume, 300 μL, volume of disperser solvent, 300 μL, applied salt content, 3.4 % and centrifuge time, 4 min.

To determine the *t*,*t*-MA concentration, a calibration curve was drawn using spiked samples of *trans*-muconic acid under the optimum conditions. The calibration graph (Fig. 4a and b) was drawn by spiked values of 0.01, 0.1, 0.5, 1 and 2 ppm. A calibration graph with $R = 0.9996$ was derived (Table III). Fig. 4a illustrates the obtained peaks.

Matrix effect

The chromatograms of two spiked urine samples with two *t*,*t*-MA concentrations extracted by the proposed DLLME method were compared with similar spiked in distilled water, each with three replicates. The results showed a significant change of peaks in urine and water because of the matrix effect (change of more than 17–20 % in *RSD*).

Thus, it was decided to perform the calibration curve in the urine sample. On the other hand, to show the presence or absence of matrix effect in different urine samples, two concentrations of *t*,*t*-MA were spiked into three urine samples obtained from persons without exposure to benzene (0.5 and 1.0 μg mL^{-1}). The change in urine samples was estimated by following the *RSD* between samples.

There was no change in *t*,*t* retention time and the *RSD* between different urine samples was lower than 7.2 (for 0.5 μg mL^{-1}) and 6.8 % (for 1.0 μg mL^{-1}). However, for better performance it could be suggested to do the calibration curve in a pool of not-exposed urine samples. Fig. 4 shows the chromatograms of spiked urine samples with concentrations of 0.01, 0.1, 0.5, 1 and 2 μg mL^{-1}.

Method validation

A number of merit measures have been evaluated to assess the effectiveness of the optimized method. These measures include quantification limit (*LOQ*), precision, linear dynamic ranges (*LDR*s), detection limit (*LOD*), correlation coefficients of the calibration curve (R^2), and relative recovery (*RR*), Table III.

To assess the precision of the proposed method, three spiked urine samples in different levels were used. Three replicates were done on three days and the relative standard deviation (*RSD*) was calculated (Table III). The *RSD*s were in the range of 5.1–6.8 %. To evaluate the method's accuracy, the average of the extraction recovery (*ER*) in the spiked samples was calculated (Table IV). The average

ER in the spiked samples was between 95.8–102 % and confirmed the ability of the extraction method for the analyte.

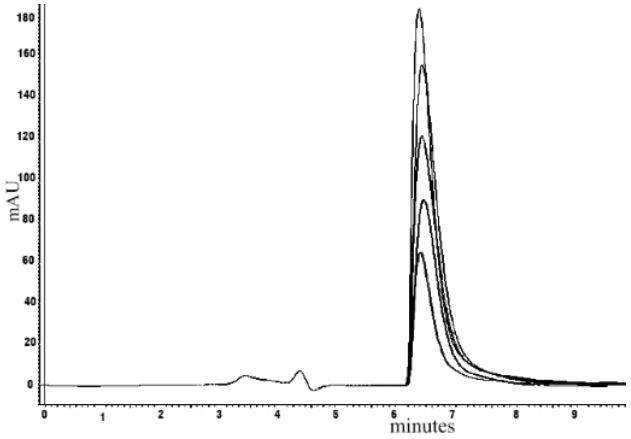

Fig. 4. Chromatogram of spiked urine samples after extraction in optimum conditions with concentrations of 0.01, 0.1, 0.5, 1 and 2 μg mL^{-1}.

TABLE IV. Results of the validation of accuracy and precision of suggested DLLME; *ER* – extraction recovery; *RSD* – relative standard deviation

Spiked level, μg/ml	Intra-day *RSD*, % (n = 3)	Average *ER*, %
0.5	<6.1	102.4
1	<6.8	98.6.5
2.5	<5.1	95.8

Application of the optimized DLLME; biomonitoring of benzene-exposed workers

The established DLLME method was applied to the four urine samples of petrochemical workers exposed to benzene. The suggested method and the conventional standard laboratory method strong anion exchange in SPE (SAX-SPE), were used to determine the quantity of *t*,*t*-MA (Table V). A good agreement was observed between the proposed and standard methods.

TABLE V. The result of real sample analysis by the suggested DLLME and standard SPE

Sample ID	Predicted conc., μg/mL		Residual μg/mL	Creatinine mg dL^{-1}	Predicted adjusted conc. (μg/g creatinine)	
	DLLME	SPE			DLLME	SPE
Worker 1	0.85	0.89	–0.04	92	923.9	967.4
Worker 2	0.745	0.692	0.053	81	919.8	854.3
Worker 3	0.38	0.43	–0.06	95	400.0	452.6
Worker 4	1.03	1.16	–0.13	88	1170.5	1318.2

Comparison with other methods

In Table S-IV (Supplementary material), a comparison of the developed DLLME with other methods is presented with previous similar methods using HPLC-UV. Based on the comparison, it can be concluded that the proposed DLLME resulted in acceptable analytical figures of merit. Further, compared with most previous methods, a lower volume of samples and solution was consumed, and the extraction times were decreased.

The proposed DLLME technique is an efficient and simple extraction method for target metabolite (*t*,*t*-MA) from the urine matrix. Additionally, the *LOD* and *LDR* values were comparable to other developed extraction methods for the urinary *t*,*t*-MA, and the analysis by HPLC–UV. The suggested DLLME method with low *LOD* (2.4 μg/L) and *LOQ* (8 μg/L) showed sufficient sensitivities for benzene biomonitoring, especially at low levels of benzene exposure. On the other hand, as can be seen in Table S-IV (Supplementary material), the extraction time is lower than in most of the previous reports, which make it suitable for the automatic extraction systems as well. Accordingly, the proposed DLLME analysis can be used to determine *t*,*t*-MA in urine samples in a sensitive, user-friendly, time- and cost-effective manner.

The method developed by Rismanchian *et al.* was the most similar to the method suggested in this study.[22] Nevertheless, there are some differences between the developed DLLME method and the PDLLME method introduced by Rismanchian *et al*. In the presented DLLME method in this study, solvents are employed in smaller amounts than the PDLLME method. According to Rismanchian *et al.* study, 5 ml of sample, 200 μL of chloroform, 2000 μL of tetrahydrofuran, 20 μL of methanol, and nitrogen result in a total of 7220 μL of sample and solvent was required.

The present DLLME method uses 2 ml of sample, 300 ml of chloroform, and 300 ml of acetonitrile (in total 4600 μL of solvent and sample). Secondly, Rismanchian *et al.*'s protocol is longer than the current protocol (more than 15 min, and the suggested method is approximately 8 min). As well as this, the linear range of the present DLLME method (0.0008–5 μg/mL) is much lower than that in Rismanchian *et al.*'s study (0.1–10 μg/mL), which is more suitable for the evaluation of metabolites at low concentrations. Additionally, Rismanchian *et al.*'s study used tetrahydrofuran (2000 μL), a volatile substance with a boiling point of 66 °C and a vapour pressure of 162 mm Hg* at 25 °C, whereas in the present study, acetonitrile (300 μL) was used, which has lower volatility (boiling point 82 °C, vapor pressure 73 mm Hg at 25 °C). Additionally, acetonitrile has a saturation concentration of 9.6 % at 20 °C and tetrahydrofuran has a saturation concentration of 19.1 % at 20 °C. Due to its higher volatility and tendency to vaporize,

* 1 mm Hg = 133.3 Pa

tetrahydrofuran will have a higher concentration in the air at the same temperature and pressure. The same working conditions result in a higher risk of the operator being exposed to tetrahydrofuran. In Rismanchian *et al.*'s protocol, three solvents and nitrogen gas were used, while in the present protocol, only two solvents were used. Therefore, the presented DLLME method has overcome the limitations of the PDLLME method by having less complexity, less extraction time, less solvent consumption, less linear range, and fewer exposures to the operator than the PDLLME method developed by Rismanchian *et al*.

CONCLUSIONS

The present study proposes a new and efficient DLLME for *t*,*t*-MA, a well--known benzene metabolite. The developed DLLME was coupled with HPLC–UV and showed significant efficiency for benzene biomonitoring. Moreover, the proposed DLLME method is highly efficient, requires a short extraction time, and exhibits high selectivity and accuracy. The proposed approach was also successfully applied to real urine samples of benzene-exposed workers with the extraction efficiency ranging from 95.8 to 102.4 %.

In this study, a multivariate approach was applied to optimize variables that could affect the preconcentration of the *t*,*t*-MA to identify the optimum conditions. It has been demonstrated that the suggested DLLME approach can be effectively applied for biomonitoring of individuals who have been occupationally exposed to benzene in industrial settings. However, the use of organic solvent is a limitation of this approach. However, the main goal of this work was to suggest a simple approach to be applicable in an automatic microextraction, which is in progress in our research group. On the other hand, very small quantities of solvent, in the microliter range, are sufficient for the suggested DLLME method.

SUPPLEMENTARY MATERIAL

Additional data and information are available electronically at the pages of journal website: https://www.shd-pub.org.rs/index.php/JSCS/article/view/12789, or from the corresponding author on request.

Acknowledgements. The present paper was a part of PhD Thesis conducted by Abolfazl Moghadasi at Shiraz University of Medical Sciences (Shiraz, Iran). The authors would like to appreciate the financial support provided by the Shiraz University of Medical Sciences (Grant No. 24565).

ИЗВОД

ДИСПЕРЗИВНА ТЕЧНО-ТЕЧНА МИКРОЕКСТРАКЦИЈА ЗА ОДРЕЂИВАЊЕ МУКОНСКЕ КИСЕЛИНЕ КАО БИОЛОШКОГ ИНДИКАТОРА БЕНЗЕНА У УРИНУ

ABOLFAZL MOGHADASI[1,2], SAEED YOUSEFINEJAD[3], ESMAEEL SOLEIMANI[2], SAJJAD TAGHVAEI[4] и SAEED JAFAI[2]

[1]Student Research Committee, Shiraz University of Medical Sciences, Shiraz, Iran, [2]Department of Occupational Health Engineering, School of Health, Shiraz University of Medical Sciences, Shiraz, Iran, [3]Research Center for Health Sciences, Institute of Health, Department of Occupational Health Engineering, School of Health, Shiraz University of Medical Sciences, Shiraz, Iran и [4]Department of Mechanical Engineering, Shiraz University, Shiraz, 71936-16548, Iran

Праћење професионалне изложености хемикалијама је од суштинског значаја за процену радног места. У случају опасних и канцерогених хемикалија, као што је бензол, надзор на раду постаје још важнији. *Trans*,*trans*-муконска киселина (*t*,*t*-MA) је један од метаболита бензена у урину. Методе претходног третмана за *t*,*t*-MA генерално укључују течно–течну и екстракцију на чврстој фази. Употреба дисперзивне течно–течно микроекстракције (DTTME) током припреме узорка и екстракције може смањити трошкове екстракције и утицаје на животну средину. Штавише, процес је исплатив и једноставан за руковање. Ова студија је имала за циљ да развије, оптимизује и валидира аналитичку методу за мерење концентрације *t*,*t*-MA у матриксу урина применом DTTME у комбинацији са течном хроматографијом високих перформанси. Пет варијабли укључујући pH, количину екстрактанта и супстанце за дисперговање, количину соли и време центрифугирања оптимизовано је применом централног композитног дизајна са методологијом површине одговора и експерименталних података. Предложени DTTME приступ је успешно примењен на реалне узорке, добијене од радника изложених бензену, са ефикасношћу екстракције од 95,8 до 102,4 %. Оптимални услови су pH 8, растварач за екстракцију, 300 μL, растварач за дисперговање, 300 μL, 3,4 % раствор соли и време центрифугирања, 3 min. Према резултатима ове студије, предложени DTTME приступ се може ефикасно применити на биомониторинг појединаца изложених бензену.

(Примљено 25. јануара, ревидирано 5. априла, прихваћено 7. јула 2024)

REFERENCES

1. C. Carvalhais, M. Querido, C. C. Pereira, J. Santos, *Work* **69** (2021) 3 (https://doi.org/10.3233/WOR-205302)
2. L. De Maria, C. Ledda, A. Caputi, F. Mansi, E. S. S. Cannone, S. Sponselli, D. Cavone, F. Birtolo, E. Cannizzaro, G. M. Ferri, V. Rapisarda, L. Vimercati, *Front. Public Heal.* **8** (2020) 271 (https://doi.org/10.3389/fpubh.2020.00271)
3. Y. R. Li, C. J. Xie, C. X. Qiu, Q. Y. Lin, Y. M. Liu, *Chin. J. Ind. Hygiene Occupat. Dis.* **37** (2019) 119 (https://doi.org/10.3760/CMA.J.ISSN.1001-9391.2019.02.007)
4. S. B. Wilbur, S. M. S. Keith, O. Faroon, D. Wohlers, *ATSDR's Toxicol. Profiles* (2002) (https://doi.org/10.1201/9781420061888_ch38)
5. N. Mirzaei, K. Naddafi, Raminnabizadeh, K. Yaghmaeian, M. S. Assanvand, S. Maroufizadeh, M. Hoseini, S. Adabi, M. Yunesian, *Acta Medica Mediterr.* **32** (2016) 1471 (https://www.actamedicamediterranea.com/archive/2016/special-issue-4/urinary-benzene-as-a-biomarker-of-environmental-exposure-to-benzene-in-males-in-the-general-population/document)

6. T. Tunsaringkarn, J. Suwansaksri, S. Soogarun, W. Siriwong, A. Rungsiyothin, K. Zapuang, M. Robson, *Asian Pacific J. Cancer Prev.* **12** (2011) 223 (https://journal.waocp.org/article_25501_cd29634a0ebf3dad97742bb9edc1e432.pdf)
7. E. A. Natelson, *Am. J. Hematol.* **82** (2007) 826 (https://doi.org/10.1002/ajh.20934)
8. M. Borgie, A. Garat, F. Cazier, A. Delbende, D. Allorge, F. Ledoux, D. Courcot, P. Shirali, Z. Dagher, *Chemosphere* **96** (2014) 122 (https://doi.org/10.1016/j.chemosphere.2013.09.034)
9. S. M. Rappaport, S. Kim, Q. Lan, R. Vermeulen, S. Waidyanatha, L. Zhang, G. Li, S. Yin, R. B. Hayes, N. Rothman, M. T. Smith, *Environ. Health Perspect.* **117** (2009) 946 (https://doi.org/10.1289/ehp.0800510)
10. E. Soleimani, *Rev. Anal. Chem.* **39** (2020) 168 (https://doi.org/10.1515/revac-2020-0116)
11. S. Viegas, M. Z. Jeddi, N. B. Hopf, J. Bessems, N. Palmen, K. S. Galea, K. Jones, P. Kujath, R. C. Duca, H. Verhagen, T. Santonen, R. Pasanen-Kase, *Int. J. Environ. Res. Public Health* **17** (2020) 5884 (https://doi.org/10.3390/ijerph17165884)
12. I. Pilia, M. Campagna, G. Marcias, D. Fabbri, F. Meloni, G. Spatari, D. Cottica, C. Cocheo, E. Grignani, F. De-Giorgio, P. Cocco, E. D'aloja, *Int. J. Environ. Res. Public Health* **18** (2021) 4644 (https://doi.org/10.3390/ijerph18094644)
13. F. Ghamari, A. Bahrami, Y. Yamini, F. G. Shahna, A. Moghimbeigi, *Anal. Chem. Insights* **2016** (2016) 65 (https://doi.org/10.4137/Aci.s40177)
14. Threshold Limit Values (TLVs®) and Biological Exposure Indices (BEIs®), 2022, https://www.techstreet.com/standards/2022-threshold-limit-values-tlvs-and-biological-exposure-indices-beis?product_id=2242171#jumps (accessed 1 January, 2022)
15. F. Dehghani, F. Omidi, O. Heravizadeh, S. Yousefinejad, *Sci. Rep.* **11** (2021) 15751 (https://doi.org/10.1038/s41598-021-95174-5)
16. A. Damokhi, S. Yousefinejad, S. Jafari, E. Soleimani, F. Dehghani, *J. Mol. Liq.* **386** (2023) 122506 (https://doi.org/10.1016/j.molliq.2023.122506)
17. D. Basu, S. Bag, S. Mukherjee, G. Goel, *J. Acad. Clin. Microbiol.* **21** (2019) 66 (https://doi.org/10.4103/jacm.jacm_20_18)
18. A. Barbieri, L. Sabatini, A. Accorsi, A. Roda, F. S. Violante, *Rapid Commun. Mass Spectrom.* **18** (2004) 1983 (https://doi.org/10.1002/rcm.1580)
19. S. Abbaszadeh, S. Yousefinejad, S. Jafari, E. Soleimani, *J. Sep. Sci.* **44** (2021) 3126 (https://doi.org/10.1002/jssc.202100044)
20. M. Tehranirokh, M. Van den Bronk, P. Smith, Z. Dai, K. Ragunathan, A. Muscalu, S. Mills, M. C. Breadmore, R. A. Shellie, *J. Chromatogr., A* **1642** (2021) 462032 (https://doi.org/10.1016/j.chroma.2021.462032)
21. M. Rezaee, Y. Yamini, S. Shariati, A. Esrafili, M. Shamsipur, *J. Chromatogr., A* **1216** (2009) 1511 (https://doi.org/10.1016/j.chroma.2008.12.091)
22. M. Rismanchian, K. Ebrahim, Z. Ordudari, *Chem. Pap.* **73** (2019) 2485 (https://doi.org/10.1007/s11696-019-00800-2)
23. S. Yousefinejad, F. Honarasa, N. Saeed, *J. Sep. Sci.* **38** (2015) 1771 (https://doi.org/10.1002/jssc.201401427)
24. M. Nekoeinia, S. Yousefinejad, A. Abdollahi-Dezaki, *Ind. Eng. Chem. Res.* **54** (2015) 12682 (https://doi.org/10.1021/acs.iecr.5b02982)
25. S. Yousefinejad, F. Honarasa, H. Montaseri, *RSC Adv.* **5** (2015) 42266 (https://doi.org/10.1039/c5ra05930e).

Journal of the Serbian Chemical Society
JSCS@tmf.bg.ac.rs • www.shd.org.rs/JSCS
J. Serb. Chem. Soc. *89* (10) S357–S360 (2024) *Supplementary material*

SUPPLEMENTARY MATERIAL TO

Dispersive liquid–liquid microextraction for determining urinary muconic acid as benzene biological indicator

ABOLFAZL MOGHADASI[1,2], SAEED YOUSEFINEJAD[3]*, ESMAEEL SOLEIMANI[2]**, SAJJAD TAGHVAEI[4] and SAEED JAFAI[2]

[1]Student Research Committee, Shiraz University of Medical Sciences, Shiraz, Iran, [2]Department of Occupational Health Engineering, School of Health, Shiraz University of Medical Sciences, Shiraz, Iran, [3]Research Center for Health Sciences, Institute of Health, Department of Occupational Health Engineering, School of Health, Shiraz University of Medical Sciences, Shiraz, Iran and [4]Department of Mechanical Engineering, Shiraz University, Shiraz, 71936-16548, Iran

J. Serb. Chem. Soc. *89* (10) (2024) 1337–1351

Table S-I. Matrix of of designed runs and related normalized peak areas

	Dispersive (μL)	Extraction (μL)	pH	Salt% (w/v%)	Centrifuge time (min)	Peak Area
1	100	150	6	4	3	7.12
2	200	100	8	6	4	64.45
3	300	250	6	4	3	90.27
4	300	150	2	4	3	5.66
5	400	100	8	2	4	1.30
6	300	150	6	4	3	44.54
7	400	200	4	6	2	1.44
8	300	150	6	8	3	66.48
9	300	50	6	4	3	5.70
10	300	150	6	4	1	55.23
11	300	150	6	4	3	36.59
12	400	200	4	2	4	4.93
13	200	200	8	6	2	49.01
14	500	150	6	4	3	72.80
15	400	100	8	6	2	61.78
16	300	150	6	4	3	51.41
17	200	200	4	6	4	69.83
18	400	200	8	2	2	35.02
19	300	150	6	0	3	35.60
20	200	100	4	2	2	29.65
21	300	150	10	4	3	100.00
22	300	150	6	4	3	52.49

* Corresponding authors. E-mail: (*)yousefinejad.s@gmail.com; (**)esoleimani61@gmail.com

23	300	150	6	4	5	37.91
24	200	200	8	2	4	97.97
25	400	100	4	6	4	46.64
26	300	150	6	4	3	47.94

Table S-II. Analysis of variance (ANOVA), summary statistics of the quadratic model, in the current microextraction study

Source of Variation	Sum of square	Df[a]	Mean Square	F-Value[b]	p-value (Prob > F)	Status
Model	20471.48	11	1861.043	41.17	< 0.0001	significant
A-Dispersive Solvent	3095.271	1	3095.271	68.48	< 0.0001	
B-Extraction Solvent	4642.807	1	4642.807	102.72	< 0.0001	
C-pH	7707.412	1	7707.412	170.52	< 0.0001	
D-Salt	907.399	1	907.399	20.08	0.0005	
E-Centrifuge Time	373.4016	1	373.401	8.26	0.0122	
AB	3626.333	1	3626.333	80.23	< 0.0001	
AC	1863.888	1	1863.888	41.24	< 0.0001	
BE	4386.713	1	4386.713	97.05	< 0.0001	
CD	589.010	1	589.010	13.03	0.0028	
CE	2688.925	1	2688.925	59.49	< 0.0001	
DE	8302.758	1	8302.758	183.69	< 0.0001	
Residual	632.787	14	45.199			
Lack of Fit	468.827	10	46.883	1.144	0.4875	not significant
Pure Error	163.960	4	40.990			
Cor Total	21104.27	25				

[a]: Degree of freedom. [b]: Test to comparing model variance with residual variance or significance of included factors.

Table S-III. Result of simplex optimization for the best recovery of tt-MA

Variables	Optimum Value
Extractant solvent volume (µL)	300
Disperser solvent volume (µL)	300
Salt amount (w/v,%)	3.4
Centrifuge time (min)	4
pH	8

Table S-IV. Comparison between the proposed DLLME method and other preconcentration methods using HPLC for the extraction of *t,t*-MA from urine matrix

Ref.	Method (analytical technique)	Extraction solvents/method	Additional solvents	Sample volume	Extraction time	LDR (µg/mL)	LOD (µg/L)
1	SLM[a] (HPLC-PDA)	m-xylene; 6-undecanone, and di-nhexyl ether, tri-n-octylphosphine oxide	Acetonitrile	3 ml	13 min	0-0.2	10
2	LLE (HPLC-UV)	Ethyl acetate	-	8 ml	-	0.25-5	16.7
3	SPE (HPLC-DAD)	Oasis®MAX sorbents	HCl, Ethyl acetate, Formic acid	50 µl	10 min>	30 min>	-
4	SPE (HPLC-UV)	SAX sorbent	10% (v/v) Acetic acid	50 ml	-	-	100
5	SPE (HPLC-UV)	Elut-SAX cartridges	Acetonitrile, Acetic acid	1 ml	13 min	0.05-2	10.8
6	MIP[b] (HPLC-UV)	Ionic exchange extraction	Phosphate buffer, Methanol	2 ml	20 min>	0.1-10	10
7	HFLPME[c] (HPLC-UV)	Trioctylphosphine oxide(TOPO)	-	11 ml	120 min	0.005-1.2	1
8	MEPS[d] (HPLC-UV)	SAX sorbent	10%(v/v) Acetic acid	0.5 ml	4 min	0.1-2	32
9	MIMEPS[e] (HPLC-UV)	MIP in packed sorbent	Ethanol, Acetic acid	500 µl	5 min	0.015-2	15
10	Ion-pair HFLPME (HPLC-UV)	1-Octanol containing 10% w/v of Aliquat-336	-	10 ml	60 min	0.001-0.9	0.1
11	PDLLME (HPLC-UV)	Chloroform	Tetrahydrofuran, Methanol	5 ml	15 min>	0.1-10	0.11
12	SPME (HPLC-UV)	zirconium-based metal–organic frameworks	Acetonitrile, Acetic acid	-	-	0.01-50	10
13	In syringe IL-DLLME (HPLC-UV)	([P14,6,6,6]Cl (ionic liquid, 40 µL)	-	6.5 ml	10 min >	0.032-10	11
14	DLLME-SFOD[f] (HPLC-UV)	1-undecanol	Methanol	10 ml	10 min >	0.02-5	6
This work	DLLME (HPLC-UV)	Chloroform	Acetonitrile	2 ml	8 min	0.008-5	2.4

[a]Supported Liquid Membrane/[b]molecularly imprinted polymer/[c]Hollow-fiber liquid-phase microextraction/[d] microextraction by packed sorbent/[e]combination of MIP and MEPS/[f]Solidiied loating organic droplet

REFERENCES

1. J. Norberg, D. Tiruye, L. Mathiasson, J. Å. Jönsson, *J. Sep. Sci.* **25** (2002) 351–355 (https://doi.org/10.1002/1615-9314(20020401)25:5/6<351::AID-JSSC351>3.0.CO;2-H)
2. P. Tharnpoophasiam, P. Kongtip, W. Wongwit, W. Fungladda, D. Kitayaporn, *Southeast Asian J. Trop. Med. Public Health* **35** (2004) 717–723 (PMID: 15689075)
3. B. L. Lee, H. Y. Ong, Y. B. Ong, C. N. Ong, *J. Chromatogr. B Anal. Technol. Biomed. Life Sci.* **818** (2005) 277–283 (https://doi.org/10.1016/j.jchromb.2005.01.009)
4. S. Jamaleddin Shahtaheri, F. Ghamari, F. Golbabaei, A. Rahimi-Froushani, M. Abdollahi, *Int. J. Occup. Saf. Ergon.* **11** (2005) 377–388 (https://doi.org/10.1080/10803548.2005.11076658)
5. V. Olmos, S. C. Lenzken, C. M. López, E. C. Villaamil, *J. Anal. Toxicol.* **30** (2006) 258–261 (https://doi.org/10.1093/jat/30.4.258)
6. A. C. Vieira, R. A. Zampieri, M. E. P. B. De Siqueira, I. Martins, E. C. Figueiredo, *Analyst* **137** (2012) 2462–2469 (https://doi.org/10.1039/c2an16215f)
7. F. Ghamari, A. Bahrami, Y. Yamini, F. G. Shahna, A. Moghimbeigi, *Anal. Chem. Insights* **11** (2016) (https://doi.org/10.4137/Aci.s40177)
8. E. Soleimani, A. Bahrami, A. Afkhami, F. G. Shahna, *Toxicol. Environ. Health Sci.* **9** (2017) 317–324 (https://doi.org/10.1007/s13530-017-0337-x)
9. E. Soleimani, A. Bahrami, A. Afkhami, F. G. Shahna, *J. Chromatogr. B Anal. Technol. Biomed. Life Sci.* **1061–1062** (2017) 65–71 (https://doi.org/10.1016/j.jchromb.2017.07.008)
10. A. Bahrami, F. Ghamari, Y. Yamini, F. Ghorbani Shahna, A. Koolivand, *J. Sep. Sci.* **41** (2018) 501–508 (https://doi.org/10.1002/jssc.201700685)
11. M. Rismanchian, K. Ebrahim, Z. Ordudari, *Chem. Pap.* **73** (2019) 2485–2492 (https://doi.org/10.1007/s11696-019-00800-2)
12. R. Rahimpoor, A. Bahrami, D. Nematollahi, F. Ghorbani Shahna, M. Farhadian, *J. Iran. Chem. Soc.* **17** (2020) 2345–2358 (https://doi.org/10.1007/s13738-020-01930-1)
13. S. Abbaszadeh, S. Yousefinejad, S. Jafari, E. Soleimani, *J. Sep. Sci.* **44** (2021) 3126–3136 (https://doi.org/10.1002/jssc.202100044)
14. F. Dehghani, F. Omidi, O. Heravizadeh, S. Yousefinejad, *Sci. Rep.* **11** (2021) 15751 (https://doi.org/10.1038/s41598-021-95174-5).

Journal of the Serbian Chemical Society
JSCS@tmf.bg.ac.rs • www.shd.org.rs/JSCS
J. Serb. Chem. Soc. *89* (10) 1353–1362 (2024)
JSCS–5792
Original scientific paper
Published 25 October, 2024

Characterization of enalapril maleate: An approach using thermoanalytical, thermokinetic and spectroscopic techniques

JOSÉ AUGUSTO TEIXEIRA[1], ADRIAN SANTOS DE SOUZA[2], LAÍS DA SILVA MENDOZA KARDEK DE MELO[2] and TIAGO ANDRÉ DENCK COLMAN[2]*

[1]*Federal Institute of Paraná, IFPR, Paranavaí, PR, Brazil and* [2]*Federal University of Grande Dourados, UFGD, Dourados, MS, Brazil*

(Received 7 December 2023, revised 1 February, accepted 17 August 2024)

Abstract: Enalapril maleate is a widely used drug for the treatment of cardiovascular diseases. Its mechanism of action is to inhibit the angiotensin-converting enzyme selectively. Therefore, it is metabolized to enalaprilat by liver cells. The thermal behaviour of enalapril maleate was investigated by simultaneous thermogravimetry and differential scanning calorimetry (TG-DSC), as well as with evolved gas analysis by simultaneous thermogravimetry and differential scanning calorimetry coupled infrared spectroscopy (TG-DSC–FTIR). The results provided information on thermal stability, purity, thermal decomposition steps and the main products formed in the heating. The enalapril maleate was found to be stable up to 148 °C. Above this temperature causes thermal degradation of the substance, which occurs in two stages in an inert atmosphere (N_2) and three stages in an oxidizing atmosphere (air). Through the TG-DSC–FTIR the released gases were identified as maleic anhydride as a thermal decomposition intermediate. DSC analysis showed that the material obtained 99.5 % purity, which indicates high purity. Employing both the Kissinger and Friedman equations, alongside model fitting methods, the study reveals key insights. The Kissinger method unveils an apparent activation energy of 47.07±15.45 kJ mol^{-1} for the complete thermal breakdown, a finding corroborated by the Friedman method. Model fitting methods, the article applies them, yielding an apparent activation energy of 55.7±3.4 kJ mol^{-1} with a three-dimensional diffusion thermal degradation model.

Keywords: thermal stability; thermal decomposition; kinetic characterization.

INTRODUCTION

Enalapril maleate (Fig. 1) is a prodrug of (*Z*)-but-2-enedioic acid; (2*S*)-1-{(2*S*)-2-[((2*S*)-1-ethoxy-1-oxo-4-phenylbutan-2-yl)amino]propanoyl}pyrrolidine-2-carboxylic acid-1-[2-(1-ethoxycarbonyl-3-phenyl-propyl)aminopropanoyl]

* Corresponding author. E-mail: tiagocolman@ufgd.edu.br
https://doi.org/10.2298/JSC231207070A

pyrolidine-2-carboxylic acid ((*Z*)-carboxylic acid), which undergoes hydrolysis of the ethyl ester in hepatic cells and is converted to enalaprilat, considered its bioactive form. Its main indication is for use in cases of heart disease, such as systemic arterial hypertension and congestive heart failure. It acts by inhibiting the angiotensin-converting enzyme, competitively by inhibiting the biotransformation of angiotensin I in angiotensin II, which promotes the therapeutic effect.[1–8]

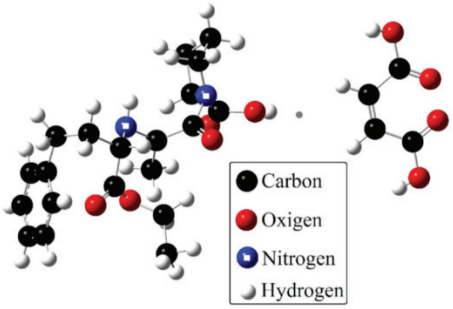

Fig. 1. Structural representation of enalapril maleate.

For the drug to be safe and effective, strict quality control must be done, which may be realized through thermoanalytical techniques. The literature demonstrates the importance of thermal analysis to characterize and evaluate the purity of drugs, active pharmaceutical ingredients (IFAs), excipients and medications since thermogravimetry and DSC are analytical, quantitative and comparative techniques.[9] These techniques are considered capable of quickly and reproducibly producing the expected results. DSC is used in the pharmaceutical industry as an important analytical tool to identify and test the purity of active principles, and it produces results quickly and efficiently. DSC is already accepted in countries such as the United States of America for quality control of raw materials used in pharmaceutical products.[8–11]

The use of analytical techniques to characterize pharmaceuticals is important. An example of this importance that can be cited is that by DSC curves, infrared, and Raman spectra, it was possible to elucidate two polymorphic forms of enalapril.[12,13]

Thus, given the importance of quality control of raw materials and pharmaceutical products, the objective of this study was to perform thermal characterization and determine the purity of the raw material, enalapril maleate, which is one of the most prescribed drugs for cardiovascular changes. In this way, to obtain information not yet described in the literature. Such as thermal and chemical stability, thermal decomposition, and the main products and gaseous intermediates released during the thermal decomposition process.

EXPERIMENTAL

Enalapril maleate was purchased commercially in a compounding pharmacy and stored in an amber bottle for further analysis.

The DSC curves were obtained in a DSC-Q200 calorimeter (TA Instr. Co., USA), which was calibrated according to the manufacturer's recommendation, and a standard indium 99.99 % purity, m.p. 156.6 °C and $\Delta H = 28.56$ J g^{-1} were used to check the calibration. A mass sample was around 2 mg and the sample was heated from 130 to 180 °C using an aluminium crucible with a perforated lid with a 1.0 mm orifice, under an N_2 atmosphere, with a flow rate of 50 mL min^{-1} and a heating rate of 1 °C min^{-1}. Universal Analysis software was used to determine the purity of the sample.[14,15]

Simultaneous TG-DTG–DSC curves were obtained on a thermal analysis System, TG--DSC1, Mettler Toledo. The purge gases were dried in air and N_2 with a flow of 50 mL min^{-1}, with a heating rate of 10 °C min^{-1}, weighing about 10.0 mg. Alumina crucibles were used to record the DSC and TG curves.[16]

The thermokinetic study was conducted using the thermal decomposition curves obtained through thermogravimetry on a calibrated Netzsch STA 449 F3 Jupiter® apparatus following the manufacturer's instructions. The analyses adhered to the recommended parameters in the literature,[17-20] with a sample mass of approximately 1.0±0.1 mg. The temperature range spanned from 30 to 700 °C in an inert N_2 atmosphere (99.99 %), employing the following heating rates: 2, 4, 6, 8 and 10 °C min^{-1}. The thermokinetic treatment was performed with THINKS, free open-source thermokinetic software.[21]

The analysis of the detected gases (TG-DSC–FTIR) was performed using a thermogravimetric analyser coupled to a Nicolet FTIR spectrophotometer with gas cells and a DTGS detector. The oven was coupled to the heated gas cell (250 °C) through a heated current (225 °C) stainless steel transfer line with 3.0 mm diameter and 120 cm length, both purged with 50 ml min^{-1}. The identification of the gaseous products was based on the reference spectra available in the spectrometer software (Omnic 8.0) and literature data.[14–16]

RESULTS AND DISCUSSION

Thermoanalytical and spectroscopic study

The purity determination of enalapril was based on the assumption that an impurity will depress the melting point of a pure material for which the fusion was characterized by melting point (T_0) and a melting enthalpy ($\Delta H_{\text{melt.}}$). The effect of a T_0 impurity on enalapril was determined by the DSC method based on the Van't Hoff equation (Eq. (1)).[16,22] The DSC curve obtained shows an endothermic event corresponding to the melting point of enalapril at 154 °C ($\Delta H_{\text{melt.}} = 29.6$ kJ mol^{-1}); the purity was 99.5 %, indicating the high purity of the material:

$$\ln \frac{k_2}{k_1} = \frac{\Delta H}{R}\left(\frac{1}{T_1} - \frac{1}{T_2}\right) \quad (1)$$

The simultaneous TG-DSC curves in dynamic dry air and N_2 atmospheres of enalapril are shown in Fig. 2a and b. In both conditions studied (Pyrolysis (N_2) and oxidation (air)), enalapril was stable up to 148 °C and, above this temperature, the TG-DSC curves showed that the thermal decomposition occurs in two (N_2) and

three (air) stages between 148–330 °C and 148–605 °C, respectively, the with total mass loss of 99.85 (N_2) and 99.95 % (air). The percentages indicated that the compound has no inorganic impurities.

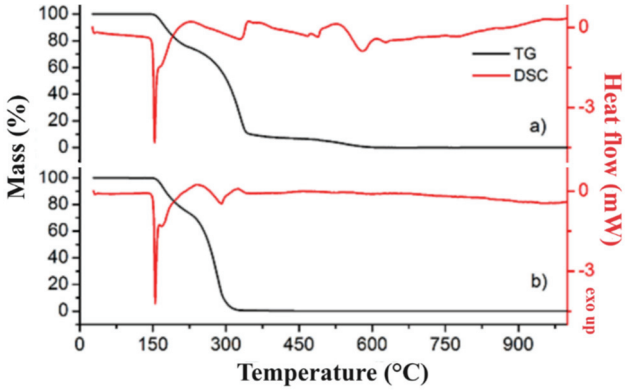

Fig. 2. Enalapril maleate TG-DSC simultaneous curves in dynamic dry air (a) and N_2 (b) atmosphere (mass (air) = 10.225 mg, mass (N_2) = 10.125 mg).

The TG-DSC curves indicate that the first mass loss occurred slowly between 148 and 230 °C (air) and 148 and 220 °C (N_2), with loss mass of 25.4 and 25.5 %, respectively. At this stage, for both analysis conditions (air and N_2) the DSC curves have an endothermic peak at 154 °C with a shoulder at 169 °C, attributed to the melting followed by thermal decomposition of Enalapril maleate, respectively. To check these attributions, the sample was heated in a glass tube until 169° C, and as indicated by the TG-DSC curves, and melting followed by thermal decomposition was observed. The infrared spectrum of the product condensed on the wall of the glass tube after the thermal decomposition of enalapril maleate was obtained (Fig. 3) and the maleic anhydride was identified as a decomposition gas product at this stage ($\Delta m_{Calc.}$ = 26.04%, Δm_{TG} = 25.4 % (air), 25.5 % (N_2)). The TGA also identified maleic anhydride at 170 °C, as the gas product from the thermal decomposition at this stage, as shown in Fig. 3.

The residue mass obtained at the end of the first mass loss stage (220 (N_2) and 230 °C (air)) indicates the formation of "pure" enalapril, the proposed mechanism for this step is shown in Scheme 1 ($\Delta Resid._{Calc.}$ = 76.74 %, $\Delta Resid._{TG}$ = 74.6 % (air), 74.5 % (N_2)).

In the air atmosphere, the second step occurs rapidly between 220 and 350 °C, with a mass loss of 66.90 %, associated with an endothermic peak at 331 °C, attributed to the "pure" enalapril thermal decomposition and the formation of carbonaceous residue at the end of the process. The formation of carbonaceous residue was confirmed by visual inspection, heating the samples to 350 °C, as indicated by the TG-DSC curves.

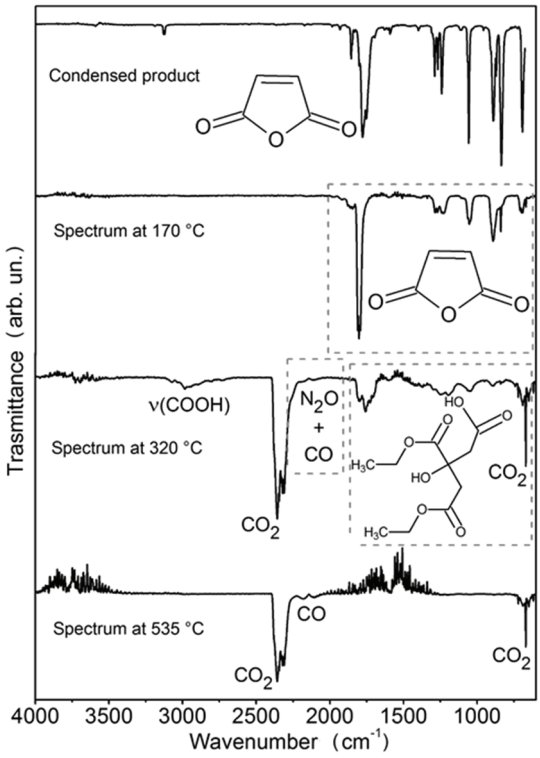

Fig. 3. Infrared FTIR spectra obtained during the thermal decomposition of enalapril maleate in air and N_2.

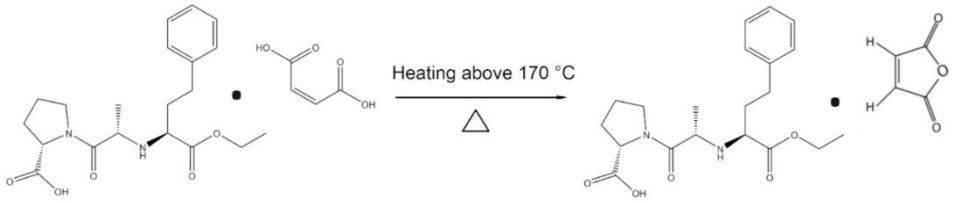

Scheme 1. Proposed mechanism for the first stage of thermal decomposition.

The last step of mass loss in the TG curve between 350-605 °C (Δm_{TG} = = 9.05 %), corresponding to exothermic peaks in the DSC curve at 475, 527 and 607 °C, is attributed to the oxidation of the carbonaceous residue formed in the previous step and/or to the gaseous products that evolved during thermal decomposition.

Regarding gases released during thermal decomposition, the main gaseous products identified by TGA were 1,2-diethyl citrate, CO, CO_2 and N_2O in the second step, and CO_2 and CO in the third stage.

In the pyrolysis condition (nitrogen atmosphere), the second and last step (pure enalapril thermal pyrolysis) in the TGA curve occurs rapidly between 220––330 °C ($\Delta m_{Calc.}$ = 76.74 %, Δm_{TG} = 73.35 %), associated with the endothermic peak in the DSC curve at 290 °C, attributed to the thermal decomposition and the pyrolysis of the material. Due to the absence of oxygen, parallel reactions are avoided, o which prevents the formation of carbonaceous residue. The infrared spectrum obtained during this thermal decomposition step by EGA is shown in Fig. 3. The main gaseous products released were CO_2, N_2O, 1,2-diethyl citrate and maleic anhydride.

Thermokinetic study

The thermal decomposition of enalapril occurs in consecutive mass loss steps; thus, a thermokinetic study was applied to all stages of thermal decomposition. Isoconversional analysis studies were conducted using the methods of Friedman and Kissinger,[23,24] as well as through model fitting (linear regression).[18,19,25] Fig. 4 shows the results obtained through the application of isoconversional analysis.

The Kissinger and Friedman equations are fundamental tools in isoconversional kinetic analysis, providing valuable insights into the thermal degradation kinetics of various materials. The Kissinger method, also known as the Kissinger––Akahira–Sunose (KAS) method, is widely used to determine the kinetic parameters of a reaction. It involves plotting the heating rate's logarithm against the temperature's reciprocal at the maximum degradation rate for different conversions. The slope of the resulting linear relationship yields the activation energy, while the intercept provides the pre-exponential factor. However, it is important to note that in cases where the isoconversional activation energy varies significantly, the Kissinger plots may appear almost perfectly linear, potentially failing to detect the inherent complexity of the processes.[24] The Friedman method is a widely used differential isoconversional for analysing thermal degradation kinetics. This method involves plotting the temperature at a given conversion against the heating rate. The resulting linear relationship provides the means to determine the activation energy and pre-exponential factor.[26]

The isoconversional analysis demonstrated an apparent activation energy for the complete thermal decomposition of enalapril maleate of 47.07±15.45 kJ mol^{-1} with an R^2 of 0.945.

Fig. 5 shows the results of the thermal kinetic analysis through model fitting. The application of various methods to determine the kinetic parameters of thermal decomposition processes is involved in model fitting. Both model-free (isoconversional) and model-fitting methods were used for this purpose, each with its advantages and limitations. Model fitting methods have been a subject of debate within the thermal analysis community, with the interests about the reliability of deriving

kinetic parameters from a single heating rate, which can lead to some unreliable and nonsensical results.[27]

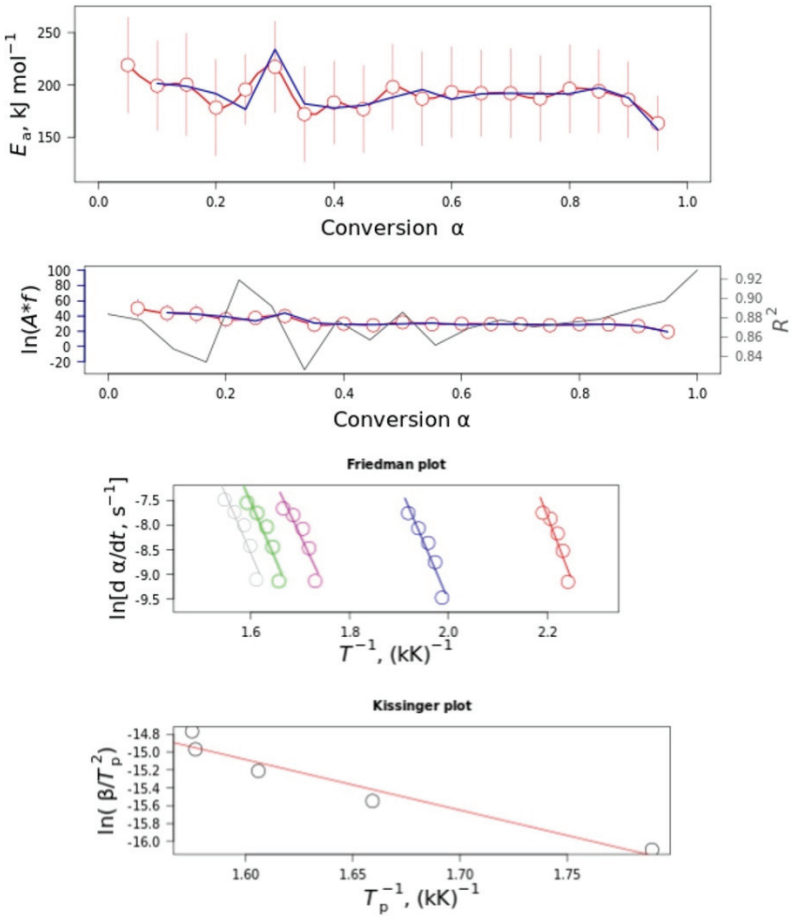

Fig. 4. Results obtained through the application of isoconversional analysis, Friedman plot, and Kissinger plot of thermal decomposition of enalapril.

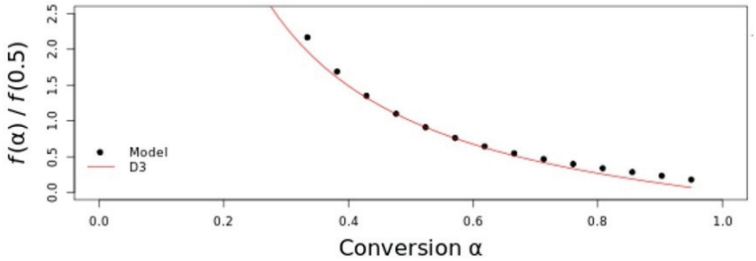

Fig. 5. Results of the thermal kinetic analysis through model fitting of thermal decomposition of enalapril.

However, model fitting methods have historically been widely used in solid-state kinetics and have shown excellent fits to experimental data, although they may produce uncertain kinetic parameters, especially for nonisothermal conditions.[28] The model fitting methods have been used to predict different reaction mechanisms for thermal disintegration processes.[29] Additionally, the model fitting methods have been employed to estimate the kinetic parameters of complex solid-state reactions.[30,31] The kinetic parameters for enalapril maleate demonstrate an apparent activation energy of 55.7±3.4 kJ mol^{-1} with a three-dimensional diffusion thermal degradation model, where $f(\alpha) = 3(1–R)^{2/3}/(2(1–(1–R)^{1/3}))$.

CONCLUSION

When submitted to heating, certain drugs undergo a series of chemical and physical reactions, including decomposition reactions, resulting in compounds different from the original. Thermal analysis can be employed to monitor the sample, while it undergoes the described processes. Thermal analysis was also effective in determining the purity of enalapril maleate.

The thermoanalytical and spectroscopic study of enalapril maleate was conducted to ascertain its purity and thermal behaviour. Purity determination, based on melting point and melting enthalpy, yielded a purity of 99.5 %. The Van't Hoff equation applied to the DSC curve confirmed the high purity, showcasing a melting point at 154 °C with a corresponding $\Delta H_{\text{melt.}}$ of 29.6 kJ mol^{-1}. Simultaneous TG-DSC curves in dynamic air and N_2 atmospheres revealed enalapril's stability up to 148 °C, beyond which thermal decomposition occurred. In air, three decomposition stages were observed between 148–605 °C, with the identified products including maleic anhydride and carbonaceous residue. In N_2, two decomposition stages occurred between 148 and 330 °C. The second step involved thermal decomposition and pyrolysis, releasing CO_2, 1,2-diethyl citrate, N_2O and maleic anhydride.

The thermal decomposition of enalapril maleate was systematically investigated through isoconversional analysis using both the Kissinger and Friedman equations, alongside model fitting methods. The Kissinger method identified an apparent activation energy of 47.07±15.45 kJ mol^{-1} for the complete thermal decomposition, exhibiting an R^2 value of 0.945. The application of the Friedman method supported these findings. Additionally, model fitting methods, despite historical debates regarding their reliability, were employed and resulted in an apparent activation energy of 55.7±3.4 kJ mol^{-1}. The chosen model involved a three-dimensional diffusion thermal degradation model.

Acknowledgments. The authors acknowledge the CNPq and CAPES, Brazil, for research funding. This work is financially supported by the National Council for Scientific and Technological Development of Brazil (CNPq Process N°: 402435/2022-2 and 200114/2022-0) and by the Financing Agency for Studies and Projects of Brazil (FINEP contract 04.13.0448.00/2013),

The authors are grateful to Professor Massao Ionashiro from the group of Thermal Analysis Laboratory Ivo Giolito (LATIG-UNESP) for FTIR technique.

И З В О Д

КАРАКТЕРИЗАЦИЈА ЕНАЛАПРИЛ-МАЛЕАТА: ПРИСТУП КОЈИ КОРИСТИ ТЕРМОАНАЛИТИЧКЕ, ТЕРМОКИНЕТИЧКЕ И СПЕКТРОСКОПСКЕ ТЕХНИКЕ

JOSÉ AUGUSTO TEIXEIRA[1], ADRIAN SANTOS DE SOUZA[2], LAÍS DA SILVA MENDOZA KARDEK DE MELO[2] и TIAGO ANDRÉ DENCK COLMAN[2]

[1]Federal Institute of Paraná, IFPR, Paranavaí, PR, Brazil, [2]Federal University of Grande Dourados, UFGD, Dourados, MS, Brazil

Еналаприл-малеат је лек који се широко користи за лечење кардиоваскуларних болести. Његов механизам деловања је да селективно инхибира ензим који конвертује ангиотензин. Због тога се ћелијама јетре метаболише у еналаприлат. Термичко понашање еналаприл-малеата је испитивано симултаном термогравиметријом и диференцијалном скенирајућом калориметријом (TG-DSC), а анализом еволуираног гаса симултаном термогравиметријом и диференцијалном скенирајућом калориметријом са инфрацрвеном спектроскопијом (TG-DSC–FTIR). Резултати су дали информације о термичкој стабилности, чистоћи, корацима термичке декомпозиције и главним производима насталим током загревања. Утврђено је да је еналаприл-малеат стабилан до 148 °C. Изнад ове температуре долази до термичке деградације супстанце, која се дешава у два степена у инертној атмосфери (N_2) и три степена у оксидационој атмосфери (ваздух). Ослобођени гасови, интермедијери термичке разградње, су идентификовани као анхидрид малеинске киселине. DSC анализа је указала на високу чистоћу материјала (99,5 %). Применом Кисинцерове и Фридманове једначине, заједно са методама уклапања модела, одређена је привидна енергија активације од 47,07±15,45 kJ mol^{-1} за потпуно термичко разлагање. Применом метода уклапања модела са тродимензионалним дифузионим моделом термалне деградације добија се привидна енергија активације од 55,7±3,4 kJ mol^{-1}.

(Примљено 7. децембра 2023, ревидирано 1. фебруара, прихваћено 17. августа 2024)

REFERENCES

1. G. S. Thind, A. Johnson, D. Bhatnagar, T. W. Henkel, *Am. Heart J.* **109** (1985) 852 (https://doi.org/10.1016/0002-8703(85)90650-7)
2. R. Kello, W. Abdelwahed, *Design and evaluation of a new formulations of enalapril maleate 20 mg tablet in a time efficient and on alarge industrial scale*, 2014 (https://api.semanticscholar.org/CorpusID:51815722)
3. R. K. Verbeeck, I. Kanfer, R. Löbenberg, B. Abrahamsson, R. Cristofoletti, D. W. Groot, P. Langguth, J. E. Polli, A. Parr, V. P. Shah, M. Mehta, J. B. Dressman, *J. Pharm. Sci.* **106** (2017) 1933 (https://doi.org/10.1016/j.xphs.2017.04.019)
4. S. P. Bhardwaj, S. Singh, *J. Pharm. Biomed. Anal.* **46** (2008) 113 (https://doi.org/10.1016/j.jpba.2007.09.014)
5. M. De Diego, S. Mennickent, G. Godoy, V. Miranda, *Curr. Pharm. Anal*. **7** (2011) 248 (https://doi.org/10.2174/157341211797458005)
6. D. M. Lima, L. D. dos Santos, E. M. Lima, *J. Pharm. Biomed. Anal.* **47** (2008) 934 (https://doi.org/10.1016/j.jpba.2008.02.030)
7. B. Stanisz, *J. Pharm. Biomed. Anal.* **31** (2003) 375 (https://doi.org/10.1016/S0731-7085(02)00325-4)
8. B. Stanisz, *Acta Pol. Pharm.* **61** (2004) 415 (https://pubmed.ncbi.nlm.nih.gov/15794332)

9. M. Juhász, Y. Kitahara, S. Takahashi, T. Fujii, *J. Pharm. Biomed. Anal*. **59** (2012) 190 (https://doi.org/10.1016/j.jpba.2011.10.011)
10. F. Q. Pires, T. Angelo, J. K. R. Silva, L. C. L. Sá-Barreto, E. M. Lima, G. M. Gelfuso, T. Gratieri, M. S. S. Cunha-Filho, *J. Pharm. Biomed. Anal.* **137** (2017) 196 (https://doi.org/10.1016/j.jpba.2017.01.037)
11. M. Herbrink, H. Vromans, J. Schellens, J. Beijnen, B. Nuijen, *J. Pharm. Biomed. Anal.* **148** (2018) 182 (https://doi.org/10.1016/j.jpba.2017.10.001)
12. A. K. Attia, M. M. Abdel-Moety, S. G. Abdel-Hamid, *Arab. J. Chem.* **10** (2017) S334 (https://doi.org/10.1016/j.arabjc.2012.08.006)
13. A. Raw, M. S. Furness, D. S. Gill, R. C. Adams, F. O. Holcombe Jr., L. X. Yu, *Adv. Drug Deliv. Rev.* **56** (2004) 397 (https://doi.org/10.1016/j.addr.2003.10.011)
14. F. X. Campos, A. L. C. S. Nascimento, T. A. D. Colman, D. A. Gálico, O. Treu-Filho, F. J. Caires, A. B. Siqueira, M. Ionashiro, *J. Therm. Anal. Calorim.* **123** (2016) 91 (https://doi.org/10.1007/s10973-015-4956-7)
15. J. A. Teixeira, W. D. G. Nunes, T. A. D. Colman, A. L. C. S. do Nascimento, F. J. Caires, F. X. Campos, D. A. Gálico, M. Ionashiro, *Thermochim. Acta* **624** (2016) 59 (https://doi.org/10.1016/j.tca.2015.11.023)
16. M. D. Colman, S. R. da S. Lazzarotto, M. Lazzarotto, F. A. Hansel, T. A. D. Colman, E. Schnitzler, *J. Anal. Appl. Pyrolysis* **119** (2016) 157 (https://doi.org/10.1016/j.jaap.2016.03.005)
17. ASTM, *ASTM International: West Conshohocken, ASTM E698-05,* PA, USA (2005) (https://www.astm.org/e0698-05.html)
18. S. Vyazovkin, A. K. Burnham, J. M. Criado, L. A. Pérez-Maqueda, C. Popescu, N. Sbirrazzuoli, *Thermochim. Acta* **520** (2011) 1 (https://doi.org/10.1016/j.tca.2011.03.034)
19. S. Vyazovkin, A. K. Burnham, L. Favergeon, N. Koga, E. Moukhina, L. A. Pérez-Maqueda, N. Sbirrazzuoli, *Thermochim. Acta* **689** (2020) 178597 (https://doi.org/10.1016/j.tca.2020.178597)
20. J. R. MacCallum, J. Tanner, *Eur. Polym. J.* **6** (1970) 1033 (https://doi.org/10.1016/0014-3057(70)90035-2)
21. N. V. Muravyev, A. N. Pivkina, N. Koga, *Molecules* **24** (2019) 2298 (https://doi.org/10.3390/molecules24122298)
22. B. Androsits, *J. Therm. Anal. Calorim.* **55** (1999) 1041 (https://doi.org/10.1023/A:1010123009883)
23. H. L. Friedman, *J. Polym. Sci., C* **6** (1964) 183 (https://doi.org/10.1002/polc.5070060121)
24. S. Vyazovkin, *Molecules* **25** (2020) 2813 (https://doi.org/10.3390/molecules25122813)
25. L. A. Pérez-Maqueda, J. M. Criado, P. E. Sánchez-Jiménez, *J. Phys. Chem., A* **110** (2006) 12456 (https://doi.org/10.1021/jp064792g)
26. A. Soria-Verdugo, E. Goos, N. García-Hernando, U. Riedel, *Algal Res.* **32** (2018) 11 (https://doi.org/10.1016/j.algal.2018.03.005)
27. A. K. Burnham, L. N. Dinh, *J. Therm. Anal. Calorim.* **89** (2007) 479 (https://doi.org/10.1007/s10973-006-8486-1)
28. M. Heydari, M. Rahman, R. Gupta, *Int. J. Chem. Eng.* **2015** (2015) 1 (https://doi.org/10.1155/2015/481739)
29. H. Mahmood, A. Shakeel, A. Abdullah, M. Khan, M. Moniruzzaman, *Polymers (Basel)* **13** (2021) 2504 (https://doi.org/10.3390/polym13152504)
30. A. Agić, E. G. Bajsić, *J. Appl. Polym. Sci.* **103** (2007) 764 (https://doi.org/10.1002/app.25040)
31. N. A. Mariano, M. A. G. Tommaselli, S. E. Kuri, *Materwiss. Werksttech.* **36** (2005) 325 (https://doi.org/10.1002/mawe.200500877).

Journal of the Serbian Chemical Society
JSCS@tmf.bg.ac.rs • www.shd.org.rs/JSCS
J. Serb. Chem. Soc. *89* (10) 1363–1385 (2024)
JSCS–5793
Original scientific paper
Published 25 October, 2024

Ultrasonic and spectroscopic investigations of molecular interactions in binary mixture of PEG-400 and DMSO at different temperatures

MONIKA DHIMAN[1], ARUN UPMANYU[1]*, DEVINDER PAL SINGH[2] and KAILASH CHANDRA JUGLAN[3]

[1]*Chitkara University Institute of Engineering and Technology, Chitkara University, Punjab, 140401, India,* [2]*Acoustics Research Center, Mississauga, L5A 1Y7, Ontario, Canada and* [3]*Department of Physics, Lovely Faculty of Technology and Sciences, Lovely Professional University, Punjab, India*

(Received 7 December 2023, revised 22 January, accepted 2 June 2024)

Abstract: In the present study, the ultrasonic velocity and density data for the binary mixture of polyethylene glycol (PEG)-400 and dimethyl sulfoxide (DMSO), at various concentrations and different temperatures (*T*, 288.15, 298.15 and 308.15 K), have been measured and further apllied to determine several physical parameters such as adiabatic and isothermal compressibility, intermolecular free length, internal pressure and free volume. The excess values of these parameters have also been computed and fitted with the Redlich–Kister (R–K) polynomial equation. The nature, type, and strength of intermolecular interactions present within the PEG-400 + DMSO mixture have been explained based on the sign and magnitude of excess values. Furthermore, partial molar volumes, excess partial molar volumes, apparent molar volumes and apparent molar volumes at infinite dilution have also been determined to investigate the solute–solvent interactions. Various mixing rules such as the ideal mixing rule (U_{im}), Nomoto relation (U_N), impedance dependence relation (U_Z), Junjie relation (U_J), van Deal–Vangeel relation (U_V) and collision factor theory (U_{CFT}) are employed to compute the ultrasonic velocity and compared with the experimental one. Among these relations, the Nomoto and Junjie relations are found to be most suitable for the given mixture. In addition to it, the present system has also been examined using Fourier transform infra-red (FTIR) and UV–Vis spectroscopic techniques. The change in intensity and shift in peak position in the FTIR and UV–Vis spectra of the PEG-400 + DMSO mixture are used to confirm the intermolecular hydrogen bonding in the given system.

Keywords: research development; industry; sustainable development; polyethylene glycol; Fourier transform infra-red (FTIR); UV–Vis.

* Corresponding author. E-mail: arun.upmanyu@chitkara.edu.in
https://doi.org/10.2298/JSC231207058D

INTRODUCTION

In recent years, several researchers have contributed to synthesizing and characterizing significant industrial materials and tuning them to specific applications.[1–5] In such chemical synthesis, the emission of sulphur dioxide (SO_2) is a serious concern that affects the health and environmental sectors.[3–5] Therefore, various processes/techniques have been developed over time to remove SO_2 from industrial products, a process called desulphurisation.[6–8] Dimethyl sulfoxide (DMSO) is a widely used organic solvent for removing SO_2 due to its high solubility for sulphur-containing compounds. However, the high freezing point (18 °C) of DMSO causes problems to use it in the low-temperature range. Adding another biocompatible polyethylene glycol (PEG)-400 into DMSO will overcome this limitation. The other advantages of the PEG-400 + DMSO mixture are its relatively low toxicity and better solubility than virgin DMSO. Furthermore, it can be easily recovered and reused in chemical processes.

A comprehensive review of the literature[6,9–12] reveals that most of the investigations into the PEG-400 and DMSO systems are made to understand their behaviour towards desulphurisation, whereas only limited work is available to explore the nature and strength of inter- and intra-molecular interactions prevalent within the system based on the ultrasonic velocity, density and viscosity. Zhang *et al.*[6] also measured the density of the PEG-400 + DMSO mixture at different concentrations and temperatures. To compare the reported density data with the present data at mutual temperatures (298.15 and 308.15 K), we have generated the fitting equation for density measured in this work:

$$d^* = Y_0 + A\exp(R_0 X_1) \quad (1)$$

where Y_0, A and R_0 are the arbitrary constants and their values at: a) T = 298.15 K are: Y_0 = 1.1216, A = –0.0244 and R_0 = -4.8551; b) T = 308.15 K are: Y_0 = = 1.1139, A = –0.0258 and R_0 = –4.0890.

Thereafter, Eq. (1) was used to compute the density (d^*) at the same mole fractions as reported in a research paper by Zhang *et al.*[6] The correlation of measured density and the one reported in literature[6] along with the absolute average percentage deviation (*AAPD*) at 298.15 and 308.15 K are given in Table S-I (Supplementary material to this paper). The perusal of Table S-I indicates that the *AAPD* is 0.1550 and 0.1488 at 298.15 and 308.15 K, respectively. For a better understanding, the density data obtained in the present study and literature,[6] along with the fitting line, are given in Figs. S-1 and S-2 (Supplementary material). Additionally, the density values of current measurement (using Eq. (1)) and literature[6] at the same mole fractions are presented in Figs. S4 and S-5 (Supplementary material). The probable reason for the deviation can be: *i*) Zhang *et al.*[6] performed the pre-processing (drying over molecular sieves (type 4A) and decompression filtration by vacuum pump), before density measurement of the

materials, whereas in the present work, these materials are used as such without any further purification; *ii*) additionally, we have measured the density using more sophisticated DSA 5000 M interferometer, with the density accuracy of 0.000001 g cm^{-3}; Zhang *et al.*[6] measured density using bicapillary pycnometer.

Moreover, there are several techniques such as infrared (IR) spectroscopy, nuclear magnetic resonance (NMR) spectroscopy, UV–Vis spectroscopy, X-ray crystallography, surface plasmon resonance (SPR), isothermal titration calorimetry (ITC), fluorescence resonance energy transfer (FRET) technique, ultrasonic, volumetric and refractometric techniques are available to investigate different types of molecular interactions in the solid/liquid systems. A literature survey[13–18] reveals that the ultrasonic technique is widely accepted to study molecular interactions for liquid systems due to its unique features like its non-destructive nature, real-time monitoring, versatility, high sensitivity and non-invasiveness. The ultrasonic technique involves measuring the speed and attenuation of ultrasonic waves as they pass through a liquid system. The speed of the ultrasonic wave is affected by the density and compressibility of the liquid mixture, while the attenuation is affected by the viscosity and molecular interactions present in the system. By analysing the changes in speed and attenuation of the ultrasonic waves, it is possible to obtain information about the nature, type, and strength of interactions among the constituent molecules of the mixture. The speed of sound in conjunction with density can be further employed to calculate several important thermodynamical parameters such as acoustic impedance, adiabatic compressibility, intermolecular free length, internal pressure, free volume, *etc*., which are generally difficult to determine experimentally. The concentration and temperature dependence of these parameters also provide useful information about inter and intra-molecular interactions, prevalent in the system. Other useful techniques to study the molecular interactions in liquid systems are FTIR, UV and NMR spectroscopy.[19–21] These techniques rely on the interaction of electromagnetic radiation with the molecules in a sample. The absorption, emission, or scattering of electromagnetic radiation by the sample is measured. The obtained data provides information about the sample's molecular structure and interactions. At present, ultrasonic and spectroscopic techniques are regularly used to investigate the molecular interactions in organic liquids, polymers, polymer blends, ionic liquids and liquid crystals.[22–24]

In the present work, ultrasonic velocity and density values are measured for PEG-400 + DMSO at different mole fractions and temperatures (288.15, 298.15 and 308.15 K). The measured data are used to compute several important thermodynamical parameters such as adiabatic and isothermal compressibility, intermolecular free length, internal pressure, free volume and their excess values. FTIR and UV–Vis spectroscopic investigation has also been taken to explore the molecular interactions in the system under study. The variations in sign and mag-

nitude of excess parameters, with changes in concentration and temperature, have been used to complement/supplement the information obtained *via* other investigative techniques about the nature, type, and strength of molecular interactions prevalent in the system under study.

EXPERIMENTAL

Materials

Polyethylene glycol (PEG) and DMSO with molar masses of 400 and 78.14 g.mol^{-1}, respectively, and purity ≥ 99% were acquired from Loba Chemie Pvt. Ltd., India. The chemicals were used without any further purification for the measurement of ultrasonic velocity (U) and density (d).

*Measurement procedure of ultrasonic velocity (*U*) and density (*d*)*

The ultrasonic velocity (U) and density (d) of the pure PEG-400, DMSO and their mixture at different mole fractions were measured at the three different temperatures (T, 288.15, 298.15 and 308.15 K) using Anton Paar DSA 5000M densimeter which worked at 3 MHZ. The inbuilt Peltier-thermostat of the densimeter controlled the temperature automatically and the working temperature was estimated accurately up to ±0.01 K. The U and d were measured by infusing the sample with a syringe inside the instrument. The instrument can measure density with an accuracy of 0.000001 g cm^{-3} and ultrasonic velocity with an accuracy of 0.01 m s^{-1}. For density measurement, the apparatus was calibrated with doubly distilled degassed water, and with dry air at atmospheric pressure. The repeatability is obtained with triplicate measurements on the same sample maintained inside the densimeter at a constant temperature at different times during the course of present measurements. The density and speed of sound measurements both had experimental uncertainties below 0.0005 g·m^{-3} and 1.0 m·s^{-1}, respectively. Binary mixtures were prepared by mass percents, using an analytical balance with a precision of 0.0001 g (Denver Instrument APX-200). The mole fraction of each mixture was obtained with an accuracy of 0.0001 from the measured masses of the components. The measured values of U and d of pure components had been compared with literature data and are reported in Table I. The contents of Table I indicates that the percentage deviation between experimental and literature values of density and ultrasonic velocity for PEG-400 and DMSO is less than 0.3 % at all temperatures. The comparisons between experimental and literature densities and ultrasonic velocity are presented in Fig. 1a–d.

TABLE I. Experimental and literature values of ultrasonic velocity (U) and density (d) of pure PEG-400 and DMSO; the standard uncertainties (u) are $u(T)$ = 0.01 K, $u(d)$ = 0.5 kg m^{-3}, $u(U)$ = 1.0 m s^{-1}

Component	T / K	U / m s^{-1}		Modulus of deviation, %	d / g cm^{-3}		Modulus of deviation, %
		Exp.	Lit.		Exp.	Lit.	
PEG-400	288.15	1629.30	–		1.13031	1.13126[25]	0.084
	298.15	1595.16	1592.8[26]	0.146	1.12199	1.1226[6]	0.060
			1595.03[27]	0.008		1.12225[25]	0.023
			1593.01[28]	0.135		1.12239[26]	0.036
			1593.20[29]	0.123		1.122308[27]	0.028
						1.12230[28]	0.028
	308.15	1561.90	1558.9[30]	0.190	1.11373	1.1139[6]	0.021
			1564.4[26]	0.162		1.1128[30]	0.081

TABLE I. Continued

Component	T / K	U / m s^{-1}		Modulus of deviation, %	d / g cm^{-3}		Modulus of deviation, %
		Exp.	Lit.		Exp.	Lit.	
			1561.58[27]	0.020		1.11433[26]	0.054
			1559.50[28]	0.153		1.11487[27]	0.103
			1558.99[29]	0.186		1.11489[28]	0.104
DMSO	288.15	1524.25	–		1.10574	–	
	298.15	1490.12	1493[31]	0.193	1.09572	1.0958[6]	0.013
			1484.8[32]	0.356		1.0952[32]	0.045
			1489.2 [33]	0.062		1.0957[19]	0.000
			1485.10[34]	0.338		1.0954[35]	0.026
			1484[36]	0.412		1.09729[33]	0.144
			1485.12[37]	0.336		1.095387[34]	0.030
			1485.5[38]	0.308		1.09537[39]	0.032
			1487[40]	0.210		1.09562[41]	0.009
			1485.12[42]	0.336		1.09537[43]	0.032
			1484.29[44]	0.392		1.09527[45]	0.041
	308.15	1456.54	1450.9[32]	0.385	1.08720	1.08070[46]	0.598
			1451.3[34]	0.357		1.0852[32]	0.181
			1451.6[39]	0.337		1.08548[10]	0.158
			1451.28[34]	0.361		1.0857[19]	0.136
						1.085348[34]	0.170
						1.08550[47]	0.156
						1.0856[48]	0.143
						1.0839[6]	0.304

FTIR and UV–Vis spectroscopy

The FTIR spectrum for the mixture under study was recorded on sophisticated FTIR (Bruker, model Eco AR Alpha II) equipped with Opus software. The spectrometer possessed auto-align energy optimization, dynamically aligned with and RockSolid™ cube corner interferometer and temperature-controlled DLaTGS-detector. Data were recorded in the spectral range of 400–4000 cm^{-1} at 4 cm^{-1} spectral resolution with standard KBr beam splitter possessing precision and accuracy of 0.05 cm^{-1} at 1576 cm^{-1} and <0.0006 cm^{-1} at 1576 cm^{-1}. A baseline correction was made for the spectra recorded in the air. For each measurement 10 μL a solution was used with sample layer thickness typically less than 2 μm. All these measurements were performed at room temperature and atmospheric pressure.

The UV–Vis spectrum for the mixture was recorded on Systronics (India) PC-based double beam UV–Vis spectrophotometer-2202. The spectrophotometer was equipped with modified Czerny–Turner monochromator geometry for better aberration correction, holographic diffraction grating with 1200 lines/mm blazed at 250 nm, and advanced beam technology with PC-controlled settings. The apparatus operates in the wavelength range from 200 to 1100 nm at a resolution of 0.1 nm with an accuracy of ±0.5 nm. In the present case, DMSO is used to make the baseline correction for the spectra.

Theoretical formulation

The experimentally measured data for U and d have been used to compute some physical parameters such as adiabatic compressibility (K_s), isothermal compressibility (K_T), inter-

molecular free length (L_f), free volume (V_f), and internal pressure (P_i) by employing following standard formulations as reported in the literature:[13]

$$K_s = \frac{1}{U^2 d} \tag{2}$$

$$K_T = \frac{1.71\times10^{-3}}{T^{4/9} U^2 d^{4/3}} \tag{3}$$

$$L_f = \frac{2V_a}{Y_S} \tag{4}$$

where $Y_S = (36\pi N V_0^2)^{1/3}$ is the molar surface area, N is Avogadro's number, and $V_0 = V - V_a$, where V is the molar volume, V_a is the available volume at any given temperature, and V_0 is the molar volume of liquid at absolute zero temperature.

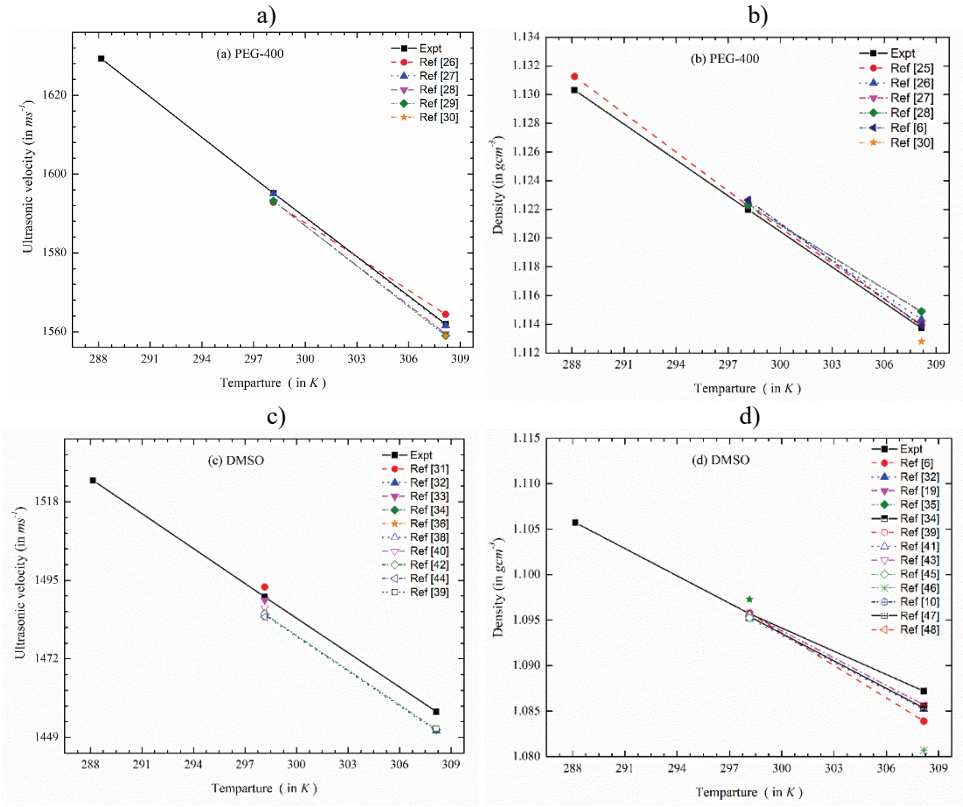

Fig. 1. The plot of experimental and literature values: a) of ultrasonic velocity of PEG-400 at 288.15, 298.15 and 308.15 K; b) of density of PEG-400 at 288.15, 298.15 and 308.15 K; c) for the ultrasonic velocity of DMSO at 288.15, 298.15 and 308.15 K; d) values for the density of DMSO at 288.15, 298.15 and 308.15 K. The solid and dotted lines are a guide for the eye.

The internal pressure (P_i) is a measure of the strength of forces between the molecules and is obtained by using the following relation:

$$P_i = \frac{T\alpha}{K_T} \tag{5}$$

where T is temperature, K_T is isothermal compressibility, and volume expansivity (α) is given by $\alpha = (0.0191 \times K_T)^{1/4}$.

Another important parameter free volume (V_f), which is the average volume of free space between the two neighbouring molecules is given below:

$$V_f = \frac{RT}{P + P_i} \tag{6}$$

where P is external pressure, which is negligible as compared to internal pressure (P_i), R is universal gas constant, and T is temperature.

The theoretical evaluation of ultrasonic velocity (U) has been done using various mixing rules *viz*., ideal mixing rule (U_{im}), Nomoto relation (U_N), impedance dependence relation (U_Z), Junjie relation (U_J), Van Deal-Vangeel relation (U_V), and collision factor theory (U_{CFT}). The mathematical formulations for these relations are given below:[13]

The ideal mixing relation (U_{im}) uses the speed of sound of pure components along with mole fraction to predict the ultrasonic velocity of the mixture, as:

$$U_{IM} = \sum_i^2 X_i U_i \tag{7}$$

where X_i and U_i (i = 1,2) are the mole fraction and sound velocity of pure components, respectively.

Nomoto relation (U_N) based on the assumption of no volume change on mixing, is given as:

$$U_N = \left(\frac{X_1R_1 + X_2R_2}{X_1V_1 + X_2V_2}\right)^3 \tag{8}$$

where V_1 and V_2 are the molar volumes and R_1 and R_2 are the molar sound velocity values of the pure components in the binary mixture.

The standard form of impedance dependence relation (U_Z) to predict ultrasonic velocity is:

$$U_Z = \frac{X_1Z_1 + X_2Z_2}{X_1d_1 + X_2d_2} \tag{9}$$

where X_1, X_2, Z_1, Z_2 and d_1, d_2 are, respectively, the mole fraction, acoustic impedance, and density values of pure components in a binary mixture.

Junjie relation (U_J) predicts ultrasonic velocity using mole fractions X_1 and X_2, molar masses M_1 and M_2, molar volumes V_1 and V_2, density d_1, and $d_2$and ultrasonic speed U_1 and U_2 of pure components:[49]

$$U_J = \frac{X_1V_1 + X_2V_2}{\sqrt{(X_1M_1 + X_2M_2)(X_1V_1 / (d_1U_1^2)) + X_2V_2 / (d_2U_2^2)}} \tag{10}$$

Van Deal and Vangeel (U_V) modified the ideal mixing relation using molar weight M_1 and M_2 of pure components;[13]

$$U_V = \frac{1}{\sqrt{(X_1M_1 + X_2M_2)(X_1/(d_1U_1^2)) + X_2/(d_2U_2^2)}} \quad (11)$$

The collision factor theory (U_{CFT}) is based on the concept of collisions taking place amongst liquid molecules and the free space available between them. It provides an expression for the calculation of ultrasonic velocities in a binary mixture, as given below:[13]

$$U_{CFT} = U_\infty(X_1S_1 + X_2S_2)\frac{X_1B_1 + X_2B_2}{V} \quad (12)$$

where U_∞ is the limiting value of sound velocity for liquids, which is taken as 1600 m s^{-1}. S_1 and S_2 are collision factors. B_1 and B_2 are geometrical volumes per mole of solute and solvent, respectively.

RESULTS AND DISCUSSION

Acoustical parameters and molecular interactions

The experimentally measured ultrasonic velocity (U) and density (d) data for PEG-400 + DMSO binary mixture at various concentrations and temperatures are reported in Table II. Therein, the obtained results are presented as a function of the mole fraction (X_1) of PEG-400 at different temperatures (288.15, 298.15 and 308.15 K).

TABLE II. Measured values of ultrasonic velocity (U) and density (d) of PEG-400 (X_1) + DMSO (X_2) at different temperatures

X_1	288.15 K		298.15 K		308.15 K	
	U / m s^{-1}	d / g cm^{-3}	U / m s^{-1}	d / g cm^{-3}	U / m s^{-1}	d / g cm^{-3}
0	1524.25	1.10574	1490.12	1.09572	1456.54	1.08720
0.0477	1564.03	1.11383	1522.6	1.10408	1489.42	1.09452
0.0790	1569.29	1.11716	1534.37	1.10604	1497.3	1.09549
0.1178	1574.43	1.11877	1547.78	1.10785	1513.44	1.09787
0.1668	1587.41	1.12024	1559.49	1.10936	1529.19	1.09934
0.2310	1598.23	1.12464	1567.88	1.11288	1539.9	1.10375
0.3185	1612.76	1.12614	1579.28	1.11712	1548.13	1.10771
0.4448	1618.22	1.12792	1583.57	1.11870	1550.07	1.11007
0.5516	1621.16	1.12855	1586.64	1.11957	1553.20	1.11104
0.6431	1623.25	1.12900	1588.84	1.12019	1555.44	1.11173
0.8278	1626.71	1.12975	1592.45	1.12122	1559.13	1.11287
1	1629.30	1.13031	1595.16	1.12199	1561.9	1.11373

Using the experimentally measured U and d values, some acoustical and thermodynamical parameters, *viz*., K_S, K_T, L_f, V_f and P_i, have been determined. These parameters are reported in Table III. Several researchers have pointed out that acoustical and thermodynamical parameters are important tools to explore the nature and strength of molecular interactions in a liquid system.[50–52] Keeping this in view, we have calculated the excess values of these acoustical and thermodynamical parameters using a standard relation as given below:

$$A^{\text{Excess}} = A^{\text{Exp}} - (A_1X_1 + A_2X_2) \quad (13)$$

where A represents K_s, K_T, L_f, V_f and P_i. A^{Excess} and A^{Exp} are the excess and experimental values of A. X_1 and X_2 are the mole fractions of the solute and the solvent, respectively.

The excess values of all these parameters as a function of the mole fraction (X_1) of PEG-400 are plotted in Figs. 2–6 at different temperatures. These excess values are also fitted with Redlich–Kister (R–K)[11] type polynomial equation given below:

$$\Delta Y = X_1X_2\sum_{K=1}^{n} A_K\,(2X_1 - 1)^{(K-1)} \quad (14)$$

where ΔY is the excess parameter to be fitted with the R–K polynomial equation, and A_K is the fitting parameter. The number of fitting parameters is optimized by using F-test.[53] The standard deviations (σ) are computed using the relation:

$$\sigma(\Delta Y) = \sqrt{\frac{\Sigma(\Delta Y_{\text{Exp}} - \Delta Y_{\text{Cal}})}{N - n}} \quad (15)$$

where N is the total number of mole fractions and n is the number of fitting parameters. ΔY_{exp} and ΔY_{Cal} are the experimental and calculated values of excess parameters. The computed values of R–K coefficients and σ are reported in Table IV.

TABLE III. Acoustical parameters, *viz*., free volume (V_f), adiabatic compressibility (K_s), isothermal compressibility (K_T), intermolecular free length (L_f) and internal pressure (P_i) for PEG-400 + DMSO at different temperatures; the standard uncertainties (u) are $u(T)$ = 0.01 K, $u(d)$ = 0.5 kg m^{-3}, $u(U)$ = 1.0 m s^{-1}

X_1	$V_f\times10^6$ / m^3 mol^{-1}	$K_s\times10^{-10}$ / Pa^{-1}	$K_T\times10^{-10}$ / Pa^{-1}	L_f / pm	P_i / MPa
			T = 288.15 K		
0	4.327±0.004	3.893±0.005	5.194±0.007	39.84±0.042	553.7±0.006
0.0477	4.133±0.004	3.670±0.005	4.886±0.007	38.69±0.035	579.7±0.006
0.0790	4.100±0.004	3.635±0.005	4.834±0.006	38.50±0.034	584.3±0.006
0.1178	4.074±0.004	3.606±0.005	4.793±0.006	38.35±0.034	588.1±0.006
0.1668	4.019±0.004	3.543±0.005	4.707±0.006	38.01±0.032	596.1±0.006
0.2310	3.962±0.004	3.481±0.005	4.619±0.006	37.68±0.030	604.6±0.006
0.3185	3.904±0.004	3.414±0.004	4.528±0.006	37.31±0.029	613.7±0.006
0.4448	3.878±0.003	3.386±0.004	4.488±0.006	37.16±0.028	617.8±0.006
0.5516	3.865±0.003	3.372±0.004	4.468±0.006	37.08±0.028	619.8±0.006
0.6431	3.856±0.003	3.361±0.004	4.454±0.006	37.02±0.027	621.3±0.006
0.8278	3.841±0.003	3.345±0.004	4.432±0.006	36.93±0.027	623.7±0.006
1	3.830±0.003	3.333±0.004	4.415±0.006	36.86±0.027	625.5±0.006
			T = 298.15 K		
0	4.466±0.004	4.110±0.006	5.418±0.008	41.70±0.050	555.0±0.006
0.0477	4.291±0.004	3.907±0.005	5.137±0.007	40.65±0.043	577.6±0.006
0.0790	4.235±0.004	3.840±0.005	5.047±0.007	40.31±0.041	585.4±0.006
0.1178	4.173±0.004	3.768±0.005	4.949±0.007	39.93±0.039	594.0±0.006

TABLE III. Continued

X_1	$V_f \times 10^6$ / m^3 mol^{-1}	$K_s \times 10^{-10}$ / Pa^{-1}	$K_T \times 10^{-10}$ / Pa^{-1}	L_f / pm	P_i / MPa
		T = 298.15 K			
0.1668	4.120±0.004	3.706±0.005	4.866±0.007	39.60±0.037	601.6±0.006
0.2310	4.074±0.004	3.655±0.005	4.794±0.006	39.32±0.036	608.4±0.006
0.3185	4.015±0.004	3.589±0.005	4.701±0.006	38.97±0.034	617.4±0.006
0.4448	3.993±0.004	3.565±0.005	4.667±0.006	38.83±0.033	620.8±0.006
0.5516	3.978±0.004	3.548±0.005	4.644±0.006	38.74±0.033	623.1±0.006
0.6431	3.968±0.004	3.536±0.005	4.628±0.006	38.68±0.032	624.7±0.006
0.8278	3.951±0.004	3.517±0.005	4.601±0.006	38.57±0.032	627.4±0.006
1	3.938±0.004	3.503±0.005	4.581±0.006	38.49±0.031	629.4±0.006
		T = 308.15 K			
0	4.607±0.004	4.336±0.006	5.647±0.008	43.61±0.059	556.1±0.006
0.0477	4.426±0.004	4.119±0.006	5.352±0.008	42.50±0.051	578.9±0.006
0.0790	4.387±0.004	4.072±0.006	5.290±0.007	42.26±0.049	584.0±0.006
0.1178	4.307±0.004	3.977±0.006	5.163±0.007	41.76±0.046	594.8±0.006
0.1668	4.235±0.004	3.890±0.005	5.048±0.007	41.31±0.043	604.9±0.006
0.2310	4.174±0.004	3.821±0.005	4.951±0.007	40.94±0.041	613.7±0.006
0.3185	4.126±0.004	3.767±0.005	4.876±0.007	40.65±0.039	620.9±0.006
0.4448	4.110±0.004	3.749±0.005	4.850±0.007	40.55±0.039	623.4±0.006
0.5516	4.094±0.004	3.731±0.005	4.756±0.007	40.45±0.038	632.6±0.006
0.6431	4.083±0.004	3.718±0.005	4.807±0.007	40.38±0.038	627.5±0.006
0.8278	4.064±0.004	3.696±0.005	4.777±0.006	40.27±0.037	630.4±0.006
1	4.050±0.004	3.681±0.005	4.756±0.006	40.18±0.037	632.6±0.006

Table IV. Coefficients of Redlich–Kister (R–K) equation and standard deviation (σ) values for liquid PEG-400 + DMSO at different temperatures

T / K	Parameter	A_0	A_1	A_2	A_3	A_4	σ
288.15	K_s^E	–9.237	5.450	–7.918	13.088		0.271
298.15		–9.922	7.449	–9.754	11.338		0.126
308.15		–10.794	10.231	–10.702	6.867		0.130
288.15	K_T^E	–12.872	7.619	–11.114	18.283		0.372
298.15		–13.665	10.123	–13.263	15.734		0.183
308.15		–14.665	13.650	–14.187	9.448		0.182
288.15	L_f^E	–4.883	2.911	–4.021	6.573		0.141
298.15		–5.201	3.947	–4.950	5.565		0.064
308.15		–5.614	5.390	–5.399	3.116		0.066
288.15	P_i^E	12.517	–11.399	–10.435	0.046	38.408	0.474
298.15		12.300	–11.202	0.828	–3.901	18.772	0.082
308.15		12.326	–12.213	9.205	–3.403	2.610	0.160
288.15	V_f^E	–0.818	0.487	–0.692	1.131		0.004
298.15		–0.859	0.640	–0.820	0.957		0.001
308.15		–0.913	0.856	–0.869	0.550		0.001

The inspection of Fig. 2 reveals that the K_s^E is throughout negative in the given concentration range at 288.15 K. The overall negative trend of K_s^E indi-

cates the presence of a hydrogen bonding between PEG-400 and DMSO.[54] Moreover, a close look at Fig. 2 shows that the magnitude of negative deviation is the highest around $X_1 \approx 0.3$. Furthermore, Fig. 2 displays that at temperatures 298.15 and 308.15 K, a similar behaviour is observed for the PEG-400 and DMSO binary system. However, a slight increase in the negative value of K_S^E is obvious. This is expected because a rise in temperature enhances the kinetic energy of molecules, leading to the weakening of molecular interactions. The variations in K_T^E values with changes in mole fraction (X_1) and rise in temperature (Fig. 3) are similar to the variations observed for K_S^E values with such changes.

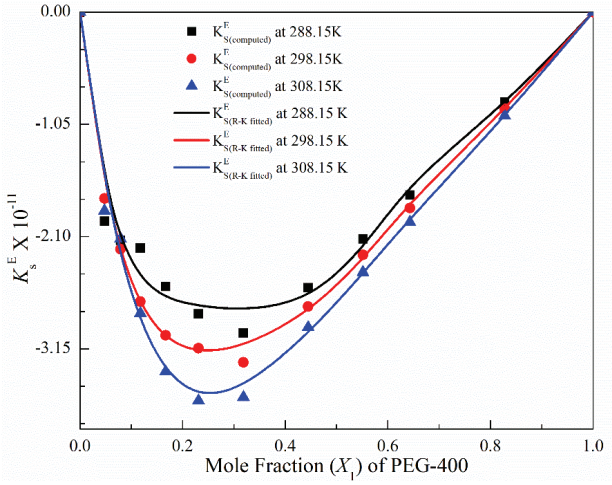

Fig. 2. Excess adiabatic compressibility (K_S^E) for PEG-400 + DMSO at different temperatures. The solid curves represent the Redlich–Kister equation fitting.

Since the intermolecular free length (L_f) and adiabatic compressibility (K_S) are directly related to each other, so with the increase in K_S values, an increase in L_f values is expected.[55] Table III reports that both K_S and L_f are decreasing with the rise in the mole fraction (X_1) of PEG-400. It is likely due to the quick uncoiling of the small-sized chain (carbon atoms = 17) of PEG-400 in a highly polar aprotic organo-sulphur solvent DMSO (dipole moment = 3.96 D*), due to the dipole-induced dipole and hydrogen bonding interactions between solute and solvent molecules. The rise in the temperature from 298.15 to 308.15 K for the mixture shows a slight increase in K_S and L_f values, which is expected, as the enhancement of thermal agitations in the system leads to a higher mobility of the molecules. The excess intermolecular free length (L_f^E) is directly linked to the weakening of intra-molecular interactions and the formation of H-bonding in the sys-

* 1 D = 3.335×10^{-30} C m

tem.[54,55] The overall negative value of L_f^E for the mixture (Fig. 4) points to the presence of inter-molecular H-bonding in the system. The minimum value of L_f^E occurs around $X_1 \approx 0.3$, indicating the presence of the greatest strength of hydrogen bonding at that concentration. The order of strength of intermolecular interactions with the increase in temperature is $(L_f^E)_{288.15\ K} > (L_f^E)_{298.15\ K} > (L_f^E)_{308.15\ K}$.

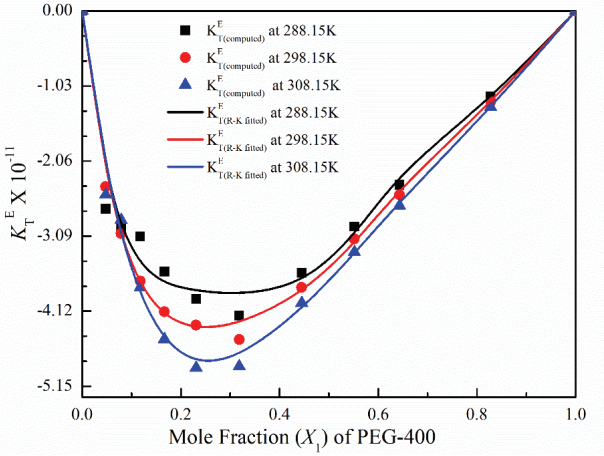

Fig. 3. Excess isothermal compressibility (K_T^E) for PEG-400 + DMSO at different temperatures. The solid curves represent the Redlich–Kister equation fitting.

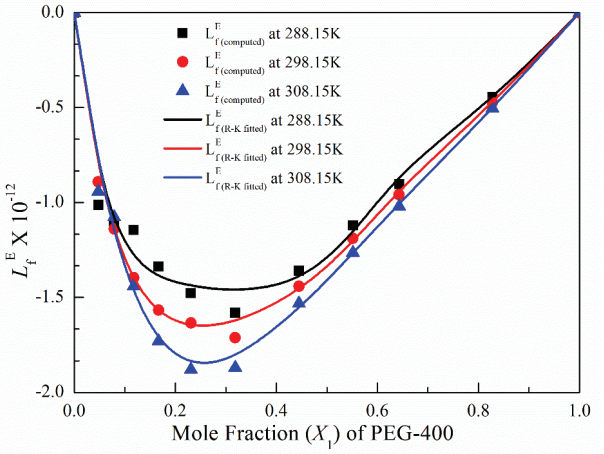

Fig. 4. Excess free length (L_f^E) for PEG-400 + DMSO at different temperatures. The solid curves represent the Redlich–Kister equation fitting.

The internal pressure (P_i), the result of the molecules' attractive and repulsive interactions, is a parameter that is sensitive to all three types of interactions, *viz*., solute–solute (A–A), solute–solvent (A–B), and solvent–solvent (B–B) inter-

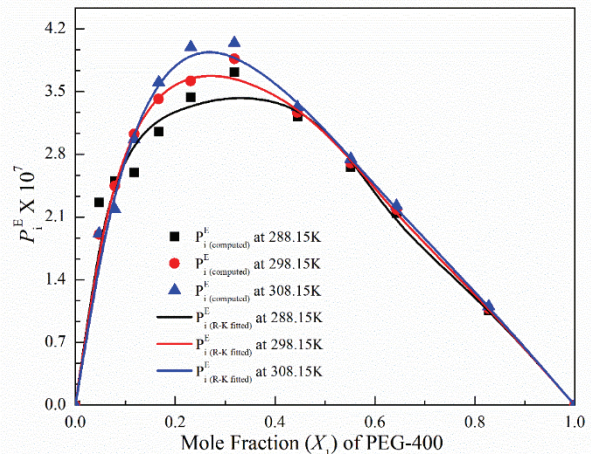

Fig. 5. Excess internal pressure (P_i^E) for PEG-400 + DMSO at different temperatures. The solid curves represent the Redlich–Kister equation fitting.

actions, in a mixture.[56] The excess internal pressure (P_i^E) is also very sensitive to the variations in the strength of the intermolecular interactions. Fig. 5 exhibits that P_i^E is positive over the entire mole fraction (X_1) range. It confirms that the A–B interactions dominate over A–A and B–B interactions. Rao *et al.*,[57]reported that an increase in P_i values leads to a decrease in free volume (V_f). The negative values of V_f^E throughout the concentration range (Fig. 6) point to the enhancement

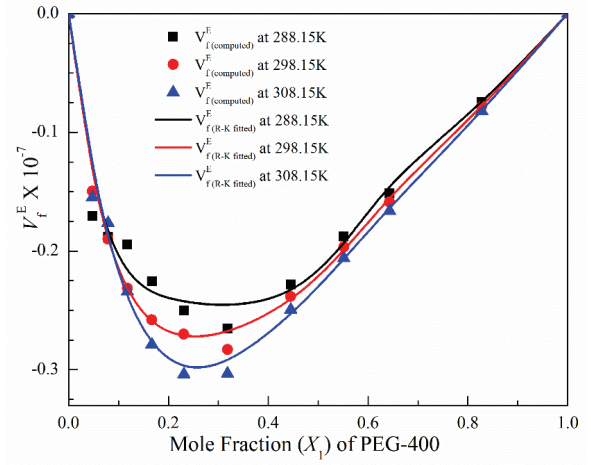

Fig. 6. Excess free volume (V_f^E) for PEG-400 + DMSO at different temperatures. The solid curves represent the Redlich–Kister equation fitting.

of compactness among the molecules of the mixture, confirming the existence of attractive interactions in the system.[58]Excess parameters, *viz.*, V_f^E, K_s^E, K_T^E, L_f^E

and P_1^E for the binary mixture studied here, are fitted with the R–K polynomial equation, determined by the least-square regression method. Table IV reports the R–K polynomial coefficients for the system in the temperature range of 288.15 to 308.15 K. The low σ values points to the suitability of the R–K polynomial equation for the system under study at all the temperatures investigated here.

Partial and apparent molar volumes

For the given system of PEG-400 + DMSO, the partial molar volume ($\bar{V}_1, \bar{V}_2$), excess partial molar volume ($\bar{V}_1^E, \bar{V}_2^E$), apparent molar volume ($V_{\varphi_1}, V_{\varphi_2}$) and apparent molar volume at infinite dilution ($\bar{V}_{\varphi_1}^{\infty}, \bar{V}_{\varphi_2}^{\infty}$) is calculated and presented in Tables V and VI. Partial molar volumes and apparent molar volumes of solute and solvent are obtained using the standard procedure reported below (Eqs. (16)–(19)):[59,60]

$$\bar{V}_1 = V + (1 - X_1)\frac{\partial V}{\partial X_1} \tag{16}$$

$$\bar{V}_2 = V + (1 - X_2)\frac{\partial V}{\partial X_2} \tag{17}$$

$$V_{\varphi_1} = V_1 + \frac{V_m^E}{X_1} \tag{18}$$

$$V_{\varphi_2} = V_2 + \frac{V_m^E}{X_2} \tag{19}$$

Here, V_m^E is the molar excess volume.

TABLE V. Partial volume, excess partial molar volume and apparent molar volume for PEG--400(1) + DMSO (2) at different temperatures; the standard uncertainties (u) are $u(T)$ = 0.01 K, $u(d)$ = 0.5 kg m^{-3}, $u(U)$ = 1.0 m s^{-1} and $U(x_1)$ = 0.0001 kg/mol

X_1	V_1 cm^3 mol^{-1}	V_2 cm^3 mol^{-1}	V_1^E cm^3 mol^{-1}	V_2^E cm^3 mol^{-1}	V_{φ_1} cm^3 mol^{-1}	V_{φ_2} cm^3 mol^{-1}
			288.15 K			
0	348.87±0.158	70.66±0.032	–5.015	0.000	–	70.66±0.032
0.0477	349.79±0.157	70.61±0.032	–4.096	–0.046	348.87±0.157	70.41±0.032
0.0790	352.60±0.158	70.40±0.032	–1.290	–0.254	349.64±0.156	70.29±0.031
0.1178	354.62±0.158	70.22±0.031	0.738	–0.435	351.37±0.157	70.32±0.031
0.1668	352.46±0.157	70.67±0.032	–1.428	0.008	352.50±0.157	70.38±0.031
0.2310	351.97±0.156	70.58±0.031	–1.919	–0.075	351.72±0.156	70.01±0.031
0.3185	353.66±0.157	70.10±0.031	–0.230	–0.561	352.45±0.156	69.99±0.031
0.4448	353.75±0.157	69.98±0.031	–0.135	–0.680	352.90±0.156	69.87±0.031
0.5516	353.96±0.157	69.82±0.031	0.071	–0.838	353.28±0.157	69.91±0.031
0.6431	353.92±0.157	69.87±0.031	0.037	–0.786	353.49±0.157	69.94±0.031
0.8278	353.90±0.157	69.95±0.031	0.010	–0.708	353.75±0.157	70.00±0.031
1	353.89±0.157	70.00±0.031	0.000	–0.661	353.89±0.157	–

TABLE V. Continued

X_1	$\bar{V}_1$ / cm^3 mol^{-1}	$\bar{V}_2$ / cm^3 mol^{-1}	$\bar{V}_1^E$ / cm^3 mol^{-1}	$\bar{V}_2^E$ / cm^3 mol^{-1}	V_{φ_1} / cm^3 mol^{-1}	V_{φ_2} / cm^3 mol^{-1}
			298.15 K			
0	351.51±0.160	71.30±0.033	–5.000	0.000	–	71.30±0.033
0.0477	354.38±0.160	71.16±0.032	–2.130	–0.144	351.51±0.159	71.05±0.032
0.0790	357.41±0.162	71.00±0.032	0.901	–0.301	353.90±0.160	71.08±0.032
0.1178	357.86±0.162	70.95±0.032	1.345	–0.353	355.21±0.160	71.13±0.032
0.1668	356.53±0.161	71.24±0.032	0.022	–0.069	356.19±0.161	71.24±0.032
0.2310	354.47±0.159	71.69±0.032	–2.042	0.390	355.77±0.160	71.08±0.032
0.3185	355.28±0.159	71.24±0.032	–1.229	–0.066	355.14±0.159	70.66±0.032
0.4448	356.59±0.159	70.61±0.032	0.082	–0.692	355.73±0.159	70.68±0.032
0.5516	356.61±0.159	70.61±0.032	0.099	–0.696	356.04±0.159	70.73±0.032
0.6431	356.56±0.159	70.68±0.032	0.051	–0.624	356.22±0.159	70.77±0.032
0.8278	356.52±0.159	70.79±0.032	0.014	–0.515	356.42±0.159	70.86±0.032
1	356.51±0.159	70.86±0.032	0.000	–0.449	356.51±0.159	–
			308.15 K			
0	355.86±0.164	71.86±0.033	–3.292	0.000	–	71.86±0.033
0.0477	359.39±0.164	71.69±0.033	0.236	–0.177	355.86±0.163	71.70±0.033
0.0790	361.29±0.165	71.65±0.033	2.137	–0.214	358.80±0.164	71.83±0.033
0.1178	360.56±0.164	71.67±0.033	1.405	–0.193	359.11±0.164	71.86±0.033
0.1668	359.06±0.163	72.03±0.033	–0.094	0.166	359.89±0.164	72.01±0.033
0.2310	356.96±0.162	72.42±0.033	–2.195	0.558	358.82±0.163	71.76±0.033
0.3185	358.03±0.162	71.97±0.032	–1.119	0.104	358.26±0.162	71.44±0.032
0.4448	359.05±0.162	71.41±0.032	–0.098	–0.452	358.49±0.161	71.33±0.032
0.5516	359.26±0.162	71.25±0.032	0.112	–0.609	358.77±0.161	71.39±0.032
0.6431	359.21±0.162	71.34±0.032	0.058	–0.527	358.92±0.161	71.44±0.032
0.8278	359.17±0.162	71.46±0.032	0.015	–0.404	359.08±0.161	71.53±0.032
1	359.15±0.162	71.53±0.032	0.000	–0.330	359.15±0.161	–

TABLE VI. Molar volume and apparent molar volume at infinite dilution for PEG-400(1) + DMSO (2) at different temperatures

T / K	$\bar{V}_1$ / cm^3 mol^{-1}	$\bar{V}_2$ / cm^3 mol^{-1}	$\bar{V}_{\varphi_1}^{\infty}$ / cm^3 mol^{-1}	$\bar{V}_{\varphi_2}^{\infty}$ / cm^3 mol^{-1}
288.15	353.89	70.66	350.44	70.40
298.15	356.51	71.30	354.11	71.16
308.15	359.15	71.86	358.22	71.85

The values of $\bar{V}_{\varphi_1}^{\infty}$ and $\bar{V}_{\varphi_2}^{\infty}$ are determined using the analytical extrapolation methods. In this approach, $\bar{V}_{\varphi_1}^{\infty}$ is obtained by taking V_{φ_1} to $X_1 = 0$ ($X_2 = 1$) and $\bar{V}_{\varphi_2}^{\infty}$ is obtained by taking the V_{φ_2} to $X_2 = 0$ ($X_1 = 1$).

The portray of Table V indicate that in general, the excess partial volumes are negative at all temperatures. It is well mentioned in literature that, the negative values of $\bar{V}_1^E$ and $\bar{V}_2^E$ is an indicative of intermolecular interaction by hydrogen bonding or due to the geometrical fitting of one component into another.[61] These findings are in agreement with the results arrived earlier for the given sys-

tem PEG-400 + DMSO. The apparent molar volume at infinite dilution is an important property to access the solute-solvent interaction of the liquid mixtures. At infinite dilution, the apparent molar volume only depends upon the solute––solvent interaction, and the contribution of solute-solute interactions disappears in the mixture; furthermore, at infinite dilution, solute–solvent interaction becomes independent of the composition of the mixture.[61] The apparent molar volume for a solute and a solvent at different temperatures are reported in Table VI. The inspection of Table VI reveals that the apparent molar volume at infinite dilution for PEG-400 and DMSO is less than that of pure molar volume, which confirms that the solute–solvent interactions in the system are present.[60] Furthermore, the differences $\bar{V}_{\varphi_1}^{\infty} - V_1$ and $\bar{V}_{\varphi_2}^{\infty} - V_2$ decrease with temperature, which indicates that the solute–solvent interactions get weaker with the rise in temperature.

Theoretical estimation of ultrasonic velocity of the mixture

Using various standard relations such as the ideal mixing relation (IMR), Nomoto relation (NR), impedance dependence relation (IDR), van Deal–Vangeel relation (VVR), Junjie relation (JR), Schaaff's collision factor theory (CFT) and the ultrasonic velocities in the PEG-400 + DMSO mixture have been determined. The experimentally measured values of ultrasonic velocity (U*) along with theoretically predicted U_{IM}, U_N, U_Z, U_V, U_J, and U_{CFT} values at 288.15, 298.15 and 308.15 K, for the binary mixture under study are reported in Table VII. It is obs-

TABLE VII. Experimental (U*) and calculated ultrasonic velocity using different mixing rules for PEG-400 + DMSO at different temperatures

X_1	U*	U_{IM}	U_N	U_Z	U_V	U_J	U_{CFT}
			T = 288.15 K				
0	1524	1524	1524	1524	1524	1524	1513
0.0477	1564	1529	1545	1529	1422	1543	1529
0.0790	1569	1533	1555	1533	1370	1553	1536
0.1178	1574	1537	1566	1537	1317	1563	1541
0.1668	1587	1542	1576	1542	1264	1574	1545
0.2310	1598	1549	1587	1549	1213	1584	1553
0.3185	1613	1558	1597	1558	1169	1595	1557
0.4448	1618	1571	1608	1572	1140	1606	1560
0.5516	1621	1582	1614	1583	1144	1613	1561
0.6431	1623	1592	1619	1592	1168	1618	1561
0.8278	1627	1611	1625	1612	1296	1625	1561
1	1629	1629	1629	1629	1629	1629	1560
			T = 298.15 K				
0	1490	1490	1490	1490	1490	1490	1510
0.0477	1523	1495	1511	1495	1390	1509	1527
0.0790	1534	1498	1521	1499	1339	1519	1532
0.1178	1548	1502	1532	1503	1287	1529	1536

TABLE VII. Continued

X_1	U^*	U_{IM}	U_N	U_Z	U_V	U_J	U_{CFT}
			T = 298.15 K				
0.1668	1559	1508	1542	1508	1236	1539	1541
0.2310	1568	1514	1553	1515	1186	1550	1547
0.3185	1579	1524	1563	1524	1143	1561	1554
0.4448	1584	1537	1574	1537	1115	1572	1557
0.5516	1587	1548	1580	1549	1119	1579	1558
0.6431	1589	1558	1584	1558	1142	1583	1559
0.8278	1592	1577	1591	1577	1268	1590	1559
1	1595	1595	1595	1595	1595	1595	1558
			T = 308.15 K				
0	1457	1457	1457	1457	1457	1457	1507
0.0477	1489	1462	1477	1462	1359	1475	1523
0.0790	1497	1465	1488	1465	1309	1485	1526
0.1178	1513	1469	1498	1469	1258	1495	1532
0.1668	1529	1474	1509	1474	1208	1506	1536
0.2310	1540	1481	1519	1481	1160	1516	1544
0.3185	1548	1490	1530	1491	1117	1527	1551
0.4448	1550	1503	1540	1504	1090	1539	1555
0.5516	1553	1515	1547	1515	1094	1545	1556
0.6431	1555	1524	1551	1525	1117	1550	1557
0.8278	1559	1544	1558	1544	1240	1557	1557
1	1562	1562	1562	1562	1562	1562	1557

TABLE VIII. Absolute percentage deviation (*APD*) for ultrasonic velocity mixing rules applied on PEG-400 + DMSO at different temperatures

T / K	U_{IM}	U_N	U_Z	U_V	U_J	U_{CFT}
288.15	2.0	0.5	2.0	18.1	0.6	3.0
298.15	2.1	0.6	2.1	18.2	0.7	1.1
308.15	2.2	0.6	2.2	18.3	0.8	-0.8

erved that U_N and U_J are well matches with U^*, whereas U_{IM}, U_Z and U_{CFT} are showing a reasonable agreement with the experimental values. However, U_V values show a large departure from experimental values. Thereby, the VVR fails to determine the ultrasonic velocity values in the given temperature and concentration range for the system. It is likely due to the large difference in size of the molecules of PEG-400 and DMSO. To have a better understanding of the compatibility of these relations to predict the ultrasonic velocity in the given concentration and temperature range for the system, the absolute percentage deviation (*APD*) values were determined. These values are presented in Table VIII. It is worth noting here that *APD* values for U_N (NR) and U_J (JR) are <1 %, ~2 % for U_{IM} (IMR) and Uz (IDR), respectively, and ~18 % for U_V (VVR) at all the working temperatures. Moreover, the *APD* value for CFT is <1 % at 308.15 K, 3.0 % at 288.15 K and 1.1 % at 298.15 K. Thus, it can be concluded that except

VVR, the other five relations investigated here can be successfully employed to predict the ultrasonic velocity for the system, in the given concentration range and at all working temperatures.

UV–Vis spectra

The UV–Vis spectra of PEG-400 with DMSO is presented in Fig. 7. A close look at Fig. 7 reveals that the absorption peak of PEG-400 is shifted from 247 to 253 nm, as DMSO concentration increases in the mixture, which indicates the possibility of hydrogen bonding between the hydrogen of the hydroxyl group of PEG-400 and the free lone pair of oxygen atom of DMSO, *i.e.*, $(CH_3)_2S{=}O{---}H{-}(OCH_2{-}CH_2{-}O)_{PEG}{-}H{---}O{=}S(CH_3)_2$.[35] It can be attributed to the n→π* electronic transition of the unshaped electronic pair of oxygen atoms in DMSO.

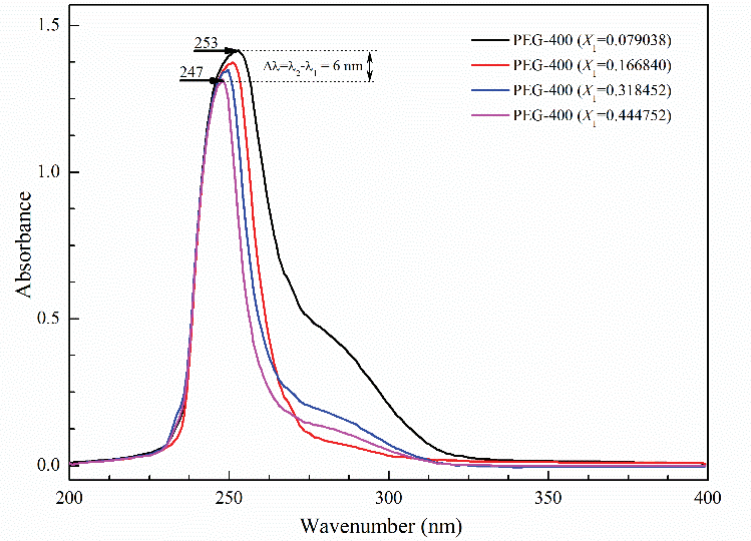

Fig. 7. UV–Vis spectra of PEG-400 + DMSO at increasing concentrations of DMSO.

FTIR spectra

The FTIR spectra of pure DMSO, pure PEG-400 and their binary mixture are presented in Fig. 8a–e, respectively. The perusal of spectra of pure DMSO (Fig. 8a) indicates a peak at wave number 3430.65 cm^{-1}, which is indicative of O–H stretching.

A peak at 1019.25 cm^{-1} describes the C–S stretching vibrations of molecules. The close look to Fig. 8 also infers a considerable shift (36–48 cm^{-1}) as well as a broadening in the 3445.39 cm^{-1} peak with the change in concentration DSMO in the mixtures (Fig 8c–e), which is most likely due to the breaking of the intra-molecular interactions of PEG-400 and the formation of intermolecular

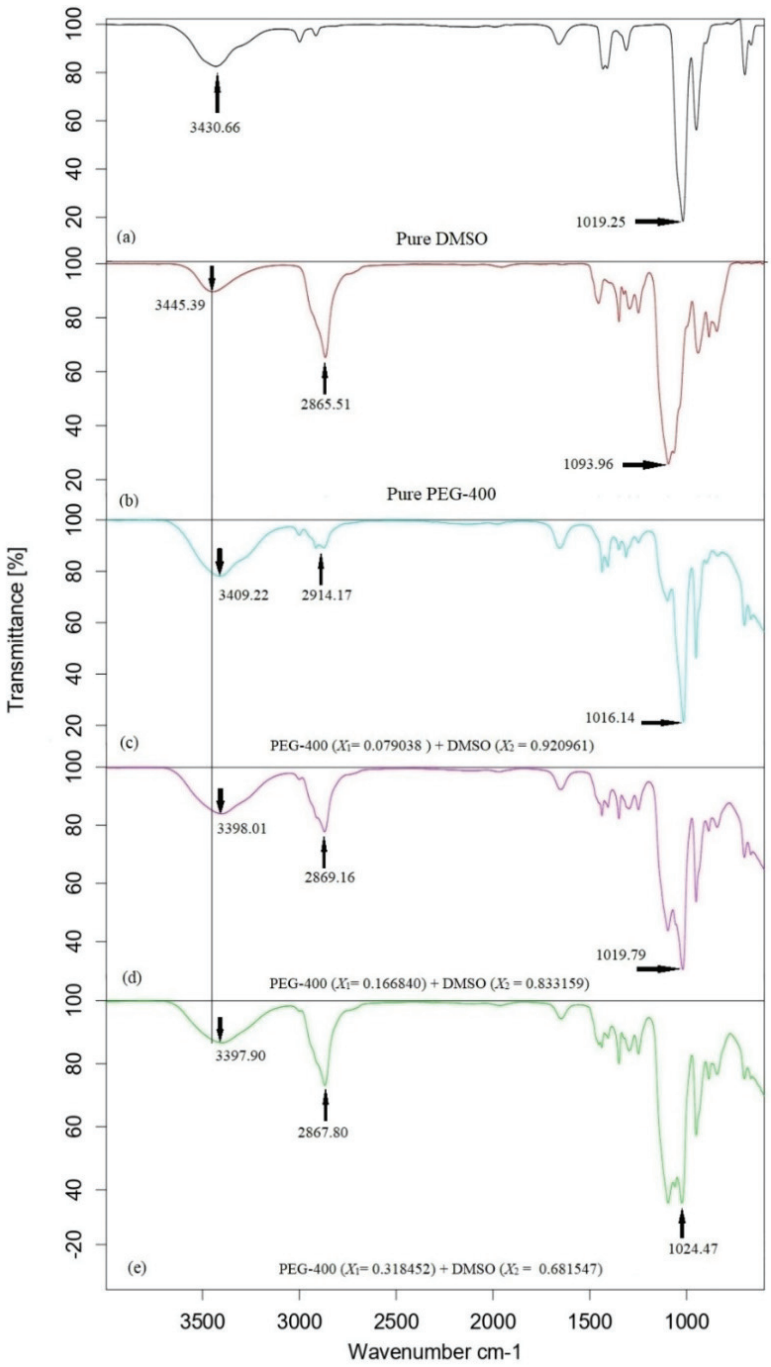

Fig. 8. FTIR spectra of pure PEG-400, pure DMSO and PEG-400 + DMSO at different concentrations.

H-bonding between PEG-400 and DMSO molecules. Moreover, when the amount of PEG-400 (solute) is increased in the mixture the peak, at wave number 1019.25 cm^{-1} of pure DMSO (Fig. 8a), splits into two peaks. It indicates the presence of intermolecular interactions and the formation of a dimmer in the system.[19] The conclusions based on FTIR spectra of the binary mixtures supplement the findings obtained using the ultrasonic technique for the system.

CONCLUSION

New experimental values of ultrasonic velocity and density have been determined for a polymer mixture of PEG-400 and DMSO at 288.15, 298.15 and 308 K. The validity of various mixing rules for the ultrasonic velocity has also been tested for the given mixtures. Based on the ultrasonic velocity and the density, some important physical parameters and their excess values are also computed. The current investigation confirms the intermolecular H-bonding between PEG--400 and DMSO molecules. The spectroscopic analysis of the given system also confirms the presence of intermolecular H-bonding between PEG-400 and DMSO. Additionally different temperatures. It can be concluded that out of six mixing rules, the Nomoto relation and the Junjie relation are found to be best suited for the given mixture. Overall, this insightful analysis of the given mixtures can find the use in industry for solvent selection, design, extraction and separation processes.

SUPPLEMENTARY MATERIAL

Additional data and information are available electronically at the pages of journal website: https://www.shd-pub.org.rs/index.php/JSCS/article/view/12720, or from the corresponding author on request.

ИЗВОД

ИСПИТИВАЊЕ МОЛЕКУЛАРНИХ ИНТЕРАКЦИЈА БИНАРНИХ МЕШАВИНА PEG-400 И DMSO НА РАЗЛИЧИТИМ ТЕМПЕРАТУРАМА УЛТРАЗВУКОМ И СПЕКТРОСКОПСКОПИЈОМ ИСТРАГЕ

MONIKA DHIMAN[1], ARUN UPMANYU[1]*, DEVINDER PAL SINGH[2] и KAILASH CHANDRA JUGLAN[3]

[1]*Chitkara University Institute of Engineering and Technology, Chitkara University, Punjab, 140401, India,* [2]*Acoustics Research Center, Mississauga, L5A 1Y7, Ontario, Canada и* [3]*Department of Physics, Lovely Faculty of Technology and Sciences, Lovely Professional University, Punjab, India*

У раду су приказани резулати мерења ултразвучне брзине и густине бинарне смеше поли(етилен-гликола), PEG-400 и диметил-сулфоксида (DMSO), при различитим концентрацијама и различитим температурама (288,15, 298,15 и 308,15 K), који су додатно искоришћени за утврђивање неколико физичких параметара као што су адиабатска и изотермална компресија, интермолекуларна слободна дужина, унутрашњи притисак и слободна запремина. Вишак вредности ових параметара је такође израчунат и фитована са Redlich–Kister (R–K) полиномном једначином. Природа, тип и јачина интермолекуларних интеракција присутних у PEG-400 + DMSO смеши објашњени су помоћу основе знака и величине вишка вредности. Поред тога одређени су парцијална запремина,

вишак парцијалне запремине и моларна запремина при бесконачном разблаживању да би се испитале интеракције растворак–растварач. Разна правила мешања као што су идеално правило мешања (U_{im}), Nomoto (U_N), однос зависности од импедансе (U_Z), Junjie (U_J), van Deal–Vangeel (U_V) и теорија фактора судара (U_{CFT}) су употребљена за израчунавање ултразвучне брзине и упоређени са експерименталним резултатима. Nomoto и Junjie једначине најбоље описују испитивану смешу. Систем је такође испитан коришћењем FTIR и UV–Vis спектроскопскопијом. Промена интензитета и померање пика у FTIR и UV–Vis спектрима PEG-400 + DMSO смеше су потврдиле водоничне везе у систему.

(Примљено 7. децембра 2023, ревидирано 22. јануара, прихваћено 2. јуна 2024)

REFERENCES

1. P. Malik, G. Chauhan, P. Kumar, A. Deep, *Liq. Cryst.* **49** (2022) 2008 (https://doi.org/10.1080/02678292.2022.2094006)
2. P. Kumar, V. Sharma, P. Malik, K. K. Raina, *J. Mol. Struct.* **1196** (2019) 866 (https://doi.org/10.1016/j.molstruc.2019.06.045)
3. S. Tian, Y. Hou, W. Wu, S. Ren, J. Qian, *J. Hazard. Mater.* **278** (2014) 409 (https://doi.org/10.1016/j.jhazmat.2014.06.037)
4. K. T. Lee, A. R. Mohamed, S. Bhatia, K. H. Chu, *J. Chem. Eng.* **114** (2005) 171 (https://doi.org/10.1016/j.cej.2005.08.020)
5. T. Zhao, J. Zhang, B. Guo, F. Zhang, F. Sha, X. Xie, X. Wei, *J. Mol. Liq.* **207** (2015) 315 (https://doi.org/10.1016/j.molliq.2015.04.001)
6. K. Zhang, J. Yang, X. Yu, J. Zhang, X. Wei, *J. Chem. Eng. Data* **56** (2011) 3083 (https://doi.org/10.1021/je200148u)
7. J. Rodríguez-Sevilla, M. Álvarez, G. Limiñana, M. C. Díaz, *J. Chem. Eng. Data* **47** (2002) 1339 (https://doi.org/10.1021/je015538e)
8. D. Nagel, R. de Kermadec, H. G. Lintz, C. Roizard, F. Lapicque, *Chem. Eng. Sci.* **57** (2002) 4883 (https://doi.org/10.1016/S0009-2509(02)00283-X)
9. F. Han, J. Zhang, G. Chen, X. Wei, *J. Chem. Eng. Data* **53** (2008) 2598 (https://doi.org/10.1021/je800464t)
10. S. Trivedi, C. Bhanot, S. Pandey, *J. Chem. Thermodyn.* **42** (2010) 1367 (https://doi.org/10.1016/j.jct.2010.06.001)
11. A. Upmanyu, M. Dhiman, D. P. Singh, H. Kumar, *J. Mol. Liq.* **334** (2021) 115939 (https://doi.org/10.1016/j.molliq.2021.115939)
12. B. V. Kumar Naidu, K. C. Rao, M. C. S. Subha, *J. Chem. Eng. Data* **47** (2002) 379 (https://doi.org/10.1021/je0101395)
13. M. Dhiman, K. Singh, J. Kaushal, A. Upmanyu, D. P. Singh, *Acta Acust. United Acust.* **105** (2019) 743 (https://doi.org/10.3813/AAA.919354)
14. M. Rani, S. Gahlyan, A. Gaur, S. Maken, *Chin. J. Chem. Eng.* **23** (2015) 689 (https://doi.org/10.1016/j.cjche.2014.12.003)
15. P. Kaur, N. Chakraborty, K. C. Juglan, H. Kumar, *J. Mol. Liq.* **315** (2020) 113763 (https://doi.org/10.1016/j.molliq.2020.113763)
16. D. P. Gupta, A. Upmanyu, M. Dhiman, D. P. Singh, Estimation of ultrasonic velocity and viscosity of polymer solutions of HTPB+ chlorobenzene at different temperatures, AIP Conf. Proc., AIP Publishing, Melville, NY, 2022 (https://doi.org/10.1063/5.0080974)
17. A. Ali, A. K. Nain, V. K. Sharma, S. Ahmad, *Phys. Chem. Liq.* **42** (2004) 375 (https://doi.org/10.1080/00319100410001679882)

18. M. Umadevi, R. Kesavasamy, K. Rathina, R. Mahalakshmi. *J. Mol. Liq.* **219** (2016) 820 (https://doi.org/10.1016/j.molliq.2016.03.085)
19. L. Ma, F. Sha, X. Qiao, Q. Li, J. Zhang, *Chin. J. Chem. Eng.* **25** (2017) 1249 (https://doi.org/10.1016/j.cjche.2017.01.001)
20. G. Arivazhagan, A. Elangovan, R. Shanmugam, R. Vijayalakshmi, N. K. Karthick, *J. Mol. Liq.* **214** (2016) 357 (https://doi.org/10.1016/j.molliq.2015.10.062)
21. L. M. Madikizela, P. S. Mdluli, L. Chimuka, *React. Funct. Polym.* **103** (2016) 33 (https://doi.org/10.1016/j.reactfunctpolym.2016.03.017)
22. T. S. Krishna, K. Raju, M. Gowrisankar, A. K. Nain, B. Munibhadrayya, *J. Mol. Liq.* **216** (2016) 484 (https://doi.org/10.1016/j.molliq.2016.01.085)
23. A. Awasthi, J. P. Shukla, *Ultrasonics* **41** (2003) 477 (https://doi.org/10.1016/S0041-624X(03)00127-6)
24. P. Malik, S. Kumar, Khushboo, A. Upmanyu, P. Kumar, P. Malik, *Liq. Cryst.* **49** (2022) 1604 (https://doi.org/10.1080/02678292.2022.2102684)
25. O. E.-A. A. Adam, A. A. Hassan, *Phys. Chem. Liq.* **56** (2018) 55 (https://doi.org/10.1080/00319104.2017.1292424)
26. N. Chaudhary, A. Kumar Nain, *Phys. Chem. Liq.* **58** (2020) 736 (https://doi.org/10.1080/00319104.2019.1636378)
27. M. T. Zafarani-Moattar, N. Tohidifar, *J. Chem. Eng. Data* **51** (2006) 1769 (https://doi.org/10.1021/je0601715)
28. M. T. Zafarani-Moattar, N. Tohidifar, *J. Chem. Eng. Data* **53** (2008) 785 (https://doi.org/10.1021/je700651e)
29. H. Patel, Z. S. Vaid, U. U. More, S. P. Ijardar, N. I. Malek, *J. Chem. Thermodyn.* **99** (2016) 40 (https://doi.org/10.1016/j.jct.2016.02.025)
30. F. M. Sannaningannavar, B. S. Navati, N. H. Ayachit, *J. Therm. Anal. Calorim.* **112** (2013) 1573 (https://doi.org/10.1007/s10973-012-2724-5)
31. J. G. Baragi, M. I. Aralaguppi, T. M. Aminabhavi, M. Y. Kariduraganavar, A. S. Kittur, *J. Chem. Eng. Data* **50** (2005) 910 (https://doi.org/10.1021/je049610v)
32. S. Baluja, R. M. Talaviya, *J. Chem. Eng. Data* **61** (2016) 1431 (https://doi.org/10.1021/acs.jced.5b00627)
33. V. K. Syal, S. Chauhan, R. Gautam, *Ultrason.* **36** (1998) 619 (https://doi.org/10.1016/S0041-624X(97)00104-2)
34. D. Keshapolla, R. L. Gardas, *Fluid Phase Equilib.* **383** (2014) 32 (https://doi.org/10.1016/j.fluid.2014.09.022)
35. T. Zhao, Q. Xu, J. Xiao, X. Wei, *J. Chem. Eng. Data* **60** (2015) 2135 (https://doi.org/10.1021/acs.jced.5b00209)
36. A. Ali, F. Nabi, *J. Dispers. Sci. Technol.* **31** (2010) 1326 (https://doi.org/10.1080/01932690903227469)
37. H. Wang, W. Liu, J. Huang, *J. Chem. Thermodyn.* **36** (2004) 743 (https://doi.org/10.1016/j.jct.2004.04.004)
38. R. K. Shukla, S. N. Dixit, P. Jain, P. Mishra, S. Sharma, *Orbital-Electron. J. Chem.* **2** (2011) 356 (https://periodicos.ufms.br/index.php/orbital/article/view/17980/12479)
39. J. C. De La Torre, *Ann. N. Y. Acad. Sci.* **411** (1983) 293 (https://doi.org/10.1111/j.1749-6632.1983.tb47311.x)
40. M. T. Zafarani-Moattar, H. Shekaari, *J. Chem. Thermodyn.* **38** (2006) 624 (https://doi.org/10.1016/j.jct.2005.07.018)
41. A. Ali, A. K. Nain, D. Chand, R. Ahmad, *Bull. Chem. Soc. Jpn.* **79** (2006) 702 (https://doi.org/10.1246/bcsj.79.702)

42. J. Krakowiak, D. Bobicz, W. Grzybkowski, *J. Mol. Liq.* **88** (2000) 197 (https://doi.org/10.1016/S0167-7322(00)00154-9)
43. H. Shekaari, M. T. Zafarani-Moattar, *Int. J. Thermophys.* **29** (2008) 534 (https://doi.org/10.1007/s10765-008-0395-z)
44. S. R. Dandwate, S. B. Deshmukh, *J. Curr. Pharma Res.* **10** (2020) 3716 (ISSN-2230-7842 CODEN-CPRUE6, www.jcpronline.in/)
45. U. R. Kapadi, S. K. Chavan, O. S. Yemul, *J. Chem. Eng. Data* **42** (1997) 548 (https://doi.org/10.1021/je960216+)
46. G. Ritzoulis, *Can. J. Chem.* **67** (1989) 1105 (https://doi.org/10.1139/v89-166)
47. M. A. Saleh, O. Ahmed, M. S. Ahmed, *J. Mol. Liq.* **115** (2004) 41 (https://doi.org/10.1016/j.molliq.2003.12.021)
48. S. B. Aznarez, L. Mussari, M. A. Postigo, *J. Chem. Eng. Data* **38** (1993) 270 (https://doi.org/10.1021/je00010a022)
49. S. Parveen, D. Shukla, S. Singh, K. P. Singh, M. Gupta, J. P. Shukla, *Appl. Acoust.* **70** (2009) 507 (https://doi.org/10.1016/j.apacoust.2008.05.008)
50. B. Nagarjun, A. V. Sarma, G. R. Rao, C. Rambabu, *J. Thermodyn.* **2013** (2013) 285796 (https://doi.org/10.1155/2013/285796)
51. A. Zhu, J. Wang, R. Liu, *J. Chem. Thermodyn.* **43** (2011) 796 (https://doi.org/10.1016/j.jct.2010.12.027)
52. A. Ali, A. K. Nain, V. K. Sharma, S. Ahmad, *Phys. Chem. Liq.* **42** (2004) 375 (https://doi.org/10.1080/00319100410001679882)
53. P. R. Bevington, D. K. Robinson, *Data reduction and error analysis for the physical sciences*, McGraw-Hill, New York, 1969, pp. 235–242 (ISBN 0-07-247227-8)
54. M. Dhiman, K. Singh, D. P. Gupta, D. P. Singh, A. Upmanyu, *Study of excess acoustical and thermo-dynamical parameters of binary solutions of polypropylene glycol-400 and n-alkanols at 303 K*, AIP Conf. Proc., AIP Publishing, Melville, NY, 2020 (https://doi.org/10.1063/5.0001107)
55. B. Thanuja, G. Nithya, C. C. Kanagam, *Ultrason. Sonochem.* **19** (2012) 1213 (https://doi.org/10.1016/j.ultsonch.2012.03.006)
56. A. Awasthi, A. Awasthi, *Phys. Chem. Liq.* **51** (2013) 112 (https://doi.org/10.1080/00319104.2012.690569)
57. G. V Rao, A. V. Sarma, D. Ramachandran, C. Rambabu, *Ind. J. Pure App. Phys.* **42** (2004) 820 (http://nopr.niscpr.res.in/handle/123456789/8851)
58. S. F. Babavali, D. Punyaseshudu, K. Narendra, C. S. Yesaswi, C. Srinivasu, *J. Mol. Liq.* **224** (2016) 47 (https://doi.org/10.1016/j.molliq.2016.09.079)
59. M. Dhiman, A. Upmanyu, P. Kumar, D. P. Singh, *Karbala Int. J. Mod. Sci.* **8** (2022) 703 (https://doi.org/10.33640/2405-609X.3270)
60. S. Gahlyan, M. Rani, S. Maken, *J. Mol. Liq.* **199** (2014) 42 (https://doi.org/10.1016/j.molliq.2014.08.011)
61. H. E. Hoga, R. B. Torres, *J. Chem. Thermodyn.* **43** (2011) 1104 (https://doi.org/10.1016/j.jct.2011.02.018).

Journal of the Serbian Chemical Society
JSCS@tmf.bg.ac.rs • www.shd.org.rs/JSCS
J. Serb. Chem. Soc. 89 (10) S361–S364 (2024) *Supplementary material*

SUPPLEMENTARY MATERIAL TO

Ultrasonic and spectroscopic investigations of molecular interactions in binary mixture of PEG-400 and DMSO at different temperatures

MONIKA DHIMAN[1], ARUN UPMANYU[1]*, DEVINDER PAL SINGH[2] and KAILASH CHANDRA JUGLAN[3]

[1]*Chitkara University Institute of Engineering and Technology, Chitkara University, Punjab, 140401, India,* [2]*Acoustics Research Center, Mississauga, L5A 1Y7, Ontario, Canada and* [3]*Department of Physics, Lovely Faculty of Technology and Sciences, Lovely Professional University, Punjab, India*

J. Serb. Chem. Soc. 89 (10) (2024) 1363–1385

Table S-1. Calculated density (d*) (using Equation 1), Literature[1] (d) density along with AAPD for PEG-400 + DMSO at 298.15 K and 308.15 K.

X_1[6]	d[6]	d*	% deviation
298.15 K			
0.0102	1.0979	1.0984	0.0427
0.0213	1.0999	1.0996	0.0284
0.0333	1.1019	1.1008	0.0969
0.0466	1.1033	1.1021	0.1060
0.0611	1.105	1.1035	0.1400
0.0773	1.1067	1.1048	0.1694
0.0952	1.1086	1.1062	0.2146
0.1152	1.1099	1.1076	0.2034
0.1378	1.1117	1.1091	0.2346
0.1633	1.1131	1.1105	0.2293
0.1927	1.1145	1.1120	0.2228
0.2266	1.1157	1.1135	0.1999
0.2662	1.1171	1.1149	0.1979
0.313	1.1184	1.1163	0.1921
0.3691	1.1194	1.1175	0.1676
0.4382	1.1204	1.1187	0.1532
0.5253	1.1211	1.1197	0.1262
0.637	1.1218	1.1205	0.1174
0.787	1.1222	1.1211	0.1020
AAPD			0.1550

* Corresponding author. E-mail: arun.upmanyu@chitkara.edu.in

Table S-I. Continued

X_1[6]	d[6]	d*	% deviation
308.15 K			
0.0102	1.0867	1.0892	0.2311
0.0213	1.0889	1.0903	0.1293
0.0333	1.0911	1.0914	0.0310
0.0466	1.0927	1.0926	0.0066
0.0611	1.0949	1.0939	0.0957
0.0773	1.0966	1.0951	0.1333
0.0952	1.0985	1.0965	0.1854
0.1152	1.1001	1.0978	0.2061
0.1378	1.1015	1.0993	0.2041
0.1633	1.1035	1.1007	0.2534
0.1927	1.1047	1.1022	0.2264
0.2266	1.1063	1.1037	0.2336
0.2662	1.1076	1.1052	0.2131
0.313	1.1088	1.1067	0.1849
0.3691	1.11	1.1082	0.1606
0.4382	1.111	1.1096	0.1244
0.5253	1.112	1.1109	0.0985
0.637	1.1128	1.1120	0.0713
0.787	1.1133	1.1129	0.0378
AAPD			0.1488

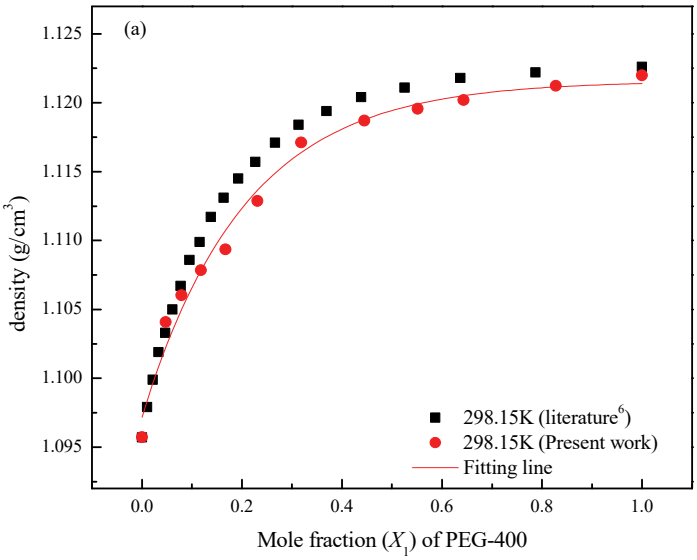

Fig. S-1. Density values from Literature[1] and present work with fitting equation at 298.15 K.

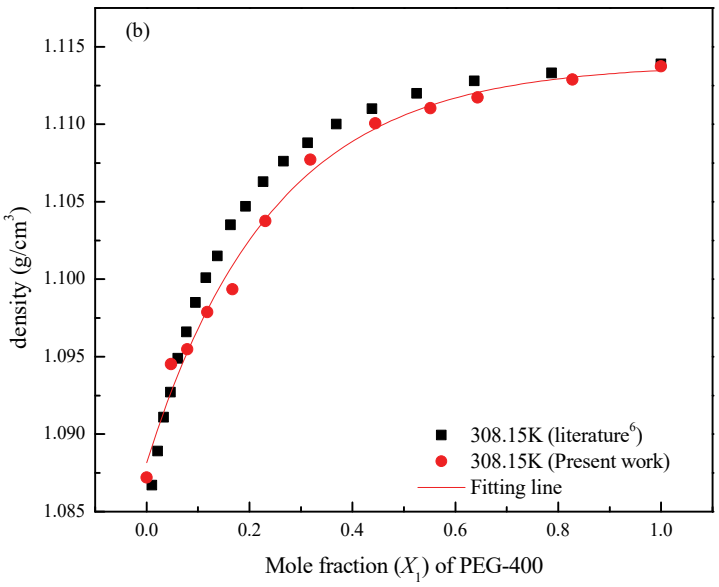

Fig. S-2. Density values from Literature[1] and present work with fitting equation at 308.15 K.

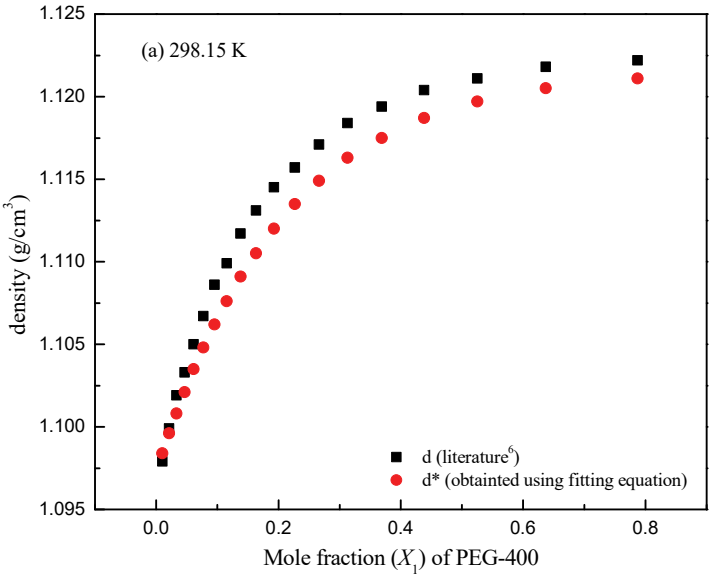

Fig. S-3. Literature[1] and computed density (d*) values 298.15 K.

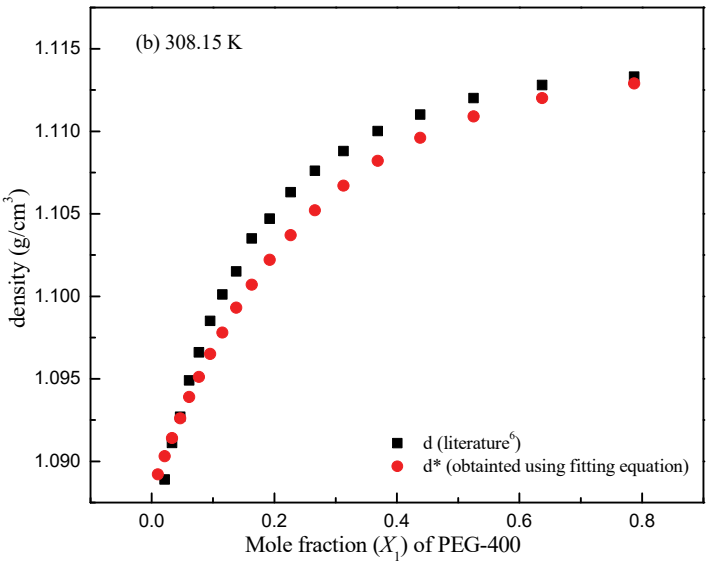

Fig. S-4. Literature[1] and computed density (d*) values 308.15 K.

REFERENCES

1. K. Zhang, J. Yang, X. Yu, J. Zhang, X. Wei, *J. Chem. Eng. Data* **56** (2011) 3083 (https://doi.org/10.1021/je200148u).

Journal of the Serbian Chemical Society
JSCS@tmf.bg.ac.rs • www.shd.org.rs/JSCS
J. Serb. Chem. Soc. 89 (10) 1387–1399 (2024)
JSCS–5794
Original scientific paper
Published 7 November, 2024

Joint characteristics and process parameters optimization on friction stir welding of AA 2024-T6 and AA 5083-H111 aluminum alloys

S. SAKTHIVEL*• and K. MOHAN

Department of Mechanical Engineering, K.S. Rangasamy College of Technology, Tiruchengode-637215, Namakkal, Tamil Nadu, India

(Received 21 September, revised 21 November, accepted 22 December 2023)

Abstract: Friction stir welding (FSW) is a recent method for welding in a solid--state environments. The FSW parameters, namely pin rotation speed, welding speed, axial force and tool tilt angle affect weld joint microstructure and tensile strength. The study optimizes process settings to enhance mechanical properties and uses Response surface methodology (RSM) to predict the ultimate tensile strength (*UTS*) of FS-welded AA 2024-T6 and AA 5083-H111.These parameters must be understood in order to get optimal mechanical qualities in manufacturing. The created model predicted tensile strength within 5 % of experimental data, helping optimize process parameters for FSW joints. Tool tilt angle affects heat, material flow, defect generation, welding force, and friction stir weld joint quality.

Keywords: aluminum alloys; friction stir welding; optimization; tensile strength.

INTRODUCTION

A new approach for joining the metals in solid-state conditions is friction stir welding (FSW). This welding is called green welding since it does not emit oxide fumes as the conventional joining procedures do. A rotating pin is inserted into the material and moved along the joint line after “dwell time”. A weld junction forms as material flows from the advancing to the receding weldment. The friction between the tool and workpiece minimizes the flow stress around the pin and shoulder. In order to identify the complex flow pattern in a cylindrical tool, a friction stir forming model was developed by employing the particle streamline tracing techniques.[1] Dissimilar joints of AA 5083 and mild steel were evaluated.[2] The experimental design predicted the mechanical characteristics and microstructure

* Corresponding author. E-mail: sundaramsakthivel791@gmail.com
• S. Sakthivel is research Scholar at Dept. of Mech. Eng., K. S. Rangasamy College of Technology, Tiruchengode-637215, Namakkal, Tamil Nadu, India.
https://doi.org/10.2298/JSC230920100S

of the heterogeneous AA 5083-AA 6061 joints.[3] The results revealed that the tool rotation speed affected joint tensile characteristics more than tool pin diameter. FSW testing on AA 6351 and AA 5083 alloys used continuous plunging force, tool rotating speed, and welding speeds with different tool probes.[4] The data showed that straight square probe joints had higher tensile strength. The mechanical properties of dissimilar alloys of aluminum and copper at different tilt angles were examined, and a tool tilt angle of 4° produced defect-free joints with excellent strength and hardness.[5] FSW joints manufactured from 2024 and 7075 aluminum alloys showed a refined microstructure and good mechanical properties, including high tensile strength and flexibility. The effects of different circumstances on microstructure and mechanical qualities were studied using the optimal welding parameters for high-quality joints.[6] Al-2024 and Al-7039 weld joints with a heterogeneous composition of base metals were studied and the failure occurred when the Cu and Zn were in excess.[7] Dissimilar weld joints on AA 6061 and AA5052 alloys exhibited a fine-grained nugget zone with an equiaxed orientation.[8] RSM was used to create the regression models and examine the friction stir welding response variables. A mathematical model predicted the friction stir-welded 6061 aluminum alloy joint tensile strength.[9] The ultimate tensile strength, yield strength, and elongation of friction stir welded aluminum 5083-H111 and 6082-T6 alloys were examined.[10] FSW was done on AA 2024 and AA 6061 plates utilizing RSM to maximize elongation and ultimate strength with a suitable FSW pin profile.[11] The aluminum alloys of AA 6101-T6 and AA 1350 AA 5052 and AA 6101 plates were linked, and statistical analysis showed that traverse speed affected weld characteristics.[12,13] Rotational speed, welding speed, tool tilt angle, and axial force must be changed to produce these properties.[14] According to the literature, the researchers prefer RSM by employing different pin profiles for different materials to produce high-quality welds for aviation structural parts. To the authors' knowledge, AA 5083-H111 and AA 2024-T6 dissimilar joints are limited by the huge ranges of four parameters within the authorized scale. In this work, the authors focused on developing a statistical model to predict the strength of the joints within the selected range of parameters. The effects of the input parameters with respect to the tensile strength model will shed new light on the material science and engineering by the optimization of process parameters and characterizing FS welded AA 2024-T6 and AA 5083-H111 alloys.

EXPERIMENTAL PROCEDURE

Materials, methods, and experimentation

The study used 5 mm thick rolled AA 2024-T6 and AA 5083-H111 aluminum alloy plates cut to 100 mm×150 mm. Fig. 1a and b illustrate the clamping mechanism and weld joint sample used to hold the plates rigidly clamped in the fixture, respectively. The shank portion of the tool was held in the spindle. AA2024-T6 was fixed in the advancing side and in the retreating side AA5083- H111 was fixed. The rotating tool pin would plunge into the workpiece surface with

a dwell time, the required spindle speed, axial load, welding speed and tilt angles, which were given as input parameters to complete the weld. Owing to its increased stirring action and the material flow, high-carbon steel and non-consumable hexagon pin tools were used to fabricate the joints. The four-sided tool pin rotated well with the shear and mixed materials. The base metals in AA 2024-T6 are 93.35 Al, 4.3 Cu, 1.315 Mg, 0.522 Mn, 0.09 Si, 0.116 Fe, 0.041 Zn, 0.005 Cr, 0.005 Ni, 0.013 Ti and, for in AA5083, the constituent metals are 93.68 Al, 0.067 Cu, 4.8 Mg, 0.744 Mn, 0.1 Si, 0.231 Fe, 0.096 Zn, 0.092 Cr, 0.009 Ni, 0.017 Ti. Fig. 1c shows the specimen preparation of tensile strength as per ASTM E8 standard using electrical discharge machine. The base final tensile strengths of 397 and 316 MPa were achieved after the tensile test. The process parameters were varied by three levels and four parameters having the rotational speed of 600, 1050 and 1500 rpm, the traverse speed of 30, 45 and 60m/min and the tilt angle of 1, 2, 4 and 5°, and axial load of 3, 6 and 9 kN were chosen. The weld joints were subjected to the tensile testing machine having a load range of 5 tons with a load accuracy of 0.1 N and cross head speed accuracy of 0.01 mm. Initially, the samples are prepared for 10 mm×10 mm and it is mounted in the press and grinding is done using different grades of emery fineness papers, while polishing is carried out to remove scratches through a rotatable disc polishing machine, for microstructure analysis Weck's reagent is used (4 g $KMnO_4$, 1 g of NaOH and 100 mL H_2O for 20 s). Then the samples were subjected to close examination through the metallurgical microscope 5 MP camera and images were taken using De-winter Material plus version-2, Model JEOL JSM7001F for characterizing the weld joints by the scanning electron microscopy.

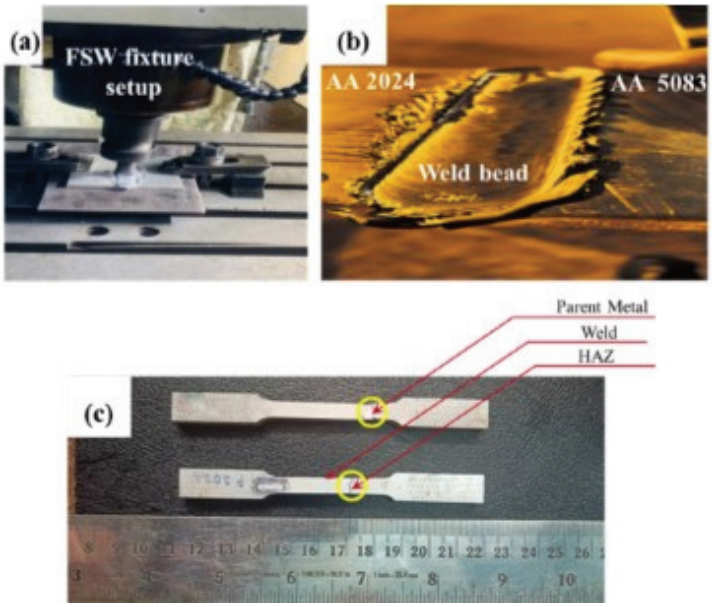

Fig. 1. a) Friction stir joining processes; b) FSW plate; c) fractured specimens.

RESULTS AND DISCUSSION

Welded joints with varied parameters were subjected to tests relating to tensile strength, and their results are discussed based on RSM; the microstructure and

fractography characterization are also discussed. Maximum and minimum tensile strengths of 320 and 284 MPa were obtained, as shown in Fig. 2.

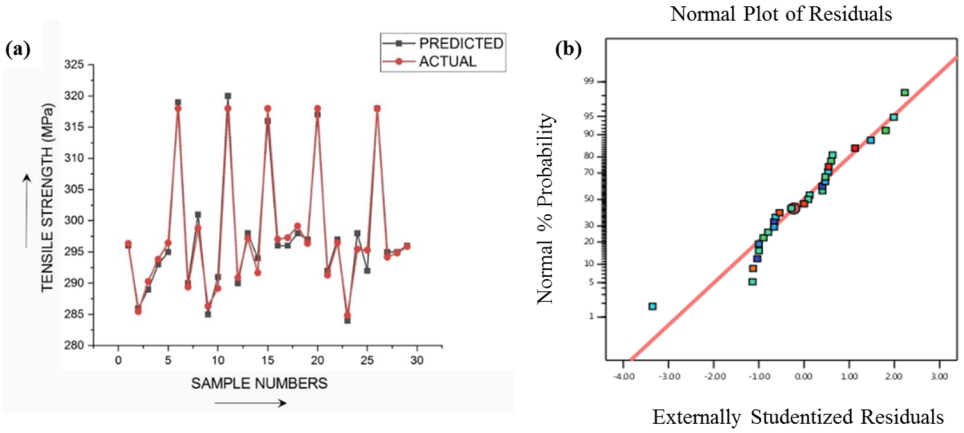

Fig. 2. a) Predicted *vs*. actual tensile strength; b) probability curve for predicted *vs*. actual tensile strength.

The TS response ANOVA results for the second-order polynomial regression model are presented in Table I. *F*-value and *P*-value determined the model and the coefficient significance. The model and coefficients were more significant, with a higher *F*-value and lower *P*-value. With an *F*-value of 8.3 and a *P*-value of 0.0001, the hypothesis is quite significant. If the *P*-value of the predicted coefficients is less than 0.05, the variables in the model are essential. If it was greater than 0.1, it was not significant. This model includes the major effects of welding speed (*B*), tilt angle (*C*) and axial load (*D*), the interaction terms *AB*, *AC* and *BC*; and the quadratic terms A^2, B^2, C^2 and D^2. According to the *F*-values, $D^2 > C^2 > B^2 > A^2 > BC > AC > AB > D > C > B$ were the most relevant parameters. The model is adequate with the estimated R^2 and adjusted R^2 values of 0.9809 and 0.9619, respectively. The multiple regression analysis of the experimental data yielded the following mathematical model in terms of coded parameters:

$$\text{Tensile strength} = 318.00 - 1.00A + 1.42B + 1.25C - 1.33D + 4.50AB + \\ + 4.50AC - 1.50AD - 5.00BC + 1.75BD + 0.7500CD - 14.00\,A^2 - \\ - 11.62\,B^2 - 12.38\,C^2 - 11.00\,D^2$$

Effect of tool rotational speed and welding speed

Choosing the correct tool rotational speed is essential for the welding success. It directly affects process heat generation, material flow and mixing.[15] Low rotating speed may not generate enough heat, resulting in poor material mixing and weak joints. Conversely, high rotational speeds can generate excessive heat, producing material flaws or tool wear.[16] A frequent case shows that tool rotation speed

impacts joint tensile strength, as seen in Fig. 3a and b. Joint tensile strength is lower than basic aluminum alloys at all tool rotating speeds. UTS escalates from 600 to 1050 rpm, and it lowers when the tool rotational speed is increased further.

TABLE I. ANOVA for tensile strength

Source	Sum of squares	*df*	Mean square	*F*-value	*P*-value	Model
Model	2885.71	14	206.12	51.45	< 0.0001	Significant
A-rotational speed	12	1	12	3	0.1055	
B-traverse speed	24.08	1	24.08	6.01	0.0279	
C-tilt angle	18.75	1	18.75	4.68	0.0483	
D-axial load	21.33	1	21.33	5.33	0.0368	
AB	81	1	81	20.22	0.0005	
AC	81	1	81	20.22	0.0005	
AD	9	1	9	2.25	0.1561	
BC	100	1	100	24.96	0.0002	
BD	12.25	1	12.25	3.06	0.1022	
CD	2.25	1	2.25	0.5617	0.466	
A^2	1271.35	1	1271.35	317.37	< 0.0001	
B^2	876.59	1	876.59	218.82	< 0.0001	
C^2	993.34	1	993.34	247.97	< 0.0001	
D^2	784.86	1	784.86	195.92	< 0.0001	
Residual	56.08	14	4.01			
Lack of fit	46.08	10	4.61	1.84	0.2915	Not significant
Pure error	10	4	2.5			
Cor Total	2941.79	28				
					R^2	0.9809
					Adjusted R^2	0.9619

Micro-voids and micro-tunnels occur in the nugget owing to the limited heat release at slow rotation, resulting in undesirable mechanical properties (Fig. 3b). The rotational speed promotes plasticizing metal heat and turbulent motion.[17] The range of tool rotational rates that can generate strong joints is restricted, and the UTS is particularly sensitive to speeds exceeding 1050 rpm. During FSW, friction and plastic deformation generate heat. The material yield strength and slide rate determine the deformation heat. At 600 rpm, the combined effects of heating and strain rate produce an IMC layer that is thin at the joint interface and does not spread IMCs in the stirred zone (SZ). A higher rotating speed may generate heat and material swirling to produce a thick intermetallic layer at the interface, particularly on the top side of the joint where the tool comes in contact. The frictional heat generation is 33 % higher at 1050 than at 600 rpm, resulting in a thicker IMC layer along the joints, which may explain the low tensile strength at this speed, as shown in Fig. 3c and d.

The tool generates 11 % less heat at 1050 than at 600 rpm; therefore, less intense material stirring may not be sufficient to form IMC across the contact,

especially in the lower joint farthest from the tool shoulder. The low joint strength may come from the 600 rpm base bonding. The FSW heat has increased the weaker zone of the foundation material, toughening it. High heat generation has delayed cooling, allowing the strengthening phases to recoil and coarse grains in the nugget to soften. Changing the tool speed creates a fine and sound weld zone with better efficiency. Precipitate dissolution, defect formation, grain coarsening, and micro--gap coalescence have weakened owing to the insufficient rotational speed of the tool (Fig. 3d).

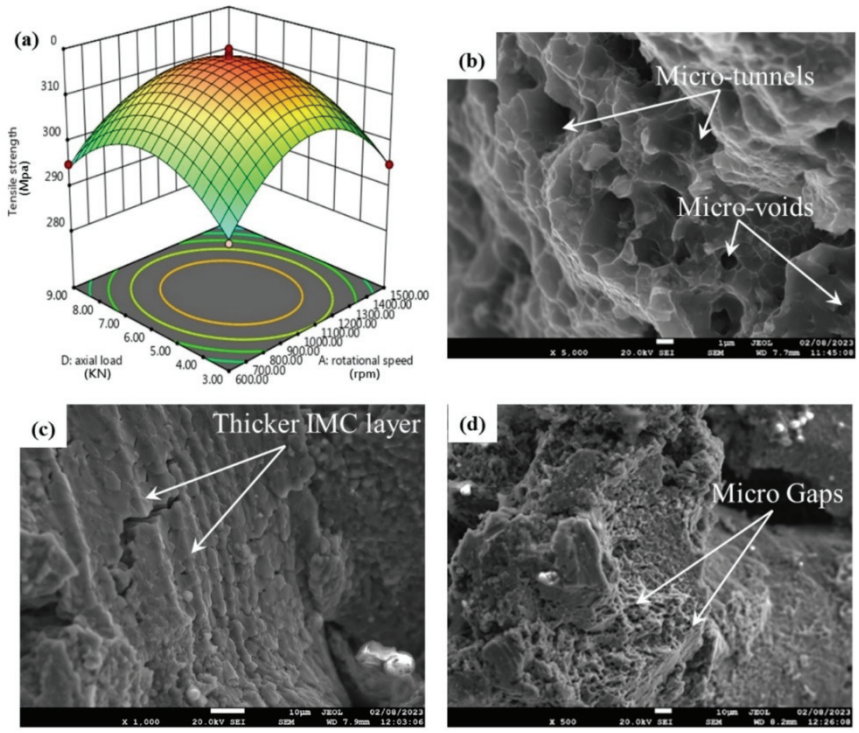

Fig. 3. a) Effect of tool rotational speed on tensile strength; b) micro-voids and micro-tunnels; c) thicker intermetallic layer (IMC); d) micro-gaps observed through scanning electron microscopy.

The tool moves along the joint at the welding speed. This severely affects the weld quality and integrity. The material flow, microstructural evolution, and heat input depend on the welding speed. The tool rotation speed, welding speed, tilt angle, axial force, and plunge depth affect the welded junction quality.[18] Fig. 4a shows the influence of welding speed in the tensile strength. The insufficient heat input at high welding speeds can result in incomplete mixing, top groove faults and material bonding.[19] Low welding speeds increase heat input, material distortion,

defects and metallurgical changes. Strong welds require the correct speed. Material mixing and bonding must be balanced by minimizing the heat input.

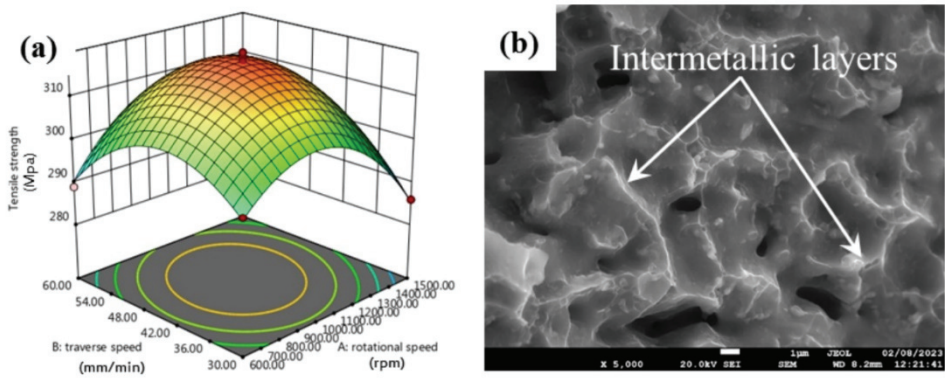

Fig. 4. a) The effect of welding speed on tensile strength; b) IMC layer at low welding speed.

The highest UTS is 45 mm/min. The UTS has changed proportionally with the welding speed on both sides of the maximum. The peak tensile strength of the joint has decreased by less than 10 %. Slow welding produces greater heat but less strain.[20] The speed of the welding has had a beneficial as well as detrimental impact on the formation of the interface IMC layer. Fig. 4b shows that when the welding speed has increased, the fewer IMCs are formed.[21] The heat has increased when the UTS declines from 30 to 45 mm/min. Moderate speeds provided a thin IMC layer at the interface, making the weld durable despite a high heat output. The UTS has dropped by 8 % with 60 mm/min welding. An increased FSW welding speed reduces metallurgical changes owing to the lower heat inputs and rapid joint cooling. Faster welding velocities provide less heat, but the IMC layer strain rate increases bond strength.[22]

Effect of axial load and tool tilt angle

Axial force is important in FSW, and it affects the weld strength and product quality. The axial force in FSW must be understood to obtain optimal results. The right axial force ensures a robust and consistent weld. This force helps to fuse materials together, resulting in a high-quality joint.[23] As shown in Fig. 5a, a low axial force might cause partial penetration and poor mixing of materials, reducing the weld strength.

The FSW joints have lost the tensile strength when the axial force is below 3 kN. The tensile strength has increased linearly from 3 to 6 kN. The tensile strength of the joint reduced when the axial force of 9 kN. All the welded joints exhibit this pattern, regardless of the tool inclination.

As can be seen in Fig. 6a the joints produced with AA 2024-T6 at a lower axial force of 3 kN have featured tunnel flaws on the advancing side of the joint,

leading to low tensile strength.[24] The weld joints subjected to a 9 kN axial stress have exhibited satisfactory welds; nevertheless, the presence of extra shear fractures on both sides have led to unfavorable tensile properties.

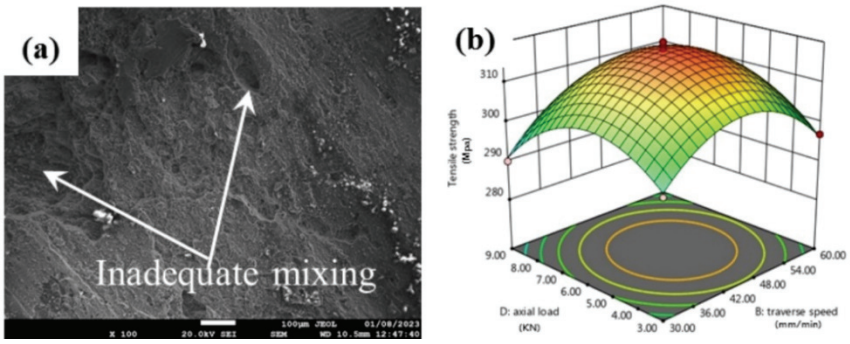

Fig. 5 a) Inadequate mixing observed through SEM; b) effect of welding speed on tensile strength.

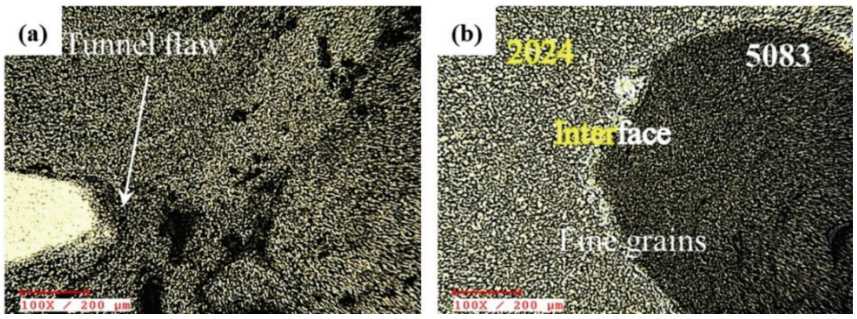

Fig. 6 a) Tunnel flaws defect in fabricated sample; b) material flow in the weld zone.

FSW frictionally heats, plasticizes, mixes, and extrudes two parts using a revolving pin-shoulder tool.[25] The linear weld load characteristics focus on the tool forces, particularly the shoulder force that governs the tool pin plunge depth into the workpiece. Tool rotation under static conditions can heat and plasticize the material. The shoulder force that controls the tool pin plunge depth into the workpiece changes significantly along the joint line. Extrusion moves the material after plastic deformation with applied forces and tool pin motion.[26] The extension of the tool pin into the workpiece depends on shoulder force.[27]

Fig. 7 shows the effect of the tool-tilt angle on the tensile strength. The inclination of the tool is relative to the workpiece surface.[28] The tool tilt angle affects the welding, the friction between the pins, and the plates are increase the heat with a larger tilt angle, which improves the material softening and mixing.[29] Void, porosity and weld joint penetration can result from an improper tool tilt angle.

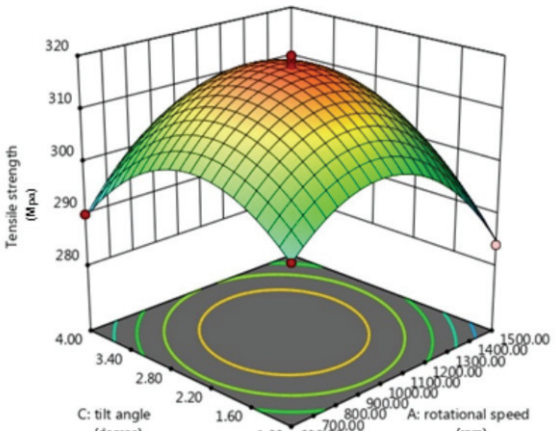

Fig. 7. Effect of tool tilt angle on tensile strength.

When the tool is tilted by 2.5°, the UTS drops by 1 % from the maximum value. The UTS decreases by 3 % when the tool tilt angle exceeds 4°. Tilting the tool enhances stirring, prevents shoulders from plunging, and increases the trailing side forging pressure, which consolidates the material.[30] However, tilting the tool beyond a certain degree affects the frictional coefficient, heat output, and material consolidation, causing the weld joint defects, including voids and pinholes, as shown in Fig. 8a. Thus, material mixing and coalescence under heat generation may explain the higher UTS projected at tool tilt angle of 2.5°. A review was conducted on the broad area of FSW and dealt with finding main process parameters of dissimilar alloys and prediction of mechanical behaviour of FSW joints. It is revealed that keeping tilt angles of 1 and 2.5° shows good plasticization besides avoiding the defects in the joints.[34]

Material straining and coalescence lower the UTS at lower tool tilt angles, heat production, and straining rate, and lower coalescence at tilt angles up to 2.5° as shown in Fig. 8b. The material strain rate increases when the tool tilt angle exceeds 4.5°; however, the effective drop in the heat output and material flow may induce a larger UTS drop. The movement of the elements and the mixing of the bonded materials improved as the tilt angle increased.[31] An improved material flow increased the mechanical characteristics of the weld joint. The mild UTS loss may be due to the reduced straining and coalescence at low tool tilt angles and increased straining rate, coalescence, and heat output at high tilt angles of up to 2.5°.

Characterization

The welding tool rotates and mixes the material, creating a unique onion ring structure, for maximum observed tensile strength of 320 MPa (Fig. 9a) which gradually transforms into a “V” shape pattern. Fig. 9b shows that the SZ formed a basin when the input heat has decreased or the cooling rate has increased. Without

the onion rings, the material viscosity improves, the strain rate increases, and the welding tool affects the material more.

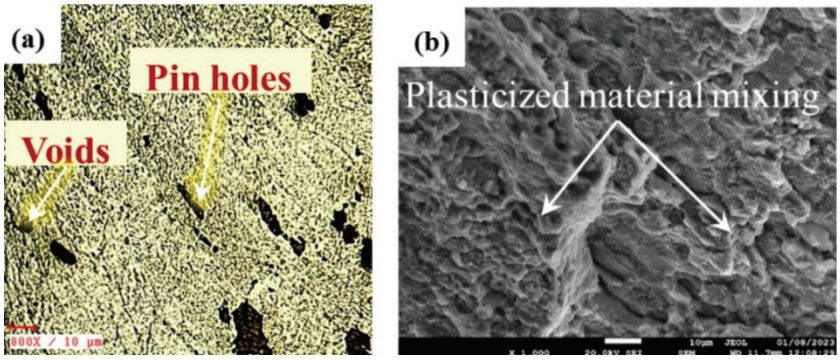

Fig. 8. a) Voids and pinholes; b) improved material mixing and coalescence during FS welding.

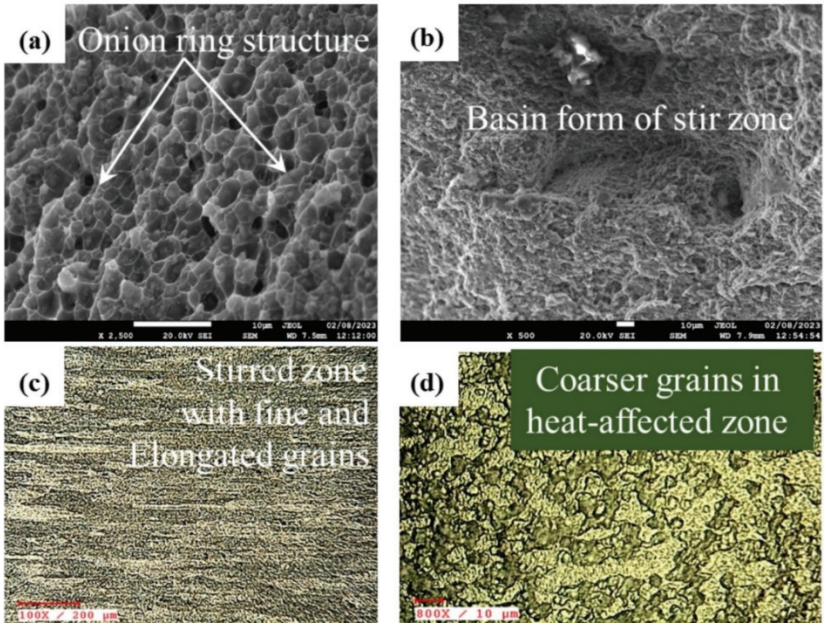

Fig. 9. a) Onion ring structure; b) basin form of stir zone; c) stirred zone (SZ); d) heat-affected zone (HAZ).

Fig. 9c illustrates the sample's stirred zone (SZ) and heat-affected zone (HAZ) cross-sectional microstructures. The dynamic recrystallization of aluminum grains is controlled by the temperature and cooling rate.[32,33] Many dislocations were observed in the induced grain boundaries when the magnification improved above 800×, as it is shown in Fig. 9d. Grain boundaries and recovery occur when there

are too many dislocations. During the mechanical stirring forced by the welding tool, these grain boundaries fluctuate and rotate. Recrystallized grains develop when the grain borders absorb the dislocations from the neighbouring grains.

CONCLUSIONS

- The friction stir welding was carried out using FSW machine and the maximum tensile strength was observed to be 320 MPa. From the ANOVA Table I it is concluded that the selected models are significant due to the value less than 0.0001.
- The R^2 value 0.9809 and the adjusted R^2 value 0.9619 are very close so that the predicted and the experimental values do not have much deviation.
- The increased heat generation and the material swirling at higher rotational rates may result in the creation of a thick IMC layer at the interface, particularly at the top portion of the joint where the tool shoulder engages.
- The inadequate bonding at the joint base at 600 rpm is likely to be the root because of its low joint strength.
- The forces produced by the tool, particularly the shoulder force that is directly responsible for the plunge depth of the tool pin into the workpiece, have been the primary focus of load characteristics associated with a linear weld.
- A greater decrease in the UTS is likely to have been caused by a decrease in heat production and material fusion when the tool tilt angle exceeds 4.5°, despite the increase in the substrate rate of strain.
- Varying the rate of welding has had both favorable and detrimental impacts on the IMC layer formation at the interface. By increasing the traverse speed, the degree of metallurgical changes may be reduced, the lower heat inputs are linked to the rapid cooling of the welded joint.

Acknowledgements. The authors are very much thankful to K. S. Rangasamy College of Technology.

ИЗВОД

КАРАКТЕРИСТИКЕ ЗАВАРЕНОГ СПОЈА И ОПТИМИЗАЦИЈА ПОСТУПКА ЗАВАРИВАЊА ТРЕЊЕМ МЕШАЊЕМ АЛУМИНИЈУМСКИХ ЛЕГУРА AA 2024-T6 И AA 5083-H111

SAKTHIVEL SUNDARAM и MOHAN KUMARASAMY

Department of Mechanical Engineering, K. S. Rangasamy College of Technology, Tiruchengode, Namakkal, Tamil Nadu, India

Заваривање трењем са мешањем (FSW) је савремени поступак спајања материјала у чврстом стању, без топљења и без употребе додатних супстанци. Најважнији параметри овог процеса: брзина ротације алата (трна), брзина заваривања, подужна сила и угао конуса алата (трна), утичу на карактеристике завареног споја, односно на микроструктуру и затезну чврстоћу. У овом раду је коришћена методологија одзивне површине (RSM) са циљем да се обезбеди могућност предвиђања и оптимизације затезне чврстоће завареног споја између легура AA 2024-T6 и AA 5083-H111. Разумевање утицаја свих параметара FSW поступка омогућава постизање оптималне чврстоће завареног споја. Вредности затезне чврстоће